University of California
Santa Barbara

High-pressure bulk crystal growth for scattering studies of quantum magnets

A dissertation submitted in partial satisfaction
of the requirements for the degree

Doctor of Philosophy
in
Materials

by

Eli Alexander Bell Zoghlin

Committee in charge:

Professor Stephen D. Wilson, Chair
Professor Susanne Stemmer
Professor Andrea F. Young
Professor John W. Harter

September 2022

The Dissertation of Eli Alexander Bell Zoghlin is approved.

Professor Susanne Stemmer

Professor Andrea F. Young

Professor John W. Harter

Professor Stephen D. Wilson, Committee Chair

August 2022

High-pressure bulk crystal growth for scattering studies of quantum magnets

Eli Alexander Bell Zoghlin

To the singing mailman, who never failed to deliver.

Acknowledgements

The work described in this thesis was performed on the unceded ancestral territory of the Chumash people. No matter how noble our current activities may be, it is important to remember that everything in Santa Barbara rests, at some point, on a bedrock of conquest, slavery and genocide.

A great expression of thanks is due to my parents, Jason and Rochelle, for their constant support and encouragement during my many years of higher education. They are a large part of how I made it to, and through, graduate school. While they failed to teach me much about neutron scattering when I was growing up, one could not ask for better parents to instill a solid work ethic and sense of self-confidence; both have been invaluable. Recognition is also due to my sister, Emma, for, among many things, always taking care of the Mothers/Fathers Day gifts. I promise to atone for my slacking now that the distraction of graduate school is over.

I have had the great privilege to live in three cooperative spaces during graduate school: the Dolores and Merton houses in Isla Vista (both part of the Santa Barbara Student Housing Cooperative) and Persimmon house in Santa Barbara. Having these places to come home to made all the difference during the many trials and tribulations faced while conducting this work. Dolores, in all its ramshackle beauty and unending disarray, was my home for my first four-and-a-half years of graduate school. I will always be grateful for the opportunities I had to build and experience community during my time there. Many thanks to my Persimmon housemates for welcoming me into a wonderful cooperative space downtown once my time in IV came to an end. Thank you to Merton house, for allowing me into your community in my last few months in Santa Barbara. Among the many, many different housemates I have had over the years (roughly 50 by my count), a few deserve special acknowledgement. Thank you to Zack Stoltz and Paige

Bradford for your friendship and support, as well as many game nights. I owe a special debt to my dear friend Andrew Ryan Johnson, who modeled for me how to best entwine the experiences of cooperative living and graduate school. Finally, a host of warm and fuzzy adjectives are due to Nadia Lee Abushanab, who I had the privilege to live with most of my time in Santa Barbara. Thank you for everything: for being my friend through thick and thin, for all of our many adventures, and for reminding me that our inescapable mortality demands doing more with my time than lab work. I am also also immensely grateful for the pre-UCSB friends whose lives I have had joy to catch up on over the years. A particular acknowledgement is due to my dear friend and fellow Carnegie Mellon Materials Department alumnus, Allison Perna, who is currently working on a PhD herself. Thank you for the phone calls filled with commiseration and mutual validation, as well as the visits and vacations filled with adventure.

No graduate student labors alone and I am grateful for all the past and current members of the Wilson group who I got to work with. Particular thanks go to Julian Schmehr, for teaching me many things (including a healthy dose of skepticism) and welcoming me into his high-pressure floating zone endeavors. Many thanks to Zach Porter for being an excellent labmate/sounding board/beamtime companion throughout our years at UCSB – I record here my sincere apologies for not informing you when Adrienne Lenker came to town. Of course, acknowledgement and thanks are due to my advisor, Stephen D. Wilson, who let me into his group despite my not knowing, at the time, what an "iridate" was. Working with Stephen I have learned many things about the art/science of growing crystals and measuring them with neutrons. I have become a better scientist under his guidance and look forward to future collaborations.

I have also had the opportunity to work with great people from outside of the Wilson group. Andy Segale, of the UCSB Physics Machine Shop, deserves many thanks for his efforts crafting the Inconel parts which are essential for the high-pressure floating zone

furnaces. I also owe him a particular debt for a last minute fix of a sample mount which saved me much stress during preparation for a neutron experiment. I also greatly benefitted from the support of Deryck Stave and Dano Pagenkopf of the Materials Processing Lab , who were both always willing to answer my questions and help me find random parts. Thanks are due to the members of David Hsieh's group at Cal Tech and of Richard Averitt's group at UCSD who performed measurements on my crystals. Specific thanks go to Alon Ron – who I had the pleasure to get to know during several long grant meetings – for his excellent (and continuing) work on my $CrSiTe_3$ samples.

The synchrotron X-ray and neutron scattering experiments which make up the most important data in this thesis would not have been possible without the support of the instrument scientists at the various facilities. In particular, I would like to thank Rebecca Dally – a former Wilson group member – for her patient explanations and assistance during my first experiments at the NIST Center for Neutron Research, as well as hosting me in her home during my time there. Thanks are also due to Yaohua Liu – former instrument scientist on the CORELLI at the Spallation Neutron Source and currently working on the Second Target Station project – for suggesting that I apply to the SCGSR program. Through that fellowship I had the opportunity to spend three productive months at Oak Ridge National Lab working with the team for the instrument SEQUOIA. Special thanks are due to my host, Matthew Stone, for all his help and mentorship in carrying out the inelastic neutron scattering measurements on Li_2CuO_2 as well as analyzing the data.

Curriculum Vitæ

Eli Alexander Bell Zoghlin

Education

2022	Ph.D. in Materials, University of California, Santa Barbara.
2018	M.A. in Materials, University of California, Santa Barbara.
2016	B.S. in Materials Science and Engineering, Carnegie Melllon University

Publications

* Indicates sample provided to collaborator for measurement

1. Zoghlin, E., Stone, M.B., and Wilson, S.D. "Discovery of multimagnon bound states in Li_2CuO_2 ", *manuscript in preparation.*
2. Jnawali, G., Pournia, S., Zoghlin, E.*, Abbasian, I.S., Wilson, S.D., Jacob Gayles, & Leigh M. Smith, "Band splitting and long-lived carrier recombination in ferromagnetic $CrSiTe_3$ nanosheets", *manuscript in review.*
3. Porter, Z., Zoghlin, E., Schmehr, J.L. & Wilson, S.D. "Crystal growth of $Sr_2Ir_xRu_{1-x}O_4$ for $x \leq 0.4$". *Journal of Crystal Growth*, **578**, p.126432 (2022).
4. Zoghlin, E., Laurita, G., Dally R., Holgate, C, Schmehr, J., Levi, C., & Wilson, S. D. "Evaluating the effect of structural disorder on the magnetic properties of $Nd_2Zr_2O_7$ ". *Physical Review Materials*, **5**, 084403 (2021).
5. Zoghlin, E., Porter, Z., Britner, S., Husremovic, S., Choi, Y., Haskel, D., Laurita, G. & Wilson, S. D. "Mapping the structural, magnetic and electronic behavior of $(Eu_{1-x}Ca_x)_2Ir_2O_7$ across a metal–insulator transition". *Journal of Physics: Condensed Matter*, **33**(5), 055601 (2021).
6. Zoghlin, E., & Wilson, S. D. Floating Zone Crystal Growth. *Fundamentals of Quantum Materials: A Practical Guide to Synthesis and Exploration*, **137** (2021).
7. Ron, A., Chaudhary, S., Zhange, G., Ning, H., Zoghlin, E.*, Wilson, S.D., Averitt, R.D., Rafael, G., & Hsieh, D. "Ultrafast enhancement of ferromagnetic spin exchange induced by ligand-to-metal charge transfer." *Physical Review Letters*, **125**(19), 197203 (2020).
8. Seyler, K.L., de la Torre, A., Porter, Z., Zoghlin, E., Polski, R., Nguyen, M., Nadj-Perge, S., Wilson, S.D. & Hsieh, D. "Spin-orbit-enhanced magnetic surface second-harmonic generation in Sr_2IrO_4". *Physical Review B*,**102**(20), p.201113 (2020).

9. Lovinger, D. J., Zoghlin, E.*, Kissin, P., Ahn, G., Ahadi, K., Kim, P., & Averitt, R. D. "Magnetoelastic coupling to coherent acoustic phonon modes in the ferrimagnetic insulator $GdTiO_3$ ". *Physical Review B*, **102**(8), 085138 (2020).
10. Schmehr, J. L., Aling, M., Zoghlin, E.,& Wilson, S. D. "High-pressure laser floating zone furnace." *Review of Scientific Instruments*, **90**(4), 043906 (2019).
11. Schmehr, J.L., Zoghlin, E., Porter, Z., Wang, X., Ruff, J.P., Tian, W., Islam, Z. & Wilson, S.D. "Preferential quenching of 5d antiferromagnetic order in $Sr_3(Ir_{1-x}Mn_x)_2O_7$". *Journal of Physics: Condensed Matter*, **31**(24), p.244003 (2019).
12. Porter, Z., Zoghlin, E., Britner, S., Husremovic, S., Ruff, J.P., Choi, Y., Haskel, D., Laurita, G. & Wilson, S.D. "Evolution of structure and magnetism across the metal-insulator transition in the pyrochlore iridate $(Nd_{1-x}Ca_x)_2Ir_2O_7$". *Physical Review B*, **100**(5), p.054409 (2019).
13. Ron, A., Zoghlin, E.*, Balents, L., Wilson, S. D., & Hsieh, D. "Dimensional crossover in a layered ferromagnet detected by spin correlation driven distortions". *Nature Communications*, **10**(1), 1-6 (2019).
14. Chen, X., Schmehr, J.L., Islam, Z., Porter, Z., Zoghlin, E., Finkelstein, K., Ruff, J.P. & Wilson, S.D. "Unidirectional spin density wave state in metallic $(Sr_{1-x}La_x)_2IrO_4$". *Nature Communications*, **9**(1), pp.1-7 (2018).
15. Aronhime, N., Zoghlin, E., Keylin, V., Jin, X., Ohodnicki, P. & McHenry, M.E. "Magnetic properties and crystallization kinetics of $(Fe_{100-x}Ni_x)_{80}Nb_4Si_2B_{14}$ metal amorphous nanocomposites". *Scripta Materialia*, **142**, pp.133-137 (2018).
16. DeGeorge, V., Zoghlin, E., Keylin, V. & McHenry, M. "Time temperature transformation diagram for secondary crystal products of Co-based Co-Fe-B-Si-Nb-Mn soft magnetic nanocomposite". *Journal of Applied Physics*, **117**(17), p.17A329 (2015).

Abstract

High-pressure bulk crystal growth for scattering studies of quantum magnets

by

Eli Alexander Bell Zoghlin

This thesis is concerned with the construction, commissioning and usage of a high-pressure, laser-based, floating-zone furnace for the purpose of synthesizing bulk single-crystals of quantum magnets and studying them via neutron scattering. Bulk single-crystals are some of the most valuable experimental platforms in condensed matter physics. This is particularly true for studies of quantum magnetism since it allows for the use of single-crystal neutron scattering, which is the premier technique for analyzing both the static and dynamic behaviors of magnetic materials in conjunction with resolution of underlying anisotropies. The floating-zone crystal growth method has been especially impactful in this regard, as it has the potential to create high-quality crystals with large volumes, an essential feature for compatibility with the flux limitations of neutron scattering. Accordingly, broadening the phase-space of materials accessible by this technique is a direct means of helping the field move forward. The furnace described in this thesis represents such an improvement. Its laser-based design allows for floating-zone crystal growth at record-setting gas pressures with simultaneous access to high temperatures via a well-defined heating zone. These features make it suitable for growth of highly volatile, metastable and low-viscosity compounds, all of which are challenging for traditional floating zone-furnaces.

I begin with a detailed overview of the floating-zone growth technique, including its advantages, disadvantages and the manner in which it is conducted (Chapter 2). This sets the stage for a description of the furnace (Chapter 3), including its key design features

and the conduction of a variety of successful commissioning growths to demonstrate its abilities. I also provide a brief reflection on challenges associated with high-pressure, laser-based, floating-zone crystal growth.

Following an attempt at defining quantum magnetism and an introduction of the basic principles of neutron scattering (Chapter 4) detailed studies of two of the commissioning materials (both quantum magnets) are presented. The first study (Chapter 5) elucidates the role of chemical disorder in modifying the fragmented magnetic state found in $Nd_2Zr_2O_7$ through a combination of thermodynamic measurements, electron probe microanalysis and neutron scattering. It is demonstrated that growth under high-pressure allows for a notable reduction in chemical disorder, which modifies the temperature range over which the different spin correlations of the fragmented state are stabilized. The second study (Chapter 6) centers around a detailed survey of the magnetic excitations in a highly stoichiometric Li_2CuO_2 sample (enabled by the high-pressure growth environment) via inelastic neutron scattering. The resulting data allowed for refinement of the existing exchange model and also revealed the presence of multi-magnon bound states. This provides the first reported observation of multi-magnon bound sates in a ferromagnetic chain by neutron scattering.

The final study presented (Chapter 7) summarizes an attempt to grow single-crystal $Eu_2Ir_2O_7$ via high-pressure floating-zone. Due to persistent decomposition at high temperatures, a detailed study on polycrystalline carrier-doped $(Eu_{1-x}Ca_x)_2Ir_2O_7$ was carried out instead. Using a wide variety of experimental probes it is demonstrated that depression of the thermal metal-insulator transition by carrier doping leads to the formation of an electronically phase-separated state in these samples, without observable change in the lattice symmetry. Comparison to literature shows that formation of this phase-separated state is dependent on synthesis method, indicating that even small amounts of disorder can dramatically modify the properties.

Contents

List of Figures

List of Tables

Chapter 1

Introduction

1.1 Overview

Condensed matter physics research – which studies the properties of solids at various length and time scales – relies on the synthetic abilities of experimentalists to produce physical approximations of theoretical models. These approximations, which often take the form of materials whose atomic structure maps to the features of a theory, provide a platform for conducting experiments in the real world. The results of these experiments then verify, disprove, or complicate the ideas of theorists, allowing them to refine their models. This process is one of the fundamental drivers of our progressing understanding of condensed matter phenomena. The basic aims of this thesis are very much compatible with the basic tenets of this process: 1) To improve/expand the synthesis capabilities of the floating-zone crystal growth technique by development and utilization of a novel high-pressure furnace and 2) to study produced crystals of quantum magnets using scattering techniques.

The first aim represents a fundamental effort to improve upon a very well-established technique. The floating-zone crystal growth technique – the details of which are discussed

in Chapter 2 – has been used extensively (and successfully) in condensed matter physics research because of its ability to produce large volume samples of high crystallinity and purity. Despite this achievement, the instrumentation used in most laboratories to carry out the growth process has not changed dramatically since the development of the "image furnace" in the 1970's. As a result, materials with features making them less amenable to floating-zone growth, primarily the presence of volatile components and/or metastability, have remained out of reach. This work is part of a collection of recent efforts to amend this state of affairs by pushing the boundaries of an important process variable in floating-zone growth: the gas pressure contained within the growth chamber. Chapter 3 discusses the motivation to perform floating-zone crystal growth at high pressure and details the design of a novel, laser-based floating-zone furnace (hereafter, "the furnace" or "the laser furnace"). Several demonstrations of the capabilities of the furnace are provided through growth of a variety of complex transition-metal oxides. The furnace allows record setting growth pressures, thereby providing a route for expanding the material phase space to which floating zone single crystal growth can be applied. This advancement represents a fundamental improvement in the production of bulk single-crystals of novel materials.

An important motivation for seeking such advancements is that bulk single-crystals are a prized platform for experimental work and are often essential to advancements in our understanding of condensed matter phenomena. Single-crystal samples enable a wide range of experiments which provide richer data sets than powder (*i.e.* polycrystalline) samples; these added details are often necessary to test the finer points of theoretical models. Binding together the two aims of this thesis, single crystal samples are particularly needed for any detailed studies of quantum magnets. A brief description of quantum magnetism, as well as the motivation for its study, is given in Chapter 4. The retention of the underlying anisotropies in a single crystal - as opposed to the averaging which occurs in powder samples - can provide important information in characterizing a

quantum magnet. As an example, the production of the first crystals of $Nd_2Zr_2O_7$ (via the floating-zone method) allowed for measurement of the anisotropic magnetization (*i.e.* the saturation magnetization along different crystallographic directions) [1, 2]. The results of these measurements provided an indication of an Ising-type magnetic anisotropy, which aided in interpretation of future neutron scattering results.

The capabilities of neutron scattering are, in turn, another reason for the prominence of single-crystal samples. Crystals produced by the floating-zone technique have been especially impactful in neutron scattering studies, as flux limitations and the relatively weak interactions of neutrons with matter require large sample sizes. In the realm of quantum magnets neutron scattering stands as one of the premier experimental tools. It allows for the direct determination and characterization of magnetic ordering transitions through parametric studies of magnetic Bragg peaks. Furthemore, the usage of large area detectors (in conjunction with other experimental methods) allows one to probe short-range/local ordering via measurement of diffuse scattering. The ability to detect and analyze the energy change of a scattered neutron due to the inelastic magnetic cross-section provides a means to characterize magnetic excitations and reveal microscopic details of the spin Hamiltonian. Analysis of such data even allows one to deduce the strength and nature of the underlying exchange interactions which give rise to both the magnetic ordering and the attendant excitations. While neutron scattering measurements of powder samples are certainly valuable (for example, they are most often easier to conduct and analyze and so are particularly useful for materials which have never been measured by neutrons before), the datasets resulting from single-crystal measurements are in general much richer, particularly for inelastic experiments. Again, this richness lies in the fact that the vector nature of the reciprocal lattice is preserved in single-crystals samples; in the language of diffraction, powder samples probe only $\left|\vec{\boldsymbol{Q}}\right|$ where as single crystals can access the full vector $\vec{\boldsymbol{Q}}$. The result is a much more fine-grained picture of

the magnetic phase behavior of the material. A select discussion of the details of neutron scattering relevant to the study of quantum magnets is provided in Chapter 4.

Chapters 5 and 6 present extensive work on two of the materials grown during commissioning of the furnace: $Nd_2Zr_2O_7$ and Li_2CuO_2 . While both of these oxides are quantum magnets, the details of the physics diverge substantially due to the structural and compositional differences. The pyrochlore $Nd_2Zr_2O_7$, discussed in Chapter 5, is a refractory material with magnetism derived from the unpaired f-electrons of the Nd^{3+} ion. At temperatures < 1 K (a temperature scale driven by the relative weakness of rare-earth exchange interactions) this compound shows a fascinating behavior where the magnetic moment appears to "fragment" into two separate order parameters. As a result, 3-dimensional magnetic order coexists with an "ice-like" state which possesses persistent quantum fluctuations. In this chapter it is demonstrated through a variety of characterization techniques (including multiple neutron scattering experiments) that these correlations are maintained to higher temperatures in samples grown under high-pressure. This effect stems from a minimization of disorder (in the form of site-mixing) during high-pressure growth and demonstrates that the magnetic correlations are relatively sensitive to Nd stoichiometry.

Chapter 6 discusses the results of an extensive survey of the spin excitations in Li_2CuO_2 via TOF neutron spectroscopy. Li_2CuO_2 is a charge-transfer insulator with an atomic structure made up of quasi-1-dimensional (quasi-1D) "ribbons" of edge sharing CuO_2 plaquettes. As a result of the structure, the magnetism (which stems from Cu^{2+} ions with electron configuration $3d^9$ and $S = 1/2$) is effectively one-dimensional, which has important implications for the magnetic excitations. Fitting the observed one-magnon mode across various high-symmetry directions reveals a minimal model with a complex set of exchange interactions, which nonetheless results in a simple magnetic order of antiferromagnetically coupled ferromagnetic chains. The most interesting result is

the observation of multi-magnon bound states; particularly striking is the observation of a three-magnon bound state, a relatively rare occurence. To the best of my knowledge, this represents the first observation of magnon bound states in a ferromagnetic states, a behavior long indicated by theory.

In Chapter 7 work on the iridate $Eu_2Ir_2O_7$, another pyrochlore quantum magnet, is presented. Motivated by the possibility of using floating-zone single crystals to analyze the evolution of the magnetic structure under a magnetic field with neutron scattering, a sustained effort to grow single-crystals by high-pressure floating zone was undertaken. However, none of the available gas environments proved able to stabilize a melt of the desired phase. An extensive set of experiments (utilizing X-ray scattering and spectroscopy, as well as bulk thermodynamic measurements) was carried out on a polycrystalline series, $(Eu_{1-x}Ca_x)_2Ir_2O_7$, in order to characterize changes in the magnetic, electronic and crystal structure across a doping-driven metal-insulator transition (MIT). The central result is the observation of a decoupling of the MIT and the magnetic order in these samples, which is attributed to the formation of an electronically phase-separated state. A survey of the literature and comparison to these results demonstrates the sensitivity of the magnetic/electronic properties of doped iridate pyrochlores to synthesis method and rare-earth magnetism.

1.2 Permissions and Attributions

1. The content in Chapter 2 is based on a published chapter written in collaboration with Stephen D. Wilson: "Fundamentals of Quantum Materials: A Practical Guide to Synthesis and Exploration", Eli Zoghlin, Stephen D. Wilson, J. Paglione (Ed.), N.P. Butch (Ed.) and E.E. Rodriguez,

2. The descriptions of the high-pressure laser furnace and its comissioning in Chapter 3, as well as a number of the images, are based on a previously published collaborative work. Reproduced from [4], with the permission of AIP Publishing.

3. The content of Chapter 5 is based on previously published work [5].

4. The content of Chapter 7 is based on previously published work [6].

Chapter 2

The Floating-zone Growth Technique

The floating-zone technique is well known to the crystal growth community, having been in continued and effective use since its inception in the early 1950's [7, 8, 9]. As a result, a variety of excellent reviews are readily available in the literature which discuss technical aspects in great detail. Here I provide a basic description of the floating zone technique and discuss the underlying principles. I also go into detail about some of the most important growth parameters and discuss the advantages and challenges of applying floating-zone growth. In anticipation of Chapter 3, where the design of a novel floating-zone furnace is discussed, I also describe the components of an optical floating-zone furnace.

2.1 Description of the Technique

The floating zone (FZ) technique is an example of a melt-based technique where crystal growth is attained by directional solidification out of a liquid of the proper stoichiom-

etry. The unique feature [1] of floating-zone growth is that this directional solidification is conducted without use of a crucible, meaning the (possibly reactive) melt never comes into contact with a foriegn material. The general procedure for such a growth is as follows. Sintered polycrystalline rods of the compound to be grown are secured above and below (the feed and seed rod, respectively) a small, well-defined hot zone maintained inside a sealable growth chamber. The heating power is then slowly increased until the material in the hot zone is completely molten and the two rods can be joined via a liquid "bridge". This floating, molten zone between the two rods is maintained by surface tension and the melt only ever comes into contact with material of the same chemical composition. A crystal is grown by continuously feeding polycrystalline material into this molten zone from above, which recrystallizes as it exits below. This is accomplished by either moving the heating source upwards along the rods or by translating the rods in tandem through the stationary hot zone. Smooth translation and rotation of the feed and seed rods is obtained by attaching them to the ends of drive shafts which pass into the growth chamber.

Upon exiting the hot zone and cooling, multiple grains initially nucleate on the seed simultaneously out of the melt. Provided the molten zone is maintained for long enough, the process known as grain "selection" allows a single crystal to eventually be obtained. It is worth a brief digression to be clear about terminology. Generically, a crystalline material is one in which the atoms are arranged in a repeating pattern known as a lattice, which is defined by a specific set of basis vectors. A "grain" is defined by a specific orientation of these basis vectors, relative to the lab frame. One may think of a polycrystalline powder as a collection of randomly oriented grains (though it is certainly

[1] There are other methods for attaining crucible free melts. For example, intermetallic materials can be magnetically levitated using *a.c.* currents (an application of Lenz's law) and melted using induction coils. However, this requires the material to be conducting and is of limited use for oxides. Levitation is also possible using jets of compressed gas. Regardless, it is hard to imagine how any of these could be easily coupled to a directional solidification process

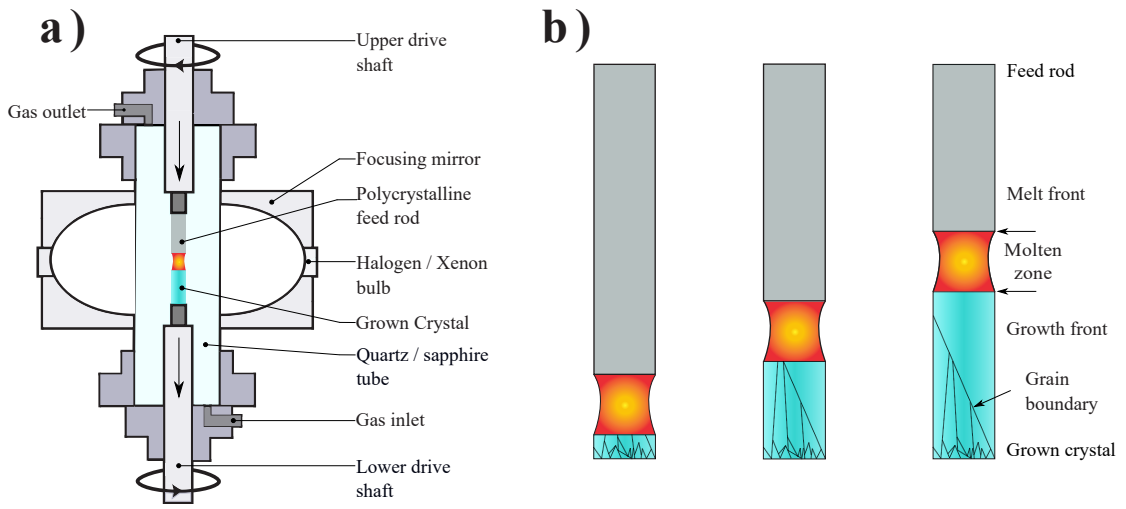

Figure 2.1: **a)** Diagram of an optical floating zone set-up **b)** Diagram of the floating-zone growth process showing the formation of a single crystal via grain growth and subsequent grain selection (left to right). The grain which eventually dominates in the rightmost image possesses the highest radial growth velocity.

possible that a single particle could contain multiple grains). An ideal single crystal is then a sample wherein a single orientation of the lattice is maintained throughout. The grains which nucleate on the seed rod form with different orientations, such that for each, in the lab frame, the crystallographic directions point in different directions. The radial growth velocity of these grains varies, due to materials-specific kinetic reasons, with certain orientations possessing faster velocities than others. As the growth proceeds, and more material is recrystallized out of the molten zone, faster grains outcompete others, until eventually only a single grain is being recrystallized. This process is illustrated generically in Figure 2.1, with a schematic of a typical optical FZ furnace for reference (see Section 2.3 for details). The resulting single crystal therefore possesses the same orientation as that of the grain with the highest radial growth velocity, which is typically referred to as the "characteristic growth direction" (defined by a specific vector in the crystal lattice). This can vary significantly between materials, though classes of materials with the same crystal structure may share a common characteristic growth direction. In

practice, the growth direction for a material may not be extremely well defined (due to a shallow maximum in the distribution of growth velocities) and therefore may vary between growths or even not map to a specific (integer) vector defined by the crystal lattice. Once a single crystal has been produced, it can be used as a seeding template for future growths and replace the polycrystalline seed - some materials with slow grain radial growth velocities require several reseeded growths before a single crystalline boule is obtained.

In typical operation, the molten zone is maintained until the feed rod has been consumed, at which point translation is stopped and the feed rod is slowly moved out of the hot zone to separate it from the grown crystal. The tip of the crystal should be kept within the hot zone during separation and as the heating power is ramped down, to minimize thermal shock. In exploratory studies, the molten zone may alternatively be quenched if its composition is of interest. Because one has optical access (typically by means of an optically shielded camera pointed at the molten zone) to the growth chamber, several growth variables (described in the next section) can be modified *in situ* to adjust the molten zone and attempt to maintain stability. This renders FZ-growth a so-called "active" crystal growth technique, similar to the Czochralski method (a crucible-based melt method) [10]. In contrast, crucible-based flux or vapor transport methods are "blind" techniques where the success of a growth run must be determined after its completion and the results used iteratively to inform future modifications of the growth parameters.

Before moving on to discuss the variety of tunable parameters available in FZ-growth, it is worth describing two advantages of this technique with respect to crystal purity. As in other melt-based methods which conduct single crystal growth via directional solidification, intrinsic impurities initially present in the polycrystalline material can be largely reduced in the grown crystal by the process of zone-refinement, which occurs throughout

the growth. As the molten zone is passed along the feed rod, impurities may either tend to be ejected from the growing crystal and accumulate in the melt or vice versa. This behavior is dependent on the phase relations (*i.e.* thermodynamics) of the system defined by the stoichiometry of the desired material and that of the impurities. These relations are captured by the segregation coefficient, k, which is the ratio of the equilibrium solubility of the impurities in the solid to that of the liquid melt. For instance, if $k < 1$, as the crystal solidifies and thermodynamic equilibrium is achieved, it continuously ejects impurities back into the melt [11]. The result is that, in the typical case that $k < 1$, impurities can be driven to one end of a single crystal boule. As mentioned previously, unlike other melt-based growth techniques, FZ provides a crucible-free growth environment. In other techniques (such as the Czochralski or Bridgman) the melt is in direct contact with a crucible. In many cases there is a finite solubility of the crucible material in the meltl, and impurities will be introduced by the hot melt dissolving some of the crucible. However in FZ, the melt only touches materials composed of the desired reagents. This eliminates the diffusion of unknown impurities into the melt which would otherwise contaminate the growing crystal. In the world of quantum magnets, growing high-purity crystals is important because even small amounts a foreign material may substantially influence, or pollute measurement of, the magnetic properties. Perhaps more importantly, interesting magnetic and electronic ground states may be susceptible to modification by disorder, such as the continually intriguing, but delicate, superconducting state found in Sr_2RuO_4[12]. This is particularly true in frustrated systems or systems where a variety of similar energy scales are present - small perturbations due to disorder can influence the ground state selection. Perniciously, it is also possible for disorder to mimic the phase behavior of more interesting physics. For example, for the quantum spin liquid candidate $YbMgGaO_4$, it was shown that the lack of observed magnetic order (a typical benchmark for quantum spin liquids) may be due to the intrinsic cation disorder between the Yb

layers, which can mimic the appearance of a QSL in neutron scattering [13].

2.2 Growth Parameters

As is familiar to anyone who has turned their hand to the ~~dark art~~ science of crystal growth, a nearly universal challenge is the size of the parameter space available for experimentation. Floating zone growth is no exception and I describe below some of the most important parameters. Synthesis of a material often requires optimizing several of these parameters at once, each of which may have competing impacts on crystal quality. These kinds of situations were encountered several times during the course of this thesis as the capabilities of the furnace were mapped out. One example is in the growth of ruthenate oxides, wherein RuO_2 both volatilizes and becomes reduced to Ru metal during melting. Dealing with this issue requires tuning the gas composition of the growth chamber, with a trade-off between high-pressure O_2, needed to prevent reduction of the RuO_2 but which also, due to the formation of a trioxide gas-phase, promotes volatility, and high-pressure Ar, which acts to reduce volatility.

Phase diagram considerations are therefore critical to navigating the large parameter space and optimizing crystal growth. For example, while the zone refining process and crucible-free nature of FZ-growth can dramatically decrease the level of foreign elements found in the crystal, it cannot prevent impurities in the form of nearby secondary phases with some or all of the same elemental constituents as the desired phase. Rather, the different parameters described below - which impact both the thermodynamics and the kinetics of the crystal growth process - must be tuned to stabilize the desired phase. Based on phase diagram considerations, compounds for FZ-growth can be broadly separated into two categories: congruently and incongruently melting compounds (see Figure 2.2). In compounds which undergo congruent melting, the composition of the liquid phase

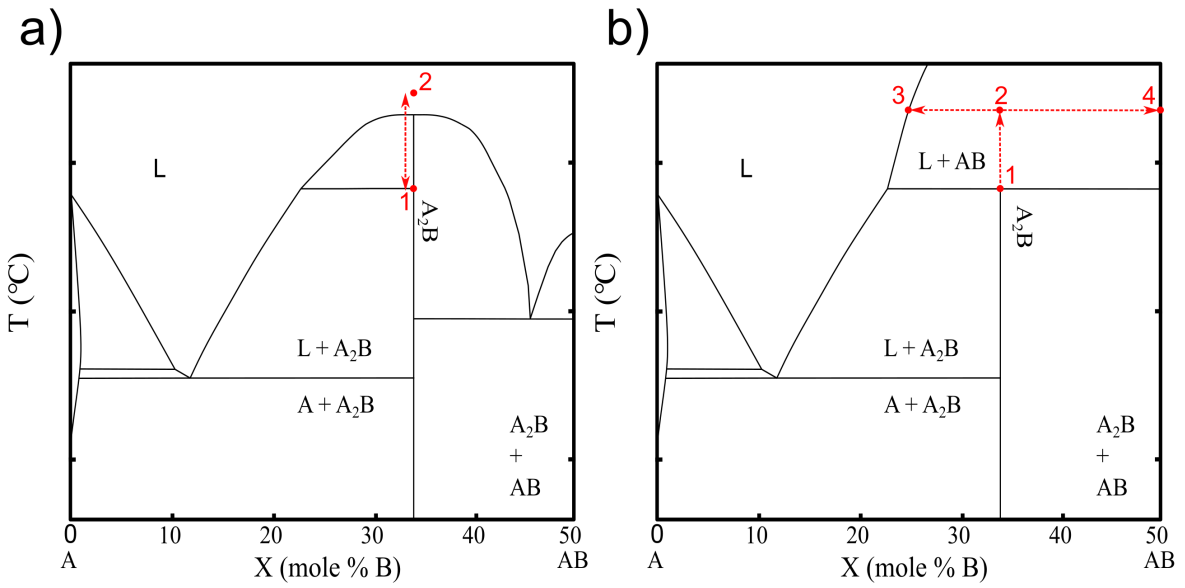

Figure 2.2: Schematic phase diagrams showing the difference between **a)** congruent and **b)** incogruent melting for the line compound A_2B. In the congruent melting case, starting with the composition A_2B and raising the temperature from point 1 to 2 will lead to a liquid with the same composition. Upon cooling, solid A_2B forms. Note that the phase region to the left (right) of the A_2B line is a two-phase equlibrium of a B-poor (A-poor) liquid and A_2B. Slight deviations of the originally melted material to the left or right of the A_2B line will therefore still recrystalize A_2B. In the incogrunent melting case raising the temperature from point 1 to 2 places the system in a two-phase equilibrium of a B-poor liquid (with composition corresponding to point 3) and the other line-phase, AB (point 4). This indicates a decomposition reaction $A_2B \rightarrow AB + L$. Melting of A_2B in this case will always result in recrystalization of AB

is maintained in the crystallization of a single solid phase. As a result, a congruently melting compound can be grown from a feed rod whose stoichiometry is that of the desired compound. The materials studied in this thesis all fall into the category of congruent melters. For incongruently melting compositions, the liquid and re-crystalized solid no longer possess the same composition and traversing the liquidus typically leads to a two phase region, such as for a compound with a peritectic point [11, 14]. In this regime, solvent based variations of the standard FZ-growth technique must be utilized. These techniques were not employed in the course of this thesis, and so will not be discussed, but I direct the interested reader to the excellent review by S.M. Koohpayeh [15].

Stability in a FZ-growth is largely determined by the ability to reach a steady state mass flow through the molten zone. In the steady state, the volume of the zone remains roughly constant, meaning that the incoming and outgoing mass flows are balanced, and the liquid bridge between the feed and growing crystal is adequately stabilized by surface tension. The shape of a stable zone in the steady state is generally symmetric in the axial and radial directions with a roughly square aspect ratio [14]. The mass flow into the melt is controlled by the speed of the feed rod and/or the hot zone, while mass flow out (neglecting the influence of volatility) is controlled via the rate of crystal growth. Growth rates found in the literature vary widely depending on the material being grown [14, 16, 11], with rates of .05 mm/hr for $Bi_2Sr_2Ca_2Cu_3O_{10}$ [17] and 240 mm/hr for GaAs [18], at the extremes. Typical rates fall between 1 - 50 mm/hr, with rates in the 1 - 10 mm/hr being most common. As a rule of thumb, the slowest stable growth speed improves crystallinity and mosaic (the spread of grain orientations defining a "single" crystal) by allowing for a uniform, close to planar, growth front (the shape of the interface between the liquid molten zone and the growing crystal) which is favorable to the grain selection process. In certain cases, a higher growth rate may be needed to deal with, for example, thermally induced cracking or volatility (by minimizing the amount of time spent molten) [16].

Most often, the feed and seed rods are counter-rotated during growth, with rates ranging from 5 to 50 rpm [11], in order to maintain a uniform composition of the melt via mixing. Additionally, the feed and seed rotation rates are typically set with a slight differential to prevent destabilizing resonances. Despite this mixing, the molten layer at the liquid-crystal interface can become depleted in one or more of the constituent elements. Based on the phase diagram, this depletion can lead to constitutional supercooling in regions of the melt near the interface, which can cause the growth front to break up and destabilize the molten zone. Both growth rate and rotation rate have been reported to

influence the formation of cracks, grain boundaries, and voids as well as the formation of second phases and inclusions, though growth rate is typically the more sensitive variable [16, 14, 11]. Zone stability may also be influenced by composition dependent properties of the melt itself, since these properties are linked to the surface tension that maintains the zone. For example, high density and low surface tension of the melt may reduce its ability to form a stable molten zone [14]. Sharpening the heating gradient at the boundaries of the hot zone (which can be done by masking the growth chamber or using focused optics, as is described in Chapter 3, can help alleviate stability issues [14, 11]. For particularly fragile molten zones increased stability can sometimes be attained by not using sample rotation during the growth process, with the trade-off that mixing of the melt will now rely entirely on the relatively slow process of thermally driven convection.

Control of the composition and pressure of the growth atmosphere is also an important consideration. Depending on the specific chemistry of the material being grown, an oxidizing (O_2), reducing (Ar + H_2) or inert (Ar, N_2, He) gas may be utilized to stabilize the growth process. Post-growth analysis often provides clues as to how the growth atmosphere should be modified, depending on the phases which are observed and their relative stoichiometries/valences. Most often in commercial furnaces, a dynamic pressure of the working gas is utilized, with flow rates typically ranging from 0.1 – 1.0 standard L/min, to keep the atmosphere at the melt consistent across the course of the growth. Gas flow can also be advantageous for growth of volatile materials, since it can act to "sweep" material away from the hot zone and help prevent extensive build-up on the point of optical access. Volatility can also be directly mitigated, to some degree, by the application of an elevated gas pressure, thereby making growth conditions more manageable. Reducing volatility can also improve stoichiometry and phase purity; the effects of pressure are, however, dependent on the specific material system under investigation. More discussion on the effects of pressure is provided in Chapter 3.

Careful preparation of the feed rod also contributes greatly to the ability to establish a stable molten zone during growth. The precursor material for FZ growth is typically powder of the desired composition, most often prepared by conventional solid-state synthesis methods. Note that the precursor powder need not necessarily be of the desired phase. Indeed in some cases this may not be possible, such as in the case of metastability; in this case the environment within the FZ furnace must be tuned to promote formation of the desired phase and the rods simply supply the right ratio of elements. The reacted powder is typically finely ground using ball milling and/or grinding in a mortar and kept dry in order to promote densification during the pressing process. The importance of using dry powder for rod preperation cannot be emphasized enough, especially when producing the thinner diameter rods used in the laser furnace. Following any preliminary reaction steps powder should either be immediately used to prepare rods or stored in a moisture free environment (*i.e.* a glovebox). Rods of the material can then be produced by cold pressing within a mold (typically a clean rubber balloon of the appropriate size) in an isostatic press, followed by a suitable sintering treatment in a furnace. For particularly hygroscopic samples it may be necesarry to load the powder into the balloon within a glovebox, in order to prevent water from interfering with the pressing process. While hot-pressing can produce high density rods, the use of metal or carbon dies, even at low temperatures, can introduce impurities. Sufficient density of the sintered rods, ρ_{rod}, relative to the theoretical density of the crystal lattice (the "X-ray density"), ρ_{xtl}, is important, with ideally $\rho_{rod} > 95\%\ \rho_{xtl}$. Low rod density can lead to the formation of gas bubbles within the molten zone, which can severely destabilize the molten zone, or to dissolving of the feed rod by the melt via capillary action [Dabkowska2010]. The value of ρ_{rod} needed for stable growth is, however, a material dependent value, as is the obtainable ρ_{rod}. Particularly refractory materials can be difficult to sinter to high densities in typical furnaces, and in certain cases, an initial rapid translation of the feed rod through

the hot zone of the FZ furnace can be used to increase density. A further consideration is that the feed rod must be made sufficiently long to allow time for grain selection to occur – typically $\approx$ 6 mm diameter rods are formed 150 - 200 mm in length. For the $\approx$ 4 mm rods utilized in the laser furnace a typical length is 100 mm - 125 mm (the maximum length allowed due to the chamber geometry). Care should be taken to make the rods as straight as possible so that they can be aligned coaxially in the furnace, thus avoiding precession of the melt out of the hot zone. A uniform diameter is also desirable to maintain a consistent input mass flow.

2.3 Description of a Typical Optical Floating-zone Furnace

There are several key features of a FZ furnace which are essential for performing crystal growth. In order to provide some context for the discussion in Chapter 3, I introduce these features here through description of a conventional type of FZ furnace: the mirror furnace. All FZ furnaces create a finely focused hot zone with a sharp axial heating gradient (along the growth direction). Mirror furnaces utilize focused optical heating to accomplish this. There are also furnaces based around induction/Joule heating but optical furnaces are, in general, are a more versatile crystal growth platform since both conducting and insulating materials can be grown. This feature has made mirror furnaces by far the most utilized type of FZ furnace, particularly because of their suitability for growing oxides, for which research interests are myriad. Another key feature is the creation of a controlled environment inside the growth chamber, typically via modification of the growth atmosphere, pressure and gas flow conditions. Optical access is required for power delivery in all optical furnaces, though, as will be discussed in the next chapter the

requirements are drastically different for mirror-based and laser-based furnaces. Lastly, all furnaces possess the ability to translate and rotate the seed and feed rods contained within the chamber; for the purpose of maintaining a stable molten zone it is important that this rotation and translation happen smoothly.

Mirror-based floating zone furnaces utilize high wattage (incoherent) light bulbs to produce the required heating power. Each bulb is positioned within an ellipsoidal mirror resulting in a high power density transmitted through the mirror's focal point. Several possible arrangements of focusing mirrors exist, but, for each geometry, the mirrors concentrate the light from aligned bulbs onto a single point along the growth axis, forming the hot zone. The hot zone is typically imaged within a quartz or sapphire vessel - which allows for large solid angles of optical access while also providing some ability to contain pressure - that is coaxial with the growth direction therefore allowing for an isolated and tunable gas environment. Dynamic seals, typically greased O-rings, maintain a pressurized environment and allow the rotating drive shafts to enter the growth vessel from above and below. Shutters or masks placed in the optical paths between the bulbs and the chamber can be used to further tailor the extent of the hot zone and narrow the axial heating gradient.

The input power range of mirror furnaces can be modified by swapping out the type of bulb utilized being utilized (a process which also involves a careful alignment and focusing procedure to make sure the bulbs are centered on the elliptical mirrors). Incandescent halogen bulbs of varying powers ($\sim$ 100 - 1500 W) are a versatile source and can be used to reach melting temperatures typically up to $\sim$ 2100 °C, depending on the optical absorption/reflectivity of the material. While higher wattage bulbs make the growth of higher melting point materials possible, they typically also provide larger starting images due to their larger filaments. This produces a larger hot zone with decreased heating gradients along the growth direction and, in some cases, can decrease the stability of the

molten zone. As an alternative, compact xenon arc lamps provide for dramatically higher power densities and allow for growths up to 3000 °C, sufficient to melt highly refractory materials. Unfortunately, the power output of xenon lamps is difficult to control precisely at low powers, often making them unsuitable for low melting point growths. New furnace designs have ameliorated this problem with innovative shutter designs.

The most commonly used mirror geometry is the horizontal one, where multiple mirrors and light sources are placed in a circular array perpendicular to the growth direction (see Figure 2.1**a**.). Commercially available horizontal mirror furnaces utilize either two-mirror or four-mirror designs. Compared to four-mirror designs, the two-mirror design may be preferable for low melting temperature applications since an accurate alignment of the bulb filaments is easier to achieve. This maximizes the axial heating gradient available from low-power/small-filament halogen bulbs. However, four-mirror designs provide increased heating power and circumferential uniformity, often allowing for larger diameter crystals ($\gtrsim$ 8 mm) of higher melting point materials to be more easily grown. Alternatively, vertical mirror geometries are also being increasingly utilized [19, 20, 21]; some further discussion on usage of this geometry for high-pressure growth will be discussed in the next chapter. In this geometry a single lamp and ellipsoidal mirror are placed coaxial with the growth direction, below the hot zone. The light from this lower mirror is focused onto the hot zone using a second ellipsoidal mirror above the lamp. This second mirror provides power input in the same plane as the previously discussed horizontal geometry and can produce extreme circumferential uniformity at high power.

Chapter 3

The High-pressure Laser Floating-zone Furnace

3.1 Challenges for the Floating-zone Method

This thesis is concerned with the development and usage of the high-pressure FZ technique. Before diving into the details of the furnace which was designed and constructed for this purpose I will briefly go over the challenges which present for traditional floating zone growth. In Section 3.3 I describe how a number of these challenges are addressed in our design.

A fundamental challenge in FZ is the fact that there exist many scientifically interesting materials which are not congruent melters. This reality means that such materials are inaccessible via the "typical" floating zone process described previously because they either melt incongruently or simply decompose into their consituents before melting. It is clearly desirable to have the ability to modify the thermodynamics of the material within the floating zone furnace in order to modify phase stability. As mentioned previously, solvent-based techniques provide one means of accomplishing this, though identifying an

appropriate solvent can be an arduous task and is not always feasible. There is also the so-called' 'self-adjusted" technique which involves taking advantage of the decomposition reaction of a certain composition to lead to an extended (but ultimately transient) period of time where the desired phase is grown. Both techniques often require having detailed knowledge of the phase diagram of the elements involved - these data are often not available, especially when one is attempting synthesis of new materials, and would have to be generated. Besides thermodynamic challenges posed by certain stoichiometries, simple chemical volatility (due to elevated vapor pressure of certain elements or compounds in the liquid state) can also prevent successful floating zone growth.

Another traditionally challenging arena for conventional FZ is the growth of materials with high melting temperatures. The typical maximum temperature for incandescent bulbs is around 2100 °C, which means many refractory materials, even if they are congruent melters, are out of reach in most laboratories. For context, $Nd_2Zr_2O_7$ melts around 2350 °C and single crystals of this material only became available upon the advent of high powered xenon arc lamps used in a vertical geometery mirror furnace. While these xenon lamps are a clear improvement, and provide heating powers commensurate with very high melting temperatures, this benefit typically comes with a degradation in the axial heating gradient. A high axial heating gradient is important variable because in addition to helping establish conditions favorable to grain selection, it can also help improve molten zone stability. This is important for another class of materials which are often challenging to grow with conventional floating zones: materials with low surface tension melts. Since stability of the molten zone relies on the surface tension of the liquid bridge, a low surface tension dramatically reduces stability and can prevent growth of a desired material. A high axial heating gradient is also helpful in preventing certain detrimental phenomena in traveling-solvent fZ growths which can lead to zone instability [22].

As will be elaborated in detail in the next section, pressure provides a more straightforward means of modifying the growth process, as well as a means of dealing with volatility. However, the pressures attainable in most floating zone furnaces are often not sufficient to enable growth of materials when these issues are present. Increasing the attainable pressure is therefore an important goal in furnace development for improved bulk crystal growth. All previous work in this direction has utilized high-powered lamps and mirrors for heating and thus was restricted to transparent growth chambers due to the continued need for large solid angles of optical access. The typical horizontal 4-mirror FZ furnaces utilized in most modern labs – which are not much different in their design (other than improved computer control and imaging) than the first such furnaces developed in the 1970s – possess pressure vessels made from fused silica and can support up to 10 bar (145 psi). Pioneering work in the 1980s by Balbashov *et al.* allowed for pressures up to 100 bar in a fused quartz pressure vessel. This accomplishment relied on the development of the single-mirror vertical geometry, coupled with high-powered xenon arc lamps. This design improved the focusing of the lamp light thus decreasing the required optical access and allowing for a shorter growth chamber which, along with increased wall thickness, increased the attainable pressure [20]. This design was subsequently pushed further by the German company ScIDre (Scientific Instruments of Dresden), which currently produces a vertical-mirror furnace capable of providing pressures up to 150 bar in a sapphire growth chamber. A further advance was made in 2019 by ScIDRE in collaboration with the PARADIM center at Johns Hopkins University with the construction of a vertical-mirror furnace capable of growth at up to 300 bar [21].

It is my opinion that this 300 bar furnace likely represents the (practical) peak of high-pressure FZ growth in mirror-based furnaces. The restriction of the required optical access necessitates the use of transparent and inherently brittle materials; while single crystal sapphire has a very high Young's modulus ($\approx$ 345 GPa) and is capable of

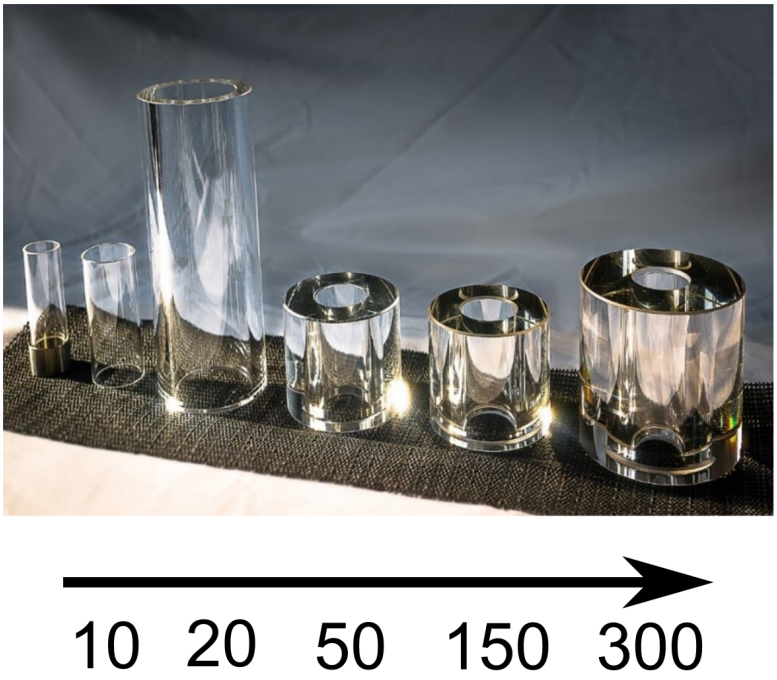

Figure 3.1: Illustration of the progression of pressure vessels for mirror-based designs. From the left, the first four cylinders are fused quartz and allow from 10 to 50 bars of pressure. The next two cylinders are made of single-crystal sapphire and allow 150 and 300 bars pressure, respectively. (Photo provided courtesy of ScIDre (Scientific Instruments of Dresden)) [10]

supporting large stresses, the failure mode remains brittle (*i.e.* "catastrophic") fracture. Furthermore, a consideration of the equations for the r-dependence of the tangential, or "hoop", stress in a thick walled cylindrical pressure vessel,

$$Tangential : \sigma_t = \frac{p_i r_i^2 - p_o r_o^2}{r_o^2 - r_i^2} + \frac{(p_i - p_o)\, r_o^2 r_i^2}{(r_o^2 - r_i^2)\, r^2} \tag{3.1}$$

suggests a geometric limit for the maximum pressure achievable in transparent pressure chambers. The dependence on $\frac{1}{r_0^2 - r_i^2}$ means that the wall thickness of transparent pressure vessels must increase rapidly at large pressures in order to keep the maximum stress well below the fracture stress, as required by the lack of a plastic deformation regime in brittle materials. Even with single crystal sapphire - which is essentially the only practically

available material that provides both the needed optical and structural properties - at increasingly higher pressures attaining the required wall thickness with any reasonable internal volume (*i.e.* internal radius) becomes impractical. Figure 3.1 illustrates this concept in practice, showing the evolution of transparent pressure vessels. As will be made clear in the Section 3.3 our design aims to move beyond this basic limitation and its impact on attainable growth pressures.

3.2 Motivation for High-pressure Floating-zone Growth

Since the design of the laser furnace is centered around the goal of increasing the available growth pressure, it is worth discussing why we care about pressure as a floating-zone process variable and elaborating on what effects it has on the growth process. It is helpful to divide these effects into two conceptual categories: *kinetic* and *thermodynamic*.

It should be clarified that in using the word "kinetic," I am not referring to the kinetics of crystallization, meaning the dynamic (and non-equilibrium) processes of nucleation and growth. A detailed discussion of the specific aspects of crystallization kinetics relevant to the floating-zone technique is beyond the scope of this thesis, however it is an active area of research with an extensive literature. Here I use kinetic to refer to how pressure acts to reduce the volatility of a component from the molten zone via a molecular collision-based effect, which comes from the kinetic theory of gasses. Due to the wide variation in the temperature dependence of vapor pressure for different elements and molecules, the temperature required to melt a compound may lead to a significant amount of one component being expelled from the melt (*i.e.* volatilizing). If a sufficiently high pressure of gas exists inside the chamber, then a statistically significant number of collisions

between the molecules of the volatile species and the gas molecules will occur at the surface of the melt. Such a reflecting collision has the potential to balance the vapor pressure of a volatile component, and thereby reduce the bulk volatility from the melt. This intuitive effect is formally described by the kinetic theory of gasses from which an expression can be derived that shows a direct dependence of the evaporation rate of a molecule on a constant that is inversely dependent on pressure [21, 23]. Excessive volatility is a common reason that single crystals of a compound are inaccessible by FZ-growth due a variety of issues. In conventional mirror-based furnaces, the build-up of a volatile component on the inside of the growth chamber can diminish the optical power imparted to the sample, eventually leading to freezing of the molten zone. Furthermore, this coating can also negatively impact the ability of the operator to image the growth process. Volatility can also cause instability of the molten zone due to depletion of the volume of material in the hot zone. In essence volatility acts as another mass flow route (in addition to the feed and crystal growth rates) which can cause the liquid bridge to collapse if not compensated by feeding in material faster. As a corollary, this extra mass flow route can lead to defect formation and off-stoichiometry in the grown crystal due to depletion of the volatile element in the molten zone, so reducing volatility by increasing gas pressure is also directly related to sample quality. This feature is of essential importance to the work on $Nd_2Zr_2O_7$ described in Chapter 5.

While the benefit of decreased volatility certainly helps to expand the realm of materials to which floating zone crystal growth can be applied [1], the biggest motivation for high-pressure floating zone growth stems from the fact that pressure provides a variable for tuning phase stability. Pressure is a thermodynamic variable, meaning it is one of a set of variables which describe the equilibrium thermodynamic state of a system without

[1] See the work by my groupmate Zach Porter on growth of $Sr_2(Ru_{1-x}Ir_x)O7$, conducted using the furnace described here, for an excellent example of how high pressure can be used to conquer extreme volatility and enable the production of new materials [24]

regards for the "path" (or history) that brought it to that state. Equilibrium thermodynamic states are described by state functions (which have thermodynamic variables as their inputs) which capture specific features of that state. In terms of phase stability (or, in an equivalent sense, the favorability of a chemical reaction) the state function of interest is the Gibbs free-energy: $G(P,T) = U - TS + PV$ where U = internal energy, T = temperature, S = entropy, P = pressure and V = volume. The stability of a phase is determined by the sign of the free energy change during the reaction that produces that phase which we can write down in an infinitesimal form as: $\mathrm{d}G = -S\ \mathrm{d}T + V\ \mathrm{d}P + \sum_{i=1}^{n} \mu_i\ \mathrm{d}N_i$, where $\mu_i = \left(\frac{\partial G}{\partial N_i}\right)_{T,P,N_{j\neq i}}$. We now directly include the chemical potential into the free energy, which represents the change in the free energy attained if we add a small amount of component i to the system. If, for some combination of P and T, (assuming constant composition) the sign of the free energy change for a reaction forming a specific phase (say, A + B $\rightarrow$ AB) is negative, meaning G is lowered upon completion of the reaction, then that phase is thermodynamically stable. If a variety of phases exist with negative free energy changes then the one with the largest free energy decrease (largest $|\Delta G|$) will be the phase that forms at equilibrium. One often speaks of free-energy "landscapes", referencing the hills and valleys in the surface of a 3-dimensional plot of $G(P,T)$.

The presence of a variable in the expression for free energy change indicates that it provides a means of modifying phase stability. Of the available variables, pressure is one of the more direct and experimentally accessible tuning knobs for chemists and materials scientists seeking to make new phases. The ability to stabilize phases via high-pressure FZ which are metastable under standard conditions has significant implications for condensed matter physics research because it improves our access to materials which map to theoretical models/Hamiltonians. By providing an ever-broader range of material platforms, including potentially long elusive compounds, new regimes of exotic electronic and magnetic states can be accessed. Furthermore, these crystals benefit from all the atten-

dant advantages of FZ-growth discussed previously: ultrahigh purity, high crystallinity, and large size.

Some further details are necessary to understand how pressure affects thermodynamics in floating zone growth and to make clear the practical benefits of high-pressure. As was made clear by Phelan *et al.* in their discussion of high-pressure FZ [21] the pressures currently attainable in floating zone furnaces (300 bar in their mirror-based design, 1000 bar in the furnace described here) are nowhere near the energy scale of atomic bonding. To put in another way, if you were able to monitor the structure of a compound which was pressurized in the furnace (say with an in situ X-ray technique as is done with diamond anvil cells capable of reaching pressures in the 10s of GPa), there are most likely no compounds which would undergo spontaneous structural phase transitions at these pressures: much higher pressures are needed to modify the free energy landscape. As an example, consider elemental Fe at room temperature (293 K): the pressure required to induce a phase transition (from body-centered cubic α-Fe to hexagonal close-packed ϵ-Fe) is $\approx$ 12500 bar [25]. 1000 bar is not enough of a perturbation to substantially change bond lengths, and therefore volume, in order to modify the free-energy landscape via the pressure term.

Rather, the thermodynamic impact of pressure relies on the gas medium being a reactive one which can participate in chemical reactions that occur as the liquid recrystallizes. The pressures attainable in current FZ furnaces interact with the free-energy landscape through direct modification of the chemical potential for ions within the melt. To put it concretely with an example: high-pressure (on the aforementioned scale) Ar, an extremely chemically inert gas, has almost zero effect on the thermodynamics of the growth process; only the kinetics of volatility are modified. However, high-pressure oxygen, for example, can often participate in chemical reactions and thereby change the thermodynamics via the chemical potential. As a result, this can allow for stabilization

of abnormally high valence oxidation states which would be far out of equilibrium at standard pressures. An excellent example of the value of high-pressure O_2 as a growth environment is the recent successes in stabilizing members of the lanthanide nickelate family of perovskites at pressures ranging from 150 ($LaNiO_3$) [26] to 300 bar ($PrNiO_3$) [27].

Besides stabilizing abnormal valences, high pressure can also suppress decomposition reactions via modification of the chemical potential. One can see this clearly by considering the following reaction for AlN and recalling Le Chatelier's principle[2]: AlN (S) $\rightarrow$ Al (S) + N2 (g). While this reaction is known to proceed to the right at high temperatures under standard conditions (*i.e.* decomposition), suitably high N_2 pressures should modify the free-energy landscape so that the reaction remains unfavorable at higher and higher temperatures.

In principle, if the decomposition temperature can be pushed above the melting point of solid AlN, a melt could be established and a crystal growth by FZ. Indeed some evidence for stabilization of an AlN melt via high nitrogen pressure has been published [28, 29]. Growth of AlN in LAPIS and LOKII was attempted several times during this thesis at N_2 pressures from 207 to 345 bar. While clear evidence of surface melting was observed, no stable molten zone could be established due the insufficient liquid volume. AlN does not couple well to either wavelength in use, and also appears to volatize/ablate intensely when heated to sufficiently high temperature. However, in general, nitrides present a profitable future avenue for high-pressure floating zone growth and efforts in this direction are being made in the Wilson group. Separately, one could also imagine

[2]Le Chatelier's principle says in essence that a well equilibrated system (*i.e.* a chemical reaction in equilibrium) which is subjected to a change in a thermodynamic state variable will move to a new state of equilibrium which acts to reduce the total change of the state variable. Thus in the example of AlN, if we are at an equilibrium state for this reaction AlN(s) $\leftarrow\rightarrow$ Al(s) + N2(g) and we apply N_2 pressure, the system will act to reduce this change by moving to an equilibrium state with more AlN(s). In this manner N_2 pressure acts to supress decomposition.

utilizing a high-pressure reducing atmosphere for stabilizing abnormally low valances..

3.3 Key Design Elements

The various elements of the laser furnace work in concert to overcome the geometric pressure limitation inherent to transparent pressure chambers while simultaneously maintaining the ability to attain high-temperature melts. From a materials selection point of view, the challenge of constructing a vessel to contain a large pressure is best solved by use of a structural metal alloy. Unlike fused silica or single-crystal sapphire, such alloys have extended plastic deformation regions of their stress strain curves - leading to higher strength - and do not typically undergo catastrophic brittle fracture. As a result metal pressure vessels can, with reasonable dimensions, safely contain much higher internal pressures than even single crystal sapphire. Furthermore, metal alloys can be much more easily machined into complex shapes. This allows for discrete points of optical access (*i.e.* high-pressure windows) to be engineered into a metal pressure vessel, a necessity for melting materials *via* optical heating. Of course, in order to keep the structural advantages of a metal chamber the transparent solid angle of these windows should be kept to a minimum. This smaller solid angles requires optical heating with much more focused light which can pass through a narrow aperture while still delivering high power densities to the sample. The solution to this challenge is to move to optical heating based on lasers, where the coherency of the light allows for tailoring of the beam profile with conventional optics. So, to summarize in reverse: the use of high-powered lasers coupled with focusing optics allows the laser furnace to provide high power densities without the need for large solid angles of optical access. The elimination of the need for large areas of optical access allows for the use of an all metal pressure chamber with discrete high-pressure windows. Such a chamber can be straightforwardly engineered to

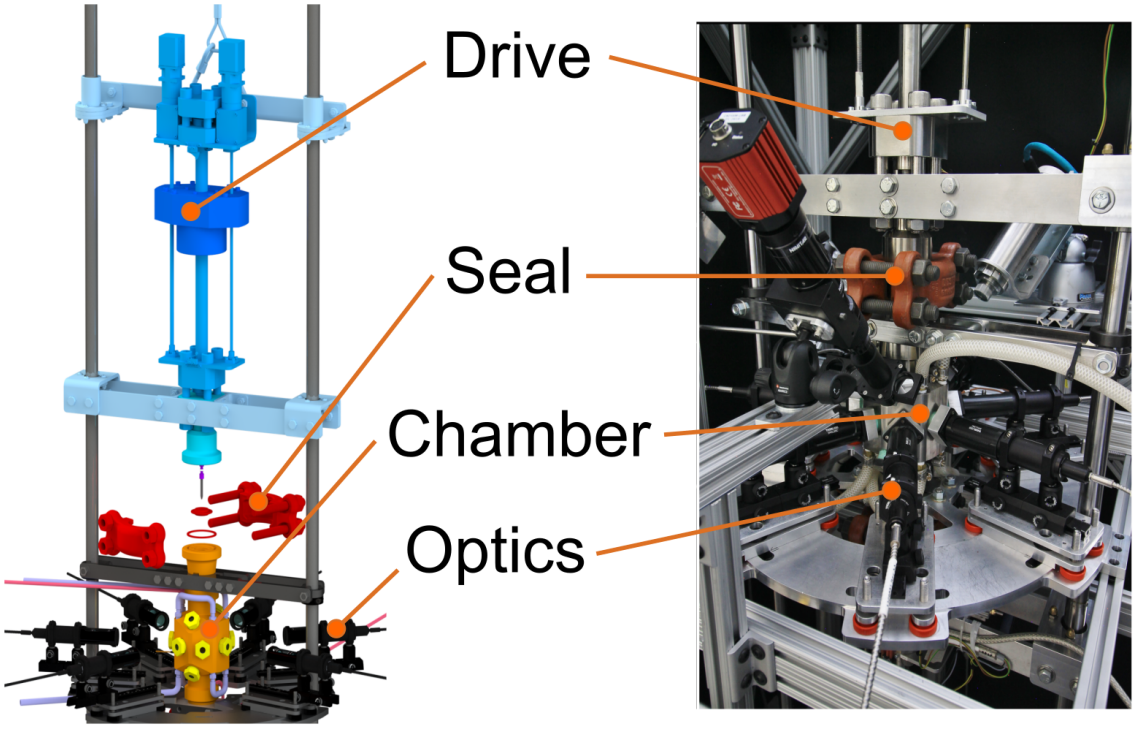

Figure 3.2: *Left*: Computer rendering of LAPIS (*credit*: Michael Ailing) with the main components labeled. A second translator for manipulation of the seed rod mates with the chamber from below (not pictured). *Right*: A photograph taken by the author of LAPIS as it appears when assembled for growth. Note the camera (foreground) and pyrometer (background) which image the zone through the out–of-plane ports. The appearance of LOKII is very similar, besides the modified chamber and usage of in-plane imaging (see Section 3.3.1)

contain significantly higher pressures than a transparent one.

During the course of this thesis, two laser furnaces based on these design elements were constructed. The prototype, known as LAPIS (Laser and Pressure Induced Synthesis) and shown in Figure 3.2, was completed in 2018 [4] and served as a very successful proof of principle. Subsequently, a second furnace, known as LOKII (Laser Operated Kristallzúchtungsanlage II) was completed in 2021 which incorporated several design improvements based on issues encountered during extended usage of LAPIS. In the following sections I describe some of the specific details of the components of these furnaces, with design issues and subsequent improvements mentioned as appropriate.

3.3.1 Pressure Chamber, Windows and Imaging

The core of the laser furnace design is the assemblage of the high-pressure metal growth chamber and high-pressure windows. The design of these chambers was predominantly performed by Michael Ailing who was, at the time, a very talented undergraduate and is now a very talented graduate student). He performed extensive mechanical simulations of the stress patterns and tolerance to surface cracking, indicating a maximum pressure of 1000 bar (15,000 psi) for the chamber and excellent fatigue behavior.

The growth chamber is constructed from a nickel-based superalloy, known as Inconel 718. First and foremost amongst the desirable properties of Inconel is its high-strength, even at elevated temperatures, and intrinsic resistance to oxidation (due to the development of a passivating layer) or chemical attack. One notable exception of Inconel's chemical resistnace is it's susceptibility to embrittlement by H_2; any reducing environment would probably operate similarly. Such properties are essential for safe use of a high-pressure oxygen environment during growth and to reduce the chance that the interaction with volatilized elements/compounds compromises the structural integrity of the furnace. Additionally, a removable shroud, in the form of a thin metal cylinder, is placed within the central bore of the chamber to protect it from direct thermal radiation and direct contact with molten or volatilized material. Initially the shroud was constructed with various ports and recessed holes which supported quartz cylinders - to provide a view through the shroud while still protecting the chamber - and individual antireflection-coated sapphire rounds, which allowed the beam to pass through. This rather complex design, which required careful alignment with the bores through which the laser light passes, was later supplanted by a much simpler one in which a special anti-reflection coated (by Deposition Sciences Inc. using a modified MOCVD process) fused quartz cylinders sits between two mating metal tubes and provide a full 360 de-

grees of optical access for the lasers. y These cylinders were found to be more resistant to cracking from chemical attack or contact with hot material, possibly due to the difference in thermal conductivity between sapphire and fused quartz. This subsequent shroud design was also made from a copper-beryllium alloy (referred to as "CuBe" though it is prediminately Cu - the content of Be is $\approx$ 2 weight %) which has better oxygen compatibility and chemical resistance than the original Al. The chambers were subjected to precipitation hardening through a specialized annealing treatment in vacuum/inert gas conditions prior to use. This hardening nucleates small precipitates in the matrix of the alloy which act to inhibit the movement of dislocations when the chamber is under stress, thus helping to suppress crack formation/propagation and improve lifetime. Several channels run through the walls of the chamber to allow for water cooling with a chiller in order to keep the chamber temperature from getting unacceptably high during growth.

A cutaway rendering of the original chamber design for LAPIS is depicted in orange in Figure 3.3**a**. The central bore ($\approx$ 25 mm in diameter) contains the hot zone where crystal growth takes place. Seven 5 mm radial bores, equally spaced around the chamber, provide access points for the focused laser light. Four larger (10 mm) bores come in from above and below the plane of the lasers. The two above-the-plane bores were used for imaging of the molten zone using a CCD camera and a two-wavelength pyrometer which looked down at the zone at a rather steep angle. It should be noted that the temperature readout of this pyrometer can vary significantly from the true sample temperature. For example, when melting alumina the pyrometer reads $\sim$200 °C below the true melting temperature. This deviation is due to the lack of an applied correction for variations in the emissivity of different samples (*i.e.* deviations from a true black-body with emissivity of one); as such, measurement of a known standard does not provide a universal correcting factor. However, the pyrometer value still serves as a helpful reference between growths

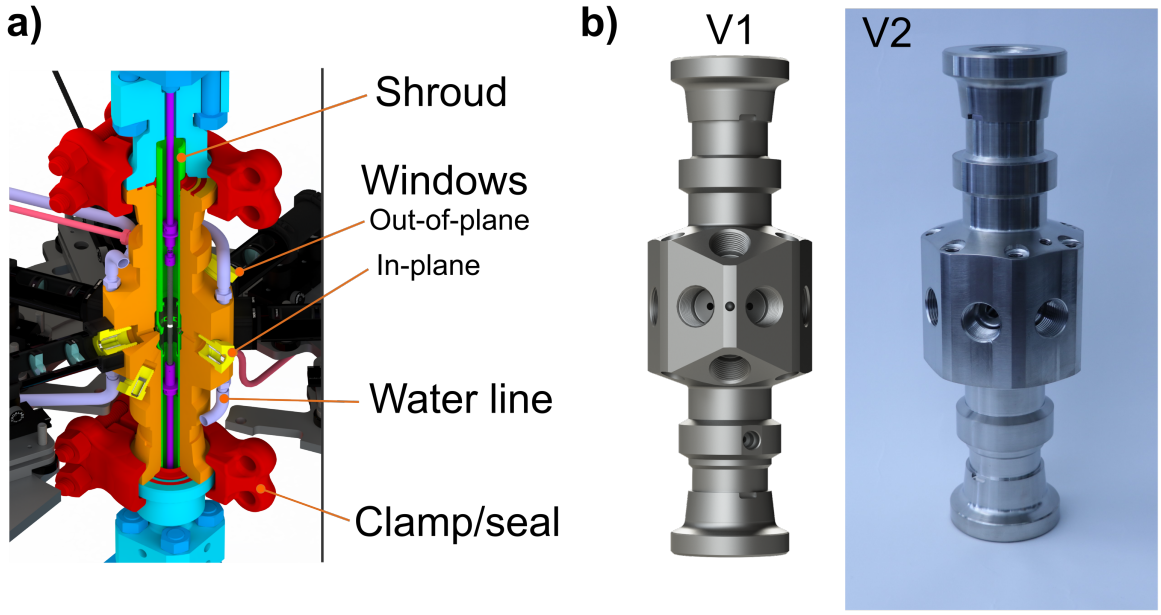

Figure 3.3: **a)** Cutaway computer rendered image of the original LAPIS chamber set-up (*credit*: Michael Ailing). Several components are labeled. **b)** Comparison of the original (V1, left, image credit: Michael Ailing) and subsequent (V2, right) chamber designs. The differences between the two chambers are described in the main text - most visible here is the removal of the out-of-plane windows for the V2 chamber

of the same material since the emissivity remains the same. Each bore on the chamber terminates (on the outside of the chamber) with a set of female tapered NPT pipe threads for replaceable mounting of the pressure windows which provide optical access. The original windows on LAPIS were provided by Encole LLC and consisted of antireflection-coated fused silica sight glasses bonded inside a stainless steel housing with male tapered NPT pipe threads.

Extensive usage of LAPIS revealed several fundamental problems with this window design. By far the primary issue was that the structural integrity of the fused silica was not reliable at high-pressures ($\geq$ 700 bar) and they were found to fracture in several instances. Luckily, the amorphous nature of the silica, and the small size of the sight glasses, made these fracture events less catastrophic than they could have been. A sec-

ond issue was the discovery of extensive galling of the housing threads, which occurred on insertion/removal of the windows into the chamber despite the use of PTFE tape. This negatively impacted reusability and likely also the seal quality at the treads. This galling can probably be attributed to the mismatch in hardness between the Inconel of the chamber and the stainless steel of the threads. Another issue realized during usage of LAPIS at high-pressure was the difficulty in imaging the zone through the intensely turbulent convection generated by the temperature difference of the molten sample and the water-cooled chamber walls. The density variations in the gas significantly disturbed image quality through either the camera and pyrometer, making it challenging to properly monitor the molten zone at high temperatures and pressures. This problem was magnified further during the growth of volatile compounds, where evaporated material further obscured the view. Both of these problems were subsequently solved during the construction of LOKII.

First, an optical apparatus for both imaging and introducing laser light through one of the in-plane ports was developed (Figure 3.4) with the goal of improving the image quality. This idea was based on the supposition that looking downward at the zone at a steep angle increased the impact of the convective mass flow on on the imaging. This gas flow occurs in a cyclical up-and-down motion as the gas is heated by the molten zone and then cooled by contact with the chamber walls as it rises. Thus the out-of-plane configuration is imaging through a longer region of density fluctuations than the in-plane configuration. Removal of the steep imaging angle would also make interpretation of the images easier, with respect to monitoring the molten zone for stability issues during a growth. In the subsequently developed apparatus, laser light is bounced off an ultrafast mirror, down through the focusing optics (see Section 3.3.3), and then off a dichroic mirror and into the chamber. The dichroic mirror has an engineered coating with very different reflectivities at two broad wavelength ranges - in this case, the dichroic mirror is reflecting

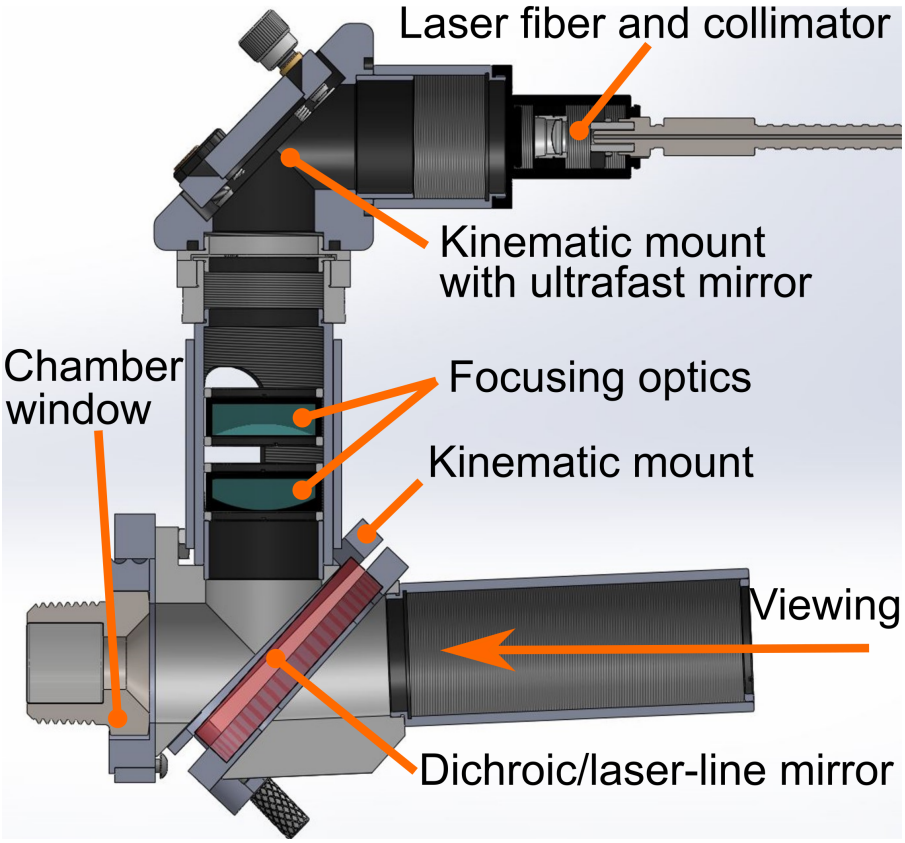

Figure 3.4: Rendering of the in-plane viewing apparatus, with key components labeled. By use of various mirrors, the camera/pyrometer can be placed in-plane while the laser light is piped in from above and then into the chamber through the same port. Image credit: Michael Ailing.

at the wavelength of the laser, but transmissive at wavelengths visible to the camera. In the case of the pyrometer, a laser line mirror was used, which is reflective only across the narrow range of the laser and transmissive elsewhere. This is necesarry to ensure the pyrometer can access the wavelengths it uses for calculation of the temperature, which is based on comparing the ratio of two wavelengths to a calculated black-body spectrum. Experiments with this apparatus on LAPIS showed that the images obtained at high-pressure and temperature with the camera in-plane were superior to those obtained with the camera out-of-plane, though the use of the dichroic mirror does introduce even more inaccuracy of the pyrometer readout (though it is not detrimental to precision). Use

of this in-plane viewing apparatus enabled fabrication of a second generation chamber (Figure 3.3**b**)which did not utilize out-of-plane windows. This design change had other advantages as well. It allowed for an increased number of water cooling lines, previously impossible due to the placement of the out-of-plane windows, which improved the ability to cool the chamber when operating at high laser power. Additionally, the increased size of the in-plane laser bores likely reduces the occurrence of stray laser light clipping the walls of the chamber on the way into the main bore. In-plane viewing was found to produce much clearer images at high-pressures, and made for easier active modification of growth parameters based on observations of the molten zone.

The issue of cracking pressure windows was solved by a complete overhaul of the window design, conducted by Jayden Plumb. The new design utilized thicker, single-crystal sapphire, sight-glasses, mounted inside an Inconel housing. The move to an Inconel housing, compatible with the Inconel pressure chamber, drastically reduced the amount of galling observed after installation and removal of a window. The new design also utilized a different sealing mechanism: rather than bonding the sight glass to the housing via an adhesive (as in the Encole design) the seal is made using a high-temperature compatible (max operating $T \approx 200$ °C) O-ring seated inside the housing. A slight pre-load is applied to the sight-glass and O-ring via a CuBe retaining ring within in the housing. A seal is then created as the internal gas pressure pushes the sight glass against the recessed O-ring, which deforms to fill in the gaps. This design worked quite well and is capable of containing pressures up to 950 bar (the highest tested). An issue with this design was encountered in the first iteration of the Inconel housings, when operating at high laser powers and thus high chamber temperatures. In several cases it was observed that the O-rings, due to the high temperature, extruded through the gap between the sapphire and the Inconel housing, eventually leading to shattering of the sight glass when it touched the housing. These housings were found to have a slight machining error where

the recesses that held the O-rings were made too small such that the O-ring had less space to expand into as it was compressed. This caused extrusion at high temperatures as the O-ring softened and eventual failure of the window. Correction of this machining error largely mitigated dramatic extrusion, however the O-rings do deform and soften over time as they are periodically exposed to high temperature.

3.3.2 Translating System

As mentioned in the previous chapter, smooth translation and rotation of the feed and seed rods is an essential part of any floating zone furnace. The translation/rotation method of typical floating zone furnaces meant for low-pressure growths, utilizing geared motor systems which push a shaft through a greased O-ring which is compressed against the shaft to form a seal, become untenable at high pressures. In order to hold 1000 bar of gas pressure, the dynamic seal would need to be compressed against the drive shafter with a very large force. This large compression translates directly into large frictional forces, which would need to be overcome by an exceptionally powerful motor to provide smooth motion of the translation shafts. A dynamical seal thus presents a substantial engineering problem. The laser furnace design evades this problem by utilizing a magnetically coupled drive system developed by SciDre GmbH - in fact, this is the same basic design as used in the high-pressure mirror furnace developed for PARADIM [21]. These drives (Figure 3.5) are made up of a translating sample shaft with several powerful permanent magnets attached to it, which sits inside of an autofrettaged metal pressure tube. An external gearbox moves up and down the pressure tube by means of a lead screw and couples to the magnets of translating shaft by a magnet pack inside the gearbox. Rotation is made possible by a keyed shaft which rotates the magnet pack in the gearbox, thus rotating the shaft. Since the sample shaft is completely enclosed within the high-pressure

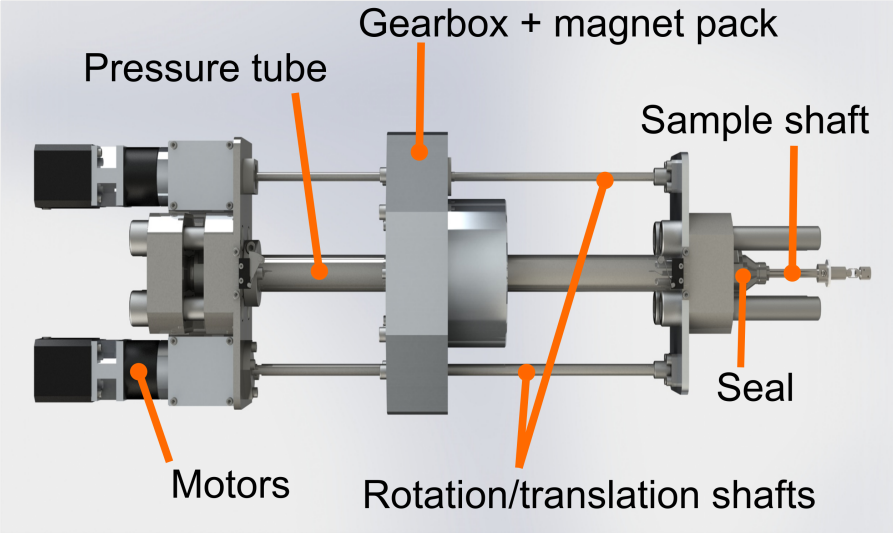

Figure 3.5: Rendering of the SciDre translating/rotating drives used in the furnaces. Key components are labeled. Image credit: Michael Ailing.

environment, there is no need for a dynamic seal, and no pressure differentials or frictional forces to overcome. The load requirements on the drive motors of the translators are thus vastly reduced and smooth rotation and translation can be accomplished.

In order to obtain the desired high-pressure growth environment, it is necessary to seal the drives to the chamber. This is accomplished in two stages. First, each drive is attached to a custom made Inconel adapting collar (see the light blue features in Figure 3.3**a**) via a meta-to-metal cone seal. The cone end of the translator (visible on the right side of Figure 3.5 where the sample shaft emerges) is compressed into a conical indent in the adapter by applying torque to four large connecting bolts. This seal was made during construction and is only undone to conduct maintenance or cleaning of the drives. The collars are then attached to the chamber by means of a reusable , MoS_2 coated, Inconel seal ring and a set of clamps (produced by Destec Inc. - see the red features in Figure 3.3). The seal ring sits between mating indentations on both the adaptors and the chamber and is compressed by applying torque to the bolts that run through the clamps. Regular access to the central pressure chamber is needed in order to install

the feed and seed rods and remove material after a growth, and these seals are made and unmade many times. During the set-up process the translators, which are attached to counterweights via a pulley system, can be moved vertically away from the chamber along guide rails.

3.3.3 Lasers and Focusing Optics

The final major components of the furnaces are the lasers which, in conjunction with the associated focusing optics, enable efficient optical heating through narrow points of optical access. The goal of the optics system is to pass the laser light through the window bores of the chamber without clipping the chamber and produce a focused spot at the position of the sample. A schematic of the optical set-up as originally used in LAPIS is shown in Figure 3.6; the set-up with the in-plane imaging apparatus is analogous. The set-up consists of seven sets of collimators and focusing lenses arranged horizontally around the pressure chamber. Note that an odd number of lasers must be used so as not to inadvertently introduce the direct beam from one laser unit into another, which could cause severe damage. Light is brought from the laser unit ino the optics via fiber optic cables that terminate in a collimator (not shown in Figure 3.6 but which attach to the outward ends of the black lens holders). Collimation is essential due to the finite divergence of the beam upon exiting the fiber. This divergence is described by the numerical aperture ($NA = n_{air}Sin(\theta_{div})$, where n_{air} is the index of refraction in air) and is a result of critical angle for total internal reflection within the fiber, which itself a function of the indices of refraction of the fiber cladding and core. The collimating lens greatly reduces the divergence of the beam though some finite divergence remains as a consequence of the finite size of the fiber, which causes it not behave as a true point source. The divergence of the beam after the collimator, α, takes the following form:

$\alpha = d/f$, where d is the diameter of the fiber core (where the light waves propagate) and f is the focal length of the collimating lens. Interestingly, α is actually the most influential variable in the structural design of the pressure chamber, because it determines how close (radially) the optics need to be to the sample to produce the desired laser spot. If α is too large, and the optics must be very close to the sample to accommodate the divergence, then the wall thickness of the chamber cannot be made large enough to contain the desired high gas pressures. α also impacts how large the diameter of the window bore must be to accommodate the beam profile. As the diameter of the window bores become larger a sharp edge begins to form between neighboring bores, which acts as a stress concentrator. This forms one of the high stress points in the chamber when it is under pressure and therefore its failure properties are the bottelneck with respect to the maximum pressure of the chamber.

Subsequently, the collimated laser light passes through two cylindrical plano-convex focusing lenses in order to tailor the beam profile and the resulting spot shape shape on the sample. The shape of the plano-convex lens is such that focusing of the refracted light occurs primarily along one principle direction. This allows a rotationally anisotropic spot to be produced by placing two lenses at different distances from the sample with orthogonal principle axes. An elliptical spot is ideal because it allows for shortening the vertical extent of the molten zone relative to its width while also decreasing inhomogeneities in heating at the boundary of the molten zone which would be exaggerated with a circular spot. Extending the horizontal axis ensures that each spot overlaps with its neighbors when they hit the sample, creating uniform circumferential heating. Simple equations are available to describe how the path of the light changes as it passes through all of the components of the optics system. Therefore, it is relatively easy to build a model which describes the profile of the beam at all points. In this way the beam profile can be tuned - by modifying the relative and absolute locations of the focusing lenses - to pass

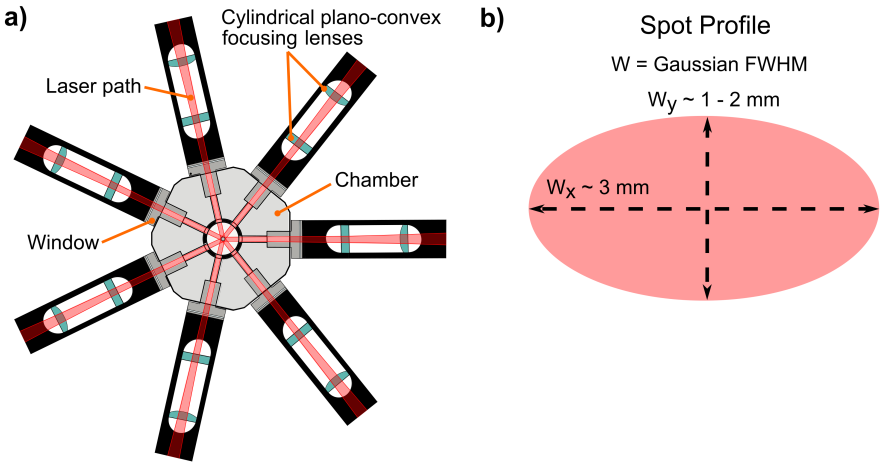

Figure 3.6: **a)** Arrangement of the focusing optics in the original LAPIS design (without the in-plane imaging apparatus). The beam profile must be carefully tailored to both produce an acceptable spot size on the sample (which defines the extent of the hot zone) and to avoid clipping the chamber as it passes through the window bores. The apparatus for in-plane imaging (shown in Figure 3.4) utilizes the same type of focusing optics.**b)** Schematic of the resulting elliptical laser spot profile at the sample. The intensity variation is a Gaussian in the vertical and horizontal directions. The lower post-collimation divergence of the lasers in use on LOKII allows for making shortening the vertical extent of the spot, which is useful for very high-pressure growths.

uninterrupted into the chamber.

Two different types of lasers were employed in the construction of LAPIS and LOKII. LAPIS employs a stack of seven 100 W "diode" lasers produced by Coherent Inc. which operate across a relatively large range of 800 - 820 nm (it was eventually discovered that, for unknown reasons, there is a minor additional sub-700 nm mode produced by these lasers). LOKII improves upon the heating capabilities of LAPIS by employing a stack of seven 200 W "fiber" lasers, produced by IPG Photonics, which operate in a very narrow band around 1070 nm ($\pm$ a few nm). The nomenclature of diode versus fiber is a bit confusing. Both utilize semiconductor-based laser diodes to produce highly coherent light, but the diode geometries are slightly different. The fiber lasers use a single optically active fiber as the gain medium while the diode lasers use two diode bar

arrays, which are lines of multiple small laser diodes. The important distinction between these two geometries is that the fiber laser couples a single optical mode to the fiber optic cable, while the diode laser couples multiple mode. This means a single-core fiber optic cable can be used for the fiber lasers while a multi-core fiber optic cable is required for the diode lasers. As a result, the fiber optic cables for the diode lasers have a larger core size which leads directly to a larger post-collimation divergence. Fiber lasers are therefore more flexible both in terms of the ability to shape the laser spot and with respect to pressure chamber design. The ability to more freely tune the vertical extent of the spot on LOKII has proven valuable. Empirically it has been found that at very high pressures the laser path is actually bent downards, pushing the spot to project onto the seed below the plane of the windows. The most reasonable explination for this behavior is the occurence of a gradient in the index of refraction of the gas due to the temperature (and thus density) variation caused by heat flow from the molten zone. This is analogous to what is happening when you see haze on a hot asphalt road. Decreasing the height of the laser spot (down to ≈ 1 mm) appears to ameliorate this problem. Furthermore, fiber lasers also generally provide higher laser power levels, which is desirable. Both lasers set-ups allow for pulsing of the produced light. By setting a finite duty cycle (such that during a time t_{duty} the laser is only for t_{on} with $t_{on} < t_{duty}$) the effective power of the laser can be lowered. This can help improve temperature control of the melt at low powers, where setting of the laser diode power is less accurate.

Up to this point I have only discussed the laser-based heating aspect of the furnace in the context of its role in enabling high-pressure growths. However laser-based heating also provides a variety of other benefits to the floating zone growth process; there are several examples of laser-based furnaces constructed prior to ours which were optimized for other purposes besides high-pressure [30, 22, 31]. The most obvious improvement, which motivated the initial development of laser-based floating zone, is the increased

power density allowing for increasingly high growth temperatures [10, 30]. Provided the laser wavelength and sample absorption spectrum are reasonably well matched, this eases the challenge of growing high melting temperature materials, increasing access to interesting refractory materials such as $Nd_2Zr_2O_7$ (Chapter 5). The improved focus of lasers offers several advantages in addition to simply attaining higher melt temperatures. Improved circumferential uniformity can be obtained because a larger number of incident laser beams can be utilized compared to what can be accomplished in mirror furnaces. This uniformity helps reduce oscillations in the surface temperature of the melt and avoid subsequent rapid freezing events which can destabilize the zone [22]. The compact optical zone formed by focused laser light also provides a much sharper axial heating gradient than lamp-based furnaces; gradients higher than 1500 °C/cm may form near the solid-liquid boundary of the molten zone [22, 32] compared to 200 - 400 °C/cm found in typical lamp-based furnaces due to the presence of non-normal incidence light from the conventional bulbs [33]. This steep axial gradient helps to sharpen molten zone boundaries which, due to its favorable effect on surface tension, can lead to more stable growths than in a mirror furnace. We observed such behavior in the growth of $GdTiO_3$ [4], which is discussed briefly in Section 3.4. Finally, the narrower melt zone obtained via lasers also leads to a reduction in the amount of molten material, which can be beneficial for the growth of volatile materials [32].

3.3.4 Gas Handling System

The gas handling system utilized in the laser furnaces is not a particularly novel constructuction but it is described here for completion. The system is broken up into low and high-pressure sides divided by a gas booster. On the low pressure side ($P \approx 70$ bar), different gas compositions (typically Ar, N_2 and an 80:20 Ar and O_2 mix) are piped into

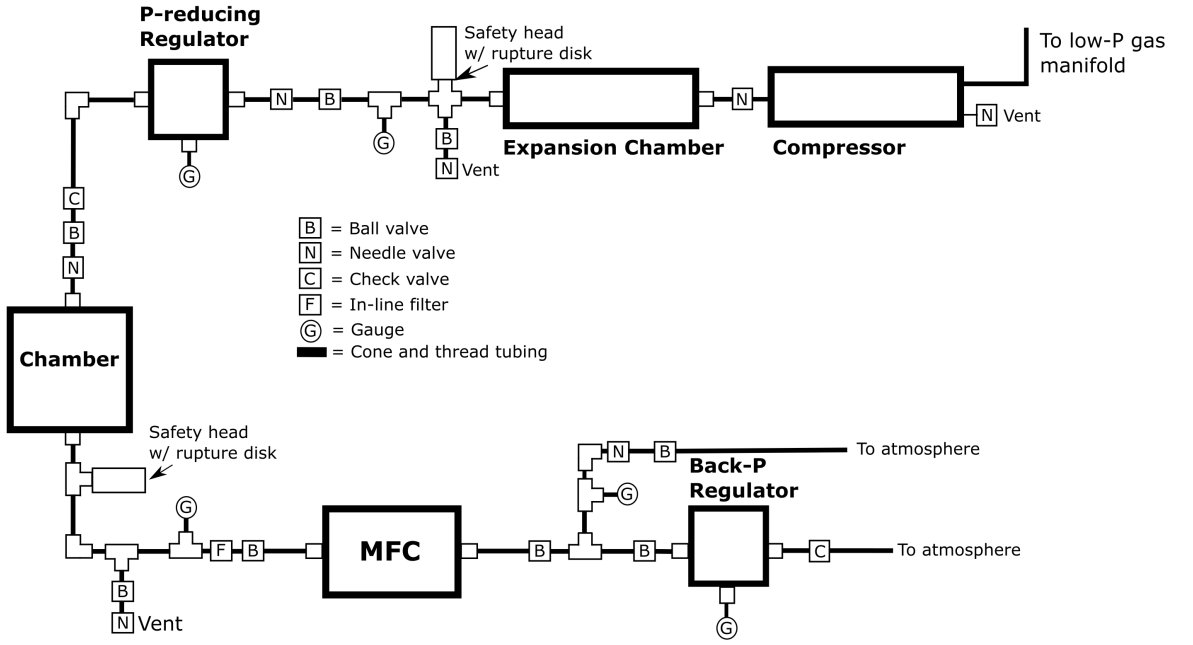

Figure 3.7: Schmatic of the high-pressure flow system. For operating pressure less than 400 bar the back-pressure regulator is not needed.

a manifold from standard gas bottles. A digital mass-flow controller (MFC) controls the flow rate into the gas booster, which helps limit the rate of chamber pressurization. For the inert gasses, an in-line, room-temperature getter allows for clean-up of trace O_2, H_2O and hydrocarbons before the gas is introduced to the chamber (essential for growths of intermetallics and nitrides). The manifold then leads to a dual-stage, air-powered gas booster (produced by MaxPro Technologies) capable of reaching up to $\approx$ 1000 bar of pressure for inert gases. The booster is limited to $\approx$ 350 bar for pure O_2, which has not yet been used with these systems due to safety concerns. High-pressure cone-and-thread piping is used to introduce the gas to the pressure chamber, which can be isolated using high-pressure valves.

For all of the materials grown during the course of this thesis, a static pressure was utilized: the chamber was sealed off after being brought to the desired pressure. However, a high-pressure flow system was designed and built towards the end of this

work, allowing for establishment of controlled mass-flow of up to 1.3 L_N/min at pressures up to 700 bar. This design is shown in Figure 3.7. The main components of this system are an accumulation chamber, a high-pressure regulator and a high-pressure MFC. The accumulation chamber is a coil (total length $\approx$ 7 m) made of large diameter ($\approx$ 1.3 cm) cone-and-thread piping which connects directly to the gas booster and is upstream of the main pressure chamber. During use this coil is pressurized to high-pressure ($\approx$ 700 - 1000 bar) and serves as a gas reservoir to allow steady flow through the main pressure chamber with only occasional action of the gas booster. The MFC sits downstream of the main pressure chamber and controls the outflow of gas, thus controlling the flow rate. To protect the more delicate valves inside the MFC, the pressure drop across it must be less than 400 bar for it to open and allow flow. For operation at pressures above 400 bar a downstream back-pressure regulator is used to independently modify the pressure drop across the MFC.

3.4 Commissioning

After construction, LAPIS was commisioned through growths of several different oxides in order to demonstrate its capabilities [4]. These growths illustrate some of the previously discussed advantages of high-pressure, laser-based FZ-growth. In early commissioning, several crystals of Al_2O_3 were grown, mostly to aid in developing a proper standard operating procedure and work out basic instrumentation issues. Al_2O_3 is a typical commissioning material for FZ furnaces because it has a fairly high melting temperature and the melt is well behaved (*i.e.* it has a high surface tension). An asthetically pleasing ruby[3] was eventually grown from high-purity Al_2O_3 doped with $\approx$ 1 atomic % Cr (Figure 3.8**a**). It is notable that this doping resulted in a lower melting power, as

[3]Note the excellent uniformity of the color, which is the highly desired "pigeon blood" hue

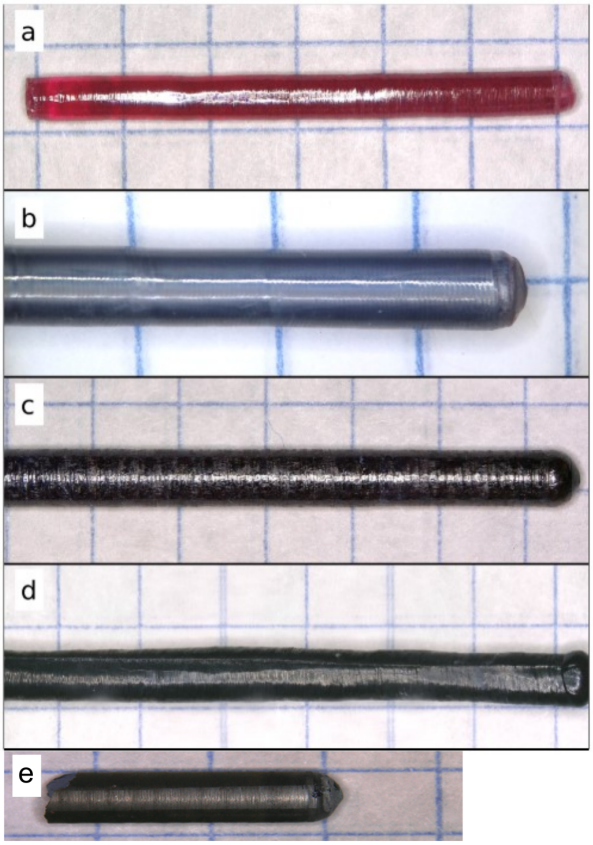

Figure 3.8: Photographs of several single-crystals grown during the commissioning of LAPIS **a**) Cr-doped Al_2O_3 *i.e.* ruby **b)** $GdTiO_3$ **c** $Nd_2Zr_2O_7$ **d** Li_2CuO_2 **e** Cu_2O

compared to pure Al_2O_3 ; the small amount of dopant was sufficient to increase the absorption at the laser wavelength.

To further demonstrate the ability of the laser furnace to sustain FZ-growth from high-temperature melts, single crystals of the refractory oxide $Nd_2Zr_2O_7$ (with $T_{melt} \approx$ 1350 °C) were grown. Despite the high T_{melt}, a molten zone of $Nd_2Zr_2O_7$ could be formed using a power of only $\approx$ 40 W/laser, less than half of the total available power. This demonstrates the effectiveness of laser heating for materials with good coupling to the laser light. Growths were performed under a variety of pressures (1, 35 or 70 bars) and gas compositions (Ar, air, Ar:O_2), all of which produced phase pure $Nd_2Zr_2O_7$; a typical crystal is shown in Figure 3.8**c**. It was found that significant volatility occured over the

course of growths conducted at low-pressure (1 bar) and that this volatility was reduced with high-pressure Ar. The consequences of this reduction in volatility, as well as the effect of different gas compositions, on the physical properties of $Nd_2Zr_2O_7$ were subsequently explore in detail (Chapter 5). The crystals for that study were grown using a constant set of parameters: translation rate (30 mm/hour for both feed and seed), rotation rate (counter rotation at 6 – 8 rpm), and molten zone temperature (2400 – 2500 °C via the uncorrected pyrometer). Three different growth environments were utilized: 1 bar air, 70 bar Ar (HP-Ar) and Ar:O_2 = 80:20 (HP-80:20). Thermally induced cracking was observed in all samples, consistent with other reports [34] and was likely exacerbated by the steep temperature gradient the lasers. Varying the growth rate modified this effect, with extreme cracking and flaking at 12.5 mm/hour and very minimal cracking at 60 mm/hour, but did not otherwise modify the results with respect to the lattice parameter or phase purity. The relatively rapid growth rate represents a compromise between constraining the thermally induced cracking to only localized fractures and maintaining crystallinity. Note that the out-of-plane windows in the V1 chamber described in Section 3.3.1, which were removed in the V2 chamber, could possibly be used to ameliorate this thermal cracking by using broadly focused lasers aimed at the growth region immediately below the molten zone. Such heating could emulate "after-heaters" utilized in conventional mirror furnaces to reduce thermal stress on the growing crystal.

As mentioned previously, the narrow and well-defined molten zone attained from laser heating postiviely impacts growth stability; this capability was demonstrated by a successful growth of $GdTiO_3$. $GdTiO_3$ is known to have a low surface tension melt relative to its density which makes the melt extend vertically over long periods of time. This eventually leads to molten zone instability making high-quality crystals challenging to grow in a conventional mirror furnace [35, 36]. Powder for this growth was synthesized based on a combination of previously reported procedures[35, 36]. The stoichiometry

$GdTiO_{2.93}$ was prepared using a mix of Gd_2O_3, TiO_2 and Ti; an oxygen deficient stoichiometry was chosen based on reported thermogravimetric analysis (TGA) of crystals grown under Ar. This stoichiometry compensates for a slight oxidation which likely occurs during reaction and sintering of the powder. The well mixed powder was pressed into a pellet and reacted on a Mo plate under vacuum (10^{-8} bar) – to avoid formation of $Gd_2Ti_2O_7$ – at1400 °C for 18 hours. Rods of the resulting powder were sintered at 1200 °C for 10 hours under the same vacuum conditions. Growth was conducted under 35 bar of Ar, following several cycles of pressurizing and venting the chamber to remove residual oxygen, using a growth rate of 10 mm/hour and a low heating power of 15 W/laser. The molten zone remained stable throughout the entire growth (total time $\approx$ 5 hours to grow a 50 mm crystal) and the resulting crystal is shown in Figure 3.8**b**. Powder diffraction confirmed the phase purity and consistency of the lattice parameters with previous reports [35, 36, 37]. Magnetic susceptibility measurements were also consistent with previous reports [amow, roth, zhou] and showed a high ferrimagnetic transition temperature (35 K) which indicates nearly ideal oxygen stoichiometry. The resulting high-quality sample was subsequently used in studies performed by collaborators at UCSD to explore the possibility of ultrafast optical control of magnetism [38].

The oxide Li_2CuO_2 was chosen to further demonstrate the ability of high-pressure growth to reduce volatility; in this material there is a high-vapor pressure of Li_2O at the melting temperature, which can lead to Li off-stoichiometry. Previous reports also indicated that a substantial partial pressure during FZ-growth is needed to reduce oxygen vacancies, which are suggested to induce a net ferromagnetic magnetization at low temperature (< 2.5 K) [39]. Therefore, this growth also demosntrates how a high-pressure Ar:O_2 mix can be used to balance reducing volatility with providing a suitibaly oxidizing environment. Growth was performed using 100 bar of Ar:O_2 = 80:20, which supressed volatility compared to growths in air. Li_2CuO_2 has a low T_{melt} and coupled very well

with the laser light so the laser power was pulsed at a frequency of 100 Hz with a 50% duty cycle to improve temperature control. The growth was conducted using an average power of only 8 W/laser, a growth rate of 10 mm/hr and counter-rotation of the rods at 8 and 9 rpm; the molten zone remained stable throughout. The resulting crystal was shown to be highly stoichiometric with respect to both Li and O content and is shown in Figure 3.8**d**. Inductively coupled pasma atomic emission analysis revealed an atomic ration of Li:Cu = 1.99:1.01, indicating effective supression of Li volatility. Furthermore no low-temperature ferromagnetism was observed in magnetic susceptibility measurements (see Chapter 6) consistent with a nearly ideal oxygen stoichiometry[39]. Subsequently, a detailed neutron scattering study was conducted on another crystal of Li_2CuO_2 in order to study its magnetic excitations; the crystal growth procedure was the same, though the powder production was slightly different (see Chapter 6). In all growths, powder diffraction on crushed pieces showed a nearly phase pure sample, besides the presence of a very small amount (estimated to be ¡ 1 mass %) of an unidentified impurity. Comparison of measurements conducted on powders produced from surface-free and surface-full samples suggests this impurity occurs as a very thin layer on the surface.

Finally, the main capability of the laser furance to allow for FZ-growth at ultra-high pressure was first demonstrated by growth of Cu_2O crystal at the record setting pressure of 675 bar of Ar. Cu_2O was selected for this demonstration because of its relatively low melting power (only 16 W/laser was needed at 675 bar), lack of volatility, well-behaved molten zone and phase stability in a pure Ar environment. Growth was performed for a total of 6 hours at a rate of 5 mm/hour and, despite intense convection and turbulent flow, the molten zone remained stable the entire time. X-ray diffraction confirmed a phase pure sample and a section of the grown crystal is shown in Figure 3.8**e**. Subsequently a large variety of other growths have been conducted at similarly high-pressure, greatly aided by the improved imaging pioneered on LOKII. For example, Andrea Capa Salinas

and I successfully stabilized congruent melting of Fe_2O_3 using 480 bar of Ar:O_2 = 80:20, which improves on the slow (0.1 mm/hour) traveling-solvent growth technique which was the previous state-of-the-art [40]. Recently Steven Gomez has produced encouraging results for growth of Sr_2IrO_4 single-crystals and conducted successful traveling-solvent FZ-growth of La_2CuO_4 using 700 bar of Ar:O_2 = 80:20. At present, the highest growth pressure utilized is $\approx$ 900 bar. Exploration of the high-pressure capabilities of LAPIS and LOKII are ongoing, and many interesting results are sure to emerge in the future.

3.5 Challenges

In the course of several years of experimental work on a wide variety of materials, a few recurring challenges specific to high-pressure laser floating-zone have been identified. The most prevalent of these challenges stems from the narrow linewidth of the laser light as compared to the incoherent light of high-powered bulbs. This narrowness linewidth leads to a dramatic sensitivity to the optical absorbance and reflectivity profile of the materials to be grown. The wavelengths chosen for LAPIS and LOKII have proven to be generally effective in melting materials for floating zone growth. However, in some cases weak coupling of the laser light - due to the material having low absorbance at the laser wavelength - results in very inefficient heating, which can prevent growth. It is possible that some materials may be more easily melted in either LAPIS or LOKII because of the different wavelengths better matching a region of large absorption, but this has not been thoroughly investigated. It has been observed in some cases of weak coupling that minimal temperature change occurs until right before some critical power level, where the temperature increases rapidly (though this is not always sufficient to enable melting of the material in question). This indicates that at some threshold temperature the coupling of the laser to the material increases dramatically. Considering this phenomenon, one

potential solution for coupling issues is to use a different material, which couples better to the lasers, as a susceptor. A feed rod of the poor-coupling material of interest can then be joined to a melt of the susceptor material, providing the initial boost in temperature to increase coupling. Steven Gomez has demonstrated the effectiveness of this approach with the growth of Ga_2O_3, which proved to be highly transparent to LAPIS's lasers when heated directly at low temperatures and could not be melted. Use of an initial melt of Al_2O_3 allowed the Ga_2O_3 to be melted, which enabled growth. Provided a suitable susceptor material can be found (*i.e.* one with high enough melting temperature and sufficient coupling) this technique will likely be of considerable utility in future growth efforts. Of course, utilizing this method requires one to check for diffusion of the susceptor material (or its constituent elements) into the grown crystal, which would be an undesirable source of extrinsic disorder.

Coupling issues were also observed to arise in the case of highly transparent seed crystals, which are typically harder to melt with the lasers than polycrystalline samples of the same material. High-density intermetallics have also proven to be more challenging to melt than oxides, likely due to the lack of absorption and the impact on reflectivity from the typical smoother surfaces (compared to the roughness of a polycrystalline oxide). Melting intermetallics typically requires substantially higher laser powers than oxides, regardless of the relative melting points. For example,$Nd_2Zr_2O_7$ ($T_{melt} \approx 2350$ °C) was regularly melted in LAPIS using $\approx 40\%$ of the maximum laser power while a rod of pure Cu ($T_{melt} = 1085$ °C) could not be melted at maximum power even after roughening the surface and decrease the volume of the heated sample. The previous example illustrates an important observation that seems general to most classes of materials which have been attempted in the laser furnaces (oxides, nitrides and various intermetallics): the ability of laser heating to melt a sample is not a simple function of the melting temperature and depends more subtly on the optical properties of the material.

Additional challenges were encountered related to the high-pressure growth environment. While the impact of the extreme convection at high-pressure on imaging of the molten zone during high-pressure growths has largely been conquered by the use of in-plane imaging, imaging can still be difficult in very volatile growths due to the swirling evaporated material. The addition of flow may help to ameliorate this but at the time of this writing this has not been tested. A large challenge is the somewhat unexpected observation that the power required to melt a material increases with growth pressure. This has been observed most dramatically in the case of Al_2O_3 , which has the characteristics of a poor coupling material in that melting happens very suddenly at the critical power without much prior increase in temperature. Under atmospheric conditions in LOKII Al_2O_3 is observed to melt at a power level of $\approx$ 25 - 30 W/laser while at 350 bar of N_2 approximately 160 W/laser was needed to melt the same sample. The dependece of this effect on gas composition is not yet clear. At present it is not definitively understood why this effect occurs and it would be of practical use to conduct systematic experiments - determining melting power for different materials at various pressures, and with different gasses - to gain an empirical understanding. One potential explanation lies in the fact that all of the gasses utilized become supercritical fluids at relatively modest pressures of 30 - 50 bar (the ' 'standard" pressure utilized in the laser furnace is 70 bar). In the supercritical regime the density of the fluid increases substantially and it is likely that this greatly increases the ability of the fluid growth environment to draw heat out of the hot zone by conduction and convection.

Chapter 4

Neutron Scattering for Studies of Quantum Magnetism

Central to the scientific aim of this thesis is the study of single crystals of quantum magnets, with neutron scattering data typically at the core of the results and conclusions. In this chapter I make an attempt at a general definition of quantum magnetism and provide some motivation for its study. Next, I present the central equations for neutron scattering and highlight the features of these equations most relevant to an experimentalist. Lastly, I discuss the time-of-flight neutron scattering method and provide some concrete illustration of its capabilties and advantages by describing two TOF instruments utilized in this thesis (SEQUOIA and CORELLI, both located at the Oak Ridge National Lab Spallation Neutron Source).

4.1 What *is* Quantum Magnetism?

As a piece of terminology "quantum magnetism" is largely tautological. All magnetism, whether that of current carrying wires studied in undergraduate E&M or the

parent state of high-T_C superconductors, is fundamentally quantum mechanical. In fact, to explain even the most basic of magnetic phenomena in solids – the existence of a finite net magnetization – one must invoke the precepts of quantum mechanics. This is captured by a well-known theorem of classical statistical mechanics, known as the Bohr-van Leeuwen theorem, which states that a classical system in thermal equilibrium cannot possess a finite magnetization [41]. This theorem considers the magnetic moments of classical electromagnetism which arise, by definition, from closed loops of current. In a material, these loops of current would arise due to circular motion of mobile electrons. However, curved orbits for electrons arise only under the action of a net magnetic field via the Lorentz force, $F = q(E + v \times B)$, and it is immediately clear that the classical viewpoint of a magnetic moment cannot capture the formation of a spontaneous magnetization in zero field, such as is observed below the Curie temperature of iron.

The Bohr-van Leeuwen theorem extends this failure to a finite field by considering the statistical mechanics of a collection of identical charged particles and demonstrating that the resulting Helmholtz free energy (F) is not a function of the applied field. Since the energy of a moment in a magnetic field is known from magnetostatics ($E = -\vec{\boldsymbol{\mu}} \cdot \vec{\boldsymbol{B}}$, $\vec{\boldsymbol{\mu}}$ = moment) one can write down the contribution of a finite magnetization to F, and therefore also derive the following Maxwell relation: $M = -(\frac{dF}{dB})_{T,V}$ [42]. If F has no dependency on B, then M is necessarily zero. One can also get a sense of this by considering the nature of the Lorentz force, which defines how an electron interacts with a magnetic field. Paraphrasing Blundell [41], the cross-product term in the Lorentz force means that a magnetic field only leads to forces perpendicular to the direction of motion of an electron. Since work is the dot product of a force and a displacement, the magnetic field does no work on the electron and thus does not alter the energy of the system.

Still another problem with the use of classical physics in considering the magnetism of materials is the occurrence of magnetic order. The transition from a high-temperature

(paramagnetic) state to a low-temperature magnetically ordered state is quite generic in magnetic materials. In fact, if magnetic order does not eventually occur, or occurs at lower than expected temperatures, this is often taken as a sign of exotic physics. In spirit, magnetic ordering arises for the same reason that we see transitions from disordered (higher symmetry) crystal structures to more ordered (lower symmetry) crystal structures with decreasing temperature: the system seeks to minimize the Gibbs free energy ($G = U - TS$), balancing minimization of the internal energy from interactions against the temperature dependent entropic term.

In the case of magnetic order the relevant interaction is the one between the moments of the magnetic ions (note that this thesis is almost exclusively concerned with the localized magnetism of insulating oxides, as opposed to the itinerant magnetism of metals). In a purely classical view the magnetic moments of neighboring magnetic ions interact via the magnetic field produced by each moment. This is the dipole-dipole interaction familiar from classical electricity and magnetism and it yields the following equation for the energy of two interacting moments (of magnitude $\mu_{1,2}$ and seperated by $\vec{\boldsymbol{r}}$) [41]:

$$E = \frac{\mu_0}{4\pi|\vec{\boldsymbol{r}}|^3}\left[\vec{\boldsymbol{\mu}}_1 \cdot \vec{\boldsymbol{\mu}}_2 - \frac{3}{|\vec{\boldsymbol{r}}|^2}\left(\vec{\boldsymbol{\mu}}_1 \cdot \vec{\boldsymbol{r}}\right)\left(\vec{\boldsymbol{\mu}}_2 \cdot \vec{\boldsymbol{r}}\right)\right] \tag{4.1}$$

where μ_0 is the permeability of free space $\approx 1.2566 \times 10^{-6} J/A^2 m$.

For two moments with magnitude 1 μ_B and a seperation of 1 Å the resulting energy is on the order of 8×10^{-22} J, or $\approx$ 6 K. Since the energy scale of the interaction between the moments should set the energy (temperature) scale of the magnetic ordering transition, one would expect magnetic d-block transition metal compounds, where the moments are on the order of 1 μ_B, to have magnetic ordering temperatures on this scale. High-temperature ordering temperatures (in the 100's of K) would only be expected for large moment atoms (say Ho^{2+} or Dy^{2+}, with moments of 11 μ_B and 10 μ_B , in the

atomic limit, respectively) with unrealistically small seperations (a bonding distance of only 1 Å is quite small for an oxide). However there are many *d*-block transition metal elements/compounds with magnetic transition temperatures well above 10 K (*e.g.* the Curie point of Fe is 1043 K) and lanthanide compounds often have very small magntic ordering temperatures on the order of 10 - 100 mK. To take an example from this work, $Eu_2Ir_2O_7$ has an Ir-Ir bond distance of ≈ 3.5 Å and $\mu_{Ir} \approx 0.005\ \mu_B$. This yields a dipole-dipole interaction energy of only 3.6×10^{-4} mK compared to the observed magnetic transition temperature 120 K. Clearly the classical dipole-dipole interaction is incapable of producing the broad range of magnetic ordering temperatures observed, and we must look elsewhere for an explanation.

These failures of classical theory presage several features of quantum mechanics which allow for the existence of materials with a finite magnetization [42]. First is the concept of "spin", whereby electrons possess an intrinsic angular momentum. This intrinsic angular momentum explains the net moment of the elecron (with the fundamental unit being the Bohr magneton, $\mu_B = \frac{e\hbar}{2m_e}$, where m_e is the electron mass), irrespecitve of any applied field. Second is the quantization of the allowed electron energy states, and therefore their associated orbital angular momentum. These momenta lead to discrete values for the total electron magnetic moment, possessing a spin (μ_S) and oribtal (μ_L) component. Moving from classical, continuum, statistical mechanics to the discrete statistical mechanics of the quantum theory modifies the result of the Bohr-van Leeuwen calculation and allows for a finite magnetization [41, 42].

Quantum mechanical considerations also provide the needed alternative to the classical dipole-dipole interaction: the "exchange" interaction, which is a purely quantum mechanical phenomenon with no classical analogue. Note that the dipole-dipole interaction is of course still operative, and may be relevant to the magnetism at low temperatures (< 1 K) such as is the case for magnetic lanthanide compounds with large moments

and weak magnetic exchange. The exchange interaction is a foundational concept in magnetism and is an essential component for understanding almost any magnetic phase behavior, including the occurence of magnetic order. As a result, much of the study of quantum magnetism reolves around understanding how the sign, symmetry, and strength of exchange interactions (which result from the stoichiometry and lattice symmetry of a material) lead to the observed magnetic order (or lack thereof) and the accompanying excitations. I provide here only a very brief and qualitative outline of the ideas behind the exchange interaction in order to further demonstrate the quantum origins of magnetism.

The root cause of the exchange interaction lies in the indistinguishable nature of quantum particles, which iteself is a consequence of the Heisenberg uncertainty principle [43]. This indistiguishability leads to the postulate that the total wave function of a collection of quantum particle should be either symmetric (bosonic) or antisymmetric (fermionic) under the exchange of two particles (swapping of position or spin). As a result, the total wave-function for electrons in a material is antisymmetric under particle exchange, meaning that the spin and spatial components must have opposite signs (one must be antisymmetric and the other symmetric). This property leads directly to the Pauli exclusion principle for fermions [43] which, in combination with minimization of the electrostatic (Coulomb) interaction between electrons, determines how unpaired electrons on a single atom are arranged. This, in addition to the relativistic spin-orbit coupling term, is the basis for Hunds rules. The exchange interaction between atomic magnetic moments (which arise in the case of an unfilled valence shell) occurs because the kinetic energy of an electron can lowered by sharing its probability distribution between orbitals on different atoms, forming a molecular wave function, and because this hopping is influenced by the need to minimize the electrostatic contribution to the total energy [41]. Both factors influence what spin arrangements on the individual atoms lead to the lowest total energy and thus the exchange interaction is equivalent to a correlation

between atomic magnetic moments which (at the most basic level) either tends to align them parallel (ferromagnetic) or antiparallel (antiferromagnetic).

This correlation is captured by the sign of the exchange integral (J) which can be though of as a calculation of the overlap between electron wave-functions on different atoms scaled by the energy difference of different alignments [41]. Note that this type of "direct" exchange is actually rarely the dominant term in the magnetism of oxides. Far more often the magnetism is mediated by the so-called "superexchange" interaction, where there is hopping to empy orbitals on an intermediate ligand (*e.g.* oxygen). There are also more complicated exchange interactions resulting from the effect of other energy scales; for example, the effect of spin-orbit coupling on hopping electrons results in the Dzyaloshinskii-Moriya interaction (or "antisymmetric" exchange) which favors a canting of collinear moments [41]. A wide range of magnetic structures can result from these effects beyond simple collinear ferromagnetism or antiferromagnetism – the "all-in-all-out" magnetic structure of $Nd_2Zr_2O_7$ and $Eu_2Ir_2O_7$ is one example. All of these J terms scale the strength of different spin-spin interaction terms in the spin Hamiltonians, which determines not just the magnetic structure, but also the nature of the magnetic excitations. It is important to remember that exchange is an "effective" interaction; there is no force carrier or associated field. It is simply a useful abstraction for modeling the emergent behavior of large numbers of electrons attempting to minimize their total energy under the restrictions of the Pauli exclusion principle.

The universal relevance of quantum mechanics to magnetism makes it difficult to write down a sharp description for what makes the "quantum" magnets considered in this thesis different from a permanent magnet attached to your refrigerator. Although the macroscopic properties are quite different (none of the materials considered here will stick to your refrigerator), the same physics is in operation at the most fundamental level. A reasonable point of view seems to be that attaching the word "quantum" to

certain magnetic materials is really a way of indicating that these materials are effective platforms for studying quantum many-body physics (in that their structures and interactions map well to existing models) and that their properies cannot be understood, even phenomenologically, without the aid of quantum mechanical concepts which often move beyond mean-field theories [44].

Of the available quantum many-body phenomena, magnetism is one for which real materials exist that, at least on some level, confrom to Hamiltonians which theorists are adept at writing down and manipulating. Additionally, the interactions and energy scales underlying magnetism happen to be relatively experimentally accessible (such as via neutron scattering, see Section 4.2) and one can often tune properties by applying magnetic fields or physical pressure. Furthermore, the basic physics of magnetism are well enough understood that theoretical investigations of many-body phenomena, which are inevitably complex, are put on a more stable foundation. In this viewpoint, the motivation to study quantum magnetism comes by way of considering it as a technique for studying situations where one is explicity forced to consider the many-body nature of $N_{Avagadro}$ worth of electrons interacting in a solid in order to explain their macroscopic properties (*e.g.* the role of electron-electron correlations in the mechanism of the thermal metal-insulator transition in $Eu_2Ir_2O_7$). Similarly, quantum magnets typically show phase behaviors which highlight the "quantumness" of magnetism and which are well beyond classical or semi-classical theories.

The study of quantum magnetism is not *just* motivated by improving our fundamental understanding of what it is that electrons are doing in a solid; it does have applications that could be called "practical". Of particular current relevance is the ongoing search for quantum spin liquids [45] which, while fascinating as examples of quantum many-body physics, also have the potential to realize quantum computers [46]. Such an achievement would be highly practical as it would allow for implementation of an algorithm capable of

breaking the most popular encryption algorithms in use today, which are depended on to secure everything from day-to-day financial information to highly classified government secrets. This sounds like the plot of a Neal Stephenson novel, but it is not. Furthmore, soon after the discovery of superconductivity at temperatures above the boiling point of nitrogen in several cuprate compounds, quantum magnetism saw a surge of interest which has been sustained to today. This is because such high-T_C superconducting phases often emerge upon doping an (AFM) magnetic insulator and magnetic correlations are thought to be relevant to the pairing mechanism of cuprate high-T_C [47]. Fundamental studies of quantum magnets with features similar to these high-T_C compounds therefore provide an avenue for understanding this pairing mechanism. In fact, this line of thought motivated many of the original studies on Li_2CuO_2 which is a canonical example of a cuprate with edge-sharing CuO_4 plaquettes (the fundamental unit of cuprate superconductivity).

4.2 Neutron Scattering

Neutron scattering continues to be one of the premier tools for advancing our understanding of quantum magnetism. The extreme utility of neutrons (in both quantum magnetism and other fields of physics and materials science) is best captured by a quote attributed to Bertram Brockhouse: "If the neutron did not exist, it would have to be invented". The essential feature of the neutron that makes it so useful for studying magnetism is, of course, that it has a net magnetic moment: μ_N = - 1.913 μ_n, where $\mu_n = \frac{e\hbar}{2m_p}$ is the nuclear magneton and m_p is the proton rest mass [48]. The negative sign indicates that the neutron behaves as a negatively charged particle with its magnetic moment antialigned with the spin. To those of us who are not particle physicists, the fact that the neutron has a moment at all, considering that it is electrically neutral, is suprising. Justification of the existence and sign of the neutron moment requires consideration of its

internal quark structure, which is clearly well out of the scope of this thesis. Regardless, this moment allows the neutron to interact with the magnetic moments in a material, leading to elastic and inelastic magnetic scattering.

As for all subatomic particles, the neutron has a de Broglie wavelength which depends on its kinetic energy. Neutrons are therefore variously described by their velocities, energies and wavelengths (see Table 4.1). By considering the relationship between energy and wavelength, one can see another serendipitous feature of neutrons that make them a special and powerful tool for condensed matter physics: for wavelengths commensurate with diffraction from the typical length scales of crystalline materials (on the order of 1 - 10 Å) neutrons have energies on par with the fundamental excitations in condensed matter (*e.g.* phonons and magnons). This makes neutrons an effective probe of both the statics *and* dynamics of the lattice and magnetic degrees of freedom [49].

Different neutron energy regimes are often described by their corresponding temperatures. In magnetism the most useful classes of neutrons are cold neutrons, with energies of 0.1 - 10 meV ($\approx$ 1 - 100 K) and thermal neutrons, with energies 10 - 100 meV ($\approx$ 100 - 1000 K) [48]. Different neutron energies are useful for different purposes. In diffraction experiments, cold neutrons (low energy, long wavelength) give better resolution at low $\vec{\boldsymbol{Q}}$ values, where magnetic scattering is strongest; thermal neutrons (higher energy, short wavelength) give access to higher $\vec{\boldsymbol{Q}}$ values, which are important in structural studies. In a typical (neutron energy loss) inelastic experiment, the energy of the incident neutron must be greater than the energy of the excitation one is trying to measure. However, experimental considerations mean one must think carefully about the E_i to utilize (see Section 4.2.3). For magnetic excitations the energy scale is that of the exchange interaction, with a typical energies of 0.1 - 100 meV (mostly favoring the lower end of this range). There are, of course, uses for higher energy neutrons within condensed matter physics. For example, studies of crystal field excitations (a single ion property) can

Quantity	Unit	Formula
Energy, E_N	meV	
Temperature, T	K	E_N/k_B
Wavelength, λ	Å	$h/\sqrt{2m_N E_n}$
Wave vector, k	Å^{-1}	$\sqrt{2E_N/m_n}$

Table 4.1: Some important conversions between neutron energy (E_N) and other quantities. h is the Planck constant $\approx 4.136 \times 10^{-12}$ meV·s , k_B is the Boltzman constant $\approx 8.617 \times 10^{-2}$ meV/K , and m_N is the mass of the neutron $\approx 1.675 \times 10^{-27}$ kg.

involve energies in the range 0.1 - 1 eV (so-called epithermal neutrons) and are often important for understanding magnetic behaviors [42, 50].

Fortuitously, the strength of magnetic scattering is comparable to that from the atomic lattice (termed nuclear scattering) – see Section 4.2.1 for details. The relative strength of magnetic neutron scattering means that it is (generally) possible to detect and deconvolve from nuclear scattering. This can be contrasted with the case of X-rays, where the interaction of the a photon with the atomic magnetic moments leads to scattering that is many, many orders of magnitude weaker than the nuclear scattering. Utilizing X-rays at an energy matched to the absorption edge of one of the elements in the sample greatly boosts the magnetic cross-section, and resonant X-ray scattering has been rapidly improving as an alternative to neutron scattering in some cases [1].

The relatively weak interaction of neutrons with matter is experimentally useful because neutrons can be easily passed through large/complex sample environments (such as magnet systems or dilution refigerators, both useful for studies of quantum magnets) without too much trouble. Compared to X-rays, it is therfore easier to accomodate experiments at environmental extremes. Small absorption cross-sections also mean that neutron scattering generally acts as a *bulk* probe of the sample, with significant numbers of neutrons scattering off the entire volume of the sample. Large sample volumes

[1] See Zach Porter's thesis for an approachable account of resonant X-ray scattering techniques

can therefore be utilized to compensate for the limitations of neutron flux (which are significantly lower than synchrotron X-ray fluxes) and to aid in looking at weak scattering features, without worrying about absorption. There can, however be issues due to extinction and multiple scattering, which is much more prevelant with neutrons than X-rays since the interaction volume is larger. A bulk probe can remove ambiguity about whether a magnetic phase behavior is coming from the entire volume of the sample or just some limited region. An example: if a magnetic transition is observed in a magnetic susceptibility measurement one may not be able to immediately say if it comes from the majority phase in the sample or a minority impurity phase (as determined by Rietveld refinement of powder X-ray diffraction data). However, magnetic neutron scattering intensity scales strongly with the number of magnetic moments, meaning that if the the magnetic transition is observed in the scattering experiment than it is most likely a property of the majority phase.

The absorption cross-section for neutrons varies significantly across the periodic table, without an easily defined trend - this should be contrasted with X-rays, where absorption increasese monotonically with atomic number, besides at absorption edges. There are certain elements with notably large neutron abosrption cross-sections, such as B (767 barns), Cd (2520 barns), and Gd (49000 barns). Absorption cross sections are given for the natural isotopic abundance average with a typical thermal neutron energy of 25 meV (293 K); these values are tabulated by NIST and can easily be found online. Many of the other lanthanides are highly absorbing as well, particularly Eu (4530 barns) and Sm (5922 barns). For more moderately strong absorbers, such as Ir (425 barns), the issue of absorption can be overcome by long count times/high-flux and attempting to minimize the path length of the scattered neutrons (in the case of powders this involves using an annularly shaped sample can). Since neutron absorption depends sensitively on the isotope of the element, absorption can also be avoided by making a sample that has been

enriched in a less absorbing isotope. This was done for the neutron scattering experiment on Li_2CuO_2 described in Chapter 6, with 7Li (0.0454 barns) being used instead of natural abundance Li (70.5 barns).

The scattering length for nuclear elastic scattering of neutrons (which encodes the strength of scattering from a particulear nucleus) similarly varies greatly across the periodic table. Again, this can be contrasted with the case for X-rays where it increases monotonically with atomic number. This fact is useful because it means that neutron diffraction is much more sensitive to certain elements than X-rays; particularly relevant for studies of oxides is the appreciable neutron scattering length of oxygen, which is essentially invisible to X-rays. Furthermore, the random variation in scattering length means that neighboring elements may have very different scattering lengths, which can improve contrast in Rietveld refinements of site occupancies. Co-refinement of powder neutron and X-ray diffraction data is a powerful way to take advantage of the abilities of both techniques (X-rays provide much better $\vec{\boldsymbol{Q}}$-resolution and higher flux) to characterize all aspects of a structure. This was utilized in Chapter 5 in order to probe disorder on both the anion and cation sublattices.

4.2.1 The Fundamental Equations and Their Interpretation

We consider a crystalline sample which hosts some relevant interaction potential and is illumintated by an incident beam of neutrons with wave vector $\vec{\boldsymbol{k}}_i$ ($|\vec{\boldsymbol{k}}_i| = 2\pi/\lambda$) and energy E_i.[2] When the neutrons enter the sample, some portion of them interact with the potential and are scattered, leaving the sample with $\vec{\boldsymbol{k}}_f$ and E_f. In parallel, some neutrons are transmitted without interaction and others are absorbed. The initial and final $\vec{\boldsymbol{k}}$ values must *always* accord with the scattering triangle: $\vec{\boldsymbol{Q}} = \vec{\boldsymbol{k}}_i - \vec{\boldsymbol{k}}_f$, where $\vec{\boldsymbol{Q}}$

[2]This section is based primarily on the books by Squires [48] and B.T.M Willis & C.J. Carlile [51] as well as the chapter by D.L. Price and F. Fernandez-Alonso [49]

is the momentum transfer ($|\vec{\boldsymbol{Q}}| = 4\pi Sin(\theta)/\lambda$, where θ is the scattering angle) along a particular direction defined by the reciprocal lattice vectors of the sample. Energy conservation must also always be obeyed, such that any change in energy of the neutron is accompanied by a corresponding change in the energy of the sample via the creation or destruction of an excitation/quasi-particle with energy $\hbar\omega = \Delta E = E_i - E_f$ [51]. In the case of elastic scattering, where the energy of the neutron is unchanged, $|\vec{\boldsymbol{k}}_i| = |\vec{\boldsymbol{k}}_f|$ and only the wave-vector direction changes (momentum is a vector quality so there is still a net momentum transfer). In the case of inelastic scattering, where the energy of the neutron changes, both the magnitude and direction of the neutron wave-vector changes.

The quantity being measured in any neutron scattering experiment is the scattering *cross-section* which is directly proportional to the scattering function, $S(\vec{\boldsymbol{Q}}, \Delta E)$, which encodes the physics of the system. The equations presented in the following discussion do not explicitly include $S(\vec{\boldsymbol{Q}}, \Delta E)$, but it is helpful to have some sense of what this function is in order to gain a better physcial understanding of the terms in the differential cross-sections [48]. In essence, $S(\vec{\boldsymbol{Q}},\Delta E)$ gives the probability that a neutron scatters off of the sample with a momentum transfer of $\vec{\boldsymbol{Q}}$ and an energy transfer of ΔE [51]. In mathematical terms, the scattering function is the Fourier transform of a time-dependent pair-correlation function, typically denoted $G(\vec{\boldsymbol{r}}, t)$ [48]. For a classical system, $G(\vec{\boldsymbol{r}}, t)$ can be understood as the probability that an atom will be found at position $\vec{\boldsymbol{r}}$ at time t, given that there was an atom at $\vec{\boldsymbol{r}}$ at $t = 0$ (strictly speaking for a quantum system this physical interpretation is no longer available to us, due to the uncertainty principle) [51]. The important point to understand is that neutron scattering is sensitive to the *correlations* in a system, which may be static (time independent) or dynamic (time dependent, *i.e.* fluctuating). The correlations in time are related to energy transfer in a manner analogous to the relationship between $\vec{\boldsymbol{r}}$ (real space) and $\vec{\boldsymbol{Q}}$ (reciprocal space): by a Fourier transform. In general terms, diffraction measures the static ($\Delta E = 0$)

correlations, which are essentially the time averaged (*i.e.* time-independent) properites of atoms and magnetic moments. Inelastic measurements measure dynamic correlations *e.g.* fluctuations of the spin or lattice subsystems. These correlations are time-dependent and possess a finite energy transfer ($\Delta E \neq 0$).

The *total* scattering cross-section tells us the number of neutrons scattered (in all directions) per second, normalized by the incident flux. This value does not discriminate between neturons scattered with or without energy change or by what interaction potential (nuclear or magnetic) nor does it give any $\vec{\boldsymbol{Q}}$-dependence, so it is not particularly useful. What is actually desired (and measured in a neutron experiment) are *differential* cross sections, which tell us the number of neutrons (with a given E_f) per second scattered out of the sample into a infinitesimal solid angle. The basic approach to calculating these differential cross-sections makes use of two equations. The first is simply a mathematical expression of the previous definition for the differential cross-section:

$$\left(\frac{\mathrm{d}\sigma}{\mathrm{d}\Omega}\right)_{\lambda_\mathrm{i}\rightarrow\lambda_\mathrm{f}} = \frac{1}{\Phi\Delta\Omega}\sum_{\mathbf{k_f}} W_{\mathbf{k}_\mathrm{i},\lambda_\mathrm{i}\rightarrow\mathbf{k}_\mathrm{f},\lambda_\mathrm{f}}, \tag{4.2}$$

where the sum over $\mathbf{k_f}$ is for all final neutron wave vectors which lie in $d\Omega$, λ represents the initial and final state of the sample, and $W_{\mathbf{k}_\mathrm{i},\lambda_\mathrm{i}\rightarrow\mathbf{k}_\mathrm{f},\lambda_\mathrm{f}}$ is the rate for the indicated transition. In order to get at this transition rate we utilize *Fermi's Golden Rule*, from first-order perturbation theory, which tells us:

$$\sum_{\mathbf{k_f}} W_{\mathbf{k}_\mathrm{i},\lambda_\mathrm{i}\rightarrow\mathbf{k}_\mathrm{f},\lambda_\mathrm{f}} = \frac{2\pi}{\hbar}\left|\langle\mathbf{k}_\mathrm{f},\lambda_\mathrm{f}|V(\vec{r})|\mathbf{k}_\mathrm{i},\lambda_\mathrm{i}\rangle\right|^2 \rho_{\mathbf{k}_\mathrm{f}}\left(E_\mathrm{f}\right), \tag{4.3}$$

where $V(\vec{\boldsymbol{r}})$ is the interaction potential of interest and $\rho_{\mathbf{k}_\mathrm{f}}(E_\mathrm{f})$ is the density of final neutron $\vec{\boldsymbol{k}}$ states per unit energy at the final enegy of the neutron. From here the main sticking points are to write down the form of the relevant interaction, calculate the matrix elements and deal with time-dependent (dynamical) factors which arise for

inelastic scattering. The last point adds considerable complexity, particularly for the magnetic inelastic cross-section. Using these expressions we can write down a general formula for the double differential cross section, which includes the possibility of inelastic scattering:

$$\left(\frac{\mathrm{d}^2\sigma}{\mathrm{d}\Omega \mathrm{d}E_\mathrm{f}}\right)_{\lambda_\mathrm{i}\to\lambda_\mathrm{f}} = \frac{k_\mathrm{f}}{k_\mathrm{i}}\left(\frac{m_\mathrm{n}}{2\pi\hbar^2}\right)^2 \left|\langle \mathbf{k}_\mathrm{f}, \lambda_\mathrm{f}|V(\vec{\boldsymbol{r}})|\mathbf{k}_\mathrm{i}, \lambda_\mathrm{i}\rangle\right|^2 \delta\left(E_{\lambda_i} - E_{\lambda_f} + E_{\mathbf{n}_i} - E_{\mathbf{n}_f}\right), \quad (4.4)$$

The delta function enforces energy conservation by preseving only processes where the change in energy of the system (λ) due to the creation or annhilation of an excitation is equal and opposite to that of the neutron ($\mathbf{n}$).

Moving from this overarching formula, we can consider the (coherent) *elastic* differential cross section. We are interested in both the nuclear and magnetic contributions to this cross-section. In the case of nuclear scattering, the relevant interaction potential is the nuclear strong force (since the neutron is interacting with the the nucleus itself, not the electron density, as with nuclear X-ray scattering). While there is no good analytical theory for this interaction potential, it is known to have a spatial range on the order of 1 fm which is much smaller than cold or thermal neutron wavelengths (on the order of 10^5 fm). This allows the potential to be effectively described as a delta function: $V_{nuc} = b_i\delta(\vec{\boldsymbol{r}} - \vec{\boldsymbol{R}})$, where b_i is the scattering length for element i and $\vec{\boldsymbol{r}}$ and $\vec{\boldsymbol{R}}$ are the real-space positions of the neutron and nucleus, respectively. An important observation to make at this point is that there is no $\vec{\boldsymbol{Q}}$-dependence to the neutron scattering power (b_i) of a nucleus, as opposed to the drop-off with $\vec{\boldsymbol{Q}}$ observed for X-rays. Plugging this into Equation 4.4, assuming the system state remains unchanged during the scattering event, and enforcing that no energy is exchanged yields the *coherent elastic differential*

cross-section [48]:

$$\left(\frac{\mathrm{d}\sigma}{\mathrm{d}\Omega}\right)_{coh,el} = N\frac{(2\pi)^2}{\nu_{uc}}\sum_{\vec{Q}}|F_N\left(\vec{Q}\right)|^2\delta\left(\vec{Q}-\vec{\tau}\right)\delta\left(E_f-E_i\right) \tag{4.5}$$

This equation is very similar to the nuclear cross section for X-rays. Here, N is the number of atoms in the unit cell, ν_{uc} is the unit cell volume and the sum is over the reciprocal vectors, $\vec{\boldsymbol{\tau}}$ of the lattice. The term $\delta(\vec{\boldsymbol{Q}}-\vec{\boldsymbol{\tau}})$ in the sum picks out only $\vec{\boldsymbol{Q}}$ which are reciprocal lattice vectors, telling us that elastic neutron scattering operates the same as X-ray Bragg diffraction. F_N is the nuclear structure factor, similar to that from X-ray scattering:

$$F_N\left(\vec{Q}\right) = \sum_{\vec{r}} b_{coh,\vec{r}}\, e^{i\vec{Q}\cdot\vec{r}}\, e^{-W_{\vec{r}}} \tag{4.6}$$

The sum is over the atomic positions, with nuclei at different $\vec{\boldsymbol{r}}$ potentially having different values of $b_{coh,\vec{\boldsymbol{r}}}$. Coherent scattering means that we are considering the ensemble average of the scattering length for a nucleus . By averaging, we ignore variations due to to isotope incoherence (presence of different isotopes of an element) and nuclear spin incoherence (which comes from the different spin states available to a nucleus with a net nuclear spin). Coherent scattering captures the interference effects which give rise to diffraction peaks and collective excitations and is related to spatial and temporal correlations between different atoms. Incoherent scattering captures the effect of the variation in scattering length for an individual nucleus and gives rise to a $\vec{\boldsymbol{Q}}$-independent scattering that is related to spatial and temporal correlations of a single atom [51, 49]. The key difference from the X-ray nuclear cross-section is that the weighting factor for the scattering power of different atoms in the structure factor is the $\vec{\boldsymbol{Q}}$-independent scattering length, rather than a $\vec{\boldsymbol{Q}}$-dependent form factor, which decreases monotonically with $|\vec{\boldsymbol{Q}}|$. As a result,

the $\vec{\boldsymbol{Q}}$-dependence of the nuclear scattering intensity for neutrons comes is less dramatic than X-rays, and is therefore generally stronger at high-$|\vec{\boldsymbol{Q}}|$. The $e^{-W_{\vec{r}}}$ term is the typical Debye-Waller factor, which captures the effect of thermal fluctuations of the atomic positions. W contains a factor of the form $cot(1/k_BT)$ and therefore acts to decrease/smear out the scattering intensity at higher temperature.

We can now move to the *magnetic* differential cross section. The interaction we are considering is the one between the magnetic moment of the neutron ($\vec{\boldsymbol{\mu}}_N$) and the total magnetic field produced by the spin ($\vec{\boldsymbol{B}}_S$) and orbital ($\vec{\boldsymbol{B}}_L$) angular momentum components of the unpaired (*i.e.* magnetic) electron in the lattice. The total magnetic field produced by an orbiting electron, $\vec{\boldsymbol{B}}_{tot} = \vec{\boldsymbol{B}}_S + \vec{\boldsymbol{B}}_L$, is derived from classical E & M [48]:

$$\vec{B}_{tot}\left(\vec{r}\right) = \frac{\mu_0}{4\pi}\left[\boldsymbol{\nabla} \times \left(\frac{\mu_e \times \hat{r}}{|\vec{r}|^2}\right) - \frac{2\mu_B}{\hbar}\frac{\vec{p}\times\hat{r}}{|\vec{r}|^2}\right] \tag{4.7}$$

where $\vec{\boldsymbol{\mu}}_e = -2\mu_B\vec{\boldsymbol{S}}$ is the (spin only) magnetic moment of the electron, with $\vec{\boldsymbol{S}}$ being the spin angular momentum operator in units of $\hbar$. $\vec{\boldsymbol{r}}$ is the vector distance from the electron, which has momentum $\vec{\boldsymbol{p}}$. The potential experienced by the neutron is then simply: $V_{mag}(\vec{\boldsymbol{r}}) = \vec{\boldsymbol{\mu}}_N \cdot \vec{\boldsymbol{B}}_{tot}(\vec{\boldsymbol{r}})$. The evaluation of the relevant matrix element is made considerably more complicated than the case of nuclear scattering because the interaction potential is long-ranged and the magnetic forces involved are "non-central" (meaning the force does not act on a line connecting the two particles). The complete derivation is rather involved, and treated in detail in several textbooks, so I only will highlight a few key points from which important statements can be made.

We start by considering the scattering from a single atom with unpaired electrons, which interact with a neutron via the previously described magnetic potential. In evaluating the matrix element in Equation 4.4 for the magnetic potential, we must also track

the spin state of the neutron ($\vec{\boldsymbol{\sigma}}$). This (eventually) yields the following expression:

$$\left(\frac{\mathrm{d}^2\sigma}{\mathrm{d}\Omega \mathrm{d}E_\mathrm{f}}\right)_{\lambda_i,\sigma_i\rightarrow\lambda_f,\sigma_f} = (\gamma\, r_0)^2\, |\langle\sigma_f,\lambda_f|\vec{\sigma}\cdot\vec{M}_{perp}|\sigma_i,\lambda_i\rangle|^2\, \delta\left(E_{\lambda_i} - E_{\lambda_f} + E_{\mathbf{n}_i} - E_{\mathbf{n}_f}\right) \quad (4.8)$$

The first conclusion to draw is that the cross-section for magnetic scattering is scaled by the constant term $(\gamma\, r_0)^2$, where γ is a collection of constants and $r_0 = \frac{\mu_0\, e^2}{4\pi m_e}$ is the classical electron radius. This term is on the order of 10^{-30} m^2 or 0.01 barns (1 barn = 10^{-28} m^2) which, though certainly weaker, is comparable to typical nuclear scattering cross sections ($\approx$ 1 barn). This justifies the earlier statement that the strength of the magnetic scattering is comparable to nuclear scattering, and thus accessible experimentally.

The second important conclusion concerns the M_{perp} term, which can be written as:

$$\vec{M}_{perp}(\vec{Q}) = \vec{Q}\times\vec{M}_{total}\times\vec{Q} = \vec{M}_{total} - (\vec{M}_{total}\cdot\hat{Q})\vec{Q} \quad (4.9)$$

$$\vec{M}_{total}(\vec{Q}) = \int [\vec{M}_L(\vec{r}) + \vec{M}_S(\vec{r})]\, e^{i\vec{Q}\cdot\vec{r}} d\vec{r} \quad (4.10)$$

We see that M_{perp} is a geometric term that involves the Fourier transform of the total real-space magnetization ($\vec{\boldsymbol{M}}_{total}(\vec{\boldsymbol{r}}) = \vec{\boldsymbol{M}}_L + \vec{\boldsymbol{M}}_S$) and the scattering vector. This geometric construction is illustrated in Figure 4.1**a**. The physical interpretation of $\vec{\boldsymbol{M}}_{perp}$ is the following important statement: *the neutron spin, $\vec{\boldsymbol{\sigma}}$, only couples to the component of the magnetic moment which is perpendicular to the scattering vector.* As a result, if we measure magnetic scattering at different values of $\vec{\boldsymbol{Q}}$ we are probing different real-space projections of the moment within our sample.

From here further details of the elastic magnetic cross-section can be best illustrated by considering a specific example. We consider a cubic structure with one magnetic

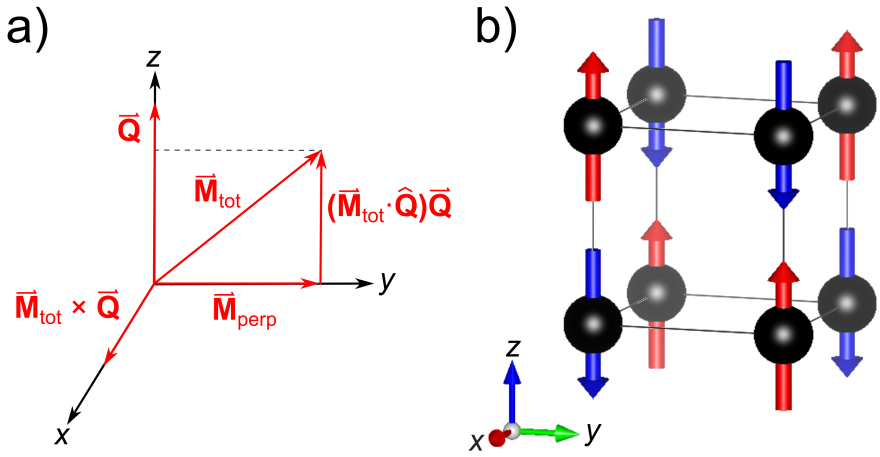

Figure 4.1: **a**) Illustration of the construction of $\vec{M}_{perp}$ for a magnetic moment ($\vec{M}_{tot}$) at the origin that lies in the yz-plane. The scattering vector, $\vec{Q}$, is along the z-direction. At this scattering vector we are only sensitive to the component of $\vec{M}_{tot}$ which lies in the xy-plane. **b**) Illustration of the simple cubic G-type antiferromagnetic structure considered in the text.

ion per unit cell, which undergoes an ordering transition to a G-type antiferromagnetic structure with moments parallel or antiparallel to the z-axis (4.1**b**). For simplicity, we take the orbital moment to be quenched, and consider scattering from the spin component of the moment only. The elastic magnetic cross-section for this unit cell is:

$$\left(\frac{\mathrm{d}\sigma}{\mathrm{d}\Omega}\right)_{mag,el} = (\gamma r_0)^2 N \frac{(2\pi)^3}{\nu_{uc}} \sum_{\vec{\tau}} |F_M(\vec{\tau})|^2 e^{-W} \left(1 - (\tau \cdot \hat{s})^2\right) \tag{4.11}$$

Here, I have omitted the $\delta(\mathbf{Q} - \tau)$ term and the sum is simply over the reciprocal vectors of the magnetic structure, since we know we are constrained by the usual Bragg diffraction condition. Note that the real-space magnetic unit cell is doubled relative to the shown nuclear unit cell ($2a \times 2a \times 2a$ versus $a \times a \times a$, where a is the lattice parameter) due to the antiferromagnetic arrangement of the moments. This results in diffraction peaks at half-integer (HKL) positions, when written in terms of the nuclear unit cell. The $\vec{M}_{perp}$ term has been re-written, with the geometric constraint now represented by the $1 - (\hat{Q} \cdot \hat{s})^2$ term. Clearly for this magnetic structure, there is no magnetic contribution

to the diffracted intensities for $\vec{\boldsymbol{Q}} \parallel \hat{z}$, which is the moment direction. The magnetic structure factor, $F_M(\vec{\boldsymbol{\tau}})$ is given by:

$$F_M = \frac{1}{2}\, g\, \langle S \rangle\, f_{mag}(\vec{\tau}) \sum_{\vec{r}} \sigma_i e^{i\,\vec{\tau}\cdot\vec{r}} \tag{4.12}$$

The sum is over vectors ($\vec{\boldsymbol{r}}$) defining the atom (moment) positions in the unit cell, g is the gyromagnetic factor for the electron, and $\langle S \rangle$ is the average spin magnitude (the same for all sites in this example). σ represents direction of the atomic moment (+1 for up, -1 for down). An important point to note is that the scattering length has been replaced by the $\vec{\boldsymbol{Q}}$-dependent *magnetic form factor*, $f_{mag}(\vec{\boldsymbol{\tau}})$. This occcurs because the neutron is scattering off of the unpaired electron density via the long-range dipole-dipole interaction, the Fourier transform of which is then necessarily dependent on $\vec{\boldsymbol{Q}}$ [48]. This function decays qualitatively similarly to the form factor for X-ray scattering, such that magnetic intensity dies off quickly at high-$|\vec{\boldsymbol{Q}}|$. The magnetic form factor varies with element (if there were different elements in our unit cell there would be an additional sum) and spin state and is readily calculated based on empirically determined functions (see https://www.ill.eu/sites/ccsl/ffacts/ffachtml.html).

Another important point is that the strength of the magnetic scattering is also proportional to the (site-averaged) total spin, which is related to the previous discussion that the cross-section can be written in terms of spin-spin correlation functions. In context of this example, the ideal paramagnetic state above the AFM order has all of the spins randomly oriented due to thermal fluctuations overcoming the correlations from exchange. Although it is not clear from Equation 4.11, one can show that there is a finite cross-section in the paramagnetic state which is independent of $\vec{\boldsymbol{Q}}$ [48], meaning that paramagnetic scattering is entirely diffuse (it typically presents as a slight increase in low-$\vec{\boldsymbol{Q}}$ background at high temperatures). As the temperature is decreased towards

the ordering temperature (T_N, where N stands for "Néel" state in reference to the French physicist Louis Néel who first proposed the existence of antiferromagnetism) the AFM correlations begin to set in. Then, just below T_N, some of the moments order into the AFM structure, which gives rise to magnetic intensity in the form of new Bragg peaks or additional intensity on the existing nuclear Bragg peaks (depending on the nature of the magnetic order). These peaks form out of the magnetic diffuse scattering as spin correlations get stronger and the full translational symmetry of the paramagnetic state is broken by the formation of the magnetic structure. This intensity increases as more of the sample orders. As a consequence, the elastic magnetic scattering allows one to directly probe magnetic ordering transitions and serves as an experimental probe of the order parameter. Demonstrating that intensity dies off with increased temperature is therefore generally an important piece of evidence that scattering is magnetic. Furthermore, indexing of the magnetic Bragg peaks and comparison of their intensities to a calculated magnetic structure factor allows one to determine the resulting magnetic structure in a manner analogous to solving nuclear structures. Symmetry analysis based on group theory is often important for this purpose – an introduction to the relevant mathematics is provided in the book by M. Tinkham [52].

The cross-sections for nuclear and magnetic *inelastic* scattering are considerably more complicateds than the elastic cross-sections. Rather than record them here, I simply list some very basic conclusions that are important for any experimentalist to know. The magnetic inelastic cross-section contains the same geometric term as the elastic cross-section (Equation 4.9). The physical interpretation of this is that the neutron couples to the components of *fluctuations* of the magnetic moment which are perpendicular to $\vec{\boldsymbol{Q}}$. The inelastic cross-section also contains the same form factor term, meaning that magnetic inelastic scattering also decays eponentially with $|\vec{\boldsymbol{Q}}|$. Lastly, the inelastic magnetic signal is associated with deviations from the ordered magnetic state *i.e.* magnons. While

it is possible to have inelastic magnetic scattering due to short-range correlations (so-called "paramagnons"), generally magnetic excitations should die above some ordering temperature. When performing an inelastic neutron scattering measurement, it is important to be able to distinuish the magnetic excitations from the lattice excitations (phonons). The temperature dependence provides one way to do this: while magnetic fluctuations decrease in intensity with increasing temperature phonon scattering has the opposite dependence, since atomic motion is enhanced by thermal fluctuations. The $|\vec{\boldsymbol{Q}}|$-dependence of the scattering intensity provides another way to distinguish between magnons and phonons. For inelastic nuclear scattering, the delta-function potential results in a factor of $|\vec{\boldsymbol{Q}}|^2$ in the cross-section, meaing the scattering power increases monotonically as $|\vec{\boldsymbol{Q}}|$ increases. By measuring the intensity of an inelastic signal at equivalent reciprocal vectors with progressively larger $|\vec{\boldsymbol{Q}}|$ *e.g.* $\vec{\boldsymbol{\tau}} = (0\ 0\ 1/2)$, $(0\ 0\ 3/2)$ and so on, one can produce evidence of a magnetic origin.

I conclude this section with a few additional concepts that are important to neutron-based studies of quantum magnets. The kinematics of neutron scattering are determnied entirely by fulfillment of the scattering triangle and thus the region of ($\vec{\boldsymbol{Q}}$, ΔE)-space for which the scattering function can be measured in an experiment. For a direct geometry spectrometer with fixed E_i (see Section 4.2.2) the accessible points in ($|\vec{\boldsymbol{Q}}|$, ΔE)-space at a constant scattering angle is given by the following equations [51, 48]:

$$|\vec{\boldsymbol{Q}}|^2 = k_i^2 + k_f^2 - 2k_i k_f \, Cos\,(2\theta) \tag{4.13}$$

$$\frac{\hbar^2 |\vec{\boldsymbol{Q}}|^2}{2m_N} = 2E_i - \hbar\omega - 2\sqrt{E_i\,(E_f - \hbar\omega)}\, Cos\,(2\theta) \tag{4.14}$$

In the Equation 4.14 the neutron wave vector has been converted to energy and $\hbar\omega = \Delta E$. For an elastic scattering measurement, the coverage concern is limited to what the

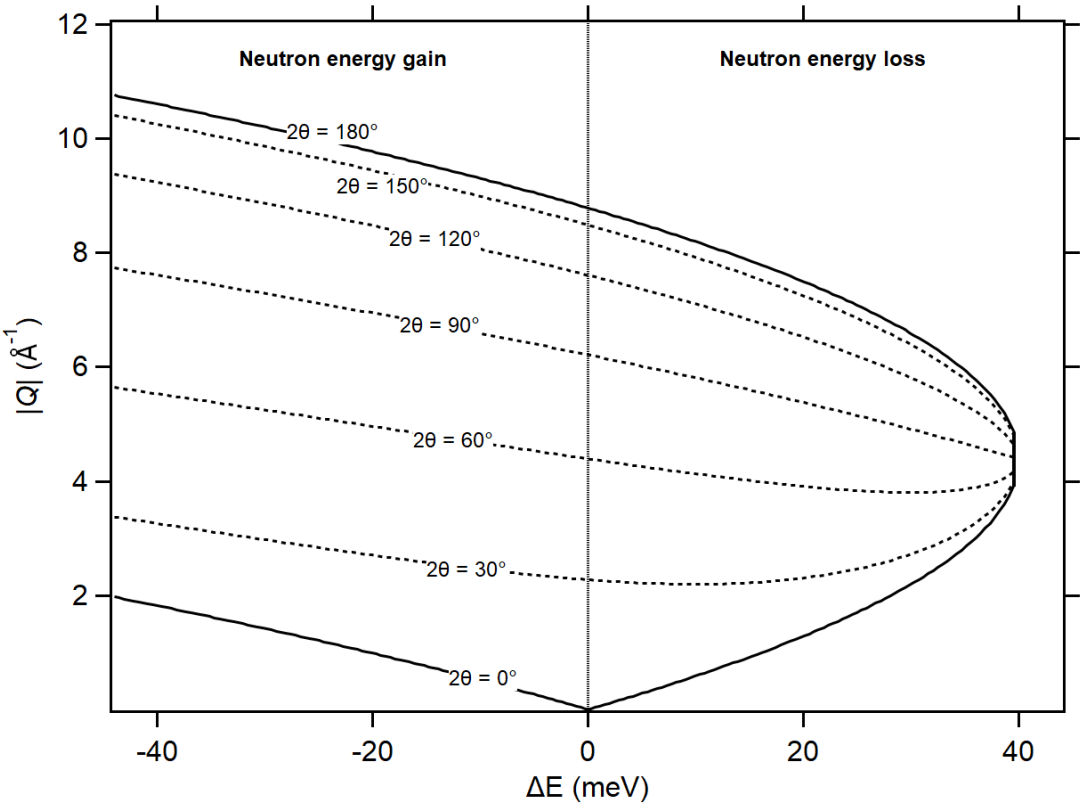

Figure 4.2: Lines of constant scattering angle (2θ for a direct geometry spectrometer with $E_i = 40$ meV calculated using Equation 4.14. The black curves ($2\theta = 0$°and 180°) define the limiting range of the coverage. On a TOF spectrometer with large detector coverage many scattering angles can be measured simultaneously. Most measurements utilize the neutron energy loss region.

accessible values of $\vec{\boldsymbol{Q}}$ or $|\vec{\boldsymbol{Q}}|$ are. This is determined purely by the incident wavelength – which defines the scattering angle (2Θ) for a given $\vec{\boldsymbol{Q}}$/d-spacing based on Bragg's law – and what scattering angles can be measured based on the placement of the detectors. For an inelastic experiment, one considers coverage along both axes. As an example relevant to this thesis, Figure 4.2 shows coverage for a direct geometery spectrometer with a constant E_i. When we consider the full three-dimensional vector nature of the momentum transfer it is clear that each line represents a finite, 4-dimensional, volume in ($\vec{\boldsymbol{Q}}$,ΔE)-space. Note that the maximum ΔE accessible is, as expected, equal to E_i, though not at all $|\vec{\boldsymbol{Q}}|$. The size of the energy loss region decreases with E_i, which leads

to the improvement in resolution at lower incident energies.

While the neutron energy gain side offers larger coverage than the neutron energy loss side, its utility is limited by the fact that as $T \rightarrow 0$, the amount of energy available for the neturon to take from the system decreases. Thus, at low temperatures, far more of the spectral weight (*i.e.* inelastic scattering intensity) is concentrated on the neutron energy loss side, with the energy loss being transferred into the creation of excitations within the system. An equivalent way of thinking about this is that the neutron energy gain process requires the system to initially be in an excited state (since the ground state is, by definition, the lowest possible energy state) and then move to a lower energy state following interaction with the neutron. Since thermal fluctuations are responsible for the initial excited state, the probability of the system being in such a state decreases with temperature as the system approaches its $T = 0$ K ground state, so the scattering of neutrons by this process decreases with temperature [48]. This is described formally by the principle of detailed balance [53, 48]:

$$S\left(\vec{\boldsymbol{Q}}, -\Delta E\right) = exp\left(-\frac{\Delta E}{k_B T}\right) S\left(\vec{\boldsymbol{Q}}, \Delta E\right) \tag{4.15}$$

A related result is the so-called "fluctuation dissipation theorem," which relates the scattering function to the dynamic susceptibility [53]:

$$\left(1 - e^{-\frac{\Delta E}{k_B T}}\right) S(\vec{\boldsymbol{Q}}, \Delta E) = \frac{1}{\pi}\chi''(\vec{\boldsymbol{Q}}, \Delta E) \tag{4.16}$$

As $T \rightarrow 0$ K, the scattering function becomes equal (with a scale factor) to the dynamic susceptibility. Practically, this relationship is important when subtracting high-temperature INS data from low-temperature data – a typical trick to isolate magnetic scattering from other contributions. Before subtraction one needs to divide both intensities (which are proportional to the scattering function) by the value of $(1-exp(-\Delta E/k_B T))$,

computed for each individual value of ΔE and thereby convert to the dynamic susceptibility. This puts both data sets on the same $T = 0$ K scale. If this "Bose factor" correction is not applied, the high-temperature data will retain spectral weight from the increased thermal fluctuations and therefore be an oversubtraction.

4.2.2 Time-of-flight Neutron Scattering

The first decades of neutron scattering, from the discovery of the particle in the 1930's to the pioneering work on diffraction and spectroscopy techniques in the 1940's and 1950's by Clifford Shull and Bertram Brockhouse, respectively, relied on fission reactors to supply the neutrons. A nuclear reactor produces neutrons via a self-supporting fission reaction, which takes place within a critical mass of radioactive material inside the reactor core. The neutrons which escape the core are moderated (described below) to useful energies and then, by poking holes in the walls of the reactor, allowed to pass into "guide" tubes internally coated with neutron reflective materials. These guide tubes pipe the neutrons to various neutron scattering instruments, providing a *time-independent* flux of neutrons for experiments. In contrast to steady-state/reactor-based instruments, "time-of-flight" (TOF) neutron scattering utilizes neutron generation techniques which provide a *pulsed* flux of neutrons. The most common of these techniques, which is the one in use at the SNS, is spallation which is described below. It should be noted that reactors can also be used for TOF neutron scattering instruments, in which case the steady-state flux of the reactor is subsequently modulated in time. The development of TOF neutron scattering as a general scientific technique (which began in earnest during the 1970's at Argonne National Laboratory [54]) came about due to the recognition that: 1) providing a more intense fluxe is essential to improving the capabilities of the technique and 2) that reactor sources face a fundamental limitation in power (and thus neutron flux) related

to the ability to deal with excess heat from the core. While a spallation neutron source attains peak fluxes significantly higher than the constant flux of a reactor source, the time it takes for each spallation event to occur is very short compared to the period between events. This makes heat management much easier than for a reactor, as there is a significant amount of time where no neutrons (and thus no heat) are produced. As a result, a higher flux can be achieved by operating at higher power levels, particularly if one makes use of the entire neutron energy spectrum of the pulse [51].

A general description of neutron production by spallation is as follows. The word spallation describes a nuclear reaction whcih occurs when a sufficiently high energy particle collides with the nucleus of a high-Z element (contained in the spallation "target"), thereby producing neutrons via a two-step decay process following absorption [50, 51]. The minimum energy for spallation comes from the fact that the colliding particles must have a sufficiently small de Broglie wavelengths ($\propto 1/\sqrt{E}$) to interact directly with the subatomic particles within the nuclei of the target material. This requires a minimum energy of ≈ 100 MeV to obtain a wavelength on the order of 1 fm (the radius of a proton is 0.84 fm) [50]. The SNS utilizes 1000 MeV protons which are produced using a linear accelerator, collected into a high-density bunch ($\approx 10^{13}$ protons/pulse) in an accumulator ring, and then directed onto a liquid Hg target with a pulse frequency of 60 Hz. The initial absorprption of the proton excites the Hg nucleus to a higher energy state via a process called *intranuclear cascade*. As the nuclei decays back towards its ground state, it releases high-energy particles (incuding neutrons), up to the energy of the original proton, which trigger an *internuclear cascade* as many other Hg nuclei are excited. The second step, known as "evaporation" is a further relaxation of the excited nucleus which results in the creation of about 20 - 40 neutrons with a range of energies up to ≈ 20 MeV – this is the main neutron yield for a spallation event [50, 51]. These spallation reactions happen *very* fast: the internuclear cascade happens on a timescale of 10^{-22} seconds, while

evaporation happens on a timescale of 10^{-16} seconds [50]. Each proton pulse is $\approx 10^{-6}$ seconds long, meaning that each neutron production event is much shorter than the time between events (60 Hz = a period of $\approx 2 \times 10^{-2}$ seconds). As a result, all of the neutrons produced during spallation (which have a range of energies) are emitted at effectively the same time. This is important, as will be further explained in the following, because it allows us to set a global "time zero" for all of the neutrons regardless of energy and thus accurately determine the time it takes for the neutron to travel from moderator to sample and then from the sample to a position on the detector bank.

Typically, a "T_0" chopper is placed immediately downstream of the spallation target and acts to block initially the initial wave of very-high energy neutrons (the "prompt pulse") which would otherwise produce very high background noise at the detectors. The T_0 chopper is essentially a spinning rotor with thick blades which blocks the neutrons path for a certain period of time after each spallation event. This creates a maximum cut-off for the neutron energies because faster/higher energy neutrons will reach the T_0 position while the rotor is still blocking the guide path. The energy of the remaining "fast" neutrons ($E = 10^8 - 10^{10}$ meV [50]) is still much too high to be of any use for neutron scattering (the wavelength of a 20 MeV neutron is a tiny 6.4×10^{-5} Å) and they must be brought down to more useful energies by using a neutron reflector to conentrate them into"moderator". A moderator can be thought of as a constant temperature (T_{mono}) heat resevoir. The initial high energy neutrons reach equilibrium within the monitor via many scattering events (this guides the choice of moderator materials: H has a high incoherent neutron scattering cross-section, leading to strong, isotropic scattering) and depart with an energy (E_n distribution described by the sum of a Maxwell-Boltzman distribution (with peak flux at $E_{peak} = k_b T_{mono}$ combined with a tail at higher energy

[55]:

$$n_{\mathrm{f}}\left(E_{\mathrm{n}}\right)\mathrm{d}E_{\mathrm{n}} = A\left(\frac{E_{\mathrm{n}}}{\left(k_{\mathrm{B}}T\right)^{2}}\mathrm{e}^{-E_{\mathrm{n}}/k_{\mathrm{B}}T} + \eta\frac{1}{E_{\mathrm{n}}}\right)\mathrm{d}E_{\mathrm{n}} \tag{4.17}$$

where $n_f(E_n)$ is the flux at E_n and η is a moderator dependent constant. The colder the moderator temperature, the lower the average energy of the neutrons which depart.

Different moderating materials are utilized to achieve different neutron energy ranges. For example at the ISIS pulsed neutron source in the UK three materials are used: ambient temperature water moderators ($T = 300$ K), which produce thermal neutrons, and liquid methane ($T = 105$ K) and supercritical liquid hydrogen ($T = 25$ K) moderators, which produce cold neutrons [51]. One will often see moderators described as "decoupled" and/or "poisoned". Decoupled indicates that a special neutron reflecting layer is installed between the moderator and the reflector which prevents neutrons below a certain cut-off energy, formed due to some of the initial fast neutrons from the spallation pulse colliding with the reflector, from entering the moderator. By keeping a narrow energy range for the neutrons which enter the moderator the energy range of the moderated neutrons can be narrowed. This improves $\vec{\boldsymbol{Q}}$-resolution in TTOF diffraction [55] as well as the ability to produce a tightly monochromated beam [51]. Poisoned indicates that some amount of a strongly neutron absorbing material (typically Cd or Gd) has been added into the moderator. This provides some additional control over pulse shape, with a net effect of narrowing the width at low energies [50]. The energy distribution of the moderated neutrons possesses a corresponding velocity distribution. While all neutrons are released simulataneously, the higher energy neutrons move faster resulting in a pulse with a finite width in space and time. Thus one speaks of a "time structure" for the neutron pulse which can typically be well described by the semi-empirical Ikeda-Carpenter function [50]. Following moderation, the neutrons are directed onto the sample where they are

scattered by the various process described in Section 4.2.1.

The general idea underpinning all TOF neutron scattering can now be described. The most important insight is that, because of the well-defined time structure of the neutron pulse, as well as the periodic nature of the pulses, the energy of the neutrons can be tracked by simply measuring the total time-of-flight it takes for them to traverse different regions of the instrument relative to the occurence of a spallation event ($t = 0$). Given that that traveled distances within the instrument are well known, the time-of-flight can be directly related to neutron velocity (v = (total distance)/(total time-of-flight)) and converted to energy and wavelength by the equations given in Table 4.1. Tagging the neutrons as they arrive at the detector bank (termed "events") by their time-of-flight therefore provides essential information for both elastic measurements (diffraction) and inelastic measurements (spectroscopy).

In the case of inelastic TOF measurements with a direct geometry chopper spectrometer, a single incident neutron energy (E_i) is selected from the white beam using a specifically timed (relative to the pulse time structure) rotating "chopper" and the total time-of-flight for each scattered neutron is determined based on when it arrives at the detector. The change in energy for each neutron ($\Delta E = E_i - Ef$) is directly related to how this total time-of-flight differs from $t_{expected} = (L_{c-s}/v_n) + (L_{s-d}/v_n) = t_{c-s} + t_{s-d}$, where L_{c-s} is the distance from the chopper to the sample, L_{s-d} is the distance from the sample to the detector, and v_n is the velocity for a neutron of the specified energy (see Table 4.1) [51]. The actual total TOF from the chopper to the detector, t_{actual} is measured directly for each neutron using special electronics which are linked to the spallation system. Since the t_{c-s} is well defined by the selected neutron energy/velocity, $t_{s-d} = t_{actual} - t_{c-s}$. This is directly related to the magnitude of the scattered neutrons wave vector and energy. If t_{s-d} is the same as the value from $t_{expected}$ the neutron has scattered elastically with no change in energy or velocity. If t_{s-d} is larger or smaller than the expected value, than the

neutron has scattered inelastically either losing ($\Delta E > 0$) or gaining ($\Delta E < 0$) energy, respectively. All the INS experiments in this thesis were conducted on direct geometry spectrometers and a specific example of this kind of configuration is discussed in the next section, including further details on how the vector nature of $\vec{\boldsymbol{k}}_f$ and $\vec{\boldsymbol{Q}}$ are determined. For indirect geometry instruments, the full spectrum of E_i is utilized and the final energy of scattered neutrons incident on the detector is set by a focusing analyzer crystal array [55]. However the general principle of determining ΔE remains the same. Indirect geometry instruments typically provide high-flux and enable access to a large ΔE range, however they typically have worse $\vec{\boldsymbol{Q}}$-resolution and larger background. With suitable optimization of the neutron guide lengths and moderator characteristics, very fine ΔE-resolution ($\sim \mu eV$) can be achieved [55].

To illustrate the particular benefits of TOF spectroscopy [3], it is helpful to consider the situation on a triple-axis spectrometer (TAS) at a steady-state reactor source. In this case, a monochromatic beam and an analyzer crystal (between the sample and detector) are used to define the ΔE of the measured neutrons. Since the positions of the sample, analyzer and detector must all be fixed to satisfy the scattering condition for a specific ($\vec{\boldsymbol{Q}}$,ΔE)-point of interest, typically only a point detector is utilized. One must therefore make measurements in a point-by-point manner, using a linear scan. While one is free, in principle, to do a scan along any direction in ($\vec{\boldsymbol{Q}}$,ΔE)-space, the easiest to interpret are those along a set $\vec{\boldsymbol{Q}}$-direction at a fixed ΔE or a along ΔE at fixed $\vec{\boldsymbol{Q}}$. Regardless, the point-by-point nature makes mapping large regions of ($\vec{\boldsymbol{Q}}, \Delta E$)-space incredibly time intensive (especially considering that inelastic features are generally weak and the neutron flux is comparatively low). Most often, one sticks to the high-symmetry directions of the Brillouin zone which are known to be information rich. The Multi Axis Crystal Spectrometer (MACS) at the NCNR is a notable exception, which

[3]Specifically, TOF spectroscopy with a direct geometry instrument.

seeks to improve the efficiency of TAS by employing a detector system with 20 discrete channels, each containing an independent analyzer crystal and detector [56]. However, even this advancement only allows for a detector with solid angle ≈ 0.2 steradians, which is still significantly smaller than what is obtained with direct geometry TOF spectrometer ($\approx$ 1 - 2 steradians) since one is not limited by analyzers [57]. The ability to have energy discrimination (via the TOF method) in combination with large detector coverage, allowing for measurement of many scattering angles and energy transfers simulataneously, makes TOF spectroscopy much more efficient at mapping large regions of $(\vec{\boldsymbol{Q}}, \Delta E)$. This is important because interesting physics does not live exclusively at the high-symmetry points, as illustrated by the diffuse scattering measurements shown in Chapter 5.

TOF diffraction instruments typically utilize the full, "white-beam", spectrum since only Bragg scattering is being considered [51]. This is exactly analogous to the case of Laue diffraction considered for X-rays, with all of the neutron wavelengths providing nested Ewald spheres inside the "limiting" sphere corresponding to E_{max} (*i.e.* λ_{min}), such that many Bragg reflections are accessible for one sample orientation. As a result, these instruments are called Laue TOF diffractometers. In this case the relevant time-of-flight for each neutron is the total time (t_{tot} from spallation to detection after scattering by the sample. The wavelength of each scattered neutron is considered to be unchanged during scattering and is thus directly related to t_{tot} by the relation: $t_{tot} = m_N L\lambda/2\pi\hbar$, where t_{tot} is in units of seconds, L is the total flight-path distance in meters and λ is in Å. Using this equation Bragg's law can be re-written as:

$$\frac{2\pi\hbar t_{tot}}{m_N L} = 2dsin\left(\theta\right), \tag{4.18}$$

where d is the interplanar spacing of the crystal and θ is the one-half the scattering angle. By using a large array of position sensitive detectors around the sample, one can collect

many scattered neutrons, with the d-spacing of the plane they scattered from determined by their measured t_{tot}. Both powder (*e.g.* the instrument POWGEN at SNS) and single crystal (*e.g.* the instrument TOPAZ at SNS) diffraction can be measured in this way. The primary advantages of TOF diffraction over reactor-based instruments are: 1) the high-flux, since the full pulse spectrum is used and 2) the ability to map large swaths of momentum space (either $\vec{\boldsymbol{Q}}$ or $|\vec{\boldsymbol{Q}}|$, as the case may be) very efficiently. The latter is especially useful for single crystal studies.

4.2.3 TOF Spectroscopy Instrumentation

In this thesis, two very different TOF spectrometers were utilized. Note that "spectrometer" implies the ability to perform energy discrimination on scattered neutrons (*i.e.* measure the scattered intensity at a specifc E_f). In contrast, a neutron "diffractometer", as described in the previous section, performs no energy discrimination and integrates the E_f distribution of the scattered neutrons (which range up to E_i) into a single scattering intensity. This is acceptable because the quantity of interset in that case (the elastic signal due to Bragg scattering) is orders of magnitude larger than the inelastic one. While both CORELLI and SEQUOIA are spectrometers, they are intended for very different purposes. SEQUOIA is used for measuring *inelastic* scattering signals in a material as a function of $\vec{\boldsymbol{Q}}$ and ΔE, using a single E_i at a time [4]. Energy discrimination is used to seperate the weak inelastic signal from the coherent and incoherent elastic signals and thereby determine the value of ΔE associated with an excitation at a particular value of $\vec{\boldsymbol{Q}}$. In contrast, CORELLI uses energy discrimination for the opposite purpose: to isolate weak *elastic* signals from inelastic ones which would obscure the elastic signal if the full range of E_f was integrated. These two instruments therefore reflect the versatility of the

[4]It is actually possible to measure excitations at multiple E_i values simultaneously using SEQUOIA using the idea of "repetition rate multiplicity" [55]. This involves being clever about the rotation frequency and phasing of the choppers and is best done in consultation with the instrument scientist.

TOF method and demonstrate how the time structure inherent to pulsed neutrons can be exploited to obtain different kinds of information.

SEQUOIA: fine-resolution fermi chopper spectrometer

SEQUOIA is a direct-geometry spectrometer which is optimized in several ways so as to satisfy an array of experimental needs. It provides a high neutron flux across a wide range of E_i while also maintaining a farily low background and excellent energy resolution. Coupled with a large detector bank (with good coverage both vertically and horizontally) made up of an immense number of detector pixels ($\approx$ 110,000) SEQUOIA is a very versatile instrument. Relevant to this thesis is that SEQUOIA provides good flux at low neutron energies, which are essential for studies of magnetic excitations. Combined with the energy and $\vec{\boldsymbol{Q}}$ resolution this allows for detailed measurement of spin waves and weak magnetic inelastic signals. The design of SEQUOIA is described in detail in several publications [58, 59, 57], which this section summarizes.

A schematic of SEQUOIA is provided in Figure 4.3 showing the general layout and indicating the essential features. Neutrons are emitted from the moderator in-phase with the spallation events (frequency = 60 Hz) and the moderator is coupled to an elliptical supermirror guide. The point of the guide is to transport the neutrons emitted from the moderator to the Fermi chopper/sample while minimizing losses due to absorption and background. As implied by the name, the guide is reflective to neutrons. Due to their wave nature, there is an index of refraction for neutrons traveling through a material. As a result, for an interface between vacuum and a material (often Ni metal, $\Theta_c \approx 0.1$ °for $\lambda = 1$ Å neutrons), one can use Snell's law to define a critical angle below which total reflection occurs for any neutron hitting the material. However, the guide on SEQUOIA employs a supermirror coating which is not based on total reflection. A supermirror is a series of stacked double layers of two different materials, with a negative gradient in

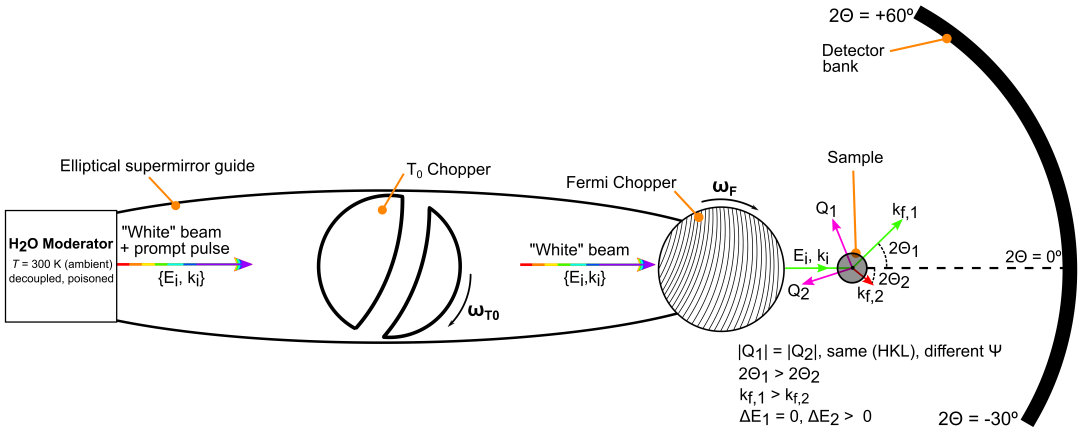

Figure 4.3: A schematic of SEQUOIA, viewed from above, with the key features noted. In reality, the sample and detector bank occupy different vessels which are evacuated independently. Two different in-plane (this plane is referred to as the "equitorial plane") scattering events are indicated for the monochromatic beam (green arrow, E_i, k_i) leaving the Fermi chopper: elastic (green, $k_{f,1}$) and inelastic (red, $k_{f,2}$). The two scattering events are conducted at the same $|Q|$, with different vector orientations to satisfy the scattering triangle for ΔE_1 and ΔE_2. Note that in the elastic case Q_1 bisects the incident and final wave vectors. Because of the significant out-of-plane detector coverate ($\pm$ 18 °) one also detects scattering events where k_f is out of the plane. One sweeps through different parts of ($\vec{\boldsymbol{Q}}$,ΔE)-space by rotating the crystal about the ϕ axis (perpendicular to the page), thereby projecting different reflections at different energy transfers onto the detector bank.

the total thickness of the double layer. Reflection is accomplished by overlapping Bragg diffraction, with neutrons of different wavelengths and different incident angles diffracting at different depths within the layer [55]. The important feature of the supermirror is that it has a much larger effective critical angle (in this case it is more properly a critical $|\vec{\boldsymbol{Q}}|$) than can be obtained with a homogeneous reflective coating; this translates to more flux downstream. Furthermore, the carefully designed elliptical cross-section of the guide acts a a neutron focusing mechanism which boosts SEQUOIA's low energy flux, an especially important feature for studies of quantum magnets. The guide is rather long (18 m from moderator to Fermi chopper) giving time for the neutron pulse to spread out as it travels, which is important for improved energy resolution

In order to obtain a monochromatic incident neutron beam, SEQUOIA uses a Fermi

chopper at the downstream end of the guide. A Fermi chopper is composed of many, thin, curved blades (the lines within the labeled circle in Figure 4.3) made from a neutron absorbing material and mounted inside a rotating mechanism. The rotation axis is out of the plane of the page and the chopper's rotation is timed relative to the spallation pulse with a well defined phase offset between the two processes. Depending on the rotational speed of the chopper (*i.e.* its frequency) and the value of the phase offset, only neutrons with a certain velocity will be able to pass through the curved, rotating channels without colliding with the blades and being absorbed. As a result, the spectrum of each pulse is "chopped" into a discrete TOF section (with some finite width corresponding to the efficiency of the monochromation), which forms a monochromatic pulse of neutrons downstream of the chopper. The transmission of the beam through the chopper is dependent on the width of the channels as well as the thickness and curvature of the blades; these parameters therefore effect the total transmitted flux and energy resolution. Multiple choppers are available at SEQUOIA for favoring more flux (the 'high-flux" chopper) or better resolution (the "high-resolution" chopper) and switching between them is completely automated.

In addition to the Fermi chopper, SEQUOIA also has a T_0 chopper, which is essentially just a Fermi chopper with a single, very wide, curved channel. As previously described, the foremost purpose of this chopper is to block the fast neutrons which are emitted immediately after the spallation event while letting a large amount of the moderated neutrons through. On SEQUOIA, some portion of the prompt pulse does still make it through the T_0 chopper and can reach the sample, potentially overlapping with slower neutrons from the previous pulse. This produces spurious signals and can pollute data collected at certain E_i values – such "spurions" are well-known to the instrument team and can generally be easily identified. Here, the T_0 chopper also acts as a "bandwidth" chopper, which definese a smaller subsection of the moderated neutron pulse (called a

"frame") prior to arrival at the Fermi chopper. As a result, the incident energy is a function of the frequency of both the T_0 and Fermi choppers, as well as their individual phase offsets relative to the pulse rate.

The sample environment sits a short distance ($\approx$ 2 m) downstream of the Fermi chopper in an evacuated chamber. The sample is rotated around an axis perpendicular to the page in Figure 4.3 which is titled ψ; the sample environemnt on SEQUOIA typically does not allow for significant tilts or other rotations. SEQUOIA is able to accomodate many different sample environments. Besides temperature control (closed-cycle or dilution refrigerators), various pressure vessels and magnets can also be emplyed. Of relevance to studies of quantum magnetism, a 14 T magnet (the design of which was led by SEQUOIA instrument scientist Matt Stone) is now available. Such high fields in a neutron experiment are not widely available and should provide valuable insights into polarized magnetic states. However, use of this magnet is somewhat complicated by its relatively large contribution to the overall background as well as geometrical constraints imposed by the limited size of the neutron-transparent window. The evacuated sample chamber is connected by a special "gate valve" to the large vacuum chamber which contains the cylindrical detector bank (the detectors need to be under vacuum to operate). This valve is closed during sample changes, protecting the vacuum of the detector bank, and then opened during measurement to provide an obstruction free flight path thereby eliminating further contributions to the background. At the time of this writing, an incident beam collimator is being designed for SEQUOIA, which would sit between the Fermi chopper and the sample. If installed, this collimator will provide the option to further reduce the background and improve the resolution, at the expense of flux.

While the TOF method yields E_f and $|\vec{\boldsymbol{k}}_f|$ of the scattered neutron, as well as the value of $|\vec{\boldsymbol{Q}}|$, we also need to know the *direction* of the scattered neutron to extract information from the full vector nature of the scattering. This information is provided

by the many ^{3}He linear position sensitive tube detectors which make up the detector bank; their diameter (which is << than their length) defines the pixel size in one direction. When a scattered neutron hits one of these detector tubes the neutron is abosorbed by a ^{3}He atom, forming ^{4}He which then decays back into ^{3}He via production of a proton: n+^{3}He $\rightarrow$^{4}He $\rightarrow$ p + ^{3}He. The position of the neutron within a specific detector can be accurately inferred from the center-of-mass of the ionized cloud created by the the charged proton, and this gives a location in terms of a Cartesian coordinate system for the laboratory reference frame. Given that the orientation of the reciprocal lattice of the sample (the sample reference frame) is known at the time of the scattering event, the laboratory coordinates can be converted to the sample reference frame (*i.e.* an H, K, L triplet) by a series of matrix transformations.

$$\begin{pmatrix} H \\ K \\ L \end{pmatrix} = \frac{\vec{\boldsymbol{Q}}_l}{2\pi} R^{-1} \cdot U^{-1} \cdot B^{-1} \tag{4.19}$$

where $\vec{\boldsymbol{Q}}_l$ is the vector corresponding to the neutron position in the laboratory frame, and R, U, and B are the transformation matrices (the inverse is employed in Equation 4.19). The B matrix transforms the vector in reciprocal space (the sample reference frame) defined by H, K and L into a Cartesian coordinate system. In the Mantid software package, which is used on SEQUOIA, the first Cartesian axis is along $\vec{\boldsymbol{a}}^*$ (reciprocal lattice basis vector), the second is in the plane defined by $\vec{\boldsymbol{a}}^*$ and $\vec{\boldsymbol{b}}^*$, and the third is perpendicular to that plane. The U matrix then converts this to a second Cartesian matrix which is attached to the ψ-goniometer. Finally, this can be translated into the stationary lab frame by applying the rotation matrix R based on the known position of the goniometer. The U and B matrices are determined (by software, thankfully) at the beginning of an experiment after placing the sample in a (hopefully well-known)

orientation on the goniometer. An alternative way to encapsulate this information is to use the $\vec{\boldsymbol{u}}$ and $\vec{\boldsymbol{v}}$ vectors, which are two reciprocal space vectors that lie in the equitorial plane such that their cross-products points directly upward (in the lab frame). These vectors do *not* need to be integers for this purpose. The previously described math gives one access to the full vector nature of $\vec{\boldsymbol{Q}}$.

A typical measurement on SEQUOIA is conducted by rotating the sample around the ψ axis in order to modify which reciprocal space vectors satisfy the diffraction condition. Such a rotation is indictated on the right side of Figure 4.3, which shows how rotating the same $\vec{\boldsymbol{Q}}$ to different positions allows one to access different energy transfers. The typical approach is to perform measurement (with a certain E_i) at a large number of ψ-values in order to sweep out a large portion of ($\vec{\boldsymbol{Q}}$,ΔE)-space without any gaps in coverage. Note that measurement times are measured in terms of proton count delivered to the spallation target, which allows the scattering data to be normalized during reduction. Due to the fact that the ψ-axis is the only sample goniometer (unlike on a triple-axis instrument, where one typically also has the ability to tilt the sample to some degree) coverage is determined entirely by the orientation of the sample upon mounting in the sample environment and the E_i utilised. As a result, it is important to think carefully about how to align the sample to ensure that the desired $\vec{\boldsymbol{Q}}$ vectors can be accessed. In low-dimensional systems, one can take advantage of the fact that fluctuations are primarily confined to one or two-dimensions and the irrelevant dimension(s) can be integrated over. For a two-dimensional sample, the relevant plane should be placed perpendicular to the beam, with one of the special directions in the equitorial plane. In one-dimension, the special direction should be placed in the equitorial plane.

Another important aspect of experiment planning is consideration of the incident energies that will be used. While changing E_i on SEQUOIA is a straightforward process, measurements of weak inelastic magnetic signals often need to be long (10's of hours) to

resolve things clearly, so it is important to choose judiciously. To zeroeth order, this is determined by the physics of your system and the energy scale of the excitations you want to measure since E_i must be greater than ΔE. While in principle one can access ΔE values up to E_i (full loss of the neutron energy to the system) in reality the constraints of the scattering condition (see Figure 4.2) mean that E_i often needs to be substantially above the ΔE of interest in order to coverage of a full Brillouin zone. However, it is also desirable to perform a measurement with the lowest E_i that provides acceses to the scattering of interest, since the absolute energy resolution is better at lower E_i. As a result, for a steep dispersion with a large extent in ΔE the best approach is to make multiple measurements at progressively larger E_i values, as was done in Chapter 6 for Li_2CuO_2 . The extent of the elastic line (leakage of the much stronger elastic scattering into the low-ΔE inelastic data, which increases with E_i) will always be present. This sets a lower limit on the ΔE which can be accurately measured with given E_i. Another consideration in choosing an E_i is that lower values provide less $\vec{\boldsymbol{Q}}$ coverage. As mentioned previously, when investigating magnetic signals it is desirable to be able to measure at multiple zones (*e.g.* at the (001), (002) etc.) to distinguish them from phonons via the intensity dependence from the magnetic form factor. For low-ΔE scattering, one can run into the issue that the low E_i needed to resolve the excitation does not provide sufficient $\vec{\boldsymbol{Q}}$ coverage for this kind of analysis. Another trade-off lies in the dependence of the incident flux on E_i (Figure 4.4**a**) which for SEQUOIA decreases away from the peak at ≈ 40 meV. These kinds of trade-offs abound in TOF spectroscopy and, to quote SEQUOIA instrument scientist Matt Stone, you always end up losing out in some way.

As the previous discussion shows, planning a SEQUOIA experiment involves balancing a number of competing factors. Fortunately, an excellent piece of software (with an approachable GUI) is available in Mantid which performs coverage calculations for all of the direct geometry spectrometers at the SNS. For a given sample orientation (defined

by $\vec{\boldsymbol{u}}$ and $\vec{\boldsymbol{v}}$ vectors), E_i and amount of ψ rotation the software calculates the region of ($\vec{\boldsymbol{Q}}$,ΔE)-space which can be accessed. One can visualize this coverage using different slices (*i.e.* (0 K 0) vs. ΔE or (H 0 0) vs. (0 K 0)). Note, however, that the software does not calculate the scattering function for your material, and so it is limited to telling you where you will be able to observe scattering, but not how strong that scattering will be. Another useful piece of software is the resolution calculator found on the SEQUOIA website (also applicable to all direct geometry instruments at SNS). For a TOF spectrometer the energy resolution at a given E_i improves at higher ΔE. The software provides an empirical polynomial function which captures this dependence. The resolution is given in full-width-half-max (FWHM) and indicates the experimental contribution to the apparent FWHM of an excitation. One needs to know the chopper frequency setting for the E_i of interest to do this calculation and, for reference, a table of these settings is shown in Figure 4.4**b**,**c** for both of the choppers available at SEQUOIA.

CORELLI: elastic diffuse scattering spectrometer

CORELLI is a somewhat unique instrument in terms of TOF spectroscopy in that it is actually intended for measurement of elastic, not inelastic, scattering. However, in contrast to a typical diffractometer, the desired elastic scattering is not that of the Bragg peaks, which are associated with the long-range pair-correlations of the lattice (*i.e.* the average structure), but the *diffuse* scattering [60]. Diffuse scattering is a local structure phenomenon which comes about due to the existence of short-range pair-correlations, which may be dynamic or static [60]. Since the scattering function is fundamentally based on a Fourier transform, the extent of pair-correlations in real space is inversely proportional to the width of the scattering in reciprocal space. As a result, diffuse scattering forms as extended structures in reciprocal space (which do not have to obey the translational symmetry of the lattice), as opposed to sharp peaks at specific (HKL)

a) Flux vs. E_i

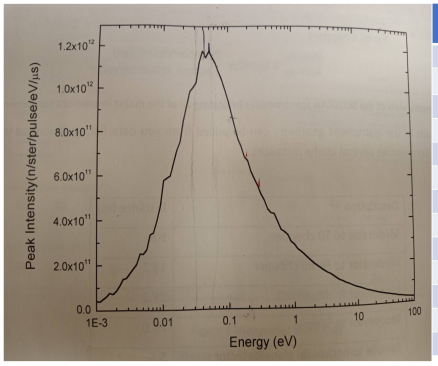

b) High-flux settings

E_i Threshold [meV]	Chopper	Chopper freq. [Hz]
0	High Resolution	60
2.5	High Resolution	120
6.5	High Resolution	180
12.5	High Flux	120
20.5	High Flux	120
45.5	High Flux	180
87.5	High Flux	240
143.5	High Flux	300
213.5	High Flux	360
297.5	High Flux	420
395.5	High Flux	480
507.5	High Flux	540
633.5	High Flux	600

c) High-resolution settings

E_i Threshold [meV]	Chopper	Chopper freq. [Hz]
0	High Resolution	120
8.25	High Resolution	180
17.5	High Resolution	240
30.1	High Resolution	300
41.5	High Resolution	360
54.75	High Resolution	420
70.5	High Resolution	480
80.05	High Resolution	540
110	High Resolution	600

Figure 4.4: **a)** A photograph of the flux vs. E_i dependency for SEQUOIA as shown in the user hand-book found in the instrument control hutch at the SNS. The reccomended "clean"' (free of spurious, instrumental signals) E_i ranges are: 8 - 11.5 meV and 18 - 4000 meV. The range 11.5 - 18 meV is polluted by a spurion at around ΔE = 7 meV. Below 8 meV only E_i = 4 meV is reasonably "clean" though it still has a spurion at around ΔE = 3 meV. Using SEQUOIA at such low E_i may not provide data suitable for detailed analysis, but it might provide ammunition for a proposal on a lower energy spectrometer (*i.e.* CNCS). **b - c)** Frequency settings for different E_i ranges for the two available choppers. The chopper frequency for a given E_i is found by choosing the row with the lowest threshold E_i that is larger than the E_i of interset. If the chosen E_i is larger than the last row, use the last row. Note that not all energies can be accessed with both choppers.

positions, since the extent of the relevant pair-correlations in real space is small. Diffuse scattering is also orders of magnitude weaker than a typical Bragg peak.

The strengths of Laue TOF neutron diffraction, notably the ability to measure large areas of $\vec{\boldsymbol{Q}}$-space efficiently and with good resolution, would seem to make it well-suited to measuring elastic diffuse scattering. Such scattering can be used to determine the presence of static local structure distortions, such as in the case of local Ti off-centering in the ferroelectric $BaTiO_3$ [61, 62, 63]. It is also a very useful probe to identify and characterize nano-scale disorder [60], as has been done to reveal short-range correlations between O vacancies in the titinate pyrochlores [64]. However, a standard diffractometer actually measures the so-called *total* scattering function, $S(\vec{\boldsymbol{Q}})$ because it integrates together all neutrons scattered at some value of $\vec{\boldsymbol{Q}}$ regardless of their ΔE (*i.e.* all inelastic

and elastic scattering processes). This is an issue for measurement of the elastic diffuse scattering because the energy integration will cause it to be convolved with any inelastic scattering signals in the system, which occur away from the Bragg points. The major inelastic contribution is thermal diffuse scattering from phonons, which can be on par with any diffuse elastic contributions and thus effectively obscure them [60]. Due to the Debye-Waller term in the phonon cross-section, the intensity scattering due to phonons decreases with temperature [48]. One attempt at a solution is to simply do measurements at very low temperatures (*i.e.* $T << $ the Deby temeprature) in order to freeze out the contribution of the phonons. However, due to the zero-point motion, some thermal diffuse scattering will always persist, even down to the coldest experimentally accessible temperatures. However, if we are interested in a local structure transition that happens at some temperature well above 0 K (such as in the case of the metal-insulator transition and collosal magnetoresistance in the manganite perovskites [65, 66, 67]) than this is not a viable option.

CORELLI solves this problem by combining the Laue TOF method with energy discrimination, so that $S(\vec{\boldsymbol{Q}}, \Delta E = 0)$ can be measured across a large range of $\vec{\boldsymbol{Q}}$ efficiently and with good resolution. Furthermore, the use of a substantial fraction of the incident neutron pulse (up to 50% compared to 1 - 5 % on a typical direct geometry instrument like SEQUOIA) provides a high flux suitable for measuring weak diffuse signals. The method used for establishing energy discrimination on CORELLI is necessarily distinct from the one for a direct geometry chopper spectrometer (as described in the previous section) because the goal is to utilize a large fraction of the neutrons in the incident pulse, not just those of a fixed E_i. As a result, elastically scattered neutrons from an unmodulated white beam cannot be determined simply based on their time-of-flight value when they hit the detector because neutrons with different ΔE may still hit the detectors with the same total time-of-flight due to their different velocities. Instead, CORELLI makes

use of the statistical technique of "cross-correlation" to extract the purely elastic (within some finite FWHM) contribution to the scattered intensity [60].

The first step in doing this is to employ a "statistical" chopper with a pseudo-random array of slits. These slits remove a total of $\approx 50\%$ of the neutron absorbing material from the outer circumference of the chopper. As each open slit passes through the beam, it allows neutrons of a single random energy through the chopper based on what section of the pulse is passing through the chopper at this point. If one were to operate the chopper at the same frequency (f_c) as the spallation pulse (f_p), this would result in a random, but repeating, selection of the neutron pulse energies, because the chopper would always be at the same point in its rotation when the pulse arrived. However, for the math of the cross-correlation technique, to work all possible random selections of the pulse must be utilized. To restate in another way: one must sample all possible phase lags, t_0, between the start of the pulse and the (arbitrarily defined) start of the chopper sequence [60, 68]. This is obtained by running the chopper at $f_c \neq nf_p$ with n an integer and $f_c > f_p$. With these settings, the full pulse spectrum of E_i is utilized after only a few pulses, with each E_i having an equal overalll probability of transmission [60, 68]. Each neutron which passes through the chopper and scatters effectively samples $S(\vec{\boldsymbol{Q}},\Delta E)$, which is, as discussed earlier in this chapter, basically a probability distribution. The resulting intensity at each detector is a function of t (the total flight time since the spallation event) and t_0 [60, 68]. Since neutrons with different E_i, defined by the time from source to chopper, t_1, which scatter with different values of ΔE, defined by the $t - t_1$, can enter the detector at the same t, CORELLI always collects the *total* scattering data.

The point of doing all this is that the scattered intensity, which is directly related to the scattering function we are interested in, is now also modulated by the transmission function of the statistical chopper $M(t)$ (a periodic function which is well known since it

was designed into the chopper). This can be experessed as [60, 68]:

$$I\left(t_0,t\right)=\int_{t-T_{\mathrm{C}}}^{t}M\left(t_1-t_0\right)\varphi\left(t_1\right)S\left(t_1,t\right)\mathrm{d}t_1+\mathrm{B}(t) \tag{4.20}$$

where φ is the incident flux at the E_i corresponding to t_1, T_c is the period of the chopper ($T_c = 1/f_c$), and $B(t)$ is a background term uncorrelated with the chopper. $S(t_1, t)$ is the scattering function which will be determined for a given t_1 and t which together define the ΔE for a scattered neutron. Due to the pseudo-random design of $M(t)$, it has the property that it's autocorrelation function can be well approximated by a delta function:

$$A^{MM}(\tau)=\frac{1}{T_{\mathrm{C}}}\int_0^{T_{\mathrm{C}}}[M(t)-c]M(t-\tau)\mathrm{d}t\simeq c_1\delta(\tau) \tag{4.21}$$

It has been shown [69] that, given such an A^{MM} for $M(t)$, computing the cross-correlation function of $I(T_0, t)$ and $M(t)$ yields the following:

$$C\left(t_1,t\right)=c_1S\left(t_1,t\right)\varphi\left(t_1\right)+\frac{B(t)}{T_{\mathrm{C}}}\int_0^{T_{\mathrm{C}}}M\left(t_1-t_0\right)\mathrm{d}t_0 \tag{4.22}$$

where c_1 is a constant related to the chopper geometry. Since $M(t)$ and $B(t)$ are well known, that term is simply a background which can be subtracted off. Then, since $\varphi(t_1)$ is well known (by detailed characterization of the time structure of the spallation pulse), $S(t_1, t)$ can be extracted from $C(t_1, t)$. Fortunately, this math is handled behind the scenes during data reduction in Mantid. Technically, CORELLI allows for measurement of inelastic signals due to it's energy discrimination. However, since each t value has contributions from different E_i and, potentially, multiple scattering processes the errors become correlated. This means the instrument is not able to measure weak inelastic signals well if they occur near (in momentum space) stronger inelastic signals. Such measurements are far more suited to the chopper spectrometer instruments at the SNS

or the triple-axis spectrometers at HFIR. A similar problem occurs also occurs if there are multiple elastic scattering channels. Therefore, in a small $\vec{Q}$ around a Bragg peak the errors of the weak diffuse scattering will be huge, since they are determined by the much stronger Bragg contribution. However, for $\vec{Q}$ values far from the Bragg peaks the diffuse scattering is typically the only elastic contribution and the cross-correlation analysis efficiently seperates it from any inelastic scattering with reasonable error bars [60].

While the previous discussion has highighted the relevance of diffuse scattering to structural problems, the magnetic cross-section can also be active in this channel. Thus the efficiency of CORELLI for measuring elastic diffuse scattering is equally applicable to measuring static, short-range magnetic correlations. An excellent example of this is in measurements of the local "two-in-two-out" magnetic ground state (the spin "ice" state in analogy with the way protons are arranged in water ice) of $Dy_2Ti_2O_7$; the magnetic moments in this compound lack long-range order, but have a well-defined structure set by local rules for how the moments are distributed on a Dy tetrahedron [70]. This capability was exploited for the measurement on $Nd_2Zr_2O_7$ described in Chapter 5, where the magnetic diffuse scattering similarly arises due to ice-like short-range correlations. A distinction is that in the case of $Nd_2Zr_2O_7$, the diffuse scattering is actually inelastic (because the ice-like state is dynamic in nature), but at a very small ΔE on the order of 10 μeV. Such a small ΔE is well within the finite extent of the elastic line of the energy discrimination provided by the cross-correlation analysis. Some of the scattering due to the magnons was therefore also captured in the cross-correlation analyzed data. In this case, the total scattering and extracted elastic data were actually fairly similar, though the cross-correlation analysis did clean up the background slightly.

The typical approach for an experiment on CORELLI is similar to that described for SEQUOIA. Planning using simulation software – in this case through CORELLI-specific

Mantid scripts provided by the beamline scientist – is also important. The accessible ψ range can be limited by complex sample environements (*e.g.* a dilution refrigerator) but the extensive detector coverage and broad spectrum of the incident beam (10 - 200 meV [60]) means that this is typically not an issue provided the orientation is properly chosen with respect to the scattering one wants to access. The data can also be symmetrized (during data reduction) using the symmetry elements of the space group in order to improve the statistics. A typical measurement involves rotating the sample in small steps in ϕ (typically 1 or 2°) to sweep the limiting Ewald sphere through the desired region of momentum space with no gaps (see Figure 2 in Welberry and Whitfield [68] for an illustration) and measure the diffuse scattering. Note that the statistical chopper is always in use and it is just a question of whether the cross-correlation analysis has been performed on the collected data. Therefore, one always gets the total scattering data, from which a seperate, elastic, data set can be extracted. In standard operation, the data pipeline is set-up to automatically produce both data sets. Comparing these two data sets allows one to demonstrate if diffuse signals are elastic or inelastic.

In addition to measuring the diffuse scattering, one can also measure Bragg peaks as in a typical TOF Laue diffractometer. Since the full white beam is used, the same (HKL) peak will be accessed by various E_i values, which show up as seperate signals on the detector. Since both t_1 and t are known for each scattered neutron, it is possible to determine both where a certain (HKL) peak will show up on the detector and which E_i it came from, for a certain sample orientation. This is especially valuable for parameteric studies, since an optimal sample position can be determined such that the scattering for the desired (HKL) due to an E_i with high-flux (peak flux occurs at roughly $E_i = 40$ meV) is well placed on the detectors (*i.e.* not nearby to any of the gaps between detector banks).

Chapter 5

Evaluating the Effects of Structural Disorder on the Magnetic Properties of $Nd_2Zr_2O_7$

In this chapter I detail further work on $Nd_2Zr_2O_7$ undertaken following successful synthesis during comissioning of the furnace.

5.1 Introduction

Rare-earth pyrochlore oxides ($A_2B_2O_7$, where A = rare-earth and B = a wide range of transition metals) have long sustained a variety of research efforts within the condensed matter community [71, 72, 73, 74]. Recently, experimental [75, 76, 77, 78] and theoretical [79, 80, 81] work has highlighted novel magnetic and electronic behaviors related to the dipolar-octupolar ground state doublet of certain (Kramers) rare-earth ions. Particular attention has been focused on $Nd_2Zr_2O_7$ following experimental observation of behavior consistent with a picture of *magnetic moment fragmentation*, where different "fragments"

of the Nd^{3+} moment operate as separate degrees of freedom.

The idea of magnetic moment fragmentation proposed in the context of emergent Coulomb phases is based on the crystallization of monopole excitations from a spin-ice ground state [82]. In this theory, a Helmholtz decomposition is used to divide the magnetization field into "divergence-full" and "divergence-free" components. Initially, the local constraint of the spin-ice state produces a magnetization that is wholly divergence-free. Fragmentation then occurs upon the crystallization of a sufficient density of monopole excitations and the development of a divergence-full contribution to the sublattice magnetization. The result is a magnetically ordered state (divergence-full) and a fluctuating Coulomb phase (divergence-free). Such a state results from a complex interplay of strong, Ising-like anisotropy, effective ferromagnetic (FM) interactions and a delicate balance of the magnetic exchange and dipolar interactions [83, 82].

The phenomenon of moment fragmentation can also be addressed by explicitly considering the dipolar-octupolar character of the ground state Kramers doublet of Nd^{3+} ions in $Nd_2Zr_2O_7$ [84]. The differing symmetries of the resulting pseudo-spin operators (τ) [79] result in a magnetization field derived from x and z terms which generate gapped magnetic fluctuations and magnetic order, respectively. Each component contributes differently to the divergence-full and divergence-free components of the total magnetization such that the fluctuations of these fields are decoupled [84].

Regardless of the precise theoretical description, $Nd_2Zr_2O_7$ shows the coexistence of magnetic order – the antiferromagnetic (AFM) "all-in-all-out" (AIAO) state with reports of T_{AFM} from 285 to 400 mK [85, 86, 87, 2, 88] – and a fluctuating Coulomb phase [83, 89]. In neutron scattering measurements, these states manifest as simultaneous magnetic Bragg peaks and an inelastic, diffuse "pinch-point" scattering pattern, respectively [84, 82, 83, 2, 90]. The availability of large, single-crystal samples of $Nd_2Zr_2O_7$ grown by the floating-zone (FZ) technique [34] has been instrumental to experimental investigations of

the proposed magnetically fragmented state and its related magnetic properties [83, 2, 89, 91, 1, 88, 92]. However, truly verifying and understanding this state requires careful investigation of crystal quality, especially considering the well-known susceptibility of the pyrochlore lattice to disorder [71, 93, 94].

In the case of $Nd_2Zr_2O_7$, deviation from unity of the Nd/Zr ratio is known to modify the cubic lattice parameter in polycrystalline samples [95]. Reported FZ-grown crystals show a marked variation in lattice parameter [91, 34] relative to the value for pristine polycrystalline samples, where the Nd/Zr ratio is well-controlled and likely very close to 1 [86, 34] (see Figure 5.1). FZ-grown crystals studied in the literature possess up to a $\approx 0.5\%$ smaller lattice parameter and often have substantially reduced AIAO ordering temperatures relative to powder data [83, 88, 34, 86, 85]. Disorder on the oxygen sublattice is also possible, where, for instance, local disorder related to the high-temperature defect-fluorite structure is known to occur [96, 97]. A visual summary of a number of key defect modes is shown in Figure 5.2.

The presence of disorder can substantially renormalize interactions relative to theoretical considerations and support a complex local coexistence of states. For example, it has been suggested that intrinsic cation disorder in $YbMgGaO_4$ leads to the lack of observed magnetic order [13], while oxygen deficiency in $Y_2Ti_2O_7$ generates a paramagnetic response [64]. Furthermore, the FZ-growth process can lead to dramatic differences between powder and single-crystal samples, such as the extensive variation (even between different FZ-grown single-crystal samples) of the heat capacity signatures in $Yb_2Ti_2O_7$ [98, 99, 100]. As such, it is important to consider what sources of structural disorder are present in $Nd_2Zr_2O_7$ single crystals and how this disorder might be managed by modifying the FZ-growth conditions. The ability to modify the amount of disorder leads naturally to addressing how disorder affects the bulk magnetic properties, including the experimental signatures of magnetic moment fragmentation [101].

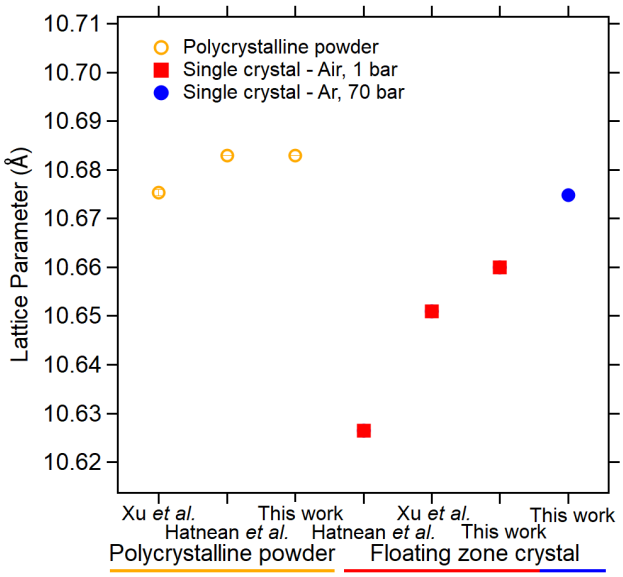

Figure 5.1: Comparison of lattice parameters for polycrystalline samples and single crystals from this work and the literature [86, 34, 91]. All lattice parameters were determined from laboratory XRD on powders at $T = 300$ K. The error bars are contained within the symbols and represent one standard deviation

We leverage the high-temperature/high-pressure (HP) capabilities of the laser-based FZ (Chapter 3) to produce samples with lattice parameters approaching those of pristine polycrystalline samples. Using a series of polycrystalline samples, we confirm the correlation between the Nd/Zr ratio and the lattice parameter and examine the effect on magnetic properties. Electron probe microanalysis (EPMA) provides direct confirmation that samples grown in atmospheric conditions (1 bar, air) with a reduced lattice parameter have Nd/Zr < 1, while those grown in HP Ar (70 bar) are nearly stoichiometric. A detailed structural investigation of powdered single-crystals studied via synchrotron X-ray and neutron diffraction clarifies that this stoichiometry imbalance is accommodated by Zr occupying vacancies on the Nd sublattice. Synchrotron diffraction data also reveal a distribution of lattice parameters within FZ-grown crystals: growth in air skews the distribution towards a smaller average lattice parameter while growth in HP Ar favors a larger average lattice parameter. Although the oxygen sublattices are close to disorder

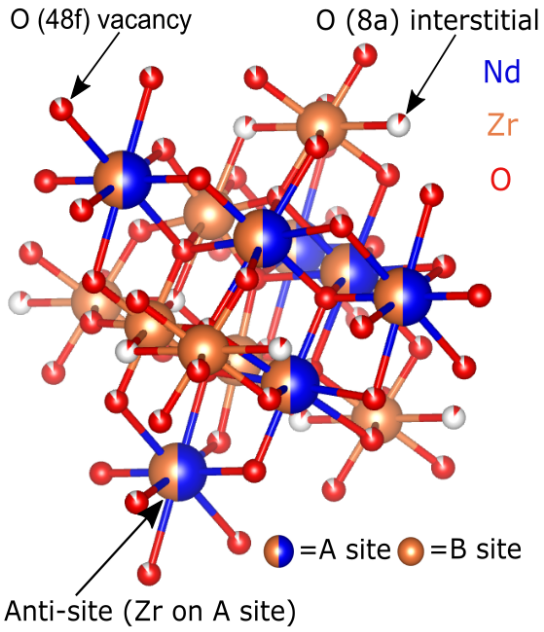

Figure 5.2: Illustration of some of the key defect modes for $Nd_2Zr_2O_7$ considered in this work.

free on the scale of the average structure ($< 2\%$ vacancies), pair-distribution function (PDF) analysis of the neutron data indicates 8 – 11 mass % of a highly local disorder of the oxygen-coordination across all samples. Crucially, we present magnetization, heat capacity, and neutron scattering measurements showing that the magnetic properties of HP Ar-grown crystals match closely with that of stoichiometric polycrystalline powders. Neutron scattering measurements on nearly stoichiometric crystals confirm the continued coexistence of AIAO magnetic Bragg peaks and a diffuse pinch-point scattering pattern, with the latter signal persisting nearly unchanged at higher temperatures than previously reported [83, 102]. These results suggest that the stability of both the AIAO magnetic order and the spin-ice correlations are linked to Nd stoichiometry.

5.2 Methods

Polycrystalline samples of $Nd_{2(1-x)}Zr_{2(1+x)}O_7$ (x = 0.2, 0.05, 0 and -0.1) were synthesized using solid state methods. Stoichiometric amounts of dried (900 °C, 12 hours) Nd_2O_3 (Afla Aesar, 99.99%) and ZrO_2 (Alfa Aesar, 99.98%) were ground together in an agate mortar and pestle and pressed into pellets at 310 MPa in a cold isostatic press. The pellets were then reacted in air in Al_2O_3 crucibles for 60 hours each at 1300, 1375 and 1450 °C with re-grinding and re-pressing between reactions. Platinum was always placed between the sample and Al_2O_3 crucible to prevent possible reaction at high temperatures. Powder X-ray diffraction (XRD) was employed to evaluate the final product. In preparation for crystal growth, the $x = 0$ powder was packed into clean rubber balloons and pressed into rods (diameter $\approx$ 4 mm, length $\approx$ 80 – 100 mm) at 310 MPa in a cold isostatic press. The rods were sintered at 1450 °C for 24 – 48 hours, in air, on sacrificial beds of $x = 0$ powder. Single crystals were then grown as described in Chapter 3.4

The composition of crystals was analyzed using an EPMA (Cameca SX-100, Gennevilliers, France) equipped with wavelength-dispersive spectroscopy. Sample disks – thin cross sections of the as-grown, cylindrical crystal boule cut perpendicular to the growth direction – were polished with colloidal diamond to a 0.25 μm finish. The mounts were carbon coated to negate electron beam charging. A 20 kV and 20 nA beam was used for the measurements, which was defocused to 2 μm to prevent sample damage. Multiple "spot" measurements were used to determine the composition at various points within a small (100×100 μm^2), region at the center of the sample disk. Line scans along the diameter of the sample disk (from edge to edge) were used to assess any compositional variance along the boule diameter. The Zr and Nd concentration measurements were standardized using a synthetic zircon ($ZrSiO_4$) standard and Nd-glass standard, respectively. In the calculation of the average formula the O was assumed to be fully

stoichiometric (*i.e.* $Nd_xZr_yO_7$). We emphasize that, due to the use of standards, the EPMA data provide an independent measurement of the Nd and Zr concentrations and the resulting formula need not show $x + y = 4$ to match the ideal formula.

Structural characterization was undertaken using synchrotron XRD and time-of-flight (TOF) neutron diffraction on powdered crystal boules. The synchrotron XRD measurements were performed at the 11-BM beamline of the Advanced Photon Source (APS) at $T = 100$ K. To minimize absorption effects, the powder was diluted with SiO_2 at a ratio of 1:7 (molar), yielding $\mu R \approx 0.6$, before being loaded into 0.8 mm diameter Kapton tubes. TOF neutron powder diffraction data were collected using the POWGEN diffractometer at Oak Ridge National Laboratory, Spallation Neutron Source (SNS). The wavelength distribution of the incident beam was centered at 1.5 Å, with a minimum of 0.967 Å and maximum of 2.033 Å, providing a Q range of ≈ 0.43 – 12.94 Å^{-1}. The powder (2.5 – 3 g of ground FZ crystal) was sealed in 6 mm diameter V cans and measured at $T =$ 100 K. The POWGEN data was reduced for pair-distribution function (PDF) analysis using Mantid [103]. Analysis of the total scattering data was then performed using the PDFgui software suite over various increments of a total r-range of 1.5 – 41.5 Å [104].

Bulk magnetic properties were measured on $\approx$ 10 mg of powder (both polycrystalline powders and ground crystals) mounted in polypropylene capsules using a MPMS3 Quantum Design SQUID magnetometer. Well-ground crystals were used to eliminate any effects of crystalline anisotropy and for comparison to the nominally stoichiometric polycrystalline sample. High-field *M(H)* measurements were carried out using a vibrating sample magnetometer (VSM) mounted on a Quantum Design DynaCool Physical Properties Measurement System (PPMS) equipped with a 14 T magnet. We only make comparisons to the literature between data sets collected using the same measurement technique (SQUID or VSM). Measurements of the low temperature specific heat (C_P) were carried out using a Quantum Design Dynacool PPMS equipped with a dilution

refrigerator insert. The samples used for the measurement were taken from the center of the crystal boules with masses < 0.5 mg. Apiezon N-grease was used to provide thermal contact.

Single-crystal neutron diffraction was performed using the instrument CORELLI at the SNS. An intial survey of samples grown under different environments was performed at the NIST Center for Neutron Research using the cold neutron triple-axis diffractometer SPINS in order to inform the CORELLI experiment. The sample consisted of a piece extracted from the crystal boule with length ≈ 2.5 cm and mass ≈ 1.3 g. Copper foil was used to attach the crystal to an oxygen-free copper mount to ensure adequate thermalization; in the CORELLI experiment a Cd mask was used to reduce scattering from the mount and N-grease was also placed at the interface between the crystal and the mount. The crystal was then mounted in a liquid helium cryostat with a dilution insert, providing a base temperature of ≈ 38 mK. Data across a large area of reciprocal space were collected at $T = 38$, 500, and 800 mK by rotating the crystal around the $[1\bar{1}0]$ direction (ψ rotation) in 1° steps with a count time of ≈ 3 minutes/step. A magnetic order parameter on the (220) reflection was collected by fixing ψ such that the peak could be measured. The CORELLI data was reduced using Mantid [105]. Confidence intervals for all error bars and uncertainties represent plus and minus one standard deviation.

5.3 Results

5.3.1 Structural Properties Characterization

To provide a baseline in understanding how the Nd/Zr ratio impacts the properties of $Nd_{2(1-x)}Zr_{2(1+x)}O_7$, a series of polycrystalline samples ("standards") were first prepared. The lattice parameter for the Nd-deficient ($x > 0$) samples decreases linearly with de-

creasing Nd/Zr relative to the $x = 0$ samples (Figure 5.3). For the Nd-enriched sample ($x < 0$), the lattice parameter deviates from the linear trend, likely reflecting the fact that it was biphasic, with ≈ 5 mass % Nd_2O_3. However, it is still clearly enhanced relative to the stoichiometric sample. Due to the lower processing temperature, the Nd/Zr ratios are assumed as the nominal values of the polycrystalline samples and these values were fixed during the refinement of the powder data used to determine the lattice parameters. The results are consistent with those of a previous study on $Nd_{2(1-x)}Zr_{2(1+x)}O_7$ powders [95].

A comparison can then be performed between the composition and structure of single crystals grown in a variety of environments. The lattice parameters of single crystals (all based on laboratory XRD) reported in the literature and in this work are summarized in Figure 5.1, with polycrystalline values plotted for comparison. Reported values for low-pressure, air-grown samples vary considerably, ranging from 10.627 [1] to 10.662 Å (this work), but are in all cases reduced compared to the polycrystalline samples ($\approx$ 10.68 Å). In contrast, samples grown in 70 bar of Ar show an elevated lattice parameter (10.675 Å) which approaches that of the polycrystalline samples.

Nd and Zr stoichiometries for two single-crystals (air and HP-Ar), determined by the EPMA measurements, are shown in Figure 5.4. Spot measurements, taken in a small, central area of the boule, show a consistent difference in stoichiometry between the two samples. The air-grown sample has Nd/Zr = .918 (average formula = $Nd_{1.90}Zr_{2.07}O_7$) while the HP Ar-grown sample has Nd/Zr = .985 (average formula = $Nd_{1.98}Zr_{2.01}O_7$). In contrast, line scans, taken across a larger extent of the sample, show an increased range of values relative to the spot measurements. The spread of the Nd and Zr stoichiometric coefficients is roughly 0.15 for the air-grown sample and 0.10 for the HP-Ar sample. However, the average stoichiometry of the line scans mirrors the behavior seen in the spot measurements: the air-grown sample has Nd/Zr < 1 while the HP-Ar sample has,

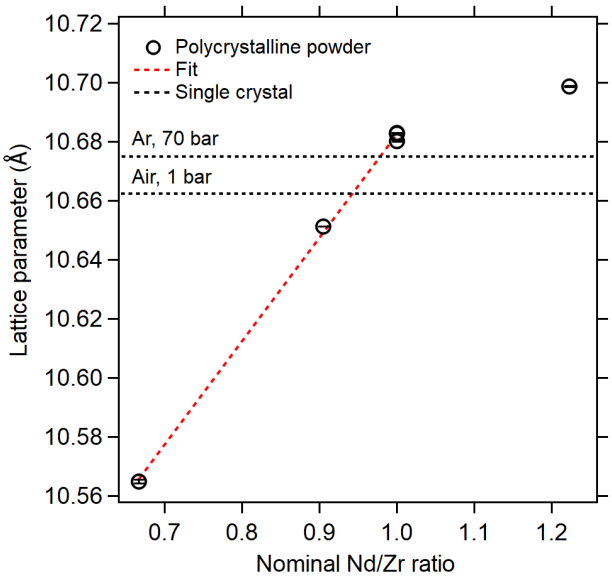

Figure 5.3: Refined room temperature lattice parameters from laboratory XRD versus nominal Nd/Zr ratio for polycrystalline samples of $Nd_{2(1-x)}Zr_{2(1+x)}O_7$ with x = 0.2, 0.05, 0, and -0.1. The error bars are contained within the symbols and represent one standard deviation. The Nd-enriched polycrystalline sample is biphasic (Nd_2O_3 + "$Nd_{2.2}Zr_{1.8}O_7$") as is expected from the change in slope. The dashed red line is a linear fit to the phase pure samples while the dashed black lines indicate the lattice parameters found by laboratory XRD for single crystal samples grown in this work.

on average, Nd/Zr closer to 1.

The synchrotron X-ray and TOF neutron powder diffraction data for the HP-Ar and air-grown samples were analyzed with a simultaneous Rietveld refinement to provide deeper insight into structural disorder on both the cation (Nd, Zr) and anion (O) sites. The refined patterns resulting from the structural model described below are shown in Figure 5.5, with the results for the refined parameters summarized in Table 5.1. For both samples, all peaks could be matched to the pyrochlore structure ($Fd\bar{3}m$, space group number 227). In this structure the Nd and Zr cations each occupy a distinct, high-symmetry, site forming separate corner-sharing sublattices of Nd and Zr tetrahedra. The O anion occupies two sites, referred to here as O1 (Wyckoff position 48f) and O2 (Wyckoff position 8b). The pyrochlore unit cell is predominately constrained by symmetry and

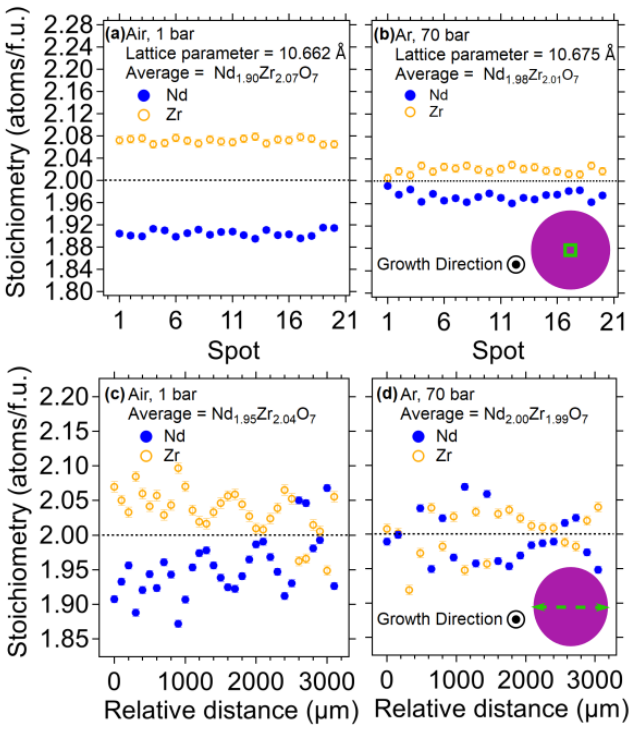

Figure 5.4: EPMA data on sample disks of the FZ crystals cut perpendicular to the growth direction. Error bars represent the statistical error reported from the measurement software. The top panels show results for a number of "spot" measurements taken at different points within a small central region of the sample disk for the **(a)** air and **(b)** HP-Ar samples. The measurement region is represented by the green square (not to scale) in the inset of **(b)**. The bottom panels show results from line scans for the **(c)** air and **(d)** HP-Ar samples. The direction of the scan is shown by the green arrow in the inset of **(d)**. The distance is measured relative to one edge of the sample disk, extending across the diameter of the slice.

provides only u, the x-coordinate of the O1-site and the lattice parameter (a) as free parameters.

Establishing a structural model for the co-refinement was complicated by the observation of a split-peak structure in the higher momentum resolution X-ray data, but not the neutron data, of both samples. To model this feature, the data were refined using two pyrochlore phases with different lattice parameters – a similar approach has been taken with other site-mixed pyrochlores *e.g.* $Ho_{2(1+x)}Ti_{2(1-x)}O_7$ [106]. We note here that comparable high-resolution X-ray data for the HP-80:20 sample were also collected and were

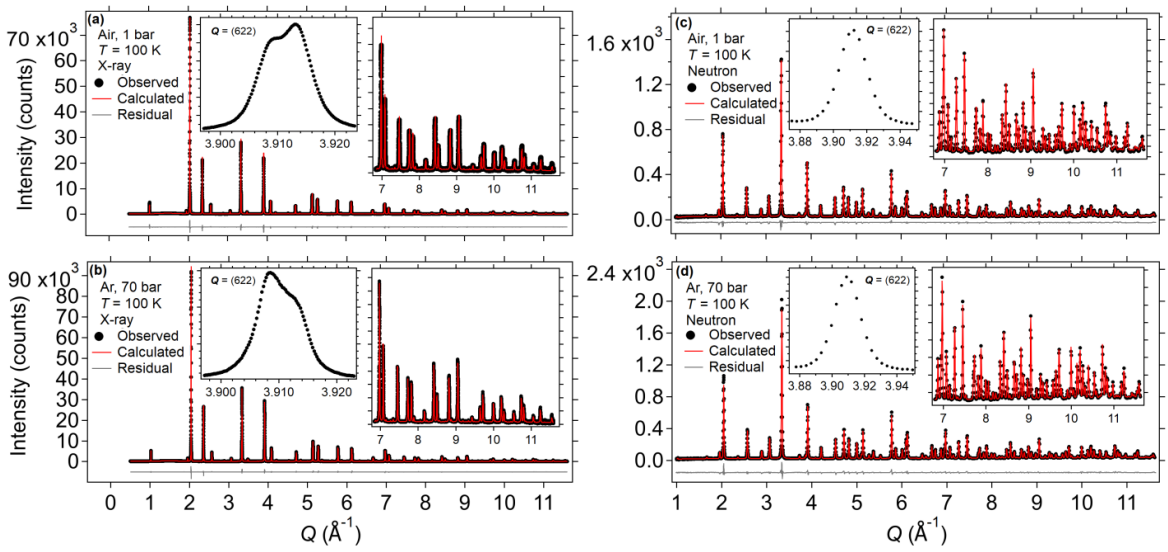

Figure 5.5: Rietveld refinement of synchrotron XRD data collected from powdered FZ-boules grown under **(a)** air and **(b)** HP-Ar. Refinement of TOF neutron diffraction data for powders of the same boules, **(c)** air and **(d)** HP-Ar. The left inset shows a close view of the (622) peak, illustrating the the variable peak shapes observed in the XRD data, but not the TOF neutron data. The right inset shows a closer view of the fit to the high-Q data.

not well fit by two pyrochlore phases, requiring the addition of further pyrochlore phases to improve the fit. In the interest of establishing a parsimonious and consistent structural model for the co-refinement we restrict our comparison to the air and HP-Ar-grown samples.

Since the TOF neutron data show only one peak, due to the coarser resolution, the lattice parameters were wholly determined by the X-ray data and fed into the calculated pattern for the neutron data. A somewhat analogous approach was taken with respect to the calculated phase fractions of each pyrochlore phase. The X-ray scale factors for the two phases (S_{X1} and S_{X2}) were refined independently while only one neutron scale factor (S_{N1}, corresponding to the majority phase, as determined by the X-ray data) was refined. The other neutron scale factor (S_{N2}) was then calculated as $S_{N2} = (S_{X2} \,/\, S_{X1}) \times S_{N1}$ to ensure the same phase fractions as determined in the X-ray data. Other values, including

the site occupancies, anisotropic displacement parameters (ADPs), and u (O1 x-position) were refined globally (*i.e.* against both patterns). Based on the EPMA data, the Nd A-site occupancy was fixed to the average value of the spot measurements (Figure 5.4) while the Zr B-site occupancy was fixed to 1. Occupation of the A-site by Zr was then allowed later in the analysis, constrained by a maximum total occupancy of 1. Refinement of the O1 and O2 site occupancies showed the O2 site to be fully occupied while the O1 site has a small number of vacancies (<2 %), consistent with the general trend in pyrochlores of oxygen vacancies occurring preferentially on the $48f$-site [96, 107, 94]. The two pyrochlore phases were constrained to have the same set of ADPs and the same value of u.

To gain insight into r-dependent behavior (*i.e.* local disorder that does not appear in the average structure) PDF spectra were refined using a "box-car" scheme. Fits to the $G(r)$ data were performed within a set r-range (r_{min} – r_{max} = 5 Å) at various length scales (e.g. 0 – 5 Å, 5 – 10 Å). Refinement using the ideal pyrochlore structure results in relatively flat difference curves and reasonable fit qualities ($R_W \approx 10\%$) for most of the r-range (not shown). However, a notable decrease in fit quality was found for all samples within the $r = 1.5 - 6.5$ Å range ($R_W \approx 13 - 16\%$), driven mainly by a poor fit to the peak at r = 2.6 Å. Calculation of site-specific partial PDF contributions reveal this peak to be composed of both Nd – O and O – O correlations, with the O – O correlations being purely due to correlations between O1 sites. Refining the O1 site occupation showed a minor reduction in O1 occupancy (< 3%) with only marginal improvement to R_W. However, inclusion of a secondary defect fluorite phase for the fit in the r = 1.5 – 5 Å range resulted in a decrease in R_W and an observable improvement in the fit of the peak at 2.6 Å (Figure 5.6). Refinement of the amount of the defect fluorite structure shows the highest phase fraction (mass %) for the air-grown sample (11.2 ± 0.22 %), the lowest for the HP-Ar sample (8.2 ± 0.18 %) and an intermediate amount (8.8 ± 0.18 %) for the HP-80:20 sample. Inclusion of this phase in the highest r-range (36.5 – 41.5

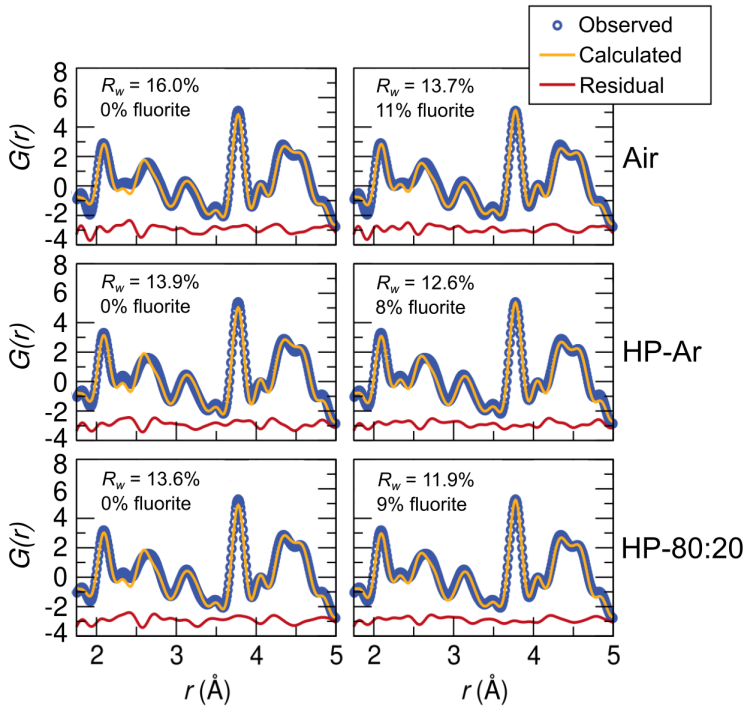

Figure 5.6: Fits to the neutron PDF spectra in the r = 1.5 – 5 Å range for the air (top), HP-Ar (middle) and HP-80:20 (bottom) samples. Defect fluorite phase fraction is quoted in mass %.

Å) produced only a marginal improvement to the fit (change in R_W of < 1 percentage point). An increase in the amount of defect fluorite is also accompanied by additional positional disorder on the O1 site, indicated by an increase in the isotropic displacement parameter. The implications of this model are further addressed in Section 5.4.

5.3.2 Magnetic Properties Characterization

Characterization of the bulk magnetic properties of the HP-Ar crystal and $x = 0$ powder are shown in Figure 5.7. The two samples show nearly identical $\chi(T)$ data. A Curie-Weiss analysis was performed by first fitting $\chi(T)$ to the equation $\chi_{VV} + C\,/\,(T - \Theta_{CW})$, with χ_{VV} capturing the temperature-independent contribution of the Van Vleck paramagnetism. $\chi(T) - \chi_{VV}$ was then fit to $C\,/\,(T - \Theta_{CW})$ in the range $10 \leq T \leq 30$ K

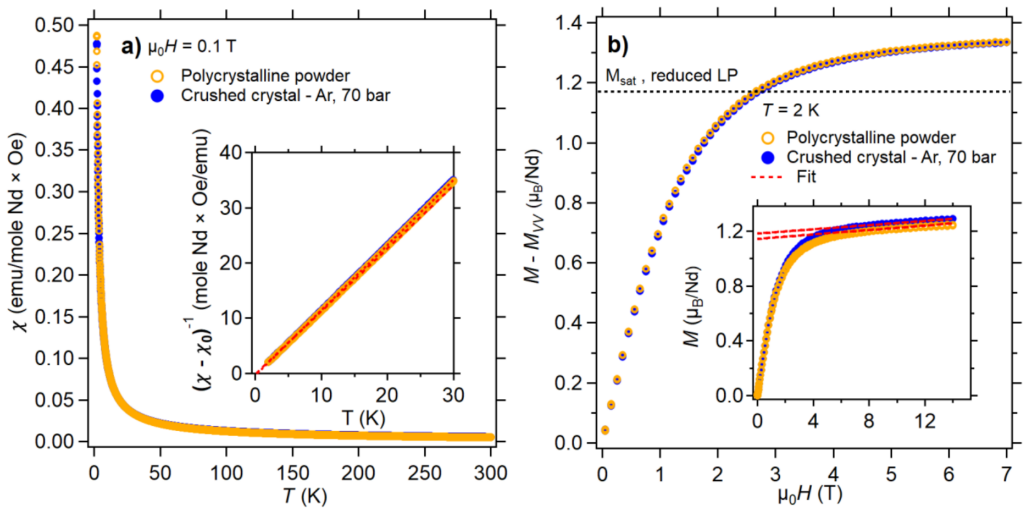

Figure 5.7: **(a)** Magnetic susceptibility (1 emu = 10^{-3}A m^2) for powder of the HP Ar-grown crystal and the $x = 0$ polycrystalline powder taken at $\mu_0 H = .1$ T (1 T = 10,000 Oe). The inset shows the inverse susceptibility for the same; the dashed red lines are the Curie-Weiss fits. **(b)** Magnetization verus field data for powder of the HP Ar-grown sample and the polycrystalline sample. The Van Vleck contribution has been subtracted. The dashed black line is the expected powder saturation value for a previously reported reduced lattice parameter (LP) single-crystal sample [1]. The inset shows magnetization data out to $\mu_0 H = 14$ T prior to subtraction of the Van Vleck contribution. The dashed red line is the linear fit from 8 – 14 T, which has been extended to low-field.

to avoid the influence of short-range magnetic correlations and crystal field effects [86]. This gave $\Theta_{CW} = 0.309(5)$ K and $\mu_{eff} = 2.60(2)$ μ_B/Nd for the HP-Ar crystal and $\Theta_{CW} = 0.386(4)$ K, $\mu_{eff} = 2.61(3)$ μ_B/Nd for the powder.

Isothermal $M(\mu_0 H)$ data at 2 K for the powder standards are plotted in Figure 5.8. The Van Vleck contribution of the Nd^{3+} ion has been subtracted using the slope of a linear fit made in the range 8 – 14 T, beyond the field values where the Nd moments saturate. The resulting saturation magnetization, M_{sat}, is lower for the Nd-deficient samples, relative to the $x = 0$ sample, and higher for the Nd-enriched sample. Curie-Weiss analysis (not shown) indicates that μ_{eff} is also decreased for Nd-deficient samples. The data for the HP-Ar crystal and $x = 0$ powder are shown together in the main panel of Figure 5.7**b**. The two are, again, very similar and both yield a $M_{sat}(\mu_0 H =$

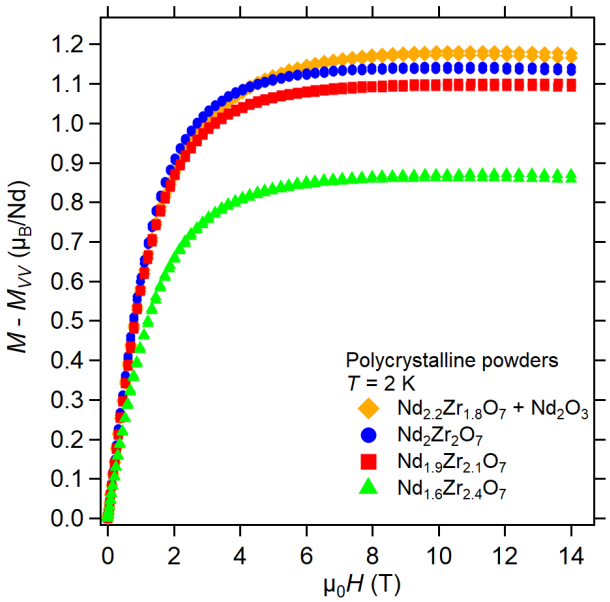

Figure 5.8: Magnetization versus field (VSM) measurements to $\mu_0 H$ = 14 T at T = 2 K on polycrystalline $Nd_{2(1-x)}Zr_{2(1+x)}O_7$ samples. The Van Vleck contribution (M_{VV}) has been subtracted.

7 T) = 1.33 μ_B/Nd. For further comparison, a value for $M_{sat}(\mu_0 H$ = 5 T) = 1.27 μ_B/Nd has been reported previously for polycrystalline $Nd_2Zr_2O_7$ [86], which agrees reasonably well with our data at the same field value. The black, dashed line is the approximate, powder-averaged, $M_{sat}(\mu_0 H$ = 7 T) for an air-grown single-crystal sample with a particularly low lattice parameter (10.627 Å) [1]. This estimate is calculated based on the reported values of $M_{sat}(\mu_0 H$ = 7 T) along the [111], [110] and [100] directions: $M_{sat} = (6M_{[100]} + 12M_{[110]} + 8M_{[111]})\,/\,26$ = 1.19 μ_B/Nd. The same calculation for a different single crystal sample grown in air (lattice parameter = 10.651 Å) also shows a value less than that of the HP-Ar crystal [2].

Extending comparisons of magnetic properties to lower temperature and into the ordered state, low-temperature $C_P(T)$ data were collected for air, HP-Ar and HP-80:20 samples (Figure 5.9). T_{AFM}, the onset of long-range magnetic order, is identified as the peak in $C_P(T)$, and the data across the series of crystals show that T_{AFM} is lowest for the

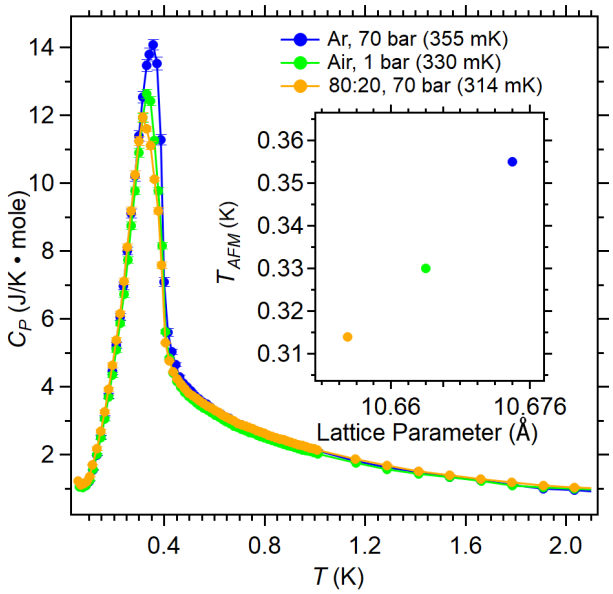

Figure 5.9: Low-temperature $C_P(T)$ data on the air, HP-Ar, and HP-80:20 samples. The inset shows T_{AFM} (taken as the peak of the $C_P(T)$ curve) versus lattice parameter from laboratory XRD.

crystal grown under HP-80:20 (314 mK) and highest for the sample grown under HP-Ar (355 mK). Compared to the air-grown crystal, the magnetic entropy associated with the phase transition (ΔS, integrated up to 2 K) is increased by $\approx 6\%$ for the HP-Ar crystal. This reflects the increase in the ordered moment due to the reduction in off-stoichiometry.

Further characterization of the magnetic order within the HP-Ar sample was accomplished by a single-crystal neutron scattering measurement at CORELLI. The integrated intensities of the (220) reflection are plotted in Figure 5.10**a**. The integrated intensity increases markedly below $T = 365$ mK. Full ψ-scans, covering a much larger area of the (hhl) scattering plane, also show a clear increase in intensity of the (113) reflections between $T = 500$ mK and 38 mK. Diffuse scattering in the (hhl) plane at $T = 38$ mK is shown in Figure 5.10**b** with a high-temperature data set ($T = 10$ K) subtracted. The data have been reduced using the cross-correlation analysis associated with the statistical chopper in place at CORELLI [60]. While the diffuse scattering is naively not polluted

by thermal diffuse scattering, the energy of the gapped pinch-point mode near 50 μeV [83, 2] is still integrated over in the finite energy window of the cross-correlation analysis. The pattern is qualitatively very similar to previous reports, showing pinch-point scattering characteristic of the spin-ice correlations within the fluctuating Coulomb phase [83, 2, 89].

To quantify the evolution of the pinch-point pattern with temperature, the diffuse scattering was integrated in a limited rectangular region containing the arm of diffuse scattering along the (hhh) direction; the result is shown in Figure 5.10**a**. Separate from this pinch-point scattering, a second region of relatively isotropic, diffuse signal was also observed at $T = 500$ mK (above T_{AFM}) around the (220) and (113) reflections (Figure 5.10**c**). Further above T_{AFM} ($T = 800$ mK), this diffuse signal broadens considerably and begins to bleed into the persistent pinch-point pattern. The two diffuse scattering signals above T_{AFM} suggest separate regimes of short-range magnetic correlations associated with the AIAO and spin-ice order parameters, which we discuss in the next section.

5.4 Discussion

The significant range of reported lattice parameters for FZ-grown $Nd_2Zr_2O_7$ single crystals (Figure 5.1) is an indicator of variable, synthesis-dependent, disorder. Characterization of $Nd_{2(1-x)}Zr_{2(1+x)}O_7$ polycrystalline samples, which have more well-controlled stoichiometries than the FZ-grown samples, provides a benchmark if this disorder occurs on the Nd and Zr sublattices. Considering the results from these samples, varying cation stoichiometry is the most likely explanation for the range of reported lattice parameters of FZ-grown samples. The melting point of $Nd_2Zr_2O_7$ ($\approx$ 2300 – 2350 °C [108]) requires a high molten zone temperature leading to significant oxide vapor pressure during FZ-growth. Laboratory XRD on volatilized powder, collected following growth under

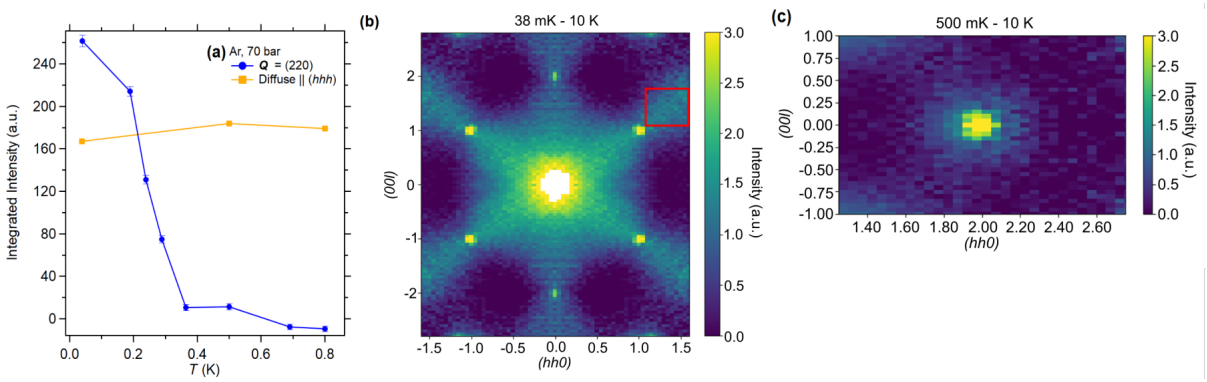

Figure 5.10: **(a)** Order parameters collected for a HP-Ar single-crystal. The blue markers show the evolution of the integrated intensity at the (220) reflection. The error bars are extracted from the uncertainty in the Gaussian fit parameters. The orange markers show the same for the diffuse scattering along the (*hhh*) direction (excluding Bragg peaks and scaled to be comparable) **(b)** Map of the static diffuse scattering in the (*hhl*) scattering plane at 38 mK. The red box indicates the integration area. A 10 K background scan has been subtracted. The concentrated intensity at the (111) is due to the imperfect removal of the nuclear Bragg scattering. **(c)** Map of of the diffuse scattering around the (220) at 500 mK. Both **(b)** and **(c)** have been averaged according to the symmetry of the lattice.

ambient conditions, showed it to be primarily Nd_2O_3. Therefore, this volatilization preferentially depletes the molten zone of Nd_2O_3, which leads to a decrease in Nd/Zr of the grown crystal and a reduced lattice parameter. Our EPMA data confirms this picture, directly linking the reduced lattice parameter to Nd/Zr < 1. In comparison, application of high-pressure Ar clearly helps to mitigate Nd_2O_3 volatility, resulting in a crystal with a larger lattice parameter which the EPMA data show to have a Nd/Zr ratio close to 1.

As a further check, the Nd/Zr ratios calculated using the fit to lattice parameters of polycrystalline standards (Figure 5.3) is found to compare well to the value extracted from EPMA data. The fit gives a Nd/Zr ratio of 0.94 for the air-grown sample and 0.98 for the HP-Ar sample while the EPMA average shows 0.92 and 0.99, respectively. For comparison, the fit implies Nd/Zr ratios of 0.84 and 0.91 for previously reported air-grown crystals with lattice parameters of 10.627 Å [83, 1] and 10.651 Å [2, 91], respectively. We note that these previously reported values may be anomalously low due to variance in

the Nd/Zr stoichiometry across a crystal boule, particularly if only a small portion of the crystals were analyzed. It is possible that the average lattice parameters are closer to the value of 10.662 Å observed in our air grown crystal.

Sample	Ar, 70 bar				Air, 1 bar			
T (K)	100				100			
a_H (Å)	10.66501(1)				10.66432(1)			
W_H(%)	63.7				41.2			
a_L (Å)	10.65254(1)				10.65069(1)			
W_L (%)	36.3				58.8			
u (O1)	0.33542(2)				0.33542(2)			
A-site occ.	Nd = 0.99 Zr = 0.010(1)				Nd = 0.95 Zr = 0.050(1)			
B-site occ.	Zr = 1				Zr = 1			
O1-site occ.	0.997(1)				0.980(1)			
O2-site occ.	1.000(2)				0.999(2)			
ADP $\times 10^{-3}$ (Å^2)	U_{11}	$U_{22} = U_{33}$	$U_{12} = U_{13}$	U_{23}	U_{11}	$U_{22} = U_{33}$	$U_{12} = U_{13}$	U_{23}
A-site	3.97(2)	3.97(2)	-0.98(4)	-0.98(4)	5.61(2)	5.61(2)	-1.13(5)	-1.13(5)
B-site	4.45(3)	4.45(3)	0.60(5)	0.60(5)	4.83(2)	4.83(2)	0.72(5)	0.72(5)
O1-site	9.60(6)	6.10(5)	0	0.63(7)	10.37(7)	6.80(4)	0	0.63(7)
O2-site	5.29(8)	5.29(8)	0	0	6.13(7)	6.13(7)	0	0
	Goodness-of-fit parameters				Goodness-of-fit parameters			
	Neutron	X-ray	Overall		Neutron	X-ray	Overall	
R_{WP}	5.44	6.84	6.15		4.71	7.91	6.39	
χ^2	4.31	1.31	1.66		3.80	1.50	1.72	

Table 5.1: Results from the simultaneous Rietveld refinement of the synchrotron X-ray and TOF neutron diffraction data for the HP-Ar and air-grown samples. Numbers in parenthesis represent plus and minus one standard deviation as reported from the refinement software. The data, by row, are as follows: T = measurement temperature, $a_{H/L}$ = lattice parameters of the pyrochlore phases (L = low lattice parameter phase, H = high lattice parameter phase), $W_{H/L}$ = phase fraction (mass %) of the pyrochlore phases, u = x-position of the O1 ($48f$) oxygen site (both phases), occupancy values for the different crystallographic sites, ADP = anisotropic atomic displacement parameters, U_{ij} (both phases) for each site, R_{WP} and χ^2 = goodness of fit parameters for the individual patterns and overall refinement.

The X-ray/neutron co-refinement results (Table 5.1) provide clarification about the nature of this cation site disorder. When Zr is allowed to refine on the A-site, the refined value in both samples reached the maximum value of 1 minus the fixed Nd occupancy. In the EPMA data, we see that Zr-enrichment occurs in tandem with the Nd-deficiency:

the corefinement shows that this Zr excess is accommodated by occupation of the depleted Nd sublattice by Zr. We note that in the pyrochlore literature the reverse of this defect (occupation of the B-site by the A-site ion) is referred to as "stuffing" and has been studied extensively (see, for example, [106, 99, 100]). The situation here, termed "negative" stuffing, has been the subject of considerably fewer studies [109, 110, 111].

The results from the two lattice parameter model are also consistent with the relationship between Nd/Zr ratio and lattice parameter derived from laboratory XRD. The HP-Ar sample, where EPMA indicates Nd/Zr close to 1, favors the high lattice parameter phase ($a_H = 10.665$ Å, $W_H = 64$ mass %) while the air-grown sample, where EPMA indicates Nd/Zr < 1, favors the low lattice parameter phase ($a_L = 10.651$ Å, $W_L = 59$ mass %). The increased variation seen across the larger length scales of the EPMA line scans (Figure 5.4**c**,**d**) suggests that, across a boule, there exists a continuous distribution of lattice parameters, rather than just two, which maps to the local Nd/Zr ratio. This likely explains why the observed set of lattice parameters is not the same between the two samples. The shift in the refined lattice parameters and weight fractions represents a change in the *average* value of a continous lattice parameter distribution. This, in turn, reflects the change in the average stoichiometry. A higher level of disorder in the air-grown sample is also indicated by the higher ADP values for all sites. The A-site shows a particularly large increase ($\approx 43\%$), consistent with the increased amount of Zr occupation.

The neutron PDF data allows us to examine the possibility of disorder within the local structure of $Nd_{2(1-x)}Zr_{2(1+x)}O_7$ crystals, which can be distinct from the disorder found by probing the average structure. Indeed, the poor fit to the peak in *G(r)* at $r =$ 2.6 Å when refining against the ideal pyrochlore structure suggests the need for a local structural model that goes beyond the variable position of the O1-site. The existence of a high-temperature disordered phase – the "defect fluorite" structure (space group

number 225, $Fm\bar{3}m$) – is well known in the pyrochlore zirconates [108, 72, 112, 96]. This provides a likely explanation for the observed local disorder since the anion sublattice of the defect fluorite structure is related to that of the pyrochlore structure by a disordering of the two distinct oxygen positions ($8b$ and $48f$), collapsing them to a single position ($8c$).

The inclusion of the defect fluorite phase only significantly affects R_W in the $r = 1.5$ – 5 Å range, indicating that the fluorite "phase" is a very local disorder effect, which is best described as follows: the local environment of the Nd and Zr cations resembles a mix of pyrochlore and fluorite-type oxygen coordination (though mostly dominated by the pyrochlore-type), while the coordination of the average, crystallographic structure is that of the ideal pyrochlore. This is represented in Figure 5.2 as occupation of the oxygen $8a$ interstitial which coordinates with the Zr (B) site. The change in the geometry of oxygen coordination (which forms a perfect cube for both sublattices in the fluorite case) is not illustrated. Based on the existing evidence for local disorder in polycrystalline samples [97, 96], this defect fluorite character is most likely endemic to all FZ-grown samples, regardless of growth parameters.

Having demonstrated the relationship between lattice parameter, Nd/Zr ratio, and growth pressure, we now turn to the impacts of defect modes on the magnetic properties. Considering the $\chi(T)$ data for the HP-Ar grown sample, the qualitative aspects of the Curie-Weiss analysis are unaffected by the decrease in disorder, relative to air-grown samples [86, 91, 1]. The Θ_{CW} remains small and positive, suggesting that the balance between the FM dipolar interactions and AFM superexchange interactions is not greatly modified. Furthermore, the effective moment in this sample ($\mu_{eff} = 2.60\ \mu_B$/Nd) remains reduced relative to the expected free-ion value for Nd^{3+} moments ($3.62\ \mu_B$/Nd). However, this μ_{eff} value is $\approx 5\%$ larger than that of a previous report which used the same Curie-Weiss procedure for an air-grown sample [2]. As indicated in Figure 5.7, M_{sat} for the

HP-Ar sample is also enhanced relative to air-grown samples [1, 2]. These results are all consistent with an increase in the amount of magnetic Nd^{3+} present in crystals grown under a high-pressure Ar environment.

The low-temperature $C_P(T)$ data also evince changes in the magnetism. Within our set of samples, the $C_P(T)$ data show T_{AFM} increases in tandem with the average lattice parameter (Figure 5.9, inset), reaching 355 mK for the HP-Ar sample. The measurement of T_{AFM} by single crystal neutron scattering (Figure 5.10**a**) – which probes a much larger sample volume than the $C_P(T)$ data – shows that the intensity on the (220) reflection increases below 365 mK, consistent with the $C_P(T)$ data given the lower density of temperatures sampled. These values remain slightly reduced relative to powder samples (T_{AFM} = 370 – 390 mK [86, 85]), which can likely be attributed to the distribution of Nd/Zr ratios present in the sample. In comparison, previously reported, air-grown crystals also yield reduced T_{AFM} values of 285 mK [88] and 310 mK [87]. These results show that the onset of long-range magnetic order is sensitive to the amount of structural disorder, which primarily manifests as a variation in the extent of negative stuffing. In contrast, the local disorder detected in the neutron PDF data does not appear to be a major factor in reducing T_{AFM}, as the fraction of defect fluorite coordination is comparable for the HP-Ar and the HP-80:20 samples.

Low defect concentrations can have outsized effects on the magnetism of frustrated systems because the ground state selection is often determined by a finely tuned balance of different interactions. $Yb_2Ti_2O_7$ provides a particularly striking example, where varying levels of disorder, consisting of O vacancies and/or ("positive") stuffing, was determined to be responsible for the variety of observed ground states [99, 100]. In the present case, there is no signature of scattering intensities being redistributed away from the expected wave vectors of AIAO order, and the AIAO state in $Nd_2Zr_2O_7$ appears robust across an appreciable range of disorder/defect densities.

Instead, more quantitative modifications to the ordered state, such as the increased T_{AFM} in the HP-Ar sample, can be well understood by a reduction in the amount of negative stuffing. The presence of non-magnetic Zr^{4+} on the A-site breaks up the Nd^{3+} superexchange network, which weakens the overall exchange interaction. This can be contrasted with disorder in $Yb_2Ti_2O_7$ where stuffing occurs via Yb^{3+} occupying the B-site [99, 100, 106]. In that case, stuffing provides an avenue for new magnetic exchange pathways and can qualitatively modify spin correlations, even at low defect densities [99, 100]. That this does not happen in the case of $Nd_2Zr_2O_7$ is rationalized by the different type of stuffing.

We turn now to the diffuse scattering at $T = 38$ mK (*i.e.* $T < T_{AFM}$) observed for the HP-Ar crystal (Figure 5.10**b**). While the appearance of the pinch-point pattern is unaffected by the reduction in disorder, the temperature evolution appears modified relative to earlier studies on air-grown samples. Previous reports have shown that the intensity is comparable at low temperature (60 mK) and 450 mK, with a slight peak near T_{AFM} and a large reduction by 750 mK [83]. Estimation of the magnetic moment which produces the pinch-point pattern follows a qualitatively similar trend [102]. Although we do not have the data to comment on the peak at T_{AFM}, the pinch-point pattern in our sample persists nearly unchanged up to 800 mK (the highest temperature measured). This is shown by the integration presented in Figure 5.10**a**, where the values at 500 mK and 800 mK are almost identical. Direct comparison of the diffuse scattering heat maps (not shown) confirms this conclusion. Based on the fact that the pinch-point pattern intensity is substantially weakened by $\approx$ 750 mK in an air-grown sample [83] and remains robust at 800 mK in a HP-Ar sample with $\approx$ 1 % negative stuffing, the spin-ice correlations seem sensitive to this degree of disorder. A recent report suggests that a separate spin-ice-like state may exist above T_{AFM} [102] however our current data are unable to address this possibility.

The main temperature-induced change in the diffuse scattering above T_{AFM} in HP-Ar grown crystals lies in the region between the arms of the pinch-point pattern, where intensity coalesces around the (113) and (220)-type reflections as the temperature is lowered from 800 to 500 mK (Figure 5.10**c**). Two possible origins for this diffuse scattering present themselves: 1) The onset of short-range, AIAO correlations and/or 2) scattering by monopole creation or hopping [89]. We cannot directly address the latter possibility since evidence for monopole dynamics comes in the form of a gapped continuum of excitations and our measurement is energy-integrated. However, assuming the former possibility, our analysis indicates an AIAO correlation length of 55 $\pm$ 10 Å at 500 mK.

5.5 Conclusions

Using a combination of EPMA and X-ray/neutron scattering we have demonstrated that the reduced lattice parameter of air-grown $Nd_2Zr_2O_7$ single-crystals is due to negative stuffing (*i.e.* occupation of the A-site by Zr). This occurs during FZ-growth due to preferential evaporation of Nd_2O_3, which we find can be largely mitigated by a 70 bar Ar overpressure. Neutron total scatting measurements also demonstrate the occurrence of a highly local form of disorder on the oxygen sublattice, which is only somewhat reduced via high-pressure growth. The HP-Ar grown crystals possess an optimized Nd stoichiometry with a lattice parameter approaching the polycrystalline value and a negative stuffing level of $\approx 1\%$. However, this reduction in disorder does not qualitatively modify the underlying physics responsible for the signatures of magnetic moment fragmentation. Instead, the reduction in disorder raises the temperature range over which the AIAO order and the diffuse pinch-point scattering are stabilized. Our results provide an important experimental demonstration of the relationship between synthesis environment, structural disorder, and magnetism in $Nd_2Zr_2O_7$.

Chapter 6

Discovery of Multi-magnon Bound States in Li_2CuO_2

In this chapter I detail further work on Li_2CuO_2 undertaken following the successful synthesis during comissioning of the furnace.

6.1 Introduction

In the realm of quantum magnetism, 1-dimensional (1D) Hamiltonians have long been studied due their theoretical tractability and support of various exotic ground states. Accordingly, quasi-1D magnetic materials, or "spin chains," have served as valuable experimental platforms. Over the years, a large number of fascinating phase behaviors have been verified, including Haldane physics [113, 114, 115, 116] fractionalized excitations (*e.g.* spinons) [117, 118, 119, 120] and quantum critical behavior [121, 122, 123, 124]. Quasi-1D materials have also been found to provide experimental access to quantum few-body phenomena, such as bound states [125, 126, 127].

The magnetism of the $S = 1/2$ spin chain Li_2CuO_2 has been studied continuously since

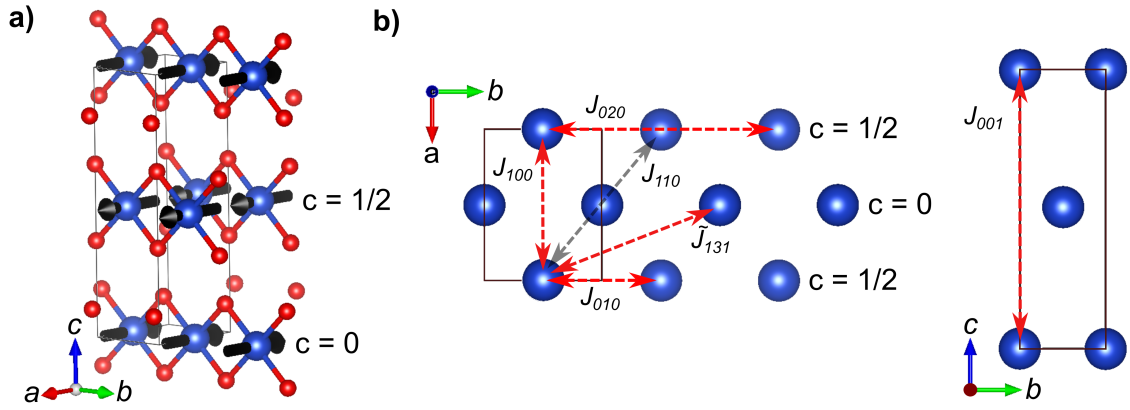

Figure 6.1: **a)** Nuclear and magnetic (black arrows) structures of Li_2CuO_2 , with the shared unit cell shown by the thin grey line (red = O, blue = Cu). The Li atoms have been omitted for clarity. The labels show the c-axis coordinate of the two distinct chain subsystems. **b)** Illustration of the exchange interactions in the ab-plane (left) and bc-plane (right). The red arrows represent interactions which were included in the final exchange model, while the arrow in black represents the J_{110} interaction which was not included in the final model.

it was first suggested as a candidate for 1D ferromagnetism (FM) [128], with later work taking it as a model system for magnetism in edge-sharing cuprates [129, 130, 131, 132]. Early on, a commensurate antiferromagnetic (C-AFM) ground state was determined [129], composed of ferromagnetically (FM) coupled chains which alternate moment direction along the extended c-axis (Figure 6.1**a**). Subsequently, there has been considerable work addressing the proper exchange model for this material [133, 134, 135, 136, 137, 138]. Despite initially contrary inelastic neutron scattering (INS) results [136], the leading interactions in Li_2CuO_2 have now been shown to be the frustrated FM nearest-neighbor (NN, J_{010}) and AFM next-nearest-neighbor (NNN, J_{020}) interactions, where the ratio $\alpha = |J_{020}/J_{010}|$ defines the degree of frustration [137]. Such a conclusion is consistent with results for other cuprate spin chains (*e.g.* $LiCuVO_4$ [139] and $PbCuSO_4(OH)_2$ [140, 141]) which are often described in the context of a J_1-J_2 model.

Recent interest in this model has been driven by theoretical phase diagrams [142, 143] which indicate the formation of exotic multipolar orders in certain parameter regimes.

These multipolar orders – which can be thought of as Bose-Einstein-like condensates of multi-magnon bound states – are potentially stabilized for $\alpha > 1/4$, with quantum fluctuations preventing the classically predicted long-range spiral state[144, 142, 143, 145, 146]. While consideration of Li_2CuO_2 within the context of a J_1-J_2 model might suggest it as a candidate for such physics ($\alpha \approx 1/3$ [137]), previous work has emphasized the importance of inter-chain interactions (specifically the NNN interaction , $\tilde{J}_{131}$) [137, 131, 135] and exchange anisotropy [147] which should suppress fluctuations and are believed to stabilize the observed C-AFM order over the expected spiral state. Although the relatively strong $\tilde{J}_{131}$ moves Li_2CuO_2 out of the regime of multipolar orders [148, 144], the inter-chain interactions are still reasonably weak compared to the intra-chain ones ($\tilde{J}_{131} \approx 0.03\times J_1$ and $0.1\times J_2$). As a result, this material can be considered as an effective system of FM spin chains with the potential to host (non-condensing) multi-magnon bound states.

The existence of multi-magnon bound states in FM Heisenberg spin chains, first revealed by Bethe in 1931 [149], has been the subject of many theoretical studies [150, 151, 152, 153, 154, 155, 156, 157]. The specific case with exchange anisotropy – the relevant situation here [137, 136] – has been studied in some detail [152, 157], with Li_2CuO_2 being considered explicitly [150]. The abundance of theoretical work on bound states in FM chains is in stark contrast with the relatively limited number of experimental demonstrations. Experiments on $CoCl_2{\cdot}H_2O$ have shown evidence for bound states using far-infrared absorption spectroscopy [158]. Indications of bound states have also been detected in $(C_6H_{11}NH_3)CuCl_3$ through FM resonance measurements [159]. Notably, both of these compounds are also two-sublattice AFMs composed of FM chains with easy-axis exchange anisotropy (though the exchange anisotropy in $(C_6H_{11}NH_3)CuCl_3$ is somewhat more complicated than the present case [159]).

Notably, to the best of our knowledge, there have been no reports observing bound

states in FM chains via INS, which is the premier tool for measuring both the energy transfer (ΔE) and momentum ($\vec{\boldsymbol{Q}}$) dependence of low-energy magnetic excitations. This is distinct from the case of Heisenberg AFM chains where several INS experiments have unveiled bound states (*e.g.* $NaMnO_2$ [125], $(VO)_2P_2O_7$ [126] and $Cu(NO_3)_2{\cdot}2.5D_2O$ [127]). Hints at possible bound states in Li_2CuO_2 were observed in a previous INS experiment [137], though the data in that case were not sufficient for detailed analysis.

In this work, we report on the discovery of multi-magnon bound states in Li_2CuO_2 via INS. Our extensive measurements of the one-magnon dispersion confirm previous results regarding the $\tilde{J}_{131}$ interaction and clarify the nature of further inter-chain interactions. We also demonstrate explicitly that only an anisotropic NN inter-chain interaction is needed to capture the spin gap. Although complex, we show this model to be parsimonious and that it describes the one-magnon dispersion well. We then demonstrate the existence of additional magnetic excitations, separate from the one-magnon dispersion, which we ascribe to the formation of two and three-magnon bound states. Analysis of their momentum dependence shows a clear splitting along H and L directions for the two-magnon bound state, which most likely stems from the $\vec{\boldsymbol{Q}}$-dependence of the magnon-magnon interaction potential.

6.2 Methods

In order to mitigate absorption effects from ^{6}Li during this neutron experiment, isotopically enriched $^7LiOH{\cdot}H_2O$ (Cambridge Isotopes, 99.9%) was utilized to produce the Li_2CuO_2 powder for floating-zone growth. The $^7LiOH{\cdot}H_2O$ was dried at 150 °C under a rough dynamic vacuum for 12 hours resulting in anhydrous ^{7}LiOH. Polycrystalline powder was then produced by grinding together (in a glovebox) a stoichiometric amount of CuO (Fisher, 99.999%) with the ^{7}LiOH, using 5 mass % excess of ^{7}LiOH over the

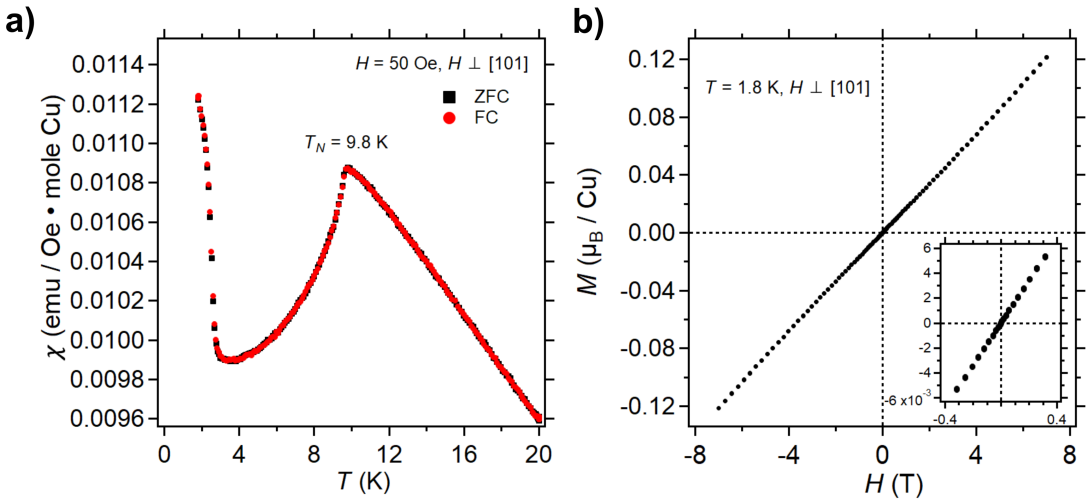

Figure 6.2: **a)** Magnetic susceptibility ($\chi \equiv M/H$) at low temperature showing $T_N = 9.8$ K. Note the lack of irreversibility at low-temperature ($T < 3$ K). **b)** Field dependence of the magnetization (M) at low-temperature. *Inset:* Low-field ($H < 0.5$ T) region.

stoichiometric amount. Note that the difference in the required excess of LiOH – determined by the amount needed for full reaction of the CuO – relative to work during comissioning of the furnace is due to differences in the water content. The reaction step for the powder, feed and seed rod preperation and floating-zone growth paramaters were all as previously described (Section 3.4).

The phase purity and lattice parameters of the resulting crystal were characterized using laboratory powder X-ray diffraction (Emperyan, Panalytical). Powder diffraction on crushed crystal pieces showed a nearly phase pure sample, besides the presence of a very small amount (estimated to be < 1 mass %) of an unidentified impurity. Comparison of measurements conducted on powders produced from surface-free and surface-full samples suggests this impurity occurs as a very thin surface layer. The refined lattice parameters were: $a = 3.66171(2)$ Å, $b = 2.86436(7)$ Å, and $c = 9.3945(2)$ Å, consistent with literature [129]. Bulk magnetic properties were measured on a small crystal (≈ 10 mg) cleaved from the main boule, which was mounted on a quartz paddle using GE varnish.

Measurements were conducted using a Quantum Design MPMS3 SQUID magnetometer in VSM mode. Field-cooled and zero-field-cooled magnetic susceptibility measurements (Figure 6.2**a**) show $T_N = 9.8$ K, with no sign of hysteresis. The field-dependence of the magnetization at $T = 1.8$ K (Figure 6.2**b**) is linear across the full measured range ($H = \pm 7$ T) and there is no evidence of significant hysteresis. The measured T_N is elevated compared to previous results for crystals grown at lower pressures ($\approx 8 - 9$ K) [160, 137, 39, 161]. Furthermore, the lack of any low-temperature ferromagnetism is tied to a fully occupied oxygen site [39]. Previous chemical analysis on the crystal grown during comissioning showed Li:Cu = 1.99:1.01 [4] further confirming the nearly stoichiometric nature of our sample.

The INS measurements were conducted on the direct-geometry time-of-flight (TOF) spectrometer SEQUOIA, at the Spallation Neutron Source (SNS). Li_2CuO_2 cleaves easily along the (101) plane and the crystal separated into pieces upon removal from the furnace. Due to the brittle nature of the fracture, the pieces could be reassembled using Al wire with reasonably good registry. The resulting sample (≈ 2 g) was attached to an Al mount and aligned in the $(0\ K\ L)$ scattering plane using the triple-axis alignment station at the High-Flux Isotope Reactor (HFIR). The sample and mount were sealed under a He environment inside an Al can to provide exchange gas. Al background data was collected by "pseudo-empty" can measurements: the sample was shielded off with the slits until no Li_2CuO_2 Bragg scattering was observed at which point the remaining scattering was measured. A thermocouple was mounted to the sample can and a closed-cycle refrigerator (base temperature ≈ 5 K) was utilized for temperature control.

On the commencement of the SEQUOIA experiment it was discovered that two minority grains existed in one part of the boule. These grains were masked off using the sample slits, yielding a diffraction pattern matching a single orientation. We estimate the total remnant mass in the beam to be ≈ 1.3 g based on the final slit positions. Following

this process, a less than ideal orientation was determined, defined by non-integer $\vec{\boldsymbol{u}}$ and $\vec{\boldsymbol{v}}$ vectors. Despite this issue, the resulting experimental geometry and subsequent ($\vec{\boldsymbol{Q}}$, ΔE) coverage proved sufficient for our problem. The mosaic of the crystal was found to be somewhat broad and possess a slight ($H\,K\,L$) dependency, similar to previous results [137]: a mosaic of 5° was measured on the (002) Bragg peak while 3.5° was measured on the (202).

Measurements were conducted by rotating the crystal around the direction normal to the equatorial plane in steps of 1 or 2 degrees (ψ-scan). Measurements were conducted with E_i = 11, 25, 50 and 185 meV to access the full bandwidth of the highly dispersive in-chain excitations. Data was predominantly collected at 5 K ($T < T_N$), with additional data collected at 20 K ($T > T_N$). The data were reduced for analysis using the software package Mantid [103] during which the data were symmeterized by folding in order to improve the counting statistics. All uncertainties in presented intensities represent plus and minus one standard deviation. The dispersion curves along high symmetry directions were extracted using Gaussian fits to sets of constant-$\vec{\boldsymbol{Q}}$ or constant-ΔE cuts through the data; ΔE cuts were only used for the steep portions of the dispersion along K (the chain direction). Analysis of the dispersion data was conducted using the SpinW software package [162]. For comparison, we also fit the data directly to the analytical form of the dispersion relation from linear spin wave theory; both approaches gave very similar results. Magnetic structure optimization was also performed with SpinW. The optimal propagation vector was determined by the Luttinger-Tisza method and then the moment direction was optimized to obtain the lowest energy configuration consistent with the propagation vector.

6.3 Results

Using an E_i up to 185 meV we were able measure the spin waves along almost all high-symmetry directions in the Brillouion zone. In Figure 6.3**a**,**b** we show the measured dispersion along the directions orthogonal to the chains. Consistent with previous measurements both directions are weakly dispersive [136, 137]. In Figure 6.3**c** we show the much steeper dispersion along the chain measured using $E_i = 185$ meV, which our measurement shows increases monotonically to a zone boundary energy of ≈ 40 meV. We saw no indications of additional strong magnetic excitations at higher energy transfers. As discussed below, the measured dispersion could be well captured by linear spin wave theory [163].

The spin system of Li_2CuO_2 has previously been described [136, 137] by the following Hamiltonian:

$$\hat{H} = \frac{1}{2}\sum_{\mathbf{n},\mathbf{r}} \left[J^z_{\mathbf{r}} \hat{S}^z_{\mathbf{n}} \hat{S}^z_{\mathbf{n+r}} + J_{\mathbf{r}} \hat{S}^+_{\mathbf{n}} \hat{S}^-_{\mathbf{n+r}} \right] \tag{6.1}$$

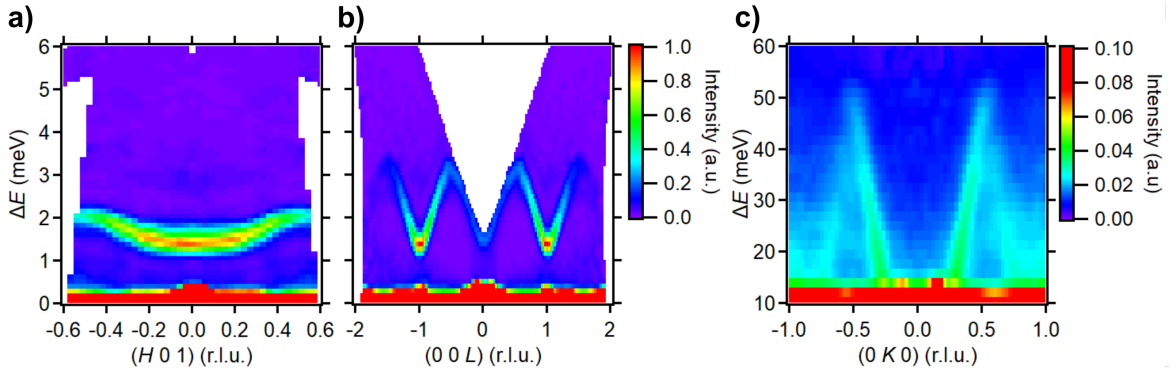

Figure 6.3: Neutron scattering data collected at $T = 5$ K along high-symmetry directions. **a)** Scattering intensity along the $(H01)$, collected using $E_i = 11$ meV. The integration bounds are: K = [-0.025, 0.025] and L = [.875, 1.125]. **b)** Scattering intensity along the $(00L)$, collected using $E_i = 11$ meV. The integration bounds are: H = [-0.125, 0.125] and K = [0.075, 0.075]. **c)** Scattering intensity along $(0K0)$ out to the zone boundary ΔE collected using $E_i = 185$ meV. The integration bounds are: H = [-2, 2] and L = [-2, 2].

Here, $J^z_{\mathbf{r}}$ is the component of the exchange interaction along the crystallographic a-axis, determined to be the magnetic easy axis by electron spin resonance measurements [164, 161]. The double sum is over the Cu-sites ($\mathbf{n}$) and the lattice vectors ($\mathbf{r}$) which connect Cu-sites. We follow the convention that $J_r < 0$ is FM. The dispersion relation derived via linear spin wave theory for this Hamiltonian is given by the following relation:

$$\omega_{\mathbf{Q}} = \sqrt{\left(J_{\mathbf{Q}} - J_{\mathbf{0}} + \tilde{J}_{\mathbf{0}} - D\right)^2 - \left(\tilde{J}_{\mathbf{Q}}\right)^2} \tag{6.2}$$

with $J_Q \equiv (1/2)\sum_{\mathbf{r}} J_r exp(i\vec{\boldsymbol{Q}}\cdot\vec{\boldsymbol{r}})$ and $J_0 \equiv (1/2)\sum_r J_r$ (the same definitions apply to $\tilde{J}$). The $\vec{\boldsymbol{q}} = [0\ 0\ 1]$ magnetic structure breaks the body-centered symmetry of the nuclear unit cell, creating two inequivalent Cu-sites and therefore two FM chain subsystems. The J exchanges represent intra and inter-chain interactions within a subsystem, while the $\tilde{J}$ exchanges represent inter-chain interactions which connect the two subsystems. In this analytical form of the dispersion, D parameterizes the magnitude of the exchange anisotropy according to: $D \equiv J^z_{\mathbf{0}} - J_0 - \tilde{J}^z_0 + \tilde{J}_0$. The spin gap, ΔE_1, arises due to the finite D but is also influenced by the magnitude of the inter-sublattice interactions:

$$\Delta E_1 = \sqrt{D(D - 2\tilde{J}_0)} \tag{6.3}$$

Within the SpinW implementation of linear spin wave theory the individual components of the exchange matrices are fitting parameters, so the exchange anisotropy can be considered in more detail as compared to fitting with Equation 6.1.

We began our analysis by fitting the extracted dispersion data using the most recently published minimal model [137] which includes the J_{010}, J_{020} and $\tilde{J}_{131}$ exchange interactions as well as exchange anisotropy (see Figure 6.1**b** for an illustration of all considered exchange interactions – note that $\tilde{J}_{131}$ is associated with $\vec{\boldsymbol{r}} = (1/2)[1\ 3\ 1]$). We set J_{010} to have an easy-axis anisotropy along the experiemntally determined moment

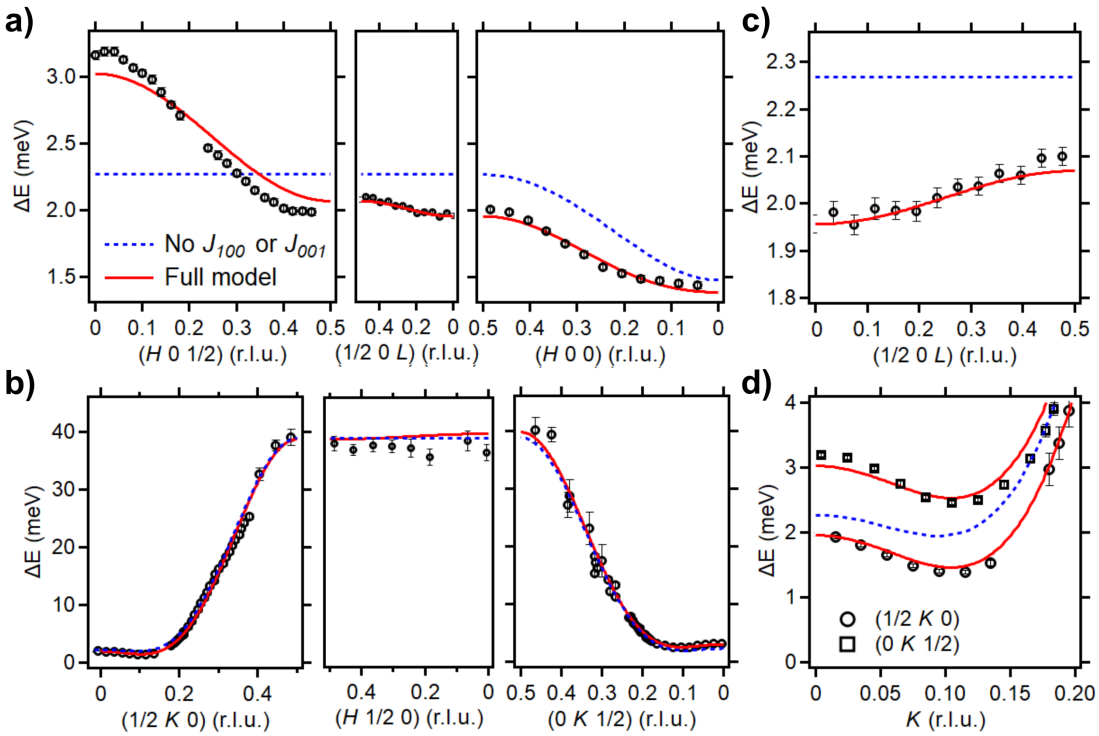

Figure 6.4: **a) - b)** The extracted one-magnon dispersion along several high symmetry directions; the x-axes are scaled by the magnitude of the corresponding reciprocal space basis vector ($c^* < a^* < b^*$). The solid red line shows the fit result from the model described in the text. The dashed blue line shows the fit result without the interactions J_{100} and J_{001}. **c)** Closer view of the (1/2 0 L) dispersion showing the small, but finite, bandwidth. **d)** Closer view of the difference in the (1/2 K 0) and (0 K 1/2) dispersions near the Γ-point.

direction [129] (*i.e.* J^z_{010} was fit independently of $J^x_{010} = J^y_{010} = J_{010}$) since it is by far the largest energy scale. This choice is also consistent with theoretical work considering the nature of a 90° Cu-O-Cu superexchange bond (the angle in Li_2CuO_2 is ≈ 94°) [133]. All other exchange interactions were set to be isotropic. While this model largely captures the behavior of the dispersion within the (0 KL) plane, including the magnitude of the spin gap, there are a number of qualitative failures with respect to the dispersion along directions with a finite H-component (Figure 6.4).

The first notable qualitative failure is the prediction of a flat mode along the (H 0 1/2) direction, when the data clearly show a finite bandwidth (Figure 6.4**a**). A second

failure is found by comparing the dispersion along (1/2 K 0) and (0 K 1/2). While the model gives an identical dispersion relation for these two directions, the data show a clear difference between them, which is most apparent near the Γ-point (Figure 6.4**d**). The third qualitative failure is considerably more subtle. We detected a small, but finite, bandwidth to the dispersion along the (1/2 0 L), seen most clearly in Figure 6.4**c**, which is dispersionless within this model.

The qualitative failures of this minimal model clearly motivate the inclusion of additional exchange interactions. Consideration of Equation 6.1 shows that only an intra-sublattice exchange with a component along L can induce finite dispersion along the (1/2 0 L) direction. Given the relatively large c lattice parameter ($\approx$ 9.395 Å) it is surprising that any dispersion along this direction can be observed at all, and so J_{001} (with the smallest associated real space distance) is the most reasonable exchange interaction to reproduce this feature. The failures regarding the (H 0 1/2) and the comparison between the (0 K 1/2) and (1/2 K 0) indicate the need for additional exchange interactions with components along H. To this end we considered the effect of adding J_{110} and J_{100} as well. Fitting the dispersion with the inclusion of these three exchange interactions greatly improved the χ^2 value and resolved the previously described issues with the original minimal model. J_{100} was found to be AFM and of a similar magnitude as $\tilde{J}_{131}$, which we found to be $\approx$ 7.7 K for this particular fit. J_{110} and J_{001} were both found to be an order of magnitude smaller and FM. We discuss these interactions further in the next section.

In addition to measuring the one-magnon dispersion, we also carefully examined the region near the zone-center where weak, above-gap, scattering had previously been detected [137]. Measurements using E_i = 11 meV at T = 5 K confirmed the presence of this scattering which is visualized with a slice along the (0 K 1) (Figure 6.5**b**). A relatively strong band of scattering, which peaks at the Γ-point, is observed at roughly double ΔE_1 (the value of the spin gap as determined from the constant-$\vec{\boldsymbol{Q}}$ cut in Figure

	J_{010}	J_{020}	$\alpha = \lvert J_{020}/J_{010} \rvert$	$\tilde{J}_{131}$	J_{100}	J_{110}	J_{001}	D
This work	-213.3(9)	67.2(3)	0.315(2)	7.44(2)	5.55(4)	*0*	-0.75(4)	-4(1)
Lorenz *et al.*	-230(2)	75(1)	0.326(1)	9.0(1)	4.8(4)	1.6(3)	*0*	-3.3(1)

Table 6.1: Comparison of the final exchange parameters (given in Kelvin) determined in this work with those given in Lorenz *et al.* Values in italics were fixed to zero. In our results, J^x_{101} and $J^y_{010} = J^z_{010} = J_{010}$ are separate fit parameters. As a result, D is no longer a fitting parameter but is calculated as $D = J^x_{010} - J_{010}$. Since D is a small difference between two large values, the resulting error is rather large - direct fits to the analytical form of the dispersion gave D with a lower error bar, and a value more similar to the results from Lorenz *et al.*

6.5**c**). A third, weaker, signal is observed at roughly triple ΔE_1. In Figure 6.5**a** we show a corresponding SpinW calculation of the neutron scattering intensity in this slice, utilizing our final exchange parameters and anisotropy value shown in Table 6.1.

More quantitative information can be extracted by examining a constant-$\vec{\boldsymbol{Q}}$ cut through these excitations (Figure 6.5**c**). In addition to the N = 1 peak, two additional peaks (N = 2, 3) can be seen, corresponding to the additional features in the slice. The peaks were fit to Gaussians with a sloping background to extract the corresponding ΔE-value and FWHM of the excitations. In reality, the asymmetrical N = 2 line-shape is not Gaussian, a point we return to in the next section. As such, the fitted location is mostly of empirical use during analysis. We note that an even weaker feature is visible near $\approx$ 5.5 meV in Figure 6.5**b** . While this feature does show up in the line cut (not shown) it is very weak and near the edge of the coverage, making analysis less reliable. Furthermore, this region is seemingly polluted by an optical phonon at slightly higher energy transfer, which makes it difficult to determine the temperature dependence of the weak signal. We defer a detailed study of this feature to a future experiment.

Comparing the (0 K 1) slices at T = 5 K and 20 K (Figure 6.6**a**) we observe a collapse of the one-magnon gap, consistent with the origin in weak exchange anisotropy.

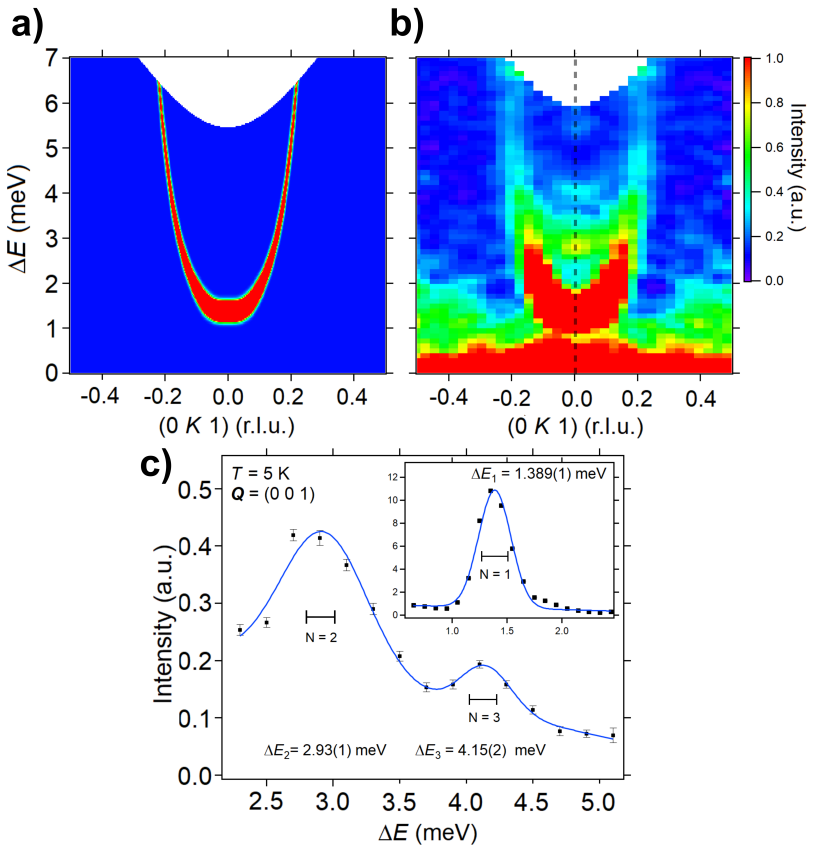

Figure 6.5: **a)** SpinW calculation of the $T = 0$ K, one-magnon dispersion along the (0 K 1) using the parameters from this work. The calculation includes the ΔE-dependent resolution function and the $\vec{Q}$-resolution was set to the Gaussian FWHM of the (0 0 1) magnetic Bragg peak. A small constant background term has been added to simulate the incoherent background present in the measured data. **b)** Experimental intensity for the same region of ($\vec{Q}$, ΔE) measured at $T = 5$ K using $E_i = 11$ meV. The data was integrated with the following bounds: H = [-0.125, 0.125], L = [0.95, 1.05]. The broad intensity below $\Delta E \approx 2$ meV at higher $|K|$ is due to the Al background, which has not been subtracted. In **a** and **b** the shared color scaling was set by first normalizing the two data sets to the value at $K = 0$ and $\Delta E = \Delta E_1$. To highlight the weak, higher-energy features observed at the Γ-point in **b**, the maximum of the color scaling was set to a low value. Both data sets were then normalized once more to this maximum value. **c)** Energy cut along the dashed line in **b**, with the Al background subtraced, showing the excitations above the one-magnon dispersion (N = 2 and 3). The blue line is a the fit described in the main text and the black lines show the instrumental energy resolution (FWHM). The cut was integrated in reciprocal space with the following bounds: H = [-0.075, 0.075], K = [-0.1, 0.1], and L = [0.95, 1.05]. *Inset:* The one-magnon (N = 1) peak using a higher ΔE point density.

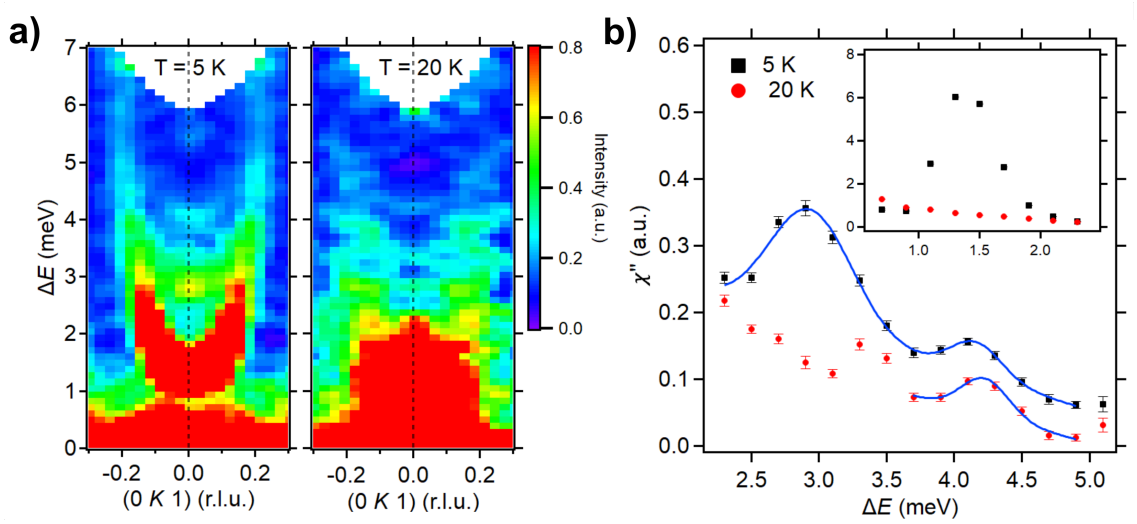

Figure 6.6: **a)** Temperature dependence of the inelastic scattering intensity along the (0 K 1) collected using $E_1 = 11$ meV. The integration ranges are: H = -0.125, 0.125], L = [0.95,1.05]. **b)** Comparison of the same energy cut shown in Figure 6.5**c** for both $T = 5$ K and 20 K ($> T_N$). The detailed balance correction has been applied to the data, following subtraction of the Al background and elastic line intensity. The blue line is a fit using a Gaussian plus a sloping background. The fit for the N = 3 excitation at 20 K uses the width resulting from the fit at 5 K fit. *Inset:* View of the one-magnon peak region at 5 K and 20 K.

Further confirmation of this is seen in the inset of Figure 6.6**b**. Strong paramagnon scattering is observed at 20 K, consistent with previous reports that Li_2CuO_2 possesses short-range correlations well above T_N [132, 161]. The slices indicate that the band of scattering corresponding to the N = 2 excitation disappears at 20 K and the energy cuts (Figure 6.6**b**) confirm this. The apparent small feature near 3.5 meV can likely be attributed to the worse statistics at 20 K, due to lower count times, and possibly inadvertent contributions from the diffuse, N = 1, paramagnon scattering. In contrast, the intensity of the N = 3 peak is largely unchanged at 20 K, with only the effective background decreasing. Fitting the energy cuts shows that the ΔE-value of the N = 3 excitation also remains nearly constant: $\Delta E_3 = 4.16(2)$ meV and 4.22(2) meV at 5 K and 20 K, respectively

To study the momentum dependence of the N = 2 and 3 excitations, we examined

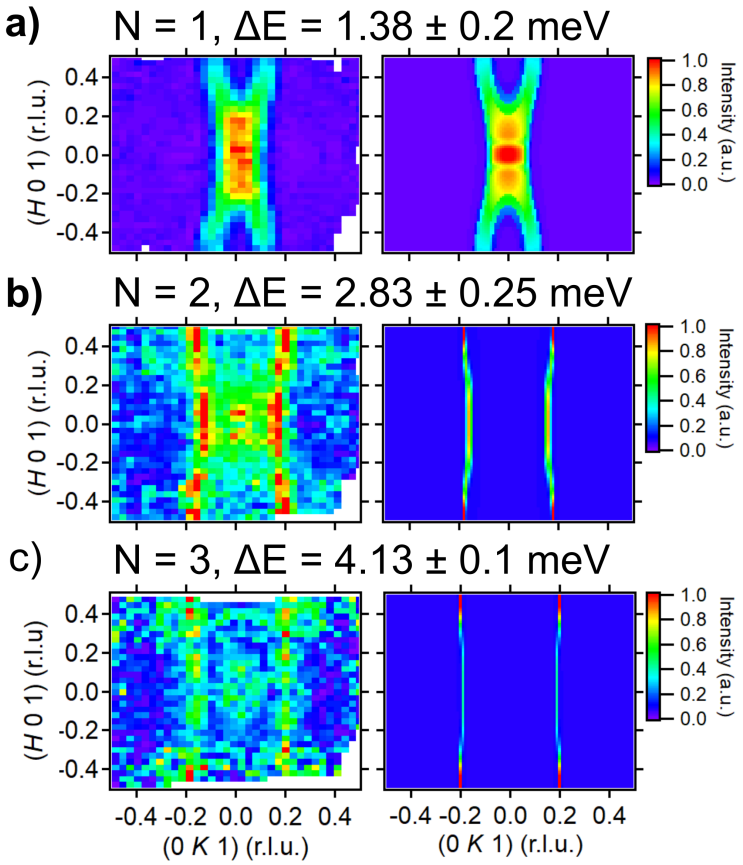

Figure 6.7: Constant ΔE slices in the $(HK\ 1)$ plane from $E_i = 11$ meV data (left); the energy integration was performed around the peak locations shown in Figure 6.5c. The figures on the right are corresponding SpinW calculations using the determined exchange constants (Table 6.1). All data has been scaled to its maximum intensity value for a consistent comparison between the measured and calculated data and the calculated values have been convolved with the instrumental ΔE-dependent resolution function. For N = 1, the $\vec{Q}$-resolution of the calculated data was set to the FWHM of the (0 0 1) magnetic Bragg peak. For N = 2 and 3, a larger $\vec{Q}$ resolution was needed to approximate the measured data. A constant value has been added to the calculated intensity to approximate the incoherent background. The integration in the orthogonal direction in momentum space is $L = [0.95,1.05]$. **a)** N = 1 excitation. **b)** N = 2 excitation **c)** N = 3 excitation.

constant-ΔE slices through the $(H\,K\ 1)$ plane, shown in Figure 6.7**b**,**c** (left). At higher ΔE the one-magnon dispersion presents as roughly parallel lines along the H-direction due to the much steeper dispersion along K. The N = 2 and 3 intensities sit between these lines, with the strongest scattering around the Γ-point. As shown in Figure 6.8, a

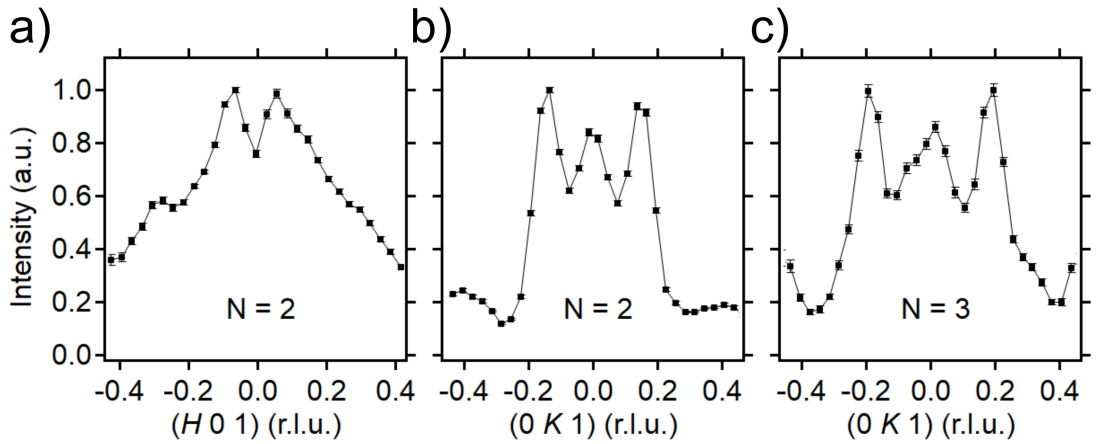

Figure 6.8: **a)** Cut along H through the N = 2 excitation with integration in ΔE = 2.93 ± 0.25 meV. The cut was integrated in reciprocal space with the following bounds: K = [-0.1, 0.1] and L = [0.95, 1.05]. **b)** Cut along K through the N =2 excitation, with the same ΔE integration. H = [-0.1, 0.1] and L = [0.95, 1.05]. **c)** Cut along K through the N = 3 excitation with integration in ΔE = 4.13 ± 0.1 meV. The cut was integrated in reciprocal space with the following bounds: H = [-0.15, 0.15] and L = [0.95, 1.05].

line-cut along the H-direction at ΔE_2 shows a symmetric two-peak structure around H = 0. A similar two-peak structure is also observed for a line-cut along the L-direction (not shown). A cut along H for the N = 3 excitation (not shown) is suggestive of the same splitting, but the poorly defined background in that direction prevented us from resolving it clearly. The data did not allow for examination of the N = 3 excitation along L. In the K-direction (where the background for the N = 3 excitation is more well-defined) we confirmed the presence of a single peak around K = 0. Note that the stronger peaks at $K \approx \pm$ 0.2 come from the line-cut crossing the steep one-magnon dispersion.

6.4 Discussion

In the interest of establishing a new minimal exchange model, we fit the data with various subsets of the additional exchange interactions. As described previously, of the considered exchange interactions, only J_{001} can cause dispersion along the (1/2 0 L)

direction. As a result, this interaction was retained in all fits: it was found to be very small ($|J_{001}| < 1$ K), consistent with the very slight dispersion, and FM in all cases. We note that this interaction also causes a finite bandwidth for the dispersion along the (0 1/2 L). We were unable to resolve this dispersion because the $K = 1/2$ zone boundary sits at relatively high ΔE, meaning a large $E_i = 185$ meV was needed to access it: the resolution at $E_i = 185$ meV is ≈ 10 meV (FWHM), which is roughly 100 times the bandwidth caused by J_{001} (≈ 0.1 meV). While we were able to extract some data points along the (H 1/2 0), similar considerations prevented us from observing the finite dispersion along that direction (Figure 6.4**b**), which is, depending on the model, due to J_{100} and/or J_{110}.

Next we considered whether both J_{100} and J_{110} are needed to capture the form of the dispersion in directions with a finite H component. Fitting without J_{110} resulted in a smaller J_{100} (15% reduction) while other parameters remained unchanged within error. Fitting without J_{100} resulted in the magnitude of J_{110} increasing by a factor of six, accompanied by a change in sign; the magnitude of J_{001} also increased by 30%, though without a change of sign. The χ^2 value increased in both cases (either without J_{100} or without J_{110}) compared to the value for the "maximal" model, which includes al ofl the considered interactions. Howeve,r for the model without J_{100} the χ^2 value increased by 37%, while for the model without J_{110} the χ^2 value increased by only 1.5%. The latter increase can likely be attributed simply to the decrease in the total number of fit parameters (from seven to six). Based on these results we concluded that J_{110} is not a relevant exchange interaction and included only J_{100}. The results of fitting with our finalized model are presented in Table 6.1. We note here that, despite the significance of the inter-chain interactions with respect to the the magnetic properties – including the nature of the long-range order [137, 131, 138, 135] and the largely undiminished Cu^{2+} moment [129] – the intra-chain interactions are still clearly the dominant energy scale

and the magnons are predominantly confined within the chain.

With an accurate description of the one-magnon scattering in hand, we turned to SpinW calculations based on our final exchange parameters. Utilizing the magnetic structure optimization capabilities, we confirmed that the experimentally observed C-AFM structure is the classical ground state for both our exchange model and the reduced model (J_{010}, $J_{020,}$ J_{131} and D). We also explored the conclusion in Lorenz *et al.* that the C-AFM state is stabilized primarily by $\tilde{J}_{131}$, with further stabilization from D. To test this, we set $\tilde{J}_{131} = 0$ and modified D to satisfy the measured spin gap. In this case the magnetic structure optimization routine yielded a spiral state. If $\tilde{J}_{131}$ is retained and the anisotropy is set to 0 (*i.e.* $D = 0$ so that $J^x_{010} = J^y_{010} = J^z_{010}$) then the same collinear AFM structure results, but the moment direction shifts to be along the c-axis. These results indicate that, within the classical calculations performed by SpinW, the collinear magnetic order is indeed stabilized by the $\tilde{J}_{131}$, with the exchange anisotropy serving to set the collinear moment direction.

SpinW calculations of the neutron scattering cross-section show clearly that the extra intensity we observe is not captured by the linear spin wave theory of single magnons. In Figure 6.5**a**,**b** we compare the calculated and observed dispersion along the (0 K 1) direction. The form of the N = 1 dispersion is reasonably well captured by the calculation but the additional above-gap intensity is notably absent. SpinW calculations for the measured constant-ΔE slices (Figure 6.7) further illustrate this point. Again, the N = 1 scattering is well captured by the calculations, but the extra scattering around the Γ-point for N = 2 and 3 is not.

From our fitting at $T = 5$ K, we find $\Delta E_2 = 2.93(1)$ meV and $\Delta E_3 = 4.15(2)$ meV, placing these excitations very close to $2\Delta E_1 = 2.778(2)$ meV and $3\Delta E_1 = 4.167(3)$ meV, respectively. The occurrence of magnetic excitations which cannot be ascribed to the one-magnon dispersion at near integer multiples of the one-magnon gap is highly indicative

of multi-magnon processes. In the case of the N = 2 excitation, the disapperance of the intensity above T_N clearly confirms its magnetic origin. As mentioned previously, the N = 2 line-shape is anisotropic, showing a broadening towards higher-ΔE, which causes the Gaussian ΔE_2 to be slightly higher than $2\Delta E_1$. Such a line-shape is consistent with a contribution from two-magnon continuum scattering, since the peak of the scattering intensity in a two-magnon continuum is shifted towards the lower boundary (which, at the Γ-point, is at $\Delta E = 2\Delta E_1$) [127, 165].

Continuing this line of reasoning, the N = 3 excitation is assigned to a three-magnon bound state. Due to the binding energy from an attractive magnon-magnon interaction potential, a three-magnon bound state should sit below the value $3\Delta E_1$. That ΔE_3 is at most $\approx$ 0.01 meV below $3\Delta E_1$ reflects the weakness of the exchange anisotropy ($D \approx$ -0.35 meV), which controls the binding energy [152]. The Gaussian full-width at half-maximum (FWHM) of the three-magnon bound state is 0.44(6) meV, relative to an instrumental resolution of 0.19 meV at 4.15 meV. While not quite resolution-limited, the excitation is still fairly sharp, indicating the three-magnon bound state is reasonably long-lived. Although the intensity of this feature does not disappear above T_N, as is typical for a coherent magnetic excitation, the intensity also does not increase with temperature, as would be expected for a phonon. We will return to this point shortly.

The existence of a three-magnon bound state implies the existence of a two-magnon one, which should sit slightly below the lower boundary of the two-magnon continuum [152]. The lack of a resolvable seperate peak on the low energy side of the N = 2 feature, below the value of $2\Delta E_1$, is also attributable to the weak exchange anisotropy and thus a small two-magnon binding energy. The splitting observed in the N = 2 excitation along H (Figure 6.8**a**) and L (not shown) represents indirect evidence for the existence of a bound state which is obscured (within the experimental resolution) by the continuum scattering. The intensity of a two-magnon continuum is expected to peak at the magnetic zone center

[165] and the appearance of an incommensurate splitting implies additional phyiscs. For completeness, we mention that the possibility for momentum space structure within the two-magnon continuum has been explored theoretically [166]. This structure occurs due to discontinuities in the two-magnon density of states induced by an asymmetry between the wave vectors of the component one-magnon excitations. However, such a mechanism would operate at the zone boundary and the features observed here occur at the zone center.

In contrast, such a splitting can be seen as a natural consequence of the presence of a bound state, since the potential which binds together the two interacting single magnons (and which does not act upon the delocalized two-particle states of the continuum [166]) possesses a $\vec{\boldsymbol{Q}}$-dependence [152]. Given the existence of significant inter-chain exchange interactions with components along H and L, there is a clear route for variation of the magnon-magnon interaction potential to lead to momentum space structure in the associated scattering. As a result, the presence of a bound state provides a natural explanation for the observed splitting.

The temperature dependence of the observed multi-magnon scattering shows that the N = 2 feature (continuum + two-magnon bound state) disappears at 20 K, while the three-magnon mode remains essentially unchanged in both intensity and energy transfer. This is puzzling given that the single-magnon excitations which make up the bound states are excitations out of the ordered state (*i.e.* single spin flips within a FM chain). A potential explanation is that extensive short-range correlations above T_N [132, 161] provide sufficient order for the continued stability of the three-magnon bound state. However, it is not clear why this would not also apply to the two-magnon bound state, so the overall temperature dependence remains an open question.

6.5 Conclusions

We have carried out a thorough measurement of the magnetic excitations in Li_2CuO_2 and used the resulting data to refine the previously published exchange model. Our analysis confirms the importance of the $\tilde{J}_{131}$ interaction and clarifies the nature of further inter-chain interactions. SpinW calculations show this exchange model to be consistent with the previously identified C-AFM order, which is stabilized by a combination of $\tilde{J}_{131}$ and the easy-axis exchange anisotropy. Based on our exchange model, it is clear that certain features of the INS spectrum cannot be described in terms of the one-magnon scattering. In addition to two-magnon continuum scattering, we identify two and three-magnon bound states with very small binding energies (on the order of 0.01 meV). To the best of our knowledge, this represents the first observation of multi-magnon bound states in an effective FM spin chain by neutron scattering.

Presently, there are two points which would benefit from further experimental and theoretical work. The first point concerns the persistence of the three-magnon excitation at $T > T_N$. Additional INS measurements at higher temperatures would be helpful to address the proposed relevance of short-range correlations. Extension of recent numerical calculations of the dynamical structure factor at finite temperature to the specific case of Li_2CuO_2 might also be enlightening [167]. The second point concerns the momentum space structure observed for the two-magnon bound state. Theoretical calculations of the momentum dependence of the magnon-magnon interaction potential would be useful to confirm our picture. On the experimental side, it would be of interest to determine the splitting of the three-magnon mode more clearly, so as to gain further insight into the behavior of the higher order magnon-magnon interactions.

Chapter 7

Mapping the Structural, Magnetic and Electronic Behavior of $(Eu_{1-x}Ca_x)_2Ir_2O_7$ Across a Metal-insulator Transition

"Sir Neville though and he thought,
about electron hopping a lot.
Until it rang like a bell,
that correlated electrons are swell,
and now we've an insulator called Mott"

7.1 Introduction

The highly accommodating nature of the pyrochlore structure allows for decoration of a geometrically frustrated lattice with a wide array of different chemistries, leading to a myriad of interesting behaviours. In particular, the pyrochlore iridates ($A_2B_2O_7$, where A = Y or a lanthanide and B = Ir) have attracted significant attention due to their comparable energy scales for spin-orbit coupling (SOC) and electron-electron correlations (U) which lead to $J_{eff} = 1/2$ Mott physics [168]. In these compounds, a thermally driven metal-to-insulator transition (MIT) occurs for A = Nd and higher atomic number (Z), with a gap between quadratic bands opening at T_{MIT}. T_{MIT} decreases in magnitude with increasing lanthanide ionic radius until $Pr_2Ir_2O_7$ is reached and a metallic ground state is formed, driven by the change in Ir valence band bandwidth [169]. The MIT is accompanied by an AFM transition (T_{AFM}) with the formation of the $\vec{q} = 0$, 'all-in-all-out' (AIAO) magnetic order on the Ir and lanthanide sublattices (Figure 7.1) [170, 171]. This magnetic order is a result of the tetrahedral arrangement of the Ir $J_{eff} = 1/2$ spins, which frustrates the (antiferromagnetic) Heisenberg exchange interaction. The frustration is lifted by the action of the Dzyaloshinsky-Moriya interaction (DMI), amplified by the strong SOC. Since the Heisenberg exchange is frustrated, the (weaker) DMI determines the magnetic order, resulting in the AIAO state [172, 173, 174].

Based on these ingredients, theoretical predictions have suggested that suppression of the MIT can lead to a novel antiferromagnetic quantum critical point [175] and the stabilization of topologically nontrivial phases [172, 176, 177]. Signatures of the Weyl semimetal phase have been observed immediately below T_{MIT}, in addition to other atypical electronic behaviors [178, 179, 180, 181, 182]. Suppression of the MIT through modification of the ratio U/W (W, valence band bandwidth) has been attained by both physical [183, 184] and chemical pressure (*i.e.* alloying with different lanthanide ions)

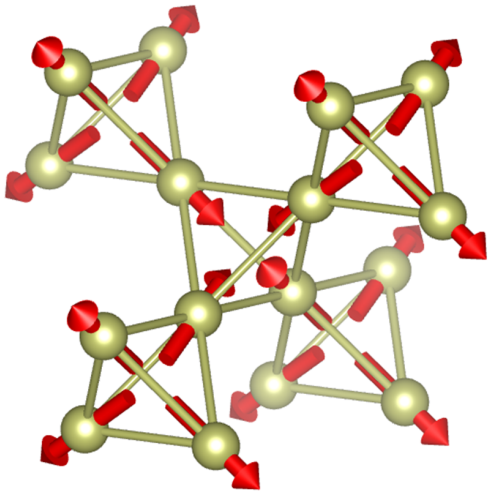

Figure 7.1: The "all-in-all-out" (AIAO) magnetic structure on the Ir sublattice in $Eu_2Ir_2O_7$. Only the Ir atoms are shown.

[184]. While these experimental techniques provide slightly different structural perturbations, both represent methods of bandwidth-control of the MIT.

Despite these efforts, no clear consensus has emerged about the mechanism for the MIT in this system and its relationship to the Ir AIAO order. Understanding this connection is vital for evaluating the nature of the metallic state formed and the potential for quantum critical phase behaviour. $Eu_2Ir_2O_7$ provides a convenient platform for this investigation since the nonmagnetic nature ($|L| = |S|$, $J = 0$) of the Eu^{3+} ion allows for direct study of the Ir AIAO magnetism absent the influence of lanthanide order. Illustratively, ARPES work on $Nd_2Ir_2O_7$ shows a continuous gap evolution immediately below T_{MIT}, consistent with a mean-field mechanism that directly connects the onset of the AIAO order with the insulating behaviour [181]. However, a more Mott-like state emerges at lower temperatures, possibly due to the ordering of the Nd moments [181]. Detailed magneto-resistance studies on $Nd_2Ir_2O_7$ samples further show a complex interplay of the Nd/Ir magnetic orders with the charge transport due to the presence of f-d exchange coupling [179, 185], furthering the motivation to study compounds with a nonmagnetic

A-site ion.

In contrast to the bandwidth-control studies, heterovalent doping of the A-site ion allows for a detailed survey of the changes in the charge transport and structural/magnetic symmetries as the valence band deviates from half-filling. Here, Ca-doping is used for this purpose since it provides a stable 2+ ion with a minimal difference in ionic radius – for comparison, Sr^{2+} is $\approx$ 20% larger than Eu^{3+}, while Ca_{2+} is only 5% larger. Ca-doping therefore allows for modification of the Ir $5d$ occupation (*i.e.* filling-control) and the SOC-driven AIAO state, providing an opportunity to study the connection to the MIT with minimal structural perturbation. Traversing the iridate phase diagram via filling-control may reveal significantly different magnetic and electronic states than what has been observed through bandwidth-control [175]. However, reports in the literature of carrier-doping iridates show varied results. With respect to the relationship between T_{MIT} and T_{AFM}, these variations can be summarized in three distinct cases: (1) T_{MIT} = T_{AFM} is maintained with doping until a fully metallic/paramagnetic state is realized [186] (2) Both T_{AFM} and T_{MIT} decrease with doping, but T_{MIT} decreases much faster, becoming decoupled from T_{AFM} [187] (3) A second, higher temperature, feature in the magnetic susceptibility emerges upon doping and eventually dominates the signal; T_{MIT} still decreases, but the original T_{AFM} appears essentially unchanged [188]. Addressing how these different cases relate to the synthesis procedure and resulting sample composition is important in order to determine the intrinsic properties of the pyrochlore iridates.

In this study, we utilize carrier-doping to drive a change in the ground state of $Eu_2Ir_2O_7$. We leverage bulk characterization and X-ray scattering/spectroscopy to detail the changes that occur in the crystallographic, magnetic and electronic structures across the series $(Eu_{1-x}Ca_x)_2Ir_2O_7$. T_{MIT} is rapidly suppressed with doping until a metallic ground state is reached between $0.04 < x < 0.07$. In parallel, T_{AFM} decreases slowly and

becomes decoupled from T_{MIT} such that the magnetic order of the parent compound survives well into the metallic regime. This behavior is interpreted as being due to the formation of an electronically phase separated state. An open question remains as to why this phase separation is seen only under certain synthetic conditions and not for samples with a magnetic A-site ion. X-ray scattering measurements indicate that the modification of T_{MIT} and T_{AFM} is not coincident with observable changes in the average or local structural symmetries. Analysis of Ir L edge X-ray absorption spectroscopy (XAS) shows a clear net change in valence with doping, confirming the occurrence of filling-control. Unexpectedly, this filling-control manifests as electron doping, rather than the expected hole doping, likely due to a compensatory defect mechanism.

7.2 Methods

Polycrystalline samples of $(Eu_{1-x}Ca_x)_2Ir_2O_7$ were made by a solid-state synthesis procedure. Stoichiometric mixtures of dry Eu_2O_3 (Alfa Aesar, 99.99%), IrO_2 (Alfa Aesar, 99.99%),) and $CaCO_3$ (Alfa Aesar, 99.99%) powders were ground together until well mixed. The loose powder was then placed in an Al_2O_3 crucible and sintered in air at 1073 K for 18 hours. The powder was then re-ground, formed into a dense pellet using a cold isostatic press at 350 MPa and fired in air at 1273 K for 100 hours. In the initial samples used for the X-ray scattering/spectroscopy studies, this process was repeated at 1373 K following re-grinding and re-pressing [189]. These samples are referred to as "air sintered" in the text. Later samples were synthesized following a modified procedure utilizing lower temperatures in air and a vacuum sintering step to reduce IrO_2 volatility [109]. Following the same initial 1073 K treatment, pellets were sintered at 1298 K three times for 100 hours with intermediate re-grinding and re-pelletizing. Next, 2 – 4 molar percent of IrO_2 was added to the powder before sintering at 1298 K for 100 hours in

an Al_2O_3 crucible sealed under vacuum in a quartz tube. In some cases, this step was repeated for more complete reaction of the Eu_2O_3 precursor. Finally, after regrinding and repressing, the pellet was fired at 1173 K for 48 hours in air. These samples are referred to as "vacuum sintered".

While single crystals of $Eu_2Ir_2O_7$ have been synthesized via a KF-flux method [190], synthesis of larger single crystals is desirable to allow for single-crystal neutron scattering studies probing the magnetic structure. To this end, we performed a systematic study using the laser furnace to determine whether $Eu_2Ir_2O_7$ could be made to melt (congruently) and thus be grown by floating-zone. As a preliminary test, vacuum sintered $Eu_2Ir_2O_7$ powder was heated in air using a standard box furnace at incrementally higher temperatures to roughly determine the decomposition temperature under standard conditions. One test was also done under vacuum ($\approx 10^{-8}$ bar) at high temperature to determine the effect of reducing the O_2 content of the reaction atmosphere. Powder from the same batch was then pressed into a 40 mm long rod at 350 MPa using a cold isostatic press. The resulting rod was fired in air on an Al_2O_3 boat at 1373 K (where $Eu_2Ir_2O_7$ is known to be stable) for 100 hours to densify it. The final purity was $\approx$ 97 mass % of $Eu_2Ir_2O_7$, with trace IrO_2 and Ir metal. Any change in stoichiometery which occurred during this step due to Ir volatility was deemed insignificant with respect to the question of melting. In order to obtain more uniform heatng during the melt tests, the end of the rod was sanded down to a "pencil tip" geometry. The sample was loaded into the seed rod position of the furnace and heated at different laser powers under various pressures of $Ar:O_2 = 80:20$. The heating time was roughly 2 hours in all cases.

Evaluation of the final doping level (x) of the polycrystalline samples was performed using a Rigaku ZSX Primus IV wavelength-dispersive X-ray fluorescence (WDXRF) spectrometer. Quantitative analysis was attained by use of a standard curve created by measurement of pressed pellets of unreacted precursor powders with known stoichiometry. A

range of dopings of the air sintered samples were studied by high-resolution, synchrotron powder X-ray diffraction (XRD) at the 11-BM beamline of the Advanced Photon Source (APS). In order to minimize the effect of absorption, a thin layer of finely ground powder was adhered using grease to the outside of a nested Kapton tube. Laboratory XRD using a Panalytical Emperyan diffractometer was utilized to monitor the progression of the reaction during the synthesis procedure and evaluate structural changes in the vacuum sintered samples. All diffraction data were refined using the TOPAS software package. VESTA was used to visualize the results of the refinements and determine the bond angles and distances [191]. The pyrochlore structure was found to be the majority phase in all samples measured at 11-BM ($\approx$ 95% purity). Impurities consisted of paramagnetic IrO_2, Ir metal and Eu_2O_3. IrO_2 and Ir were found at levels typically $\leq$ 1.5% while the fraction of unreacted Eu_2O_3 was generally larger, up to 2.5% in some samples. The vacuum sintered samples were found to have a higher $Eu_2Ir_2O_7$ phase fraction due to a more complete reaction of the Eu_2O_3. Based on lab XRD these samples contained smaller amounts of IrO_2, Ir and Eu_2O_3 ($\approx$ 1% each).

Synchrotron total scattering data for pair distribution function (PDF) analysis were collected on the 6-ID-D beamline at the APS using powder taken from the same batches as the 11-BM samples. The well-ground powder was sieved using 325 mesh wire cloth (0.044 mm opening size) to prevent pin-holing. This powder was then sealed into Kapton tubes using copper wire and epoxy in a He-filled glove-bag to provide a thermal exchange gas. The samples were measured in transmission using an area detector. The 2D data was integrated to 1D diffraction data utilizing the Fit2D software [192]. Corrections to obtain the *I(Q)* and subsequent Fourier transform with a Q_{max} of 24 Å to obtain the *G(r)* were performed using the program PDFgetX2 [193]. Analysis of the total scattering data was performed using the PDFgui software suite [104] over a range of 1.75 – 10.0 Å.

Bulk characterization of the magnetic and electronic properties was carried out for

samples across the series. Measurements of the field and temperature dependence of the magnetic susceptibility were performed on powder samples ($\leq$ 20 mg) mounted in polypropylene capsules. $\chi(T)$ and *M(H)* measurements were collected using a MPMS3 Quantum Design SQUID magnetometer. Magnetization measurements at higher fields were taken using a vibrating sample magnetometer (VSM) mounted on a Quantum Design DynaCool physical properties measurement system (PPMS) equipped with a 9 T magnet. Charge transport measurements were taken on well-sintered pellets using a four-probe configuration in a DynaCool PPMS. The samples were sanded into a bar geometry and mounted to the sample puck with GE varnish, while contacts were made using silver paste.

XAS and XMCD measurements at the Ir $L_{2,3}$ absorption edges were performed on beamline 4-ID-D at the APS. Powder samples (from the same batches used at 11-BM for the same x) were prepared by first sieving to a maximum particle size of 5 microns to prevent pin-holing. The sieved powder was then adhered to layers of tape which were stacked until a uniform sample thickness corresponding to roughly two absorption lengths was obtained. All measurementswere performed using the transmission geometry. Energy selectivity was obtained using a double-crystal [111] Si monochromator while circularly polarized x-rays for the XMCD measurements were produced using a diamond crystal phase retarder optic in Bragg-transmission geometry, operated in helicity-switching mode at 13.1 Hz. In all cases, the absorption signal was detected using a diode with a lock-in amplifier [194]. In order to remove instrumental artifacts from the data, the XMCD measurements were performed with field ($\mu_0 H = 5$ T) oriented both parallel and antiparallel to the incident wave-vector.

7.3 Results

7.3.1 Floating-Zone Growth Attempts

Temperature, Time	Atmosphere	Result
1523 K, 4 hours	air, 1 bar	Minor decomposition
1573 K, 4 hours	air, 1 bar	Major decomposition
1623 K, 4 hours	air, 1 bar	Near complete decomposition
1673 K, 2 hours	air, 1 bar	Near complete decomposition
1673 K, 2 hours	vacuum, 10^{-11} bar	Near complete decomposition

Table 7.1: Results of heating nearly phase pure $Eu_2Ir_2O_7$ at various temperatures in air and under vacuum.

The results of heat treatments conducted under ambient conditions are given in Table 7.1. At 1523 K the $Eu_2Ir_2O_7$ phase fraction from XRD decreased slightly ($\approx$ 91 mass %) in parallel with formation of a small amount of Eu_2O_3 and a slight increase in the amounts of IrO_2 and Ir metal. This most likely indicates that decomposition begins to occur at 1523 K, though with slow enough kinetics that the system has not yet reached equilibrium after 4 hours[1]. At 1573 K the decomposition rate increased dramatically, with a large increases in the amount of Eu_2O_3, IrO_2, and Ir metal , and only a minor amount of $Eu_2Ir_2O_7$ remaining ($\approx$ 4 mass %). Above this temperature only trace amounts of $Eu_2Ir_2O_7$ could be detected in the final sample, which could not be quantified. Heating the sample under a dynamic vacuum at 1673 K did not modify the nearly complete decomposition of $Eu_2Ir_2O_7$ which was observed in air. The only difference observed was that no significant IrO_2 remained after heating in vacuum (the sample was a mix of Eu_2O_3 and Ir). These results suggest that the atmospheric decomposition temperature for $Eu_2Ir_2O_7$ is around 1523 K and that the decomposition reaction proceeds as: $Eu_2Ir_2O_7$

[1]That the system is not in equilibrium can be seen by considering the Gibbs Phase rule: F = C - P + 2, where F = degrees of freedom, C = number of components (elements) and P = number of phases. Since T and P are effectively fixed this reduces to F = C - P. Thus at equilibrium a system with C = 3 can have at most 3 phases.

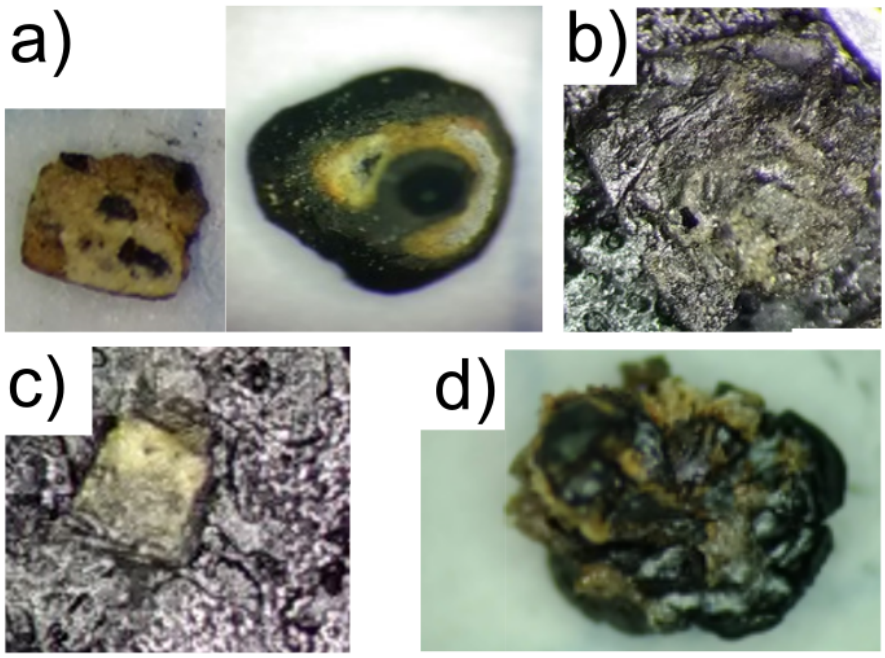

Figure 7.2: Images of the sintered $Eu_2Ir_2O_7$ rod after heating in the laser furnace under high-pressure 80:20. **a)** P = 207 bar, T 1673 K **b)** P = 207 bar, T = 2273 K **c)** P = 620 bar, T = 1673 K **d)** P = 620 bar, T = 2273 K

$\rightarrow Eu_2O_3 + 2IrO_2 \rightarrow Eu_2O_3 + IrO_2 + Ir + O_2$ (g). The second step is due to the (partial) decomposition of the IrO_2 into Ir metal. Volatility of the IrO_2 likely also occurs at the same time.

The sintered rod was heated in the laser furnace under 207 and 620 bar of 80:20. For both pressures, a melt test was attempted at $\approx$ 1673 K and 2273 K, based on the fact that $Eu_2Ir_2O_7$ was determined to decompose at these temperatures in ambient air/vacuum. The temperature was determined by first "calibrating" the pyrometer using molten Al_2O_3 and using the difference between the pyrometer reading and the true melting temperature of Al_2O_3 as a constant offset (the pyrometer value at melting was found to be $\approx$ 100 K above the true melting temperature). Visual inspection of the sintered rod after heating suggested that decomposition occured at all temperature and pressure combinations, indicating that high-O_2 pressure does not stabilize congruent melting of $Eu_2Ir_2O_7$. Yellow

and white crystalline material typically formed in the heated region, along with some shiny/metallic regions. Representative samples are shown in Figure 7.2.

7.3.2 Structural Characterization

Data from synchrotron X-ray scattering experiments were collected on air sintered samples to determine the effect of increasing Ca-doping on the symmetry of the average and local structures. While neutron powder diffraction is a natural complement to this data, particularly for insight into oxygen-dependent behaviors, such an experiment was not carried out due to the high absorption cross section of both Ir and Eu [195]. The average pyrochlore structure is composed of interpenetrating networks of corner-sharing tetrahedra formed by the A (Eu) and B (Ir) site ions. In $Eu_2Ir_2O_7$, the AIAO magnetic order consists of Ir moments aligned along the local $\langle 111 \rangle$ axes of the tetrahedra and arranged such that, for each tetrahedra, all moments point either into or away from the center. The B-site ion is coordinated by a trigonally distorted octahedra of oxygen atoms, with the degree of distortion and Ir-O-Ir bond angle controlled by the x-coordinate of the $48f$ oxygen site (u). This is the only free structural variable besides the lattice parameter (a). An undistorted octahedron is attained for $u = 0.3125$. Fits to the $T = 300$ K synchrotron XRD data are shown in Figure 7.3. At all measured temperatures, the patterns are well fit by the cubic $Fd\bar{3}m$ (#227) pyrochlore structure, with the additional presence of up to 2.5% Eu2O3 and $\leq 1.5\%$ of both IrO_2 and Ir impurities. Comparison of lab XRD indicates that the vacuum sintered samples tend to have a higher $Eu_2Ir_2O_7$ phase fraction. This is most likely driven by the second addition of IrO_2 prior to the vacuum sintering process, which compensates for volatilized IrO_2. The refined value of u decreases marginally with Ca-doping, which results in a slight modification of the Ir-O-Ir bond angle. The refined value of a also decreases with Ca-doping. A qualitatively similar

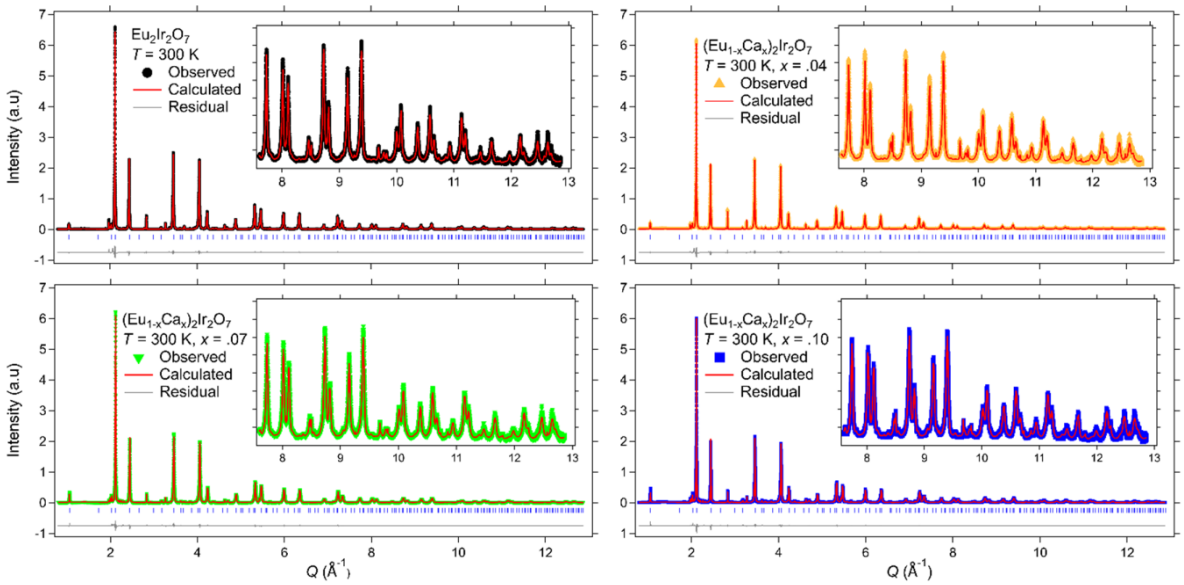

Figure 7.3: Rietveld refinements of synchrotron X-ray powder diffraction data for air sintered $x = 0$, 0.04, 0.07, and 0.10 samples taken at $T = 300$ K. The calculated curves include the pyrochlore phase and impurity phases (Ir, IrO_2,and Eu_2O_3). The blue ticks above the residuals indicate the location of pyrochlore peaks only. Other peaks come from the impurity phases (*e.g.* Ir at 2.8 $Å^{-1}$) as quantified and described in the text. *Insets*: high-Q regions of the data and refinements.

trend for u and a was found from laboratory XRD on the vacuum sintered samples

Several different models were explored during the refinement process and the results of the final model are shown in Table 7.2. A slight asymmetry toward low-Q was observed for the $Eu_2Ir_2O_7$ peaks, as has been seen in other pyrochlore iridates [109] and which is most likely due to a distribution of strain in the lattice. This distribution was modeled by including a second $Eu_2Ir_2O_7$ phase with an increased lattice parameter (typically $\approx$ 0.1%) and a broad line shape, which significantly improved the fit. Comparison was made between fits with Ca on either the Eu or Ir site, and in all cases substitution of Ca for Ir produced inferior fits.

Due to the low scattering amplitude of the dilute Ca dopant, refinement of the Ca occupancy value proved unreliable. Subsequently, Ca occupancy was fixed to the x value determined via WDXRF. For the parent sample, initial refinement of the Eu and Ir site

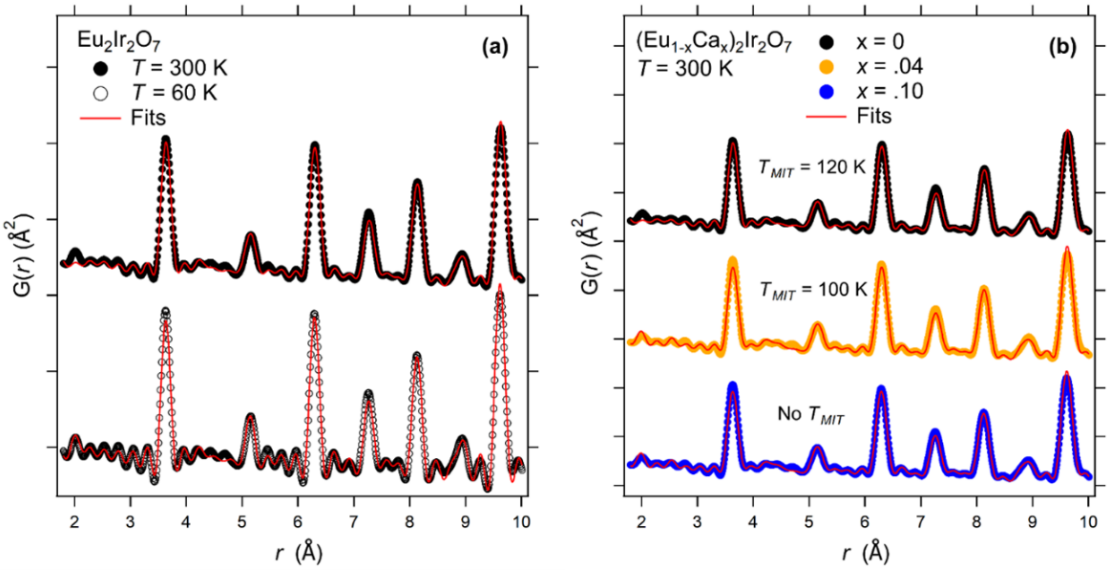

Figure 7.4: PDF refinement of synchrotron X-ray total scattering data on air sintered samples. Curves offset for clarity. **(a)** Refinements for $x = 0$ at T = 300 (top, R_W = 9.6%) and 60 K (bottom, RW = 14.1%) with T_{MIT} = 120 K **(b)** Refinements for x = 0(R_W = 9.6%), 0.04 (R_W = 10.6%) and 0.10 (R_W = 9.3%) at T = 300 K.

occupancies showed complete occupancy. When site mixing was allowed between the Eu and Ir sites – such that any decrease in Eu (Ir) occupancy on the A (B) site was compensated by Ir (Eu), with total occupancy constrained to 1 – a maximum of 2% anti-site defects on the Ir sublattice was observed, with other values all <1%. For the $x > 0$ samples, the Eu and Ir occupancies were initialized at the values of 1-x and 1, respectively. The Eu site occupancy consistently refined to a value close to the nominal Eu stoichiometry (1 - x_{nom} in Table 7.2). All refinements of the $x > 0$ samples showed <0.5% anti-site defects on both sublattices. Generally, this site-mixing is of the same magnitude as the reported errors and inclusion in the model only marginally improves the goodness-of-fit parameters. For the $x > 0$ samples, the refined Eu occupancy, when considered with the XRF-determined value of x, suggests that there is a variable concentration of vacancies on the A-site ranging from $< 1\%$ ($x = 0.04$) to roughly 4% ($x = 0.10$).

The PDF data (Figure 7.4) show little change across the series and the data for the

x_{nom}	0	0.05	0.1	0.15	0	0.05	0.1
x_{XRF}	0	.044(1)	0.071(1)	0.102(1)	0	0.044(1)	0.071(1)
T	300 K				90 K		
a (Å)	10.28330(3)	10.28076(3)	10.27588(3)	10.27004(2)	10.27381(2)	10.27107(3)	10.26563(2)
u (O_{48f})	0.3341(2)	0.3334(2)	0.3321(1)	0.3316(1)	0.3354(2)	0.3343(2)	0.3340(2)
∠Ir-O-Ir (°)	129.1(2)	129.5(2)	130.2(2)	130.4(3)	128.4(4)	129.0(3)	129.2(3)
∠O-Ir-O (°)	81.9(5)	82.1(3)	82.6(4)	82.8(1)	81.5(1)	81.8(3)	81.9(3)
Eu, A occ.	0.996(1)	.948(1)	0.903(4)	0.857(4)	0.996(2)	0.950(1)	0.901(1)
Ir, A occ.	0.004(1)	0.002(3)	0.001(4)	0.000(3)	0.004(2)	0.001(1)	0.003(1)
Ir, B occ.	0.992(1)	1.000(4)	1.000(3)	0.995(3)	0.979(2)	1.000(1)	1.000(1)
Eu, B occ.	0.008(1)	0.000(4)	0.000(3)	0.005(1)	0.021(2)	0.000(1)	0.002(1)
A, U_{iso} (Å^2)	0.00736(6)	0.00747(3)	0.00734(3)	0.00826(3)	0.00405(3)	0.00333(3)	0.00424(8)
B, U_{iso} (Å^2)	0.00419(4)	0.00384(1)	0.00260(4)	0.00183(1)	0.00255(1)	0.00114(1)	0.00108(5)
$Eu_2Ir_2O_7$ (%)	94.71	95.52	94.80	94.49	94.44	95.60	97.39
R_{WP} (%)	8.69	8.35	7.45	7.31	8.84	8.50	8.28
χ^2	1.94	1.89	1.67	1.66	1.99	1.88	1.53

Table 7.2: Results from Rietveld refinement of the synchrotron X-ray powder diffraction data. x_{nom} and x_{XRF} are the nominal and quantitative WDXRF values of the Ca-substitution, respectively. All x values in the text refer to the x_{XRF} value. The data (by row) are as follows: a = pyrochlore cubic lattice parameter, u = x-position of the O $48f$ site, angles within the IrO_6 octahedra, Eu and Ir occupancy values on the A-and B-sites ($A_2B_2O_7$), U_{iso} = isotropic thermal parameters for the A-and B-sites, pyrochlore phase fraction (weight %), Rietveld goodness of fit parameters. At all times during the refinement, oxygen occupancies and U_{iso} values were fixed to 1 and 0.001, respectively. Further details on the refinement model are provided in the text.

x = 0, 0.04, and 0.10 air sintered samples taken at 300 K are all very similar. No new peaks or observable changes in peak shape in the $G(r)$ are observed with increased x or between high and low temperatures *i.e.* as one cools below the magnetic transition or the MIT (if present). The data remain well fit to a model corresponding to the average pyrochlore structure found by XRD in this work and in the literature [196], out to the highest doping studied. The goodness of fit parameter, R_w, falls between 9% and 15% for all fits. Results from these refinements are shown in Figure 7.5. The $A_2B_2O_7$ structure

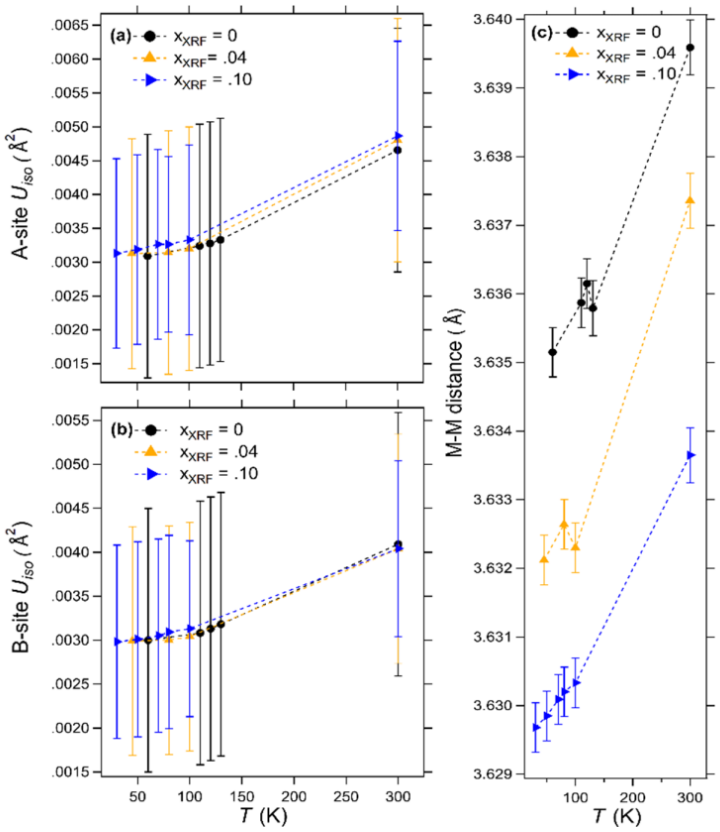

Figure 7.5: Results from PDF refinement of synchrotron X-ray total scattering data on air sintered samples at various temperatures **(a)** A-site atomic displacement parameters **(b)** B-site atomic displacement parameters **(c)** metal-to-metal (M-M) bond distance.

allows only one pairwise metal-to-metal (M-M) length even as the M-O-M angles change. As such, the refined M-M distance is an average over all pairwise combinations of M-M nearest neighbors (Eu-Eu, Ir-Ir, Ca-Ir etc.). The dependence of the M-M distance on temperature is roughly linear for each sample, showing a small decrease in parallel with the lattice parameter, consistent with the average structure data. No strong feature is observed at T_{MIT} or T_N although the $x = 0$ and 0.04 samples do show a slight deviation (within error) from the linear decrease. The isotropic atomic displacement parameters for Ir and Eu remain small and of similar magnitude for all x values studied and decrease with temperature as expected.

7.3.3 Charge Transport and Magnetism

We now turn to the changes observed in the charge transport and magnetism that accompany the introduction of Ca onto the Eu-site. The resistivity measurements on vacuum sintered samples (Figure 7.6 – results for air sintered samples can be found in Appendix A) show that T_{MIT}, identified via the inflection in $\partial\rho/\partial T$, is fully suppressed-within the doping range $0.04 < x < 0.07$. This is in agreement with a previous report on $(Eu_{1-x}Ca_x)_2Ir_2O_7$ [186]. At $x = 0.04$ the upturn in $\rho(T)$ is considerably less sharp and weakened compared to the parent sample, and the insulating state is less well-defined. This is quantified by the inverse relative resistivity ratio, 1/RRR = 2500 for the parent, compared to 1/RRR $\approx$ 10 for $x = 0.04$. The resistivity takes a clear metallic form for x = 0.07 and 0.13, with no upturn observed down to 2 K. In the nominally metallic regime ($T > T_{MIT}$) of parent $Eu_2Ir_2O_7$, both air and vacuum sintered samples show $\partial\rho/\partial T$ <0 (incoherent) transport behavior as has been reported previously for both polycrystalline and single crystal samples [169, 183]. Ca-doping leads quickly to $\partial\rho/\partial T$ >0 at high temperatures, reminiscent of the crossover behaviour observed under increasing hydrostatic pressure [183], as is illustrated by $\rho(T)$ for the $x = 0.02$ air sintered sample (see Appendix A).

Magnetic susceptibility measurements (Figure 7.7) show the presence of a weak irreversibility in all samples. This irreversibility is associated with the emergence of the AIAO order on the Ir sublattice, as demonstrated by muon spin relaxation/rotation [197] and resonant X-ray diffraction [170] experiments on the parent material. Although the mechanism for the irreversibility has not been unambiguously determined, it is typically attributed to a slight canting of the tetrahedral arrangements of Ir spins [198, 199]. T_{AFM} is therefore best visualized by the subtraction $\chi_{FC} - \chi_{ZFC}$ shown in Figure 7.7**b** and is defined here by the onset of irreversibility (*i.e.* the point in $\chi_{FC} - \chi_{ZFC}$ where the curve

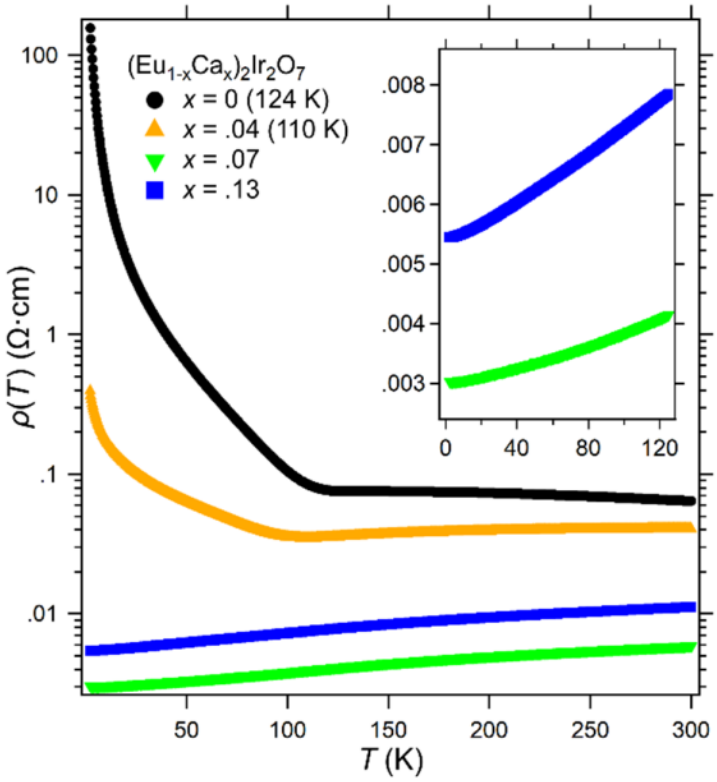

Figure 7.6: Resistivity measurements on pellets of vacuum sintered samples. All data were taken on warming from 2 K to 300 K. The values in parenthesis are T_{MIT}, determined as described in the text. *Inset*: the low temperature (T <125 K) behavior of the metallic samples.

increases rapidly). While the MIT and AIAO ordering occur together in the parent sample ($T_{AFM} = T_{MIT} = 124$ K), the transitions quickly become decoupled in the doped samples. T_{AFM} shows only a small decrease even as T_{MIT} is fully suppressed. $M(H)$ data for both air and vacuum sintered samples (not shown) shows a linear response at all temperatures and all doping levels for fields up to $H = 9$ T, with no clear indication of saturation or significant hysteresis. The magnetism is largely dominated by the Van Vleck susceptibility of the Eu^{3+} ion, which is roughly 75% of the total signal. Subtraction of the Van Vleck term (discussed later in this section) did not qualitatively change the form of the $M(H)$ curves.

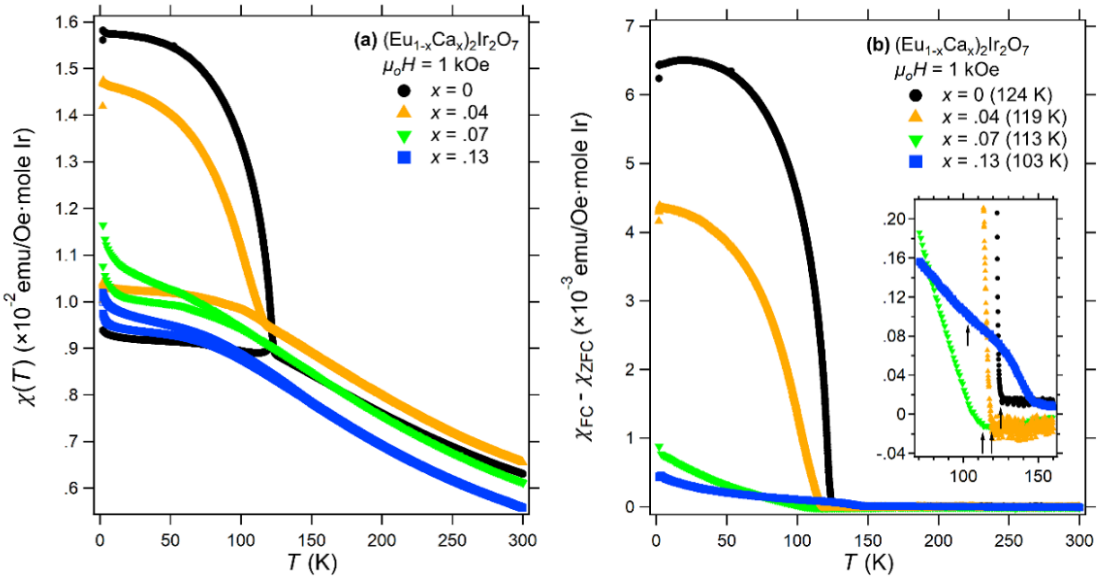

Figure 7.7: **(a)** Magnetic susceptibility, χ = M/H versus temperature data for vacuum sintered samples. All curves were taken on warming from 2 K to 300 K with a field of 1 kOe. The lower curve was taken after cooling in zero field (ZFC) and the upper curve was taken after cooling in a field of 1 kOe **(b)** subtraction of the ZFC curve from the FC one, used to represent the evolution of the irreversibility with Ca-substitution. The values in parenthesis are T_{AFM} as described in the text. *Inset*: closer view of$\chi_{FC} - \chi_{ZFC}$ in the region around T_{AFM} (arrows), as defined in the main text.

While increased Ca-doping decreases the difference between the χ_{FC} and χ_{ZFC} curves, this irreversibility suprisingly persists into the regime where $\rho(T)$ is metallic, as seen clearly in the $x = 0.07$ sample. Direct determination of T_{AFM} is difficult for the metallic $x = 0.13$ sample because the irreversibility data is obscured by a slight, extrinsic upturn in $\chi_{FC} - \chi_{ZFC}$ at 150 K. This 150 K feature is seen much more clearly in the air sintered samples, even at significantly lower doping levels, and dominates the overall susceptibility at higher doping. This is a small moment, synthesis-dependent impurity effect that is dramatically reduced in vacuum sintered samples. Nevertheless, this impurity effect remains weakly resolvable in the $x = 0.13$ sample where the primary magnetic order is almost quenched. As a result, T_{AFM} for the $x = 0.13$ sample cannot be extracted by direct examination of the $\chi_{FC} - \chi_{ZFC}$ curve and has been estimated by linearly extrapolating

from the lower doping values. Examination of the first derivative of the $\chi_{FC} - \chi_{ZFC}$ curve supports this extrapolated value, though it remains an estimate. We note here that, other than this 150 K transition, no qualitative difference is observed between the air and vacuum sintered samples (*i.e.* the charge transport and structural properties). Further details on this point are provided in Appendix A, where we argue that the extra 150 K feature in the susceptibility is due to a secondary state within the sample.

7.3.4 XAS and XMCD

XAS and magnetic circular dichroism (XMCD) provide an element-specific means of probing the spin-orbit coupled nature of the $5d^5$ states of Ir^{4+} [200]. XAS and XMCD spectra collected at the Ir L_2 ($2p_{1/2} \rightarrow 5d_{3/2}$) and L_3 ($2p_{3/2} \rightarrow 5d_{3/2,5/2}$) absorption edges for a range of air sintered samples are shown in Figure 7.8. Select results from the analysis are presented in Table 7.3. In the XAS data, a clear enhancement of the integrated intensity of the white-line, $I_{L2,L3}$, is seen for the L_3 edge relative to the L_2 edge (a description of the calculation can be found in Porter *et al.* [185], following Clancy *et al.* [201]). This increase is quantified by the branching ratio, BR = I_{L3}/I_{L2}, which shows a significant increase over the 'statistical' value of BR = 2, though it decreases with Ca-doping. The statistical value is expected for states with negligible SOC, where the ratio of I_{L3} and I_{L2} is dependent only on the relative numbers of initial core electron states [202, 203, 204]. Due to dipole selection rules in the XAS process ($\Delta J = 0, \pm 1$), the enhancement of the BR indicates a predominant $J = 5/2$ character for the $5d$ hole states. Thus, deviation from the statistical BR indicates a significant influence of SOC, which reconstructs the t_{2g} manifold [168, 205, 201]. These observations are in-line with expectations for the $J_{eff} = 1/2$ state [168, 201]. The influence of SOC can be further seen in the expectation value of the spin-orbit operator, $<L \cdot S>$, which can be directly

related to the BR via the relation $BR = (2+r)/(1-r)$ and $r = <L\cdot S>/\ n_h$ where n_h is the average number of $5d$ holes (equal to 5 for Ir^{4+})[202, 203, 204, 205]. While not equivalent to the SOC term in the Hamiltonian ($H_{SOC} = \zeta L\cdot S$), the large value of $<L\cdot S>$observed here indicates the persistent influence of substantial SOC and that the orbital component of the angular momentum has not been quenched [201].The XMCD measurement at 5 K (Figure 7.8) shows a small, but well-resolved signal, at the L_3 edge, with roughly 0.3% difference in absorption between the two X-ray helicities. A very weak signal is observed at the L_2 edge for the parent sample, while there is no signal resolvable for the $x = 0.10$ sample. The occurrence of a large Ir L_3 XMCD signal with minimal L_2 signal in both samples is characteristic of the $J_{eff} = 1/2$ state. The persistence of this behavior in the metallic $x = 0.10$ sample contrasts with the nearly zero Ir L_2 and L_3 XMCD signals seen for metallic/paramagnetic $Pr_2Ir_2O_7$ [206]. This disparity highlights that carrier-doping provides a distinct mechanism from chemical pressure for modifying T_{AFM} / T_{MIT} and indicates a tangible distinction between the resulting metallic states.

Calculations based on application of the sum rules reveal a small Ir moment of $\approx$ 0.005 μ_B/Ir. Details on this calculation and estimation of the $<T_Z>$term can be found in Porter *et al.* [185]. A previous measurement for Sr_2IrO_4, which also contains Ir^{4+} in a cubic CEF environment, showed a L_3 XMCD signal of 3%, with a corresponding net moment of $\approx 0.05\ \mu_B$/Ir in the weakly ferromagnetic state [207]. This scales well with our own results. The calculated ratio $L_Z/S_Z = 3.3$ and 2.4 for $x = 0$ and 0.10, respectively, indicates a large orbital contribution to the total moment and the positive sign indicates parallel spin and orbital moments (unlike what is expected for the atomic $J = 1/2$ state [168]). The decrease with doping is driven by the change in the L_2 XMCD and is likely exaggerated since an L_2 signal was not well resolved in the measurement of the $x = 0.10$ sample (note that the L_Z/S_Z ratio is independent of the number of holes). These results, together with the enhanced BR from the XAS data, provide a clear indication of a J_{eff}

= 1/2 state in $Eu_2Ir_2O_7$, which is gradually weakened with Ca-doping and the onset of metallic behavior but is not completely destabilized.

	n_h (q_e)		Ir valence					
x	Nominal	XAS	Nominal	XAS	BR ($a.u.$)	$<L\cdot S>$	m_{tot} (μ_B/Ir)	L_z/S_z
0	5	–	4+	–	5.7(3)	2.77(9)	0.0045(9)	3.3
0.06	5.06	4.97(8)	4.06+	3.97(8)	5.6(2)	2.70(9)	–	–
0.1	5.08	4.84(8)	4.10+	3.84+	4.8(2)	2.32(9)	0.0053(6)	2.3

Table 7.3: Results from analysis of the XAS (T = 300 K and x = 0, 0.06, 0.10) and XMCD (T = 5 K and x = 0, 0.10) at the Ir $L_{2,3}$ edges. The nominal n_h and Ir valence is determined by the x value. The XAS n_h and Ir valence is calculated by multiplying the valence in the parent (4+) by the ratio of I_{doped}/I_{parent}, where $I = I_{L2} + I_{L3}$. BR = branching ratio, $<L\cdot>$= expectation value of the spin-orbit operator, m_{tot} = sum of the spin (m_s) and orbital (m_l) moments at H = 5 T, $L_Z/S_Z = m_l/m_s$.

The calculated moment from XMCD ($\approx 0.005\ \mu_B$/Ir) is similar to values found from bulk DC magnetometry measurements (magnetization versus field) at T = 5 K for other pyrochlore iridates with non-magnetic A-sites: $Y_2Ir_2O_7$ (0.005 μ_B/Ir) [188] and $Lu_2Ir_2O_7$ (0.01 μ_B/Ir) [208]. Reported magnetization measurements for $Eu_2Ir_2O_7$, as well as our own, show a net magnetization of 0.09 μ_B/Ir at 5 T [187, 209]. The origin of the discrepancy is due to the Van Vleck contribution of Eu^{3+}, which does not contribute to the Ir XMCD. To deconvolve the Van Vleck and AIAO contributions, we measured $\chi(T)$ for a similarly prepared sample of $Eu_2Ir_2O_7$ under the same field conditions as that used for the XMCD experiment (1 T field-cool, 5 T measurement field). The data above T_{AFM} (125 K $< T <$ 300 K) were fit to the form $\chi_{VV}(T) + \chi_0$ where χ_{VV} is the Van Vleck contribution with a single fitting parameter (λ, the spin-orbit coupling constant) [210]. χ_0 is a (positive) constant Pauli paramagnetic term and was constrained to be close to the essentially temperature independent susceptibility above T_{AFM} seen for $Y_2Ir_2O_7$ and $Lu_2Ir_2O_7$ ($\approx 5\ 10^{-4}$ emu/mole Ir $\cdot$ Oe) [188, 208]. After subtracting

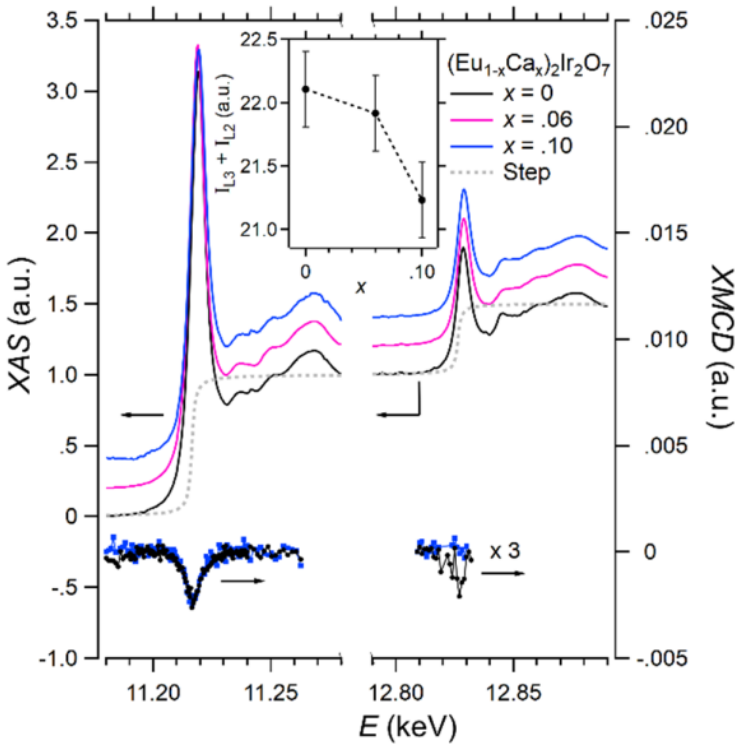

Figure 7.8: X-ray spectroscopy measurements collected on air sintered samples. The solid lines correspond to the XAS data (T = 300 K) while the markers show the XMCD (T = 5 K,1 T field-cool, 5 T measurement). The dashed line is the step function used in the XAS analysis. *Inset*: sum of the L_2 and L_3 white-line integrated intensities ($I_{tot} = I_{L3} + I_{L2}$) for the measured samples.

the Van Vleck contribution, the moment from DC magnetometry at $T = 5$ K is ≈ 0.008 μ_B/Ir, in reasonable agreement with the XMCD moment.

Due to the sensitivity of the XAS process to unoccupied $5d$ states, carrier-doping can be quantified by analysis of the white-line features [201, 205]. Since the sum $I_{L2} + I_{L3}$ is proportional to the local density of unoccupied $5d$ states, comparison of Ca-doped samples to the parent compound reflect changes in the average Ir valence. Generally, this change can also be seen through shifts of the energy of the white-line, with a positive shift indicating an increase in valence. Here we see only small shifts in the white-line position for our Ca-substituted samples (on the order of 0.1 eV), which do not show a consistent direction. The small shift at these doping values is in-line with the observed change

of 1.3 eV/hole from a survey of 4+, 5+ and 6+ iridates [201]. Considering the energy resolution and repeatability of the monochromator (1 and 0.1 eV, respectively) the lack of a consistent trend in the white line shifts is not surprising. Since the substitution of Ca^{2+} for Eu^{3+} should result in the addition of holes to the originally half-filled $J_{eff} = 1/2$ state of Ir^{4+} the value of $I_{L2} + I_{L3}$ is also expected to increase. Note that in the strong SOC limit, holes in the J_{eff} state are accessed preferentially by the L_3 edge since those states are derived from the $J = 5/2$ states of the SOC split $5d$ manifold [168]. As such I_{L3} is much more sensitive to changes in the $J_{eff} = 1/2$ hole population than I_{L2} and they need not change in tandem. However, we observe a marked *decrease* in I_{L3} from the parent to the $x = 0.10$ sample. The observed trend in BR is also opposite what would be expected for hole-doping, though the magnitude of the change is greater than would be expected from the small changes in Ir valence. These results are suggestive of electron doping rather than the expected hole doping.

7.4 Discussion

Clear changes in the structure and magnetism accompany the breakdown of the SOC-assisted Mott insulating state across the series $(Eu_{1-x}Ca_x)_2Ir_2O_7$. The structural evolution with increasing Ca-doping indicates that the crystallographic symmetry of the parent compound is maintained across the series and below T_{MIT} for both the average (long-range) and local (short-range) structures. Although the symmetry of the average structure is maintained with Ca-substitution, features of the structure are still modified. First, u decreases with increasing Ca-content, leading to a slight increase of the Ir-O-Ir bond angle. This observation implies that that Ca-doping leads to a small, sterically driven increase in the Ir valence bandwidth due to greater overlap of the Ir $5d$ t_{2g} orbitals [211]. However, the value of the Ir-O-Ir bond angle remains less than the value found for

metallic $Pr_2Ir_2O_7$ ($\approx 132°$) [190] for all samples.

Counter-intuitively, despite 8-fold coordinated Ca^{2+} being larger than Eu^{3+}, the other structural change induced by Ca-doping is a decrease in the lattice parameter. This behavior is consistent with results from a previous study [186] and the fact that an early report of $Ca_2Ir_2O_7$ shows a lattice parameter significantly smaller than $Eu_2Ir_2O_7$ [212]. Even though the bond angle change is analogous to what is seen upon moving to a larger A-site cation, the lattice parameter changes in the opposite direction. This indicates that the structural response to Ca-doping is not simply dependent on the difference in ionic radius relative to the ion that is being replaced (*i.e.* a steric effect), but other effects such as an electronic deformation potential may dominate the lattice response. The resulting reduction in interatomic distances may also contribute to a small increase in the Ir valence bandwidth. However, the weak dependence of T_{MIT} on pressure [183], which effects both the Ir-O-Ir bond angle and lattice parameter [213] means that these small changes in bandwidth most likely do not contribute meaningfully to the depression of T_{MIT}. Rather, filling-control is seen as the dominant cause of metallic behavior in $(Eu_{1-x}Ca_x)_2Ir_2O_7$, as discussed later. The small increase in the bandwidth may still be partially responsible for the accelerated decrease of the BR, since it acts to mix the J_{eff} states [214].

The XAS data indicate that a clear change in the Ir valence accompanies the depression of T_{MIT} with Ca-doping. However, the nature of this filling-control is, based on the change in the white-line intensities, a net *increase* in the number of electrons in the Ir $J_{eff} = 1/2$ state (*i.e.* electron doping). Based on the robust Ca^{2+} oxidation state this suggests an active compensatory mechanism for the holes added by Ca-doping. A bond valence sum (BVS) calculation for Ca^{2+} in $(Eu_{1-x}Ca_x)_2Ir_2O_7$, using the Ca/Eu-O distances derived from the results of the synchrotron XRD refinement, shows that Ca is consistently overbonded (*i.e.* the calculated BVS value for 8-fold coordination is greater

than the formal valence of 2+). Such overbonding can be a sign of compensating defects or displacements within the oxygen sublattice [215]. Oxygen vacancies, which are known to occur readily in the pyrochlore structure[71, 216, 211] are therefore a natural candidate for the proposed compensatory mechanism. The presence of A-site vacancies – suggested by the sum of the XRF determined value of the A-site Ca occupancy and the refined value of the A-site occupancy from synchrotron XRD being <1 – should also favor compensating oxygen vacancies.

Unfortunately, characterizing the O-site occupancy in $Eu_2Ir_2O_{7-y}$ is challenging as X-rays lack relative sensitivity to oxygen and, as previously mentioned, absorption issues impede a high-resolution application of powder neutron diffraction. A simple calculation based on charge neutrality with the A-site vacancy concentration indicated by the synchrotron XRD refinement and the XAS determined Ir valences yields y-values of 0.18 and 0.56 for the $x = 0.06$ and 0.10 samples, respectively. This rough estimate of the oxygen content is on par with what is found for $(Bi_{1-x}Ca_x)_2Ir_2O_{7-y}$ synthesized in air, where powder neutron diffraction shows y-values of $\approx$ 0.1 - 0.2 [215, 216] although no comparable relationship between x and y was noted previously [215]. This indicates that, if y scales with x, electron-doping via oxygen vacancies can dominate over the effect of Ca-doping.

It should be noted that the parent iridates do not seem to suffer a propensity to form oxygen vacancies [217, 218]. Therefore, other possible explanations for the XAS data should also be considered. Since the Ir-O bond lengths in the IrO_6 octahedra depend directly on the value of the lattice parameter and u, Ca-doping also shortens these bonds. Therefore, an alternative explanation for the XAS data is that these shortened bond lengths enhance the hybridizationof the O $2p$ and Ir $5d$ orbitals (*i.e.* increase covalency), causing compensatory charge transfer to the Ir site. BVS analysis provides support for increased covalency of the Ir–O bond. In $Eu_2Ir_2O_7$,the Ir^{4+} BVS is found to be 4.07,

relatively close to the formal valence. For Ir^{5+} in $Ca_2Ir_2O_7$ [212] the value (6.33) is substantially higher that the formal valence, consistent with increased covalency. Charge transfer has also been invoked to explain the decrease in the XAS $I_{tot} = I_{L2} + I_{L3}$ with increasing (physical) pressure observed for the hyper-kagome iridate compound $Na_3Ir_3O_8$ [214]. In the case of $Na_3Ir_3O_8$, the change in Ir-O bond distance is relatively small ($\approx$ 0.1% from ambient to 10 GPa) yet a significant ($\approx$ 10 %) decrease in I_{tot} is observed. In $Eu_2Ir_2O_7$ the change in Ir-O bond length is significantly larger (changing roughly linearly with $\approx 0.65\%$ difference between $x = 0$ and $x = 0.10$) while the change in I_{tot} is less ($\approx$ 4 %). The difference in magnitude could potentially be accounted for by the fact that the added holes from Ca-doping are driving I_{tot} in the opposite direction. While we cannot directly determine whether one, or both, of these compensatory mechanisms causes the observed valence change, these results indicate that direct determination of the Ir valence should be considered an essential component in interpreting doping studies of pyrochlore iridates.

Returning to the X-ray data, the total scattering measurements provide a means for examining whether changes in the local structure are relevant to the mechanism of the MIT. Changes in local structure can dramatically modify electronic and magnetic behaviors, as has been studied in the manganite perovskites [67, 66, 65]. However, the consistency of the PDF spectra for $Eu_2Ir_2O_7$ across the thermal T_{MIT} (Figure 7.4**a**) does not support this idea. The lack of new correlation peaks, changes in peak shape at low temperature, or significant modification of the high temperature peaks, indicates that the symmetry of the local structure at the A and B-sites does not deviate at $T < T_{MIT}$ (within resolution) from that of the average structure. The similarity of the room temperature spectra for all samples (Figure 7.4**b**) further indicates that the addition of Ca does not alter the local structure symmetry.

All spectra of doped compounds remain well fit by the crystallographic structure

of the parent, and this similarity suggests that Ca enters the lattice homogeneously without observable nanophase chemical separation. If inhomogeneous local distortions were occurring with doping, then one would expect broadening of peaks associated with the M–M distances or formation of a new correlation peak due to the different nearest neighbor distance for a Ca-Ca pair. This is not observed. Focusing on the highest doped sample ($x = 0.10$), where local distortions would be most readily detected, we see that the data remains well described by a disordered, high-symmetry model. The M-M distances (Figure 7.5) show only a small, roughly linear, decrease with doping with no distinct feature at T_{MIT}. The values and trend agree well with the changes in the average structure refined from the synchrotron XRD data. The lack of dependence of the isotropic atomic displacement parameters on doping, essentially unchanged within error, further supports the picture of homogeneous carrier-doping and suggests minimal disorder of the local structure. However, the data presented here is not sensitive enough, at this level of doping, to rule out changes in the local structure around the Ca ions. It remains possible that oxygen and/or A-site vacancies occur preferentially near the Ca or that the overbonding of the Ca results in neighboring displacements on the oxygen sublattice.

The approach to a fully metallic state is characterized by two related features in the magnetization: the decoupling of T_{AFM} from T_{MIT} and the persistence of the irreversibility in $\chi(T)$. This irreversibility coincides with the formation of the AIAO state confirmed for the parent compound [170] and thus provides an easily observed metric for the evolution of the magnetism. The decrease in the magnitude of the irreversibility is therefore interpreted as an indication of the gradual breakdown of the AIAO state, with likely short-range AIAO correlations remaining at intermediate (metallic) levels of Ca-doping. The persistence of this signature in the metallic state suggests the occurrence of electronic phase separation, without, as evidenced by the total scattering experiments,

observable corresponding chemical phase separation. Initial muon spin relaxation (μ^+SR) experiments on $(Eu_{1-x}Ca_x)_2Ir_2O_7$ also offer some support for this picture, as the observed magnetic volume fraction decreases with increased Ca-doping [219]. Additionally, a separate μ^+SR study on isovalent substitution in $(Eu_{1-x}Bi_x)_2Ir_2O_7$ reported an eventual cross-over to short-range magnetic order [220]. Analogous behavior has also been observed for electron-doped $(Sr_{1-x}La_x)_2IrO_4$, where the separation between χ_{FC} and χ_{ZFC} below the AFM transition is similarly depressed with doping and persists even as the charge gap is destabilized [221]. In the present case, the addition of charge carriers in $(Eu_{1-x}Ca_x)_2Ir_2O_7$ results in local regions where the $J_{eff} = 1/2$ state deviates from half-filling and the Mott gap collapses locally. This behavior is summarized in the phase diagram shown in Figure 7.9.

As noted earlier, different relative evolutions of T_{AFM} and T_{MIT} have been reported in similar doping studies. The observation for $(Y_{1-x}Ca_x)_2Ir_2O_7$ of T_{AFM} showing no decrease with doping [188] is most likely due to the obscuring, extrinsic effect of the synthesis dependent high-temperature transition. Interestingly, $(Eu_{1-x}Ca_x)_2Ir_2O_7$ powder samples produced using high-pressure synthesis [186] do not show the decoupling of T_{MIT} and T_{AFM} observed in our study. Instead, T_{MIT} and T_{AFM} decrease in tandem. The origin of this discrepancy merits further investigation and comparison of the chemical and crystallographic details between powders synthesized under ambient and high-pressure conditions; however, at a minimum, it reveals that the coupling between the two transitions is sensitive to subtle structural details. Notably, for $(Nd_{1-x}Ca_x)_2Ir_2O_7$, synthesized in the same manner as reported here, T_{MIT} and T_{AFM} remained locked together. Therefore, it appears that the magnetism (or lack thereof) of the A-site ion may determine whether the compound can enter a phase separated state. Determining the root cause of this variability - as related to both synthesis method and the magnetism of the A-site ion - seems likely to shed light on the connection between the MIT and the AIAO order

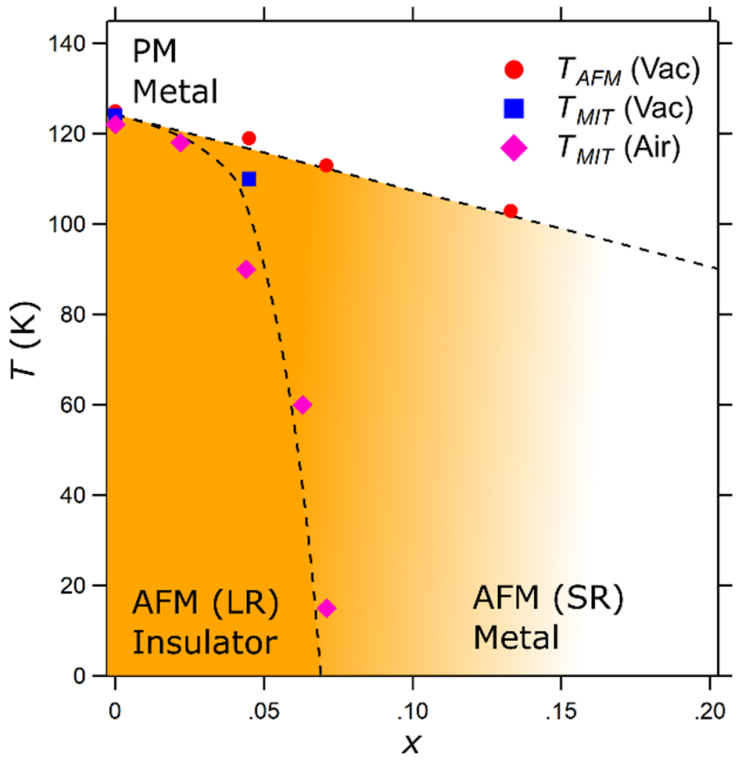

Figure 7.9: Phase diagram of $(Eu_{1-x}Ca_x)_2Ir_2O_7$ based on bulk magnetization (T_{AFM}) and charge transport measurements (T_{MIT}). T_{MIT} is shown for both vacuum and air sintered samples. Dashed lines indicate suggested phase boundaries while the color gradient represents the gradual evolution from long-range (LR) to short-range (SR) antiferromagnetism, followed by the eventual collapse of the AIAO state.

in this materials class.

Finally, we consider again the small moment determined from the Ir L edge XMCD measurement. It should be emphasized that, while XMCD probes the net ferromagnetic moment of the system, there are still two distinct mechanisms which may contribute to the measured signal: net ferromagnetism concomitant with the formation of AIAO order and/or a field-dependent response of the AIAO order. More specifically, the former contribution could be weak ferromagnetism arising from the AFM domain walls (present due to the existence of both "all-out-all-in" and "all-in-all-out" domains [222, 223] while the latter could be spin-canting within the AIAO structure. That the measured Ir moment is consistent with other pyrochlore iridates with non-magnetic A-sites (A = Y, Lu)

points to a common basis for the Ir XMCD signal. We also note that a parallel XMCD measurement on $Nd_2Ir_2O_7$ yielded a very similar value [185]. The source of this signal remains an open question, and XMCD measurements of the remanence (*i.e.* hysteresis loops) will be needed to distinguish between these two contributions. However, it is notable that the moment is identical within error upon progressing from an insulating ($x = 0$) to a metallic ($x = 0.10$) state. Regardless of the mechanism, this stability seems consistent with a picture of electronic phase separation: local pockets of the parent insulating/AIAO state, in which the weak Ir magnetic polarization is unchanged, remain deep into the metallic regime.

7.5 Conclusions

Our data indicate that substitution of Ca for Eu in $(Eu_{1-x}Ca_x)_2Ir_2O_7$ occurs without an observable change in lattice or site symmetry. T_{MIT} is depressed with Ca-doping, and changes in the Ir valence and the Ir-O-Ir bond angle/Ir-O distance show that the low-temperature insulating state collapses under the majority influence of filling-control. The overall nature of the filling-control on the Ir-sites, contrary to expectation, is electron doping, suggesting that a significant compensatory mechanism is at work. The presence of oxygen vacancies, which scale with Ca-doping, or, alternatively, increased covalency of the Ir-O bonds, are suggested as possibilities. The AIAO ordered state survives locally well into the metallic state, with T_{AFM} responding only weakly to Ca-doping. This behavior is understood to be the result of the formation of an electronically phase separated state with carrier-doping. The dependence of this phase separation on the synthesis method, as well as other variations in bulk properties of doped and un-doped $Eu_2Ir_2O_7$, illustrates that even minor stoichiometry variations can dramatically alter the observed properties. Careful attention to synthesis and bulk characterization will be needed to ascertain the

intrinsic properties of the pyrochlore iridates and realize unconventional states within them. Lastly, XMCD measurements reveal a weak Ir signal that appears to be a generic property of the Ir sublattice, although further measurements are needed to determine its origin.

Appendix A

Magnetism and Charge Transport of Air Sintered $(Eu_{1-x}Ca_x)_2Ir_2O_7$

We provide here a brief discussion of the magnetism and charge transport of the air sintered samples and their dependence on synthesis method. The main qualitative difference between the air and vacuum sintered samples is the occurrence of additional irreversibility at $T^* = 150$ K in $\chi(T)$, above T_{AFM}. Figure A.1 shows clearly that this is a synthesis dependent feature which is reduced upon vacuum sintering. It should be noted that this feature is also not seen in $(Eu_{1-x}Ca_x)_2Ir_2O_7$ synthesized under high-pressure [186]. In air sintered samples, the strength of the irreversibility at T^* trades off with T_{AFM} with Ca-doping until T^* eventually dominates the magnetism and T_{AFM} becomes hard to define. However, no upturn in the Ir XMCD (for the air sintered samples) was seen in the region $T_{AFM} < T < T^*$. No corresponding signature of T^* is seen in the charge transport (Figure A.2) which is qualitatively similar to what was seen in the vacuum sintered samples, albeit with a more gradual decrease in T_{MIT}. The air sintered parent sample also has a much lower *1/RRR* value than the vacuum sintered one ($\approx$ 490 and 2500, respectively). The change in *1/RRR* of the parent sample likely reflects an improved

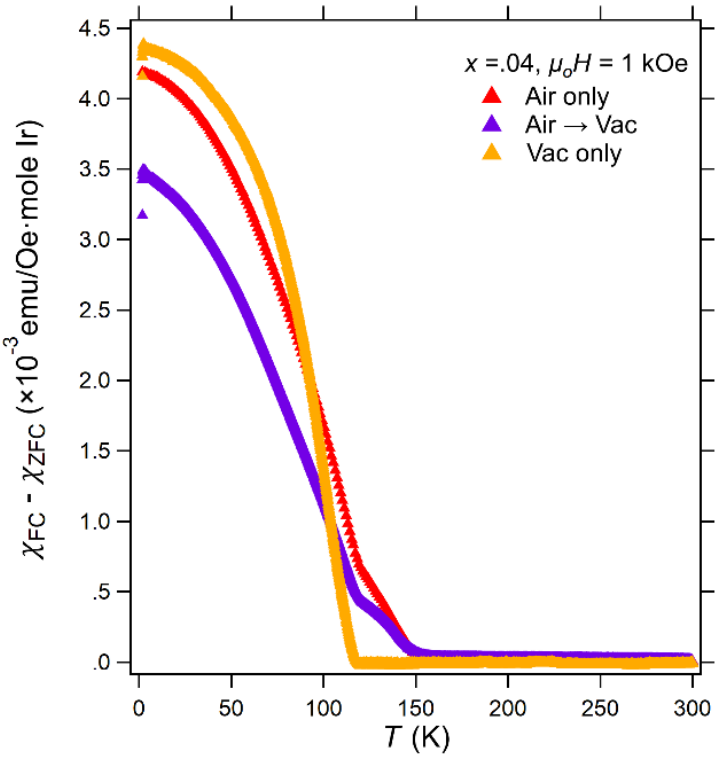

Figure A.1: Comparison of the FC – ZFC magnetic susceptibility for $x = 0.04$ samples synthesized using different procedures. The "Air only" curve was synthesized completely in air (the first procedure in the Section 7.2). The "Air → Vac" curve is the same sample, following the addition of excess IrO_2 and vacuum sintering. The "Vac only" curve is a new sample, synthesized with the complete vacuum sintering procedure (the second procedure in Section 7.2)

stoichiometry of the Ir sublattice [198], particularly since vacuum sintering reduces the loss of IrO_2 via the reaction $IrO_2 + O_2$ (g) $\rightarrow IrO_3$ (g) [109].

Analogous behavior was reported in a study on polycrystalline $(Y_{1-x}Ca_x)_2Ir_2O_7$ synthesized in a similar manner as the air sintered procedure in Section 7.2 [188]. In that case, a secondary transition in $\chi(T)$ develops at $T^* = 190$ K and grows with Ca-doping to dominate the feature at 160 K which corresponds to the T_{MIT} in the $x = 0$ sample. This synthesis dependent phenomenon may therefore be generic in carrier-doped pyrochlore iridates. While the source of this additional feature is currently unresolved, the elimination of T^* via vacuum sintering implies the mechanism is related to defects

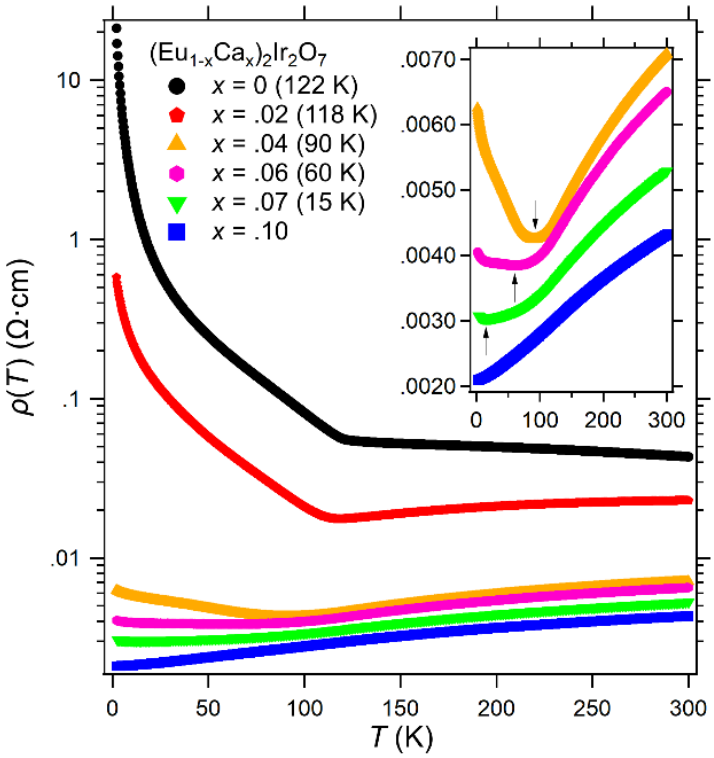

Figure A.2: Resistivity measurements on pellets of air sintered samples. All data were taken on warming from 2 K to 300 K. The values in the parenthesis are T_{MIT} determined as described in the main text. *Inset*: closer view of the higher x samples. Black arrows indicate the minima in $\rho(T)$.

on the Ir sublattice.

Bibliography

[1] M. C. Hatnean, M. R. Lees, O. A. Petrenko, D. S. Keeble, G. Balakrishnan, M. J. Gutmann, V. V. Klekovkina, and B. Z. Malkin *Phys. Rev. B* **91** (2015), no. 17 174416.

[2] J. Xu, O. Benton, V. K. Anand, A. T. M. N. Islam, T. Guidi, G. Ehlers, E. Feng, Y. Su, A. Sakai, P. Gegenwart, *et. al. Phys. Rev. B* **99** (2019), no. 14 144420.

[3] J. Paglione, N. P. Butch, and E. E. Rodriguez, eds., *Fundamentals of Quantum Materials: A Practical Guide to Synthesis and Exploration*. World Scientific, first ed., 2021.

[4] J. L. Schmehr, M. Aling, E. Zoghlin, and S. D. Wilson *Rev. Sci. Instrum.* **90** (2019), no. 4 043906.

[5] E. Zoghlin, J. Schmehr, C. Holgate, R. Dally, Y. Liu, G. Laurita, and S. D. Wilson *Phys. Rev. Mater.* **5** (2021), no. 084403 1–11.

[6] E. Zoghlin, Z. Porter, S. Britner, S. Husremovic, Y. Choi, D. Haskel, G. Laurita, and S. D. Wilson *J. Phys.: Condens. Matter* **33** (2021), no. 055601 1–13.

[7] H. C. Theuerer, "Method of processing semiconductive materials." U.S. Patent No. 3,060,123.23, 1962.

[8] P. H. Keck and M. J. E. Golay *Phys. Rev.* **89** (1953), no. 6 1297.

[9] P. H. Keck, W. Van Horn, J. Soled, and A. MacDonald *Rev. Sci. Instrum.* **25** (1954), no. 4 331–334.

[10] J. L. Schmehr and S. D. Wilson *Annu. Rev. Mater. Res.* **47** (2017) 153–174.

[11] H. A. Dabkowska, A. B. Dabkowski, R. Hermann, J. Priede, and G. Gerbeth in *Handbook of Crystal Growth: Bulk Crystal Growth: Part A*, pp. 281–329. Elsevier, 2014.

[12] A. Mackenzie, R. Haselwimmer, A. Tyler, G. Lonzarich, Y. Mori, S. Nishizaki, and Y. Maeno *Phys. Rev. Lett.* **80** (1998), no. 1 161.

[13] Z. Zhu, P. A. Maksimov, S. R. White, and A. L. Chernyshev *Phys. Rev. Lett.* **119** (2017), no. 15 157201.

[14] H. A. Dabkowska and A. B. Dabkowski in *Springer Handbook of Crystal Growth*, pp. 367–391. Springer, 2010.

[15] S. M. Koohpayeh *Prog. Cryst. Growth Char. Mater.* **62** (2016), no. 4 22–34.

[16] S. Koohpayeh, D. Fort, and J. Abell *Prog. Cryst. Growth Char. Mater.* **54** (2008), no. 3-4 121–137.

[17] T. Fujii, T. Watanabe, and A. Matsuda *J. Cryst. Growth* **223** (2001), no. 1-2 175–180.

[18] A. Cröll, M. Schweizer, A. Tegetmeier, and K. Benz *J. Cryst. Growth* **166** (1996), no. 1-4 239–244.

[19] D. Souptel, W. Löser, and G. Behr *J. Cryst. Growth* **300** (2007), no. 2 538–550.

[20] A. Balbashov and S. Egorov *J. Cryst. Growth* **52** (1981) 498–504.

[21] W. A. Phelan, J. Zahn, Z. Kennedy, and T. M. McQueen *J. Solid State Chem.* **270** (2019) 705–709.

[22] T. Ito, T. Ushiyama, Y. Yanagisawa, Y. Tomioka, I. Shindo, and A. Yanase *J. Cryst. Growth* **363** (2013) 264–269.

[23] I. Langmuir *Phys. Rev.* **2** (1913), no. 5 329.

[24] Z. Porter, E. Zoghlin, J. L. Schmehr, and S. D. Wilson *J. Cryst. Growth* **578** (2022) 126432.

[25] D. A. Porter and K. E. Easterling, *Phase transformations in metals and alloys*. CRC press, 2009.

[26] J. Zhang, H. Zheng, Y. Ren, and J. Mitchell *Cryst. Growth & Design* **17** (2017), no. 5 2730–2735.

[27] H. Zheng, J. Zhang, B. Wang, D. Phelan, M. J. Krogstad, Y. Ren, W. A. Phelan, O. Chmaissem, B. Poudel, and J. Mitchell *Crystals* **9** (2019), no. 7 324.

[28] A. V. Kostanovsky and A. V. Kirillin *Int. J. Thermophys.* **17** (1996) 507–513.

[29] W. Class, *Contractor report*, Tech. Rep. NASA-CR-1171, NASA, 1968.

[30] D. B. Gasson and B. Cockayne *J. Mater. Sci.* **5** (1970) 100–104.

[31] J. S. Haggerty, *Final report*, Tech. Rep. NASA-CR-120948, NASA, 1972.

[32] P. Telang, A. Maljuk, D. Rout, R. Hu, M. Skoulatos, K. Karmakar, S. Seiro, B. Roessli, U. Stuhr, B. Buchnerb, S.-W. Cheong, and S. Singha *J. Cryst. Growth* **507** (2019) 406–412.

[33] S. Koohpayeh, D. Fort, A. Bradshaw, and J. Abell *J. Cryst. Growth* **311** (2009), no. 8 2513–2518.

[34] M. C. Hatnean, M. R. Lees, and G. Balakrishnan *J. Cryst. Growth* **418** (2015) 1–6.

[35] H. Roth, *Single crystal growth and electron spectroscopy of d1-systems*. PhD thesis, Universität zu Köln, 2008.

[36] G. Amow, J.-S. Zhou, and J. Goodenough *J. Solid State Chem.* **154** (2000), no. 2 619–625.

[37] H. Zhou and J. Goodenough *J. Phys.: Condens. Matter* **17** (2005), no. 46 7395.

[38] D. Lovinger, E. Zoghlin, P. Kissin, G. Ahn, K. Ahadi, P. Kim, M. Poore, S. Stemmer, S. Moon, S. Wilson, *et. al. Phys. Rev. B* **102** (2020), no. 8 085138.

[39] G. J. Shu, J. C. Tian, C. K. Lin, M. Hayashi, S. C. Liou, W. T. Chen, D. P. Wong, H. L. Liou, and F. C. Chou *New J. Phys.,* **20** (2018), no. 5 059501.

[40] A. N. Chiaramonti, *Structure and thermodynamics of model catalytic oxide surfaces*. PhD thesis, Northwestern University, 2005.

[41] S. J. Blundell, *Magnetism in Condensed Matter*. Oxford University Press, 2001.

[42] M. P. Marder, *Condensed Matter Physics*. John Wiley and Sons, second ed., 2010.

[43] J. J. Sakurai and J. J. Napolitano, *Modern Quantum Mechanics*. Pearson Education, Inc., second ed., 2011.

[44] R. R. P. Singh, W. E. Pickett, D. W. Hone, and D. J. Scalapino *arXiv:cond-mat/0007086v1* (2000).

[45] L. Savary and L. Balents *Rep. Prog. Phys* **80** (2016), no. 1 016502.

[46] A. Kitaev *Anal. Phys.* **321** (2006), no. 1 2–111. January Special Issue.

[47] P. A. Lee, N. Nagaosa, and X. G. Wen *Rev. of Mod. Phys.* **78** (2006), no. 1 17–85.

[48] G. L. Squires, *Introduction to the Theory of Thermal Neutron Scattering*. Cambridge University Press, 1978.

[49] D. L. Price and F. Fernandez-Alonso *Exp. Meth. Phys. Sci.* **44** (2013) 1–136.

[50] F. J. Bermejo and F. Sordo *Exp. Meth. Phys. Sci.* **44** (2013) 137 – 243.

[51] B. T. M. Willis and C. J. Carlile, *Experimental Neutron Scattering*. Oxford University Press, first ed., 2009.

[52] M. Tinkham, *Group theory and quantum mechanics*. Courier Corporation, 2003.

[53] S. W. Lovesey, *Theory of Neutron Scattering from Condensed Matter*, vol. 2. Oxford University Press, 1986.

[54] J. M. Carpenter *Nucl. Instrum. Methods* **145** (1977), no. 1 91–113.

[55] M. Arai *Exp. Meth. Phys. Sci.* **44** (2013) 245 – 320.

[56] J. Rodriguez, D. Adler, P. Brand, C. Broholm, J. Cook, C. Brocker, R. Hammond, Z. Huang, P. Hundertmark, J. Lynn, *et. al. Meas. Sci. Technol.* **19** (2008), no. 3 034023.

[57] M. B. Stone, J. L. Niedziela, D. L. Abernathy, L. DeBeer-Schmitt, G. Ehlers, O. Garlea, G. Granroth, M. Graves-Brook, A. I. Kolesnikov, A. Podlesnyak, *et. al. Rev. Sci. Instrum* **85** (2014), no. 4 045113.

[58] G. Granroth, A. Kolesnikov, T. Sherline, J. Clancy, K. Ross, J. Ruff, B. Gaulin, and S. Nagler in *J. Phys.: Conference Series*, vol. 251, p. 012058, IOP Publishing, 2010.

[59] G. E. Granroth, D. H. Vandergriff, and S. E. Nagler *Physica B: Cond. Matter* **385** (2006) 1104–1106.

[60] F. Ye, Y. Liu, R. Whitfield, R. Osborn, and S. Rosenkranz *J. Appl. Crystallogr.* **51** (2018), no. 2 315–322.

[61] R. Comes, M. Lambert, and A. Guinier *Solid State Commun.* **6** (1968), no. 10 715–719.

[62] M. Senn, D. Keen, T. Lucas, J. Hriljac, and A. Goodwin *Phys. Rev. Lett.* **116** (2016), no. 20 207602.

[63] C. M. Culbertson, A. T. Flak, M. Yatskin, P. H.-Y. Cheong, D. P. Cann, and M. R. Dolgos *Sci. Rep.* **10** (2020), no. 1 1–10.

[64] G. Sala, M. J. Gutmann, D. Prabhakaran, D. Pomaranski, C. Mitchelitis, J. B. Kycia, D. G. Porter, C. Castelnovo, and J. P. Goff *Nat. Mater.* **13** (2014), no. 5 488–493.

[65] A. P. Ramirez *J. Phys.: Condens. Matter* **9** (1997), no. 39 8171.

[66] L. Martín-Carrón, A. De Andres, M. Martínez-Lope, M. Casais, and J. Alonso *Phys. Rev. B* **66** (2002), no. 17 174303.

[67] A. Millis *Nature* **392** (1998), no. 6672 147–150.

[68] R. Welberry and R. Whitfield *Quantum Beam Science* **2** (2018), no. 1 2.

[69] S. Rosenkranz and R. Osborn *Pramana* **71** (2008), no. 4 705–711.

[70] T. Fennell, O. A. Petrenko, B. Fåk, S. Bramwell, M. Enjalran, T. Yavors'kii, M. Gingras, R. Melko, and G. Balakrishnan *Phys. Rev. B* **70** (2004), no. 13 134408.

[71] J. S. Gardner, M. J. Gingras, and J. E. Greedan *Rev. Mod. Phys.* **82** (2010), no. 1 53.

[72] M. A. Subramanian, G. Aravamudan, and G. V. Subba Rao *Prog. Solid State Chem.* **15** (1983), no. 2 55–143.

[73] A. P. Ramirez *Annu. Rev. Mater. Sci.* **24** (1994), no. 1 453–480.

[74] J. G. Rau and M. J. Gingras *Annu. Rev. Condens. Matter Phys.* **10** (2019) 357–386.

[75] J. Gaudet, E. M. Smith, J. Dudemaine, J. Beare, C. R. C. Buhariwalla, N. P. Butch, M. B. Stone, A. I. Kolesnikov, G. Xu, D. R. Yahne, *et. al. Phys. Rev. Lett.* **122** (2019), no. 18 187201.

[76] R. Sibille, N. Gauthier, E. Lhotel, V. Poré, V. Pomjakushin, R. A. Ewings, T. G. Perring, J. Ollivier, A. Wildes, C. Ritter, *et. al. Nat. Phys.* **16** (2020), no. 5 546–552.

[77] B. Gao, T. Chen, D. W. Tam, C.-L. Huang, K. Sasmal, D. T. Adroja, F. Ye, H. Cao, G. Sala, M. B. Stone, *et. al. Nat. Phys.* **15** (2019), no. 10 1052–1057.

[78] C. Mauws, A. M. Hallas, G. Sala, A. A. Aczel, P. M. Sarte, J. Gaudet, D. Ziat, J. A. Quilliam, J. A. Lussier, M. Bieringer, *et. al. Phys. Rev. B* **98** (2018), no. 10 100401.

[79] Y.-P. Huang, G. Chen, and M. Hermele *Phys. Rev. Lett.* **112** (2014), no. 16 167203.

[80] Y.-D. Li and G. Chen *Phys. Rev. B* **95** (2017), no. 4 041106.

[81] X.-P. Yao, Y.-D. Li, and G. Chen *Phys. Rev. Research* **2** (2020), no. 1 013334.

[82] M. E. Brooks-Bartlett, S. T. Banks, L. D. C. Jaubert, A. Harman-Clarke, and P. C. W. Holdsworth *Phys. Rev. X* **4** (2014), no. 1 011007.

[83] S. Petit, E. Lhotel, B. Canals, M. C. Hatnean, J. Ollivier, H. Mutka, E. Ressouche, A. R. Wildes, M. R. Lees, and G. Balakrishnan *Nat. Phys.* **12** (2016), no. 8 746–750.

[84] O. Benton *Phys. Rev. B* **94** (2016), no. 10 104430.

[85] H. W. J. Blöte, R. F. Wielinga, and W. J. Huiskamp *Physica* **43** (1969), no. 4 549–568.

[86] J. Xu, V. K. Anand, A. K. Bera, M. Frontzek, D. L. Abernathy, N. Casati, K. Siemensmeyer, and B. Lake *Phys. Rev. B* **92** (2015), no. 22 224430.

[87] L. Opherden, J. Hornung, T. Herrmannsdörfer, J. Xu, A. T. M. N. Islam, B. Lake, and J. Wosnitza *Phys. Rev. B* **95** (2017), no. 18 184418.

[88] E. Lhotel, S. Petit, S. Guitteny, O. Florea, M. C. Hatnean, C. Colin, E. Ressouche, M. R. Lees, and G. Balakrishnan *Phys. Rev. Lett.* **115** (2015), no. 19 197202.

[89] J. Xu, O. Benton, A. T. M. N. Islam, T. Guidi, G. Ehlers, and B. Lake *Phys. Rev. Lett.* **124** (2020), no. 9 097203.

[90] C. L. Henley *Annu. Rev. Condens. Matter Phys.* **1** (2010), no. 1 179–210.

[91] J. Xu, A. T. M. N. Islam, I. N. Glavatskyy, M. Reehuis, J.-U. Hoffmann, and B. Lake *Phys. Rev. B* **98** (2018), no. 6 060408.

[92] E. Lhotel, S. Petit, M. C. Hatnean, J. Ollivier, H. Mutka, E. Ressouche, M. R. Lees, and G. Balakrishnan *Nat. Commun.* **9** (2018), no. 1 1–6.

[93] L. Minervini, R. W. Grimes, and K. E. Sickafus *J. Am. Ceram. Soc.* **83** (2000), no. 8 1873–1878.

[94] P. J. Wilde and C. R. A. Catlow *Solid State Ionics* **112** (1998), no. 3-4 173–183.

[95] P. Anithakumari, V. Grover, C. Nandi, K. Bhattacharyya, and A. K. Tyagi *RSC Adv.* **6** (2016), no. 100 97566–97579.

[96] J. L. Payne, M. G. Tucker, and I. R. Evans *J. Solid State Chem.* **205** (2013) 29–34.

[97] P. E. R. Blanchard, R. Clements, B. J. Kennedy, C. D. Ling, E. Reynolds, M. Avdeev, A. P. J. Stampfl, Z. Zhang, and L.-Y. Jang *Inorg. Chem.* **51** (2012), no. 24 13237–13244.

[98] A. Yaouanc, P. Dalmas De Réotier, C. Marin, and V. Glazkov *Phys. Rev. B* **84** (2011), no. 17 172408.

[99] K. A. Ross, T. Proffen, H. A. Dabkowska, J. A. Quilliam, L. R. Yaraskavitch, J. B. Kycia, and B. D. Gaulin *Phys. Rev. B* **86** (2012), no. 17 174424.

[100] D. F. Bowman, E. Cemal, T. Lehner, A. R. Wildes, L. Mangin-Thro, G. J. Nilsen, M. J. Gutmann, D. J. Voneshen, D. Prabhakaran, A. T. Boothroyd, *et. al. Nat. Commun.* **10** (2019), no. 1 1–8.

[101] C. Mauws, N. Hiebert, M. L. Rutherford, H. D. Zhou, Q. Huang, M. B. Stone, N. P. Butch, Y. Su, E. S. Choi, Z. Yamani, *et. al. J. Phys.: Condens. Matter* (2021).

[102] M. Léger, E. Lhotel, M. C. Hatnean, J. Ollivier, A. R. Wildes, S. Raymond, E. Ressouche, G. Balakrishnan, and S. Petit *Phys. Rev. Lett.* **126** (2021) 247201.

[103] O. Arnold, J. Bilheux, J. Borreguero, A. Buts, S. Campbell, L. Chapon, M. Doucet, N. Draper, R. Ferraz Leal, M. Gigg, *et. al. Nucl. Instrum. Meth. in Phys. Res. A* **764** (2014) 156–166.

[104] C. Farrow, P. Juhas, J. Liu, D. Bryndin, E. Božin, J. Bloch, T. Proffen, and S. Billinge *J. Phys.: Condens. Matter* **19** (2007), no. 33 335219.

[105] J. Taylor, O. Arnold, J. Bilheaux, A. Buts, S. Campbell, M. Doucet, N. Draper, R. Fowler, M. Gigg, V. Lynch, *et. al. Bull. Am. Phys. Soc.* **57** (2012).

[106] K. Baroudi, B. D. Gaulin, S. H. Lapidus, J. Gaudet, and R. J. Cava *Phys. Rev. B* **92** (2015), no. 2 024110.

[107] R. Ubic, I. Abrahams, and Y. Hu *J. Am. Ceram. Soc.* **91** (2008), no. 1 235–239.

[108] M. C. Hatnean, C. Decorse, M. R. Lees, O. A. Petrenko, and G. Balakrishnan *Crystals* **6** (2016), no. 7 79.

[109] P. Telang, K. Mishra, A. K. Sood, and S. Singh *Phys. Rev. B* **97** (2018), no. 23 235118.

[110] A. Ghasemi, A. Scheie, J. Kindervater, and S. M. Koohpayeh *J. Cryst. Growth* **500** (2018) 38–43.

[111] A. Mostaed, G. Balakrishnan, M. R. Lees, and R. Beanland *Acta Materialia* **143** (2018) 291–297.

[112] M. J. D. Rushton, R. W. Grimes, C. R. Stanek, and S. Owens *J. Mater. Res.* **19** (2004), no. 6 1603–1604.

[113] S. Schiffler and H. Müller-Buschaum *Z. Anorg. Allg. Chem.* **532** (1986), no. 1 10–16.

[114] M. Yamashita, T. Ishii, and H. Matsuzaka *Coord. Chem. Rev.* **198** (2000), no. 1 347–366.

[115] G. Xu, J. F. DiTusa, T. Ito, K. Oka, H. Takagi, C. Broholm, and G. Aeppli *Phys. Rev. B* **54** (1996) R6827–R6830.

[116] T. Yokoo, T. Sakaguchi, K. Kakurai, and J. Akimitsu *J. Phys. Soc. Japan* **64** (1995), no. 10 3651–3655.

[117] S. E. Nagler, D. A. Tennant, R. A. Cowley, T. G. Perring, and S. K. Satija *Phys. Rev. B* **44** (1991) 12361–12368.

[118] D. A. Tennant, T. G. Perring, R. A. Cowley, and S. E. Nagler *Phys. Rev. Lett.* **70** (1993) 4003–4006.

[119] D. A. Tennant, R. A. Cowley, S. E. Nagler, and A. M. Tsvelik *Phys. Rev. B* **52** (1995) 13368–13380.

[120] B. Kim, H. Koh, E. Rotenberg, S.-J. Oh, H. Eisaki, N. Motoyama, S.-i. Uchida, T. Tohyama, S. Maekawa, Z.-X. Shen, *et. al. Nature Phys.* **2** (2006), no. 6 397–401.

[121] A. W. Kinross, M. Fu, T. J. Munsie, H. A. Dabkowska, G. M. Luke, S. Sachdev, and T. Imai *Phys. Rev. X* **4** (2014) 031008.

[122] C. M. Morris, R. Valdés Aguilar, A. Ghosh, S. M. Koohpayeh, J. Krizan, R. J. Cava, O. Tchernyshyov, T. M. McQueen, and N. P. Armitage *Phys. Rev. Lett.* **112** (2014) 137403.

[123] Q. Faure, S. Takayoshi, S. Petit, V. Simonet, S. Raymond, L.-P. Regnault, M. Boehm, J. S. White, M. Månsson, C. Rüegg, *et. al. Nature Phys.* **14** (2018), no. 7 716–722.

[124] S. K. Niesen, G. Kolland, M. Seher, O. Breunig, M. Valldor, M. Braden, B. Grenier, and T. Lorenz *Phys. Rev. B* **87** (2013) 224413.

[125] R. L. Dally, A. J. R. Heng, A. Keselman, M. M. Bordelon, M. B. Stone, L. Balents, and S. D. Wilson *Phys. Rev. Lett.* **124** (2020) 197203.

[126] A. W. Garrett, S. E. Nagler, D. A. Tennant, B. C. Sales, and T. Barnes *Phys. Rev. Lett.* **79** (1997) 745–748.

[127] D. A. Tennant, C. Broholm, D. H. Reich, S. E. Nagler, G. E. Granroth, T. Barnes, K. Damle, G. Xu, Y. Chen, and B. C. Sales *Phys. Rev. B* **67** (2003) 054414.

[128] K. Sreedhar and P. Ganguly *Inorg. Chem.* **27** (1988), no. 13 2261–2269.

[129] F. Sapina, J. Rodriguez-Carvajal, M. Sanchis, R. Ibanez, A. Beltran, and D. Beltran *Solid State Commun.* **74** (1990), no. 8 779–784.

[130] K. Okuda, S. Noguchi, K. Konishi, H. Deguchi, and K. Takeda *J. Magn. Magn. Mater.* **104-107** (1992) 817–818. Proceedings of the International Conference on Magnetism, Part II.

[131] Y. Mizuno, T. Tohyama, S. Maekawa, T. Osafune, N. Motoyama, H. Eisaki, and S. Uchida *Phys. Rev. B* **57** (1998) 5326–5335.

[132] S. Ebisu, T. Komatsu, N. Wada, T. Hashiguchi, P. Kichambare, and S. Nagata *J. Phys. Chem. Solids* **59** (1998), no. 9 1407–1416.

[133] V. Y. Yushankhai and R. Hayn *Europhys. Lett.* **47** (1999), no. 1 116–121.

[134] R. Weht and W. E. Pickett *Phys. Rev. Lett.* **81** (1998) 2502–2505.

[135] H. J. Xiang, C. Lee, and M. H. Whangbo *Phys. Rev. B* **76** (2007) 220411.

[136] M. Boehm, S. Coad, B. Roessli, A. Zheludev, M. Zolliker, P. Böni, D. M. Paul, H. Eisaki, N. Motoyama, and S. Uchida *Europhys. Lett.* **43** (1998), no. 1 77–82.

[137] W. E. A. Lorenz, R. O. Kuzian, S.-L. Drechsler, W.-D. Stein, N. Wizent, G. Behr, J. Málek, U. Nitzsche, H. Rosner, A. Hiess, *et. al. Europhys. Lett.* **88** (2009), no. 3 37002.

[138] S. Giri, H. Chudo, H. Nakamura, and M. Shiga *J. Alloys Compd.* **326** (2001), no. 1 61–64.

[139] M. Enderle, C. Mukherjee, B. Fåk, R. K. Kremer, J.-M. Broto, H. Rosner, S.-L. Drechsler, J. Richter, J. Malek, *et. al. Europhys. Lett.* **70** (2005), no. 2 237–243.

[140] A. U. B. Wolter, F. Lipps, M. Schäpers, S.-L. Drechsler, S. Nishimoto, R. Vogel, V. Kataev, B. Büchner, H. Rosner, M. Schmitt, *et. al. Phys. Rev. B* **85** (2012) 014407.

[141] K. C. Rule, B. Willenberg, M. Schäpers, A. U. B. Wolter, B. Büchner, S.-L. Drechsler, G. Ehlers, D. A. Tennant, R. A. Mole, J. S. Gardner, *et. al. Phys. Rev. B* **95** (2017) 024430.

[142] T. Hikihara, L. Kecke, T. Momoi, and A. Furusaki *Phys. Rev. B* **78** (2008) 144404.

[143] J. Sudan, A. Lüscher, and A. M. Läuchli *Phys. Rev. B* **80** (2009) 140402.

[144] S. Nishimoto, S.-L. Drechsler, R. Kuzian, J. Richter, and J. van den Brink *Phys. Rev. B* **92** (2015) 214415.

[145] A. V. Chubukov *Phys. Rev. B* **44** (1991) 4693–4696.

[146] A. V. Syromyatnikov *Phys. Rev. B* **86** (2012) 014423.

[147] D. Dmitriev and V. Y. Krivnov *Russ. J. Phys. Chem. B* **3** (2009), no. 2 280–285.

[148] S. Nishimoto, S.-L. Drechsler, R. O. Kuzian, J. van den Brink, J. Richter, W. E. A. Lorenz, Y. Skourski, R. Klingeler, and B. Büchner *Phys. Rev. Lett.* **107** (2011) 097201.

[149] H. Bethe *Z. Phys.* **71** (1931), no. 3 205–226.

[150] D. V. Dmitriev and V. Y. Krivnov *Phys. Rev. B* **79** (2009) 054421.

[151] F. D. M. Haldane *J. Phys. C: Solid State Phys.* **15** (1982), no. 36 L1309–L1313.

[152] T. Schneider *Phys. Rev. B* **24** (1981) 5327–5339.

[153] B. W. Southern, R. J. Lee, and D. A. Lavis *J. Phys.: Condens. Matter* **6** (1994), no. 46 10075–10092.

[154] G. Huang, Z.-P. Shi, X. Dai, and R. Tao *J. Phys.: Condens. Matter* **2** (1990), no. 50 10059–10067.

[155] M. Hood *J. Phys. C: Solid State Phys.* **17** (1984), no. 8 1367–1373.

[156] L. Kecke, T. Momoi, and A. Furusaki *Phys. Rev. B* **76** (2007) 060407.

[157] H. Onishi *J. Phys.: Conf. Ser.* **592** (2015) 012109.

[158] J. B. Torrance and M. Tinkham *Phys. Rev.* **187** (1969) 595–606.

[159] R. Hoogerbeets, A. J. van Duyneveldt, A. C. Phaff, C. H. W. Swuste, and W. J. M. de Jonge *J. Phys. C: Solid State Phys.* **17** (1984), no. 14 2595–2608.

[160] E. Chung, G. McIntyre, D. M. Paul, G. Balakrishnan, and M. Lees *Phys. Rev. B* **68** (2003), no. 14 144410.

[161] S. Kawamata, K. Okuda, and K. Kindo *J. Magn. Magn. Mater.* **272-276** (2004) 939–940.

[162] S. Toth and B. Lake *J. Phys.: Condens. Matter* **27** (2015), no. 16 166002.

[163] T. Oguchi *Phys. Rev.* **117** (1960) 117–123.

[164] H. Ohta, N. Yamauchi, T. Nanba, M. Motokawa, S. Kawamata, and K. Okuda *J. Phys. Soc. Japan* **62** (1993), no. 2 785–792.

[165] T. Huberman, R. Coldea, R. A. Cowley, D. A. Tennant, R. L. Leheny, R. J. Christianson, and C. D. Frost *Phys. Rev. B* **72** (2005) 014413.

[166] T. Barnes *Phys. Rev. B* **67** (2003) 024412.

[167] M. Nayak and F. Mila *Phys. Rev. B* **105** (2022) 094407.

[168] B. Kim, H. Jin, S. Moon, J.-Y. Kim, B.-G. Park, C. Leem, J. Yu, T. Noh, C. Kim, S.-J. Oh, *et. al. Phys. Rev. Lett.* **101** (2008), no. 7 076402.

[169] K. Matsuhira, M. Wakeshima, Y. Hinatsu, and S. Takagi *J. Phys. Soc. Japan* **80** (2011), no. 9 094701.

[170] H. Sagayama, D. Uematsu, T.-h. Arima, K. Sugimoto, J. Ishikawa, E. O'farrell, and S. Nakatsuji *Phys. Rev. B* **87** (2013), no. 10 100403.

[171] K. Tomiyasu, K. Matsuhira, K. Iwasa, M. Watahiki, S. Takagi, M. Wakeshima, Y. Hinatsu, M. Yokoyama, K. Ohoyama, and K. Yamada *J. Phys. Soc. Japan* **81** (2012), no. 3 034709.

[172] X. Wan, A. M. Turner, A. Vishwanath, and S. Y. Savrasov *Phys. Rev. B* **83** (2011), no. 20 205101.

[173] V. N. Kotov, M. Elhajal, M. E. Zhitomirsky, and F. Mila *Phys. Rev. B* **72** (2005), no. 1 014421.

[174] M. Elhajal, B. Canals, R. Sunyer, and C. Lacroix *Phys. Rev. B* **71** (2005), no. 9 094420.

[175] L. Savary, E.-G. Moon, and L. Balents *Phys. Rev. X* **4** (2014), no. 4 041027.

[176] D. Pesin and L. Balents *Nature Phys.* **6** (2010), no. 5 376–381.

[177] W. Witczak-Krempa and Y. B. Kim *Phys. Rev. B* **85** (2012), no. 4 045124.

[178] A. B. Sushkov, J. B. Hofmann, G. S. Jenkins, J. Ishikawa, S. Nakatsuji, S. Das Sarma, and H. D. Drew *Phys. Rev. B* **92** (2015), no. 24 241108.

[179] K. Ueda, J. Fujioka, B. J. Yang, J. Shiogai, A. Tsukazaki, S. Nakamura, S. Awaji, N. Nagaosa, and Y. Tokura *Phys. Rev. Lett.* **115** (2015), no. 5 056402.

[180] K. Ueda, J. Fujioka, and Y. Tokura *Phys. Rev. B* **93** (2016), no. 24 245120.

[181] M. Nakayama, T. Kondo, Z. Tian, J. J. Ishikawa, M. Halim, C. Bareille, W. Malaeb, K. Kuroda, T. Tomita, S. Ideta, *et. al. Phys. Rev. Lett* **117** (2016), no. 5 056403.

[182] S. Nakatsuji, Y. Machida, Y. Maeno, T. Tayama, T. Sakakibara, J. van Duijn, L. Balicas, J. Millican, R. Macaluso, and J. Y. Chan *Phys. Rev. Lett.* **96** (2006), no. 8 087204.

[183] F. F. Tafti, J. J. Ishikawa, A. McCollam, S. Nakatsuji, and S. R. Julian *Phys. Rev. B* **85** (2012), no. 20 205104.

[184] K. Ueda, J. Fujioka, C. Terakura, and Y. Tokura *Phys. Rev. B* **92** (2015), no. 12 121110.

[185] Z. Porter, E. Zoghlin, S. Britner, S. Husremovic, J. P. Ruff, Y. Choi, D. Haskel, G. Laurita, and S. D. Wilson *Phys. Rev. B* **100** (2019), no. 5 054409.

[186] R. Kaneko, M.-T. Huebsch, S. Sakai, R. Arita, H. Shinaoka, K. Ueda, Y. Tokura, and J. Fujioka *Phys. Rev. B* **99** (2019), no. 16 161104.

[187] A. Banerjee, J. Sannigrahi, S. Giri, and S. Majumdar *Phys. Rev. B* **96** (2017), no. 22 224426.

[188] W. Zhu, M. Wang, B. Seradjeh, F. Yang, and S. Zhang *Phys. Rev. B* **90** (2014), no. 5 054419.

[189] G. Prando, R. Dally, W. Schottenhamel, Z. Guguchia, S. H. Baek, R. Aeschlimann, A. U. B. Wolter, S. D. Wilson, B. Büchner, and M. J. Graf *Phys. Rev. B* **93** (2016), no. 10 104422.

[190] J. N. Millican, R. T. Macaluso, S. Nakatsuji, Y. Machida, Y. Maeno, and J. Y. Chan *Mater. Res. Bull.* **42** (2007), no. 5 928–934.

[191] K. Momma and F. Izum *J. Appl. Crystallogr.* **44** (2011), no. 6 1272–1276.

[192] A. P. Hammersley, S. O. Svensson, H. M, and D. Fitch, A N & Hausermann *High Press. Res.* **14** (1996), no. 4-6 235–248.

[193] X. Qiu, J. W. Thompson, and S. J. Billinge *J. Appl. Crystallogr.* **37** (2004), no. 4 678–678.

[194] D. Haskel, Y. Tseng, J. Lang, and S. Sinogeikin *Rev. Sci. Instrum.* **78** (2007), no. 8 083904.

[195] F. V. Sears *Neutron News* **3** (1992), no. 3 26–37.

[196] H. Takatsu, K. Watanabe, K. Goto, and H. Kadowaki *Phys. Rev. B* **90** (2014), no. 23 235110.

[197] S. M. Disseler, C. Dhital, A. Amato, S. R. Giblin, C. de la Cruz, S. D. Wilson, and M. J. Graf *Phys. Rev. B* **86** (2012) 014428.

[198] J. J. Ishikawa, E. C. T. O'Farrell, and S. Nakatsuji *Phys. Rev. B* **85** (2012), no. 24 245109.

[199] K. Ueda, J. Fujioka, Y. Takahashi, T. Suzuki, S. Ishiwata, Y. Taguchi, M. Kawasaki, and Y. Tokura *Phys. Rev. B* **89** (2014), no. 7 75127.

[200] B. Thole, P. Carra, F. Sette, and G. van der Laan *Phys. Rev. Lett.* **68** (1992), no. 12 1943.

[201] J. Clancy, N. Chen, C. Kim, W. Chen, K. Plumb, B. Jeon, T. Noh, and Y.-J. Kim *Phys. Rev. B* **86** (2012), no. 19 195131.

[202] B. T. Thole and G. van der Laan *Phys. Rev. B* **38** (1988) 3158–3171.

[203] B. T. Thole and G. van der Laan *Phys. Rev. A* **38** (1988) 1943–1947.

[204] G. van der Laan and B. T. Thole *Phys. Rev. Lett.* **60** (1988) 1977–1980.

[205] M. Laguna-Marco, P. Kayser, J. Alonso, M. Martínez-Lope, M. Van Veenendaal, Y. Choi, and D. Haskel *Phys. Rev. B* **91** (2015), no. 21 214433.

[206] L. Guo, N. Campbell, Y. Choi, J.-W. Kim, P. J. Ryan, H. Huyan, L. Li, T. Nan, J.-H. Kang, C. Sundahl, *et. al. Phys. Rev. B* **101** (2020), no. 10 104405.

[207] D. Haskel, G. Fabbris, M. Zhernenkov, P. Kong, C. Jin, G. Cao, and M. Van Veenendaal *Phys. Rev. Lett.* **109** (2012), no. 2 027204.

[208] W. Yang, W. Zhu, H. Zhou, L. Ling, E. Choi, M. Lee, Y. Losovyj, C.-K. Lu, and S. Zhang *Phys. Rev. B* **96** (2017), no. 9 094437.

[209] H. Liu, D. Liang, S. Chen, J. Bian, Y. Feng, and B. Fang *Wuhan Univ. J. Nat. Sci* **22** (2017), no. 3 215–222.

[210] Y. Takikawa, S. Ebisu, and S. Nagata *J. Phys. Chem. Solids* **71** (2010), no. 11 1592–1598.

[211] H.-J. Koo, M.-H. Whangbo, and B. J. Kennedy *J. Solid State Chem.* **136** (1998), no. 2 269–273.

[212] A. W. Sleight *Mater. Res. Bull.* **9** (1974), no. 9 1177–1184.

[213] J. Clancy, H. Gretarsson, E. Lee, D. Tian, J. Kim, M. Upton, D. Casa, T. Gog, Z. Islam, B.-G. Jeon, *et. al. Phys. Rev. B* **94** (2016), no. 2 024408.

[214] F. Sun, H. Zheng, Y. Liu, E. Sandoval, C. Xu, J. Xu, C. Jin, C. Sun, W. Yang, H. Mao, *et. al. Phys. Rev. B* **98** (2018), no. 8 085131.

[215] G. Giampaoli, J. Li, A. P. Ramirez, A. W. Sleight, and M. Subramanian *Inorg. Chem.* **56** (2017), no. 8 4706–4715.

[216] B. J. Kennedy *J. Solid State Chem.* **123** (1996), no. 1 14–20.

[217] H. Guo, C. Ritter, and A. Komarek *Phys. Rev. B* **94** (2016), no. 16 161102.

[218] S. M. Disseler, C. Dhital, T. C. Hogan, A. Amato, S. R. Giblin, C. de la Cruz, A. Daoud-Aladine, S. D. Wilson, and M. J. Graf *Phys. Rev. B* **85** (2012), no. 17 174441.

[219] U. Widyaiswari, J. Angel, H. Nomura, T. Taniguchi, K. Matsuhira, B. Kurniawan, and I. Watanabe *Riken: Accel. Prog. Report* **52** (2019).

[220] G. Prando, P. Telang, S. D. Wilson, M. J. Graf, and S. Singh *Phys. Rev. B* **101** (2020) 174435.

[221] X. Chen, T. Hogan, D. Walkup, W. Zhou, M. Pokharel, M. Yao, W. Tian, T. Z. Ward, Y. Zhao, D. Parshall, *et. al. Phys. Rev. B* **92** (2015), no. 7 075125.

[222] T. Arima *J. Phys. Soc. Japan* **82** (2012), no. 1 013705.

[223] S. Tardif, S. Takeshita, H. Ohsumi, J.-i. Yamaura, D. Okuyama, Z. Hiroi, M. Takata, and T.-h. Arima *Phys. Rev. Lett.* **114** (2015), no. 14 147205.